# Electronic & Ionic Conduction & Correlated Dielectric Relaxations in Molecular Solids

MANESH ZACHARIAH

**Supervisors:**

Dr. Roberto MACOVEZ

Prof. Dr. Josep Llus TAMARIT MUR

**Barcelona, September 2016**

PhD programme in Computational and Applied Physics

Departament de Fisica


UNIVERSITAT POLITÈCNICA DE CATALUNYA BARCELONATECH

# Abstract

The study of crystalline materials has played a prominent role in the traditional approach to solid state physics: the study of the solid state emerged from crystallography, and the basic theories of solid state physics were formulated for the case of crystalline matter. However, many practical applications use materials which are more abundant in nature, and that are weakly or strongly disordered, such as molecular crystals, glasses (amorphous solids), plastic crystals, liquids, liquid crystals, etc. In glasses, for example, the arrangement of the constituent atoms or molecules lacks the slightest vestige of long range order. The advances that have been made in the physics and chemistry of amorphous solids have contributed to the Nobel awards earned by N. F. Mott, P. W. Anderson, and P. J. Flory. Much of the intellectual fascination about disordered solids arises from the fact that scientific insight must be achieved without the help of the well-mastered solid-state concepts associated with periodicity which describe the crystalline solid state. While some old approaches remain useful for disordered solids, significant advances have been made only by developing new approaches such as localization theory and percolation.

From an applied perspective, much of the intense research interest in disordered solids is driven by the technological importance of these materials, which includes the use of ultra-transparent optical fibers in telecommunications, the use of amorphous semiconductors in xerography and solar cells, the use of liquid crystals in display technology, and the ubiquitous everyday uses of polymers and organic glasses as structural materials. From a fundamental viewpoint, a deeper understanding of the properties of disordered materials is needed to explore the many fascinating condensed matter issues related with disorder.

Disordered materials display low electrical conductivities than their crystalline counterparts, due to localization of valence electrons, so that electron hopping is the

main charge transport mechanism. On the other hand, some disordered materials are able to conduct electricity by the diffusion of ions through interstitial sites and their ionic conductivity is normally higher than the crystalline counterparts. The disorder of these materials may be dynamic, rather than static, and the study of the dynamics both in the glass state and at higher temperature helps unveiling the origin of the physical properties of the glass state. The type of disorder present in a material, for example, whether it only involves orientational degrees of freedom (as in a plastic crystal) or only translational (as in a liquid crystal) or both (as in window glass), or whether it is static (as in amorphous solids) or dynamic (as in a liquid) all these factors have an important impact on the conductivity and other physical properties such as viscosity, plasticity or stiffness.

This thesis focuses on the experimental study of the conduction properties and molecular dynamics of molecular solids made of fullerene derivatives, and plastic co-crystals based on the succinonitrile molecule. The studied materials display, depending on the case, electronic, protonic and ionic conduction. The experimental technique employed to investigate these materials is broadband dielectric spectroscopy, which allows studying simultaneously molecular dynamics and electrical conductivity in broad range of frequency and temperature (Chapter 3).

Fullerenes are relatively simple molecules; pristine fullerenes such as $C_{60}$ and $C_{70}$ and several of their derivatives are excellent electron acceptor and n-type semiconductors, in some cases with high electron mobility. Some fullerene solids even display superconductivity at low temperatures, while some fullerene salts with small cations show remarkably high ionic conductivities. We study in particular the intrinsic and water-induced charge transport in a highly symmetric organic fullerene derivative, $C_{60}(ONa)_{24}$, which is synthesized as a polycrystalline hydrate and which can be obtained as a pure material by heating to sufficiently high temperature. We show that while the pure material is an n-type (electron) semiconductor, exposing it to humid atmosphere leads to a dramatic conductivity enhancement which is due to charge transport through the hydration layers present on the surface of the crystalline grains, likely due to a proton exchange mechanism. We also show that the dc conductivity of the hydrate is strongly temperature dependent across the dehydration

process, and that both pure and hydrated materials display a conductivity-related dynamic process associated with accumulation of electrons at grain boundaries (Chapter 4). We argue that presence of water has strong impact on the conduction properties, both in the case of the dc transport and the frequency-dependent charge-accumulation dynamics. In Chapter 5 we focus on a brominated fullerene derivative, namely $C_{60}Br_6$, which shows n-type electronic conduction below room temperature and a non-trivial phase behavior. Finally, in Chapter 6 we analyze the relaxation dynamics and the ionic conductivity of plastic-crystalline ionic conductors based on the succinonitrile ($C_4H_4N_2$) molecule, which behave as a solid ion or proton conductor in the presence of ionic impurities or when doped with acids or lithium salts, suggesting a possible application as plastic electrolyte. We observe that the plastic co-crystals of succinonitrile with a similar molecule, glutaronitrile ($C_5H_6N_2$), represent the first ever known plastic crystals to display a perfect correlation between the ion drift and the on-site reorientational dynamics. These surprising results, never reported before in an ordered solid, are interpreted in terms of a perfect correlation between the time scale of translational diffusion and that of purely reorientational on-site dynamics, which is reminiscent of the similar relaxation timescales of ethanol in its supercooled liquid and plastic-crystalline phases. Doping the co-crystals with lithium salts boosts the conductivity but breaks such perfect correlation, which indicates that the rotation-drift correlation is only valid when charge transport is dominated by self-diffusion of molecular ions intrinsic to succinonitrile or glutaronitrile, while the motion of smaller atomic ($Li^+$) ions is decoupled from the molecular dynamics.

# Contents

# Chapter 1

# Introduction

The physics of disordered materials is a lively subfield of condensed matter physics. In nature disordered materials are more common than the crystalline materials. Crystalline solids have translational and orientational symmetry: the constituent particles (such as atoms, molecules or ions) are arranged in a highly ordered microscopic structure, forming a crystal lattice that extends in all directions. Disordered materials have a less ordered structure, or may lack any long-range order, as a liquid or a gas. The disordered materials have many advantages such as being easier and cheaper to be manufactured than (single or poly) crystalline ones. For example, organic semiconductors such as conjugated polymers or fullerene derivatives are soluble and can thus be deposited from the liquid phase to print low-cost, low-weight circuits and devices on flexible substrates. The study of disordered materials was initially stimulated by the discovery of the semiconducting glasses, such as amorphous selenium and chalcogenide glasses, obtained by quenching from the melts. Such glassy semiconductors first gave rise to the hope that, in device applications based on the motion of electronic charge carriers, one would be able to replace rather expensive crystalline semiconductors (such as crystalline silicon) by

much cheaper and better manufacturable semiconductor glasses. In the 1960s and 1970s this caused a real burst in experimental and theoretical study of glassy semiconductors.[1,2]

In practice, disordered semiconductors have poorer electronic conduction properties than their crystalline counterparts, leading to lower-efficiency devices; nonetheless, their lower efficiency is also accompanied by a smaller economic and energy cost for device production. Moreover, some disordered materials are able to conduct electricity not by the motion of electrons but by the diffusion of ions, as in a salt solution, and their ionic conduction properties are in general much better than in their crystalline counterparts, whose ionic conduction is negligible. These features make them interesting materials for low-cost electrical, optoelectronic or electrochemical applications.

## 1.1 Conduction Mechanisms in Condensed Matter

The material property that gives a measure for the magnitude of the current that runs under the application of a certain electric field is the electrical conductivity, σ. Its definition is the local form of Ohm's law, namely, $J = \sigma E$, where J is the current density and E is the electric field. The unit that is most often used for σ is Siemens per centimeter, abbreviated as S/cm. In most materials the conductivity is due to the motion of electrons. The conductivities of such materials vary over many orders of magnitude. A division is made between materials that conduct currents very well, materials that do not (or hardly) conduct any current, even at high temperatures, and materials that have conductivity in between these two extremes. The first class of materials are called conductors or metals. They have a conductivity σ that is typically higher than $10^2$ S/cm at room temperature. The second class of materials are called insulators. Their conductivity is lower than $10^{-8}$ S/cm at room temperature. The materials with conductivities that lie in between these two values are called semiconductors.

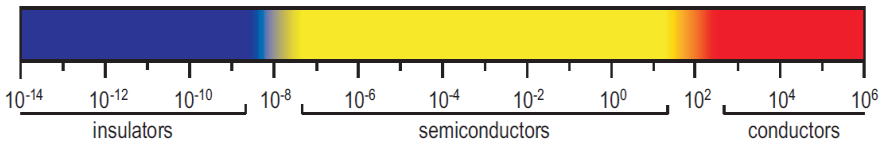


Figure 1.1: Division of materials according to their conductivity levels at room temperature. The conductivities are given in S/cm. The division in conductivity levels is only rough; the real distinction between insulators, semiconductors, and conductors/metals is based on the origin of the charge carriers.

Most known highly conductive materials are metals such as silver, copper, aluminum etc., and they have high electrical conductivity due to their abundance of delocalized electrons that move freely, usually only hindered by the vibrations of the atom cores. In the band theory this is depicted as a half-filled or only partially filled conduction band, so that Fermi level lies within in the conduction band and empty states are readily available for conduction band electrons at no energy cost. As the lattice vibrations increase when the temperature becomes higher, the conductivity of crystalline solids decreases with increasing temperature.

In crystalline semiconductors, the electronic charge carriers, classified respectively as electrons or holes depending on whether they lie in the upper (conduction) band, or if they are empty states on the lower (valence) band, have to overcome an energy barrier before they can contribute to the charge transport. It is easier to overcome this barrier at a higher temperature. Therefore, the conductivity increases with temperature in semiconductors. At a temperature of 0 K, none of the charge carriers can overcome the barrier, leading to vanishing conductivity. This kind of transport is called 'activated'.

A similar behavior is found in disordered materials and in molecular ones, where however the electronic states are not delocalized over many atoms, but are instead localized over small regions or individual molecules, and electric conduction is best visualized as an activated migration/diffusion of such localized electrons. Also in the case of solid ionic conductors ("solid electrolytes"), the ions diffuse through the material matrix in an activated way.[3]

From a microscopic point of view, when an electric field E is established across a ordered or disordered material (whether it is a metal, a semiconductor, or an insulator), the majority free charges (electrons, or holes, or ions) respond by moving with an average velocity $\upsilon$, called the drift velocity, proportional to the field. The mobility $\mu$ is defined as $\upsilon = \mu E$. The relation between electric conductivity and charge-carrier mobility can be easily obtained as $\sigma = ne\mu$, where n is the concentration of (monovalent) charge carriers and *e* is the elementary charge.

There are two reasons for the great interest of researchers in the conducting properties of disordered materials. On the one hand, disordered systems represent a challenging field in a purely academic sense. For many years the theory of how semiconductors perform charge transport was mostly confined to crystalline systems where the constituent atoms are in regular arrays. As mentioned, the discovery of how to make solid amorphous materials and alloys led to an explosion in measurements of the electronic properties of these new materials. However, the concepts often used to describe charge carrier transport in crystalline semiconductors are based on an assumption of long-range order, and so they cannot be applied to electronic transport in disordered materials. On the other hand, the explosion in research into charge transport in disordered materials is related to the various current and potential device applications of disordered inorganic and organic materials in photovoltaics (i.e., as functional materials in solar cells), in electrophotography, in large area displays, in electrical switching threshold and memory devices, in light-emitting diodes, in linear image sensors, and in optical recording devices.[1,4]

Many characteristics of charge transport in disordered materials differ markedly from those in perfect crystalline systems. As mentioned, the charge conduction in disordered system can be either electronic or ionic in nature, thus one should distinguish between disordered materials with ionic conduction and those with electronic conduction. In both cases, however, lattice vibrations provides the energy for hopping transport, and thus, this type of conduction is phonon-assisted and the electric conductivity increases with increasing temperature.[5]

In solid ionic conductors, often thermal energy is sufficient for the mobile ions to dissociate from their site. When an external voltage is applied, ions can drift by hopping over potential barriers to empty sites in the matrix, so that electrical conduction happens by diffusion of ions through the interstitial sites.[6]

In liquid electrolytes, it has been found empirically that the Walden rule is often obeyed well, especially in solutions of large and only weakly coordinating ions in solvents with non-specific ion-solvent interaction. In this case diffusion of ion through the matrix can be described by Stokes Einstein equation: $D = \mu k_B T$, where D is the diffusion coefficient of an ion, $\mu$ is its mobility and $k_B$ is the Boltzmann's constant. This relationship can be extended to ionic liquids and, as we show in this thesis, to some plastic crystals.[7]

The materials investigated in this thesis are small-molecule organic molecular materials. Most organic molecular solids behave as insulating or disordered semiconductors, with low electrical conductivity. In some cases cations or protons are present either as constituents or as impurities, and they can also contribute to and increase the overall conductivity. In some cases, proton conduction in molecular systems can be the result of the presence of water, for example in hydrates, aqueous mixtures and hygroscopic salts. The proton (hydrogen ion) is chemically the simplest type of cation, and one could expect that what has been said so far about solid or liquid electrolytes holds also in the case of proton conductors. However, labile hydrogens are so because they are shared between different atomic species participating in a hydrogen bond. As a result, protonic conduction falls mainly in two categories: it either occurs by a lone proton migration along hydrogen bonds, called "Grotthuss mechanism" or "proton shuttling", or else by migration of a charged molecular proton carrier (such as the $H_3O^+$ cation, for example), called "vehicle mechanism". The vehicle mechanism is really a molecular diffusion mechanism involving protonated or deprotonated molecular ions (for water moieties, for example, such ions may be $H_3O^+$ or $OH^-$ ions). In the Grotthuss mechanism, protons move from hydrogen-bonding moieties such as oxygen or nitrogen by simultaneously breaking a hydrogen bond and forming a new one (no molecular carrier accompanies such proton motion). In order to determine the occurrence of

proton conduction, the dc conductivity is often measured as function of relative humidity (and possibly temperature), although this approach is not conclusive to discriminate between proton and ion conduction as ionic charge transport is also affected by the relative humidity.[8,9,10,11]

As a graphical summary, Figure 1.2 shows the different conduction mechanism in condensed phases[4] (see also section 2.5 of Chapter 2).

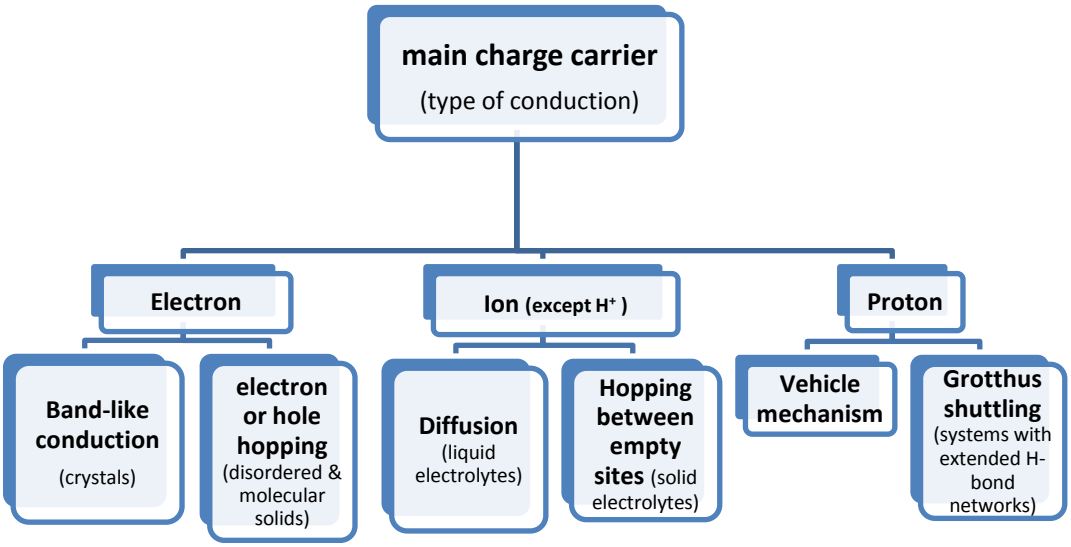


Figure 1.2: Scheme of the different conduction mechanisms in condensed phases.

## 1.2 Molecular Dynamics in Condensed Phases

In physics, a state of matter is one of the distinct forms that matter takes on. Three states of matter are observable in everyday life: solid, liquid and gas. In gaseous state, particles are well separated and in constant motion with no binding force between them. The particles in a liquid or solid are fairly close together and their mutual interactions cannot be ignored; these two states of matter, and those of similar density such as glasses, polymers, colloids, or liquid crystals, constitute what is called "condensed matter". By cooling (lowering the temperature) or compressing (increasing the pressure), the physical state of matter changes from gas to liquid, and

further on from liquid to solid. When the temperature is decreased from the gas phase, interactions between molecules become more and more important and correlations between the motions of different constituents emerge and a new dense phase appears as the liquid, in which molecules still move around and do not display any long-range order. Liquids are perhaps the simplest case of disordered condensed phases, because the structural randomness is most pronounced in this case. As the temperature of the liquid is further decreased, the molecules starts to pack together in a more regular way and reach a higher density state. Then the liquid has crystallized, with each molecule occupying a specific location on a lattice: a solid crystal is formed. In many systems, the liquid phase does not crystallize right away, but rather it can be supercooled below the melting point without acquiring any translational or orientational order. In the "supercooled liquid" state, further cooling forces the system to freeze into a disordered state: a glass has formed[12,13] (see Figure 1.3). In some molecular crystals the centers of mass of the molecules form a lattice, but the molecular orientations are dynamically or statically disordered. In the case of dynamic orientational disorder, the orientational degrees of freedom of the molecules give rise to a characteristic state, called "plastic phase", which exists between the liquid phase and the perfectly crystalline phase. The molecular compounds which display a plastic state are called orientationally disordered crystals (ODIC).[14] The dynamic orientational disorder can freeze yielding glassy crystals or orientational glass (OG). Another class of disordered phase called liquid crystals in which molecules keep an at least average orientational order but organize in layers with inner translational disorder.[15]

In addition to the translational and orientational disorder, another type of disorder that can be present in molecular materials is the conformational disorder. This can be displayed by materials whose constituent molecules can exist in more than one possible isomeric form. If different molecular isomers are present in the liquid phase, they are usually preserved in the glass phase and they may even be present in the crystalline or ODIC phases (conformationally disordered materials may also display at the same time also translational and/or orientational disorder).

The structural glassy state can be defined as a state with a collective molecular motion ("relaxation") time above 100 seconds or equivalently a state in which the viscosity takes a value of the order of $\eta = 10^{13}$ poise. The temperature at which the glass transition takes place is called glass transition temperature, $T_g$ and it is different for different cooling rates due to the dynamic character of the glass transition, which is a kinetic transition rather than a thermodynamic one, although this is still in a lively discussion.[16] A smaller cooling rate allows the sample to stay closer to equilibrium (i.e., the supercooled liquid state) until lower temperatures.

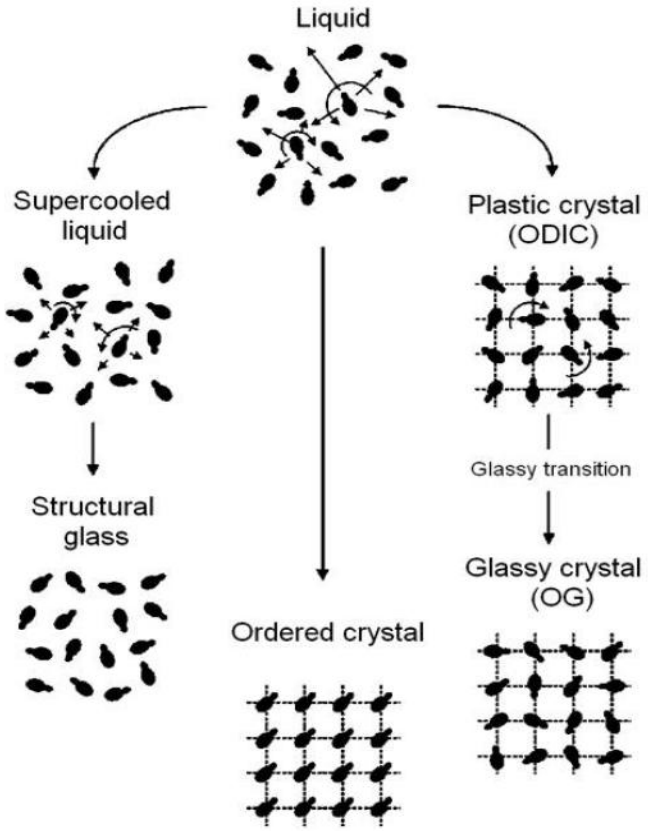


Figure 1.3: Schematic representation of the possible transitions from the liquid state of dipolar molecules into a structural glass (SG), an ordered crystal or an orientational glassy phase (OG).[14]

In the study of glass-forming system, the most important dynamic process is the so-called primary (α) relaxation process, which corresponds to the cooperative, collective rearrangement of the constituent molecules and is closely associated with the glass transition.[17] The frequency of the α process decreases with decreasing temperature, and displays in fact a continuous, dramatic slow-down by several decades in a short temperature interval upon approaching $T_g$. Other molecular dynamic processes can occur in addition to the primary relaxation. These molecular motions are usually less cooperative and occur at longer frequency than the α relaxation, and are called secondary (β) relaxations. These secondary relaxations may be quasi single molecule motions,[18] or else correspond to the motion of mobile side groups or parts of the constituent molecule.

## 1.3 Materials of Choice and Main Experimental Tool

### 1.3.1 Fullerenes and their derivatives

Fullerenes are the fourth known allotrope of carbon after diamond, graphite and amorphous carbon. They exist in the form of hollow molecular cages of quasi-spherical or ellipsoidal shape, as nested cages (carbon onions), and as hollow or nested tubes (carbon nanotubes). An interesting type of fullerene is the bukmintserfullerene $C_{60}$, which is built up from 60 carbon atoms in alternating hexagonal and pentagonal rings to form a shape similar to a football (see Figure 1.4). The structure of a buckminsterfullerene is a truncated icosahedron with 60 vertices and 32 faces (20 hexagons and 12 pentagons where no pentagons share a vertex) with a carbon atom at the vertices of each polygon and a bond along each polygon edge (each carbon atom in the structure is bonded covalently with 3 others). The van der Waals diameter of the $C_{60}$ molecule is approximately 1 nm.

Fullerenes and several of its derivatives are excellent organic semiconductors, with some rather unique features, such as high electron mobility and low LUMO level. They have therefore been used extensively as the

active material in OFETs, and as the electron acceptor material in Organic Photovoltaics (OPV) devices.[19,20]

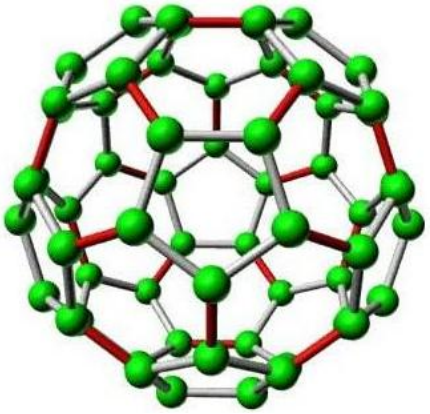

Figure 1.4: Molecular structure of $C_{60}$.

In the room-temperature solid phase of $C_{60}$, the molecules form a (face-centered) cubic lattice and rotate very rapidly, resulting in an orientationally disordered phase. Below 260 K this free-rotor motion is reduced to a ratcheting motion between two preferred orientations.[21, 22, 23] Such order-disorder phase transition displays a temperature hysteresis of 5 K, and takes place at unusually high temperature compared with other systems. The merohedral twinning motion of the $C_{60}$ molecules finally freezes out at a glassy transition at 90 K, below which the lattice structure is simple cubic. What makes $C_{60}$ a nice "playground" to study organic solids are its simple chemical formula, its symmetric shape, and its ability to form many different compounds with other elements or organic molecules. When salts of $C_{60}$ ("fullerides") are formed with alkali metals, $C_{60}$ converts from a semiconductor into a relatively good organic electronic conductor, and even to a superconductor at low temperature.[24] Some alkali fullerides even display ionic conduction.[25]

In their pure form, fullerenes and their derivatives form electrically insulating or semiconducting solid-state phases. Since fullerenes and their derivatives are electron acceptors, they typically behave as "n-type semiconductors", in which charge carriers are electrons in the upper band derived from empty molecular orbitals rather

than holes in the lower band derived from filled molecular orbitals. If cations or protons present either as constituents or as impurities, can also contribute to and even dominate the overall charge transport.[26] In this thesis we have studied two fullerene derivatives, namely $C_{60}(ONa)_{24,}$ which is a strongly hygroscopic material that even forms a crystalline hydrate, and $C_{60}Br_6$ a dipolar bromofullerene derivative. Both display electronic hopping conduction in suitable temperature ranges.

### 1.3.2 Succinonitrile (SN)

The succinonitrile molecule ($N{\equiv}C{-}CH_2{-}CH_2{-}C{\equiv}N$) forms a plastic crystalline phase with significant structural disorder, resulting in greater mechanical plasticity and enhanced self-diffusion compared with most other plastic crystals (including solid $C_{60}$, which displays no visible mechanical plasticity) (Figure 1.5). The orientationally disordered phase also displays conformational disorder, with most conformers possessing a dipole moment, which leads to a dielectric constant of 55 at room temperature in the solid state.[27, 28,29] In contrast to other plastic crystals, it is difficult to supercool and at $T < 233$ K the material transforms into an orientationally ordered crystal. The plastic-crystalline phase of succinonitrile has (body centered) cubic structure; the disorder in such phase is associated both with isomeric fluctuations involving a rotation about the central C−C bond of the molecules, and to molecular jumps from one diagonal position of the bcc cell to another.[30,31,32]

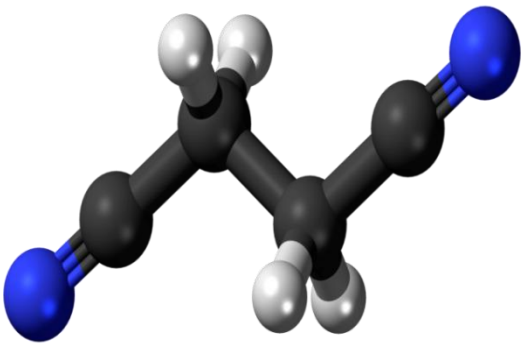

Figure 1.5: Molecular structure of Succinonitrile.

The plastic-crystal phase of SN is limited to the temperature range of about 233 - 331 K. However, the addition of the related molecular compound glutaronitrile ($N{\equiv}C{-}(CH_2)_3{-}C{\equiv}N$) strongly extends the plastic-crystalline region, enabling the transition into an orientational glass. In this thesis we study the conduction properties, phase behavior, and molecular dynamics of co-crystals of succinonitrile with two other nitriles (glutaronitrile and acetonitrile), both pure and doped with lithium salts. We find that the succinonitrile-rich co-crystals with glutaronitrile display a perfect correlation between the molecular self-diffusion and the on-site reorientational dynamics. In detail, these co-crystals are found to obey the Walden rule[7] which is usually seen in (ideal) liquid electrolytes.

### 1.3.3 Method

In order to probe molecular dynamics and charge transport in disorder system we used broadband dielectric spectroscopy (BDS). Due to its unique ability to probe molecular fluctuations and charge transport over a broad frequency and temperature range, BDS has proven indispensable in the quest to understand the underlying mechanisms of charge transport and dynamic motion in disordered systems. Its advantage is that it allows studying in the same experiment both the conduction properties and the dielectric polarization response of a sample. BDS studies can be performed on a very wide range of disordered organic and inorganic systems ranging from amorphous semiconductors and glasses to metal-cluster compounds to polymers and polymer composites.[33,34,35]

## 1.4 Outline of the Thesis

This thesis focuses on the molecular dynamics and conduction mechanisms of three different materials. Chapter 2 gives an introduction to the theoretical concepts of the dielectric relaxation processes and charge transport mechanisms in disordered systems, while Chapter 3 provides information about the experimental techniques and the methods used for the acquisition and analysis of experimental data. The presentation, analysis and discussion of the obtained results are presented in the

following three chapters (one for each organic solid under scrutiny). Chapters 4 and 5 discuss the conductivity mechanism and related dielectric loss in two fullerene derivatives. In particular, Chapter 4 deals with solid $C_{60}(ONa)_{24}$, which is studied both in pure form and as crystalline hydrate, and is found to display both electronic and protonic conduction. Chapter 5 deals with the electron transport properties and phase behavior of the $C_{60}Br_6$ derivative. The last chapter on experimental results (chapter 6) deals with the cooperative and non-cooperative relaxations and ionic conduction in pure and lithium-salt doped succinonitrile co-crystals.

# References:


[1] Safa Kasap and Peter Capper, *Handbook of Electronic and Photonic Materials*, Springer **2006**.

[2] Brutting, W.; Adachi, Ch. (Ed.s). *Physics of Organic Semiconductors*, 2nd Ed. Wiley **2012**.

[3] Stallinga, P. Electronic transport in organic materials: Comparison of band theory with percolation/(variable range) hopping theory, *Adv. Mater.* **2011**, 23, 3356–3362.

[4] Baranovski, S. *Charge Transport in Disordered Solids with Applications in Electronics*. Wiley **2006**.

[5] van Staveren, M. P. J.; Brom, H. B.; de Jongh, L. J. Metal-Cluster Compounds and Universal Features of the Hopping Conductivity of Solids. *Phys. Rep.* **1991**, 208, 1-96.

[6] Kwan Chi Kao, *Dielectric phenomena in solids with emphasis on physical concepts of electronic processes,* Elsevier **2004**.

[7] Walden, P. Z. Organic solvents and Ionization Media. III. Interior Friction and its Relation to Conductivity. *Phys. Chem.* 1**906**, 55, 207-246.

[8] Cramer, C.; De, S.; and Schönhoff, M. Time-Humidity-Superposition Principle in Electrical Conductivity Spectra of Ion-Conducting Polymers. *Phys. Rev. Lett.* **2011**, 107, 028301.

[9] Gränicher, H.; Jaccard, C.; Scherrer, P.; Steinemann, A. Dielectric Relaxation and the Electrical Conductivity of Ice Crystals. *Discuss. Faraday Soc.* **1957**, 23, 50–62.

[10] Vilčiauskas, L.; Tuckerman, M. E.; Bester, G.; Paddison, S. J.; Kreuer, K. D. The Mechanism of Proton Conduction in Phosphoric Acid. *Nat. Chem.* **2012**, 4, 461–466.

[11] Knight, C and Voth, G. A. The Curious Case of the Hydrated Proton. *Acc. Chem. Res.* **2012**, 45, 101–109.

[12] Anderson,P. W. Through the Glass Lightly. *Science* **1995**, 267, 1615-1616.

[13] Lunkenheimer, P.; Schneider, U.; Brand, R and Loidl, A. Glassy Dynamics. *Contemporany Physics* **2000**, 41, 15-36.

[14] Brand, R.; Lunkenheimer, P. and Loidl, A. Relaxation Dynamics in Plastic Crystals. *J Chem. Phys.* **2002**, 116, 10386-10400.

[15] Drozd-Rzoska, A.; Rzoska, S.J.; Pawlus, S.; Martinez-Garcia, J.C.; Tamarit, J.Ll.; Evidence for Critical-Like Behavior in Ultraslowing Glass-Forming Systems. *Phys. Rev. E* **2010,** 82, 031501.

[16] Albert, S.; Baue, Th.; Michl, M.; Biroli, G.; Bouchaud, J.-P.; Loidl, A.; Lunkenheimer, P.; Tourbot, R.; Wiertel-Gasquet, C.; Ladieu, F. Fifth-Order Susceptibility Unveils Growth of Thermodynamic Amorphous Order In Glass-Formers. *Science* **2016**, 352, 1308-1311.

[17] Angell, C. A.; Ngai, K. L.; McKenna, G. B.; McMillan, P. F.; Martin, S. F. Relaxation in Glassforming Liquids and Amorphous Solids. *J. Appl. Phys.* **2000**, 88, 3113-3115.

[18] Johari, G.P. and Goldstein, M. Viscous Liquids and the Glass Transition. II. Secondary Relaxations in Glasses of Rigid Molecules. *J. Chem. Phys.* **1970**, 53, 2372-2388.

[19] Lai, Y.-Y.; Cheng, Y.-J.; Hsu, C.-S. Applications of Functional Fullerene Materials in Polymer Solar Cells. *Energy Environ. Sci.* **2014,** 7, 1866–1883.

[20] Anthopoulos, T.D.; Singh, B.; Marjanovic, N.; Sariciftci, N.S.; Ramil, A.M.; Sitter, H.; Cölle, M.; de Leeuw, D.M. High Performance N-Channel Organic Field-Effect Transistors and Ring Oscillators Based on $C_{60}$ Fullerene Films. *Appl. Phys. Lett.* **2006**, 89, 213504.

[21] Vaughan, G. B. M.; Chabre, Y.; Dubois, D. Effect of Stacking Disorder on the Orientational Ordering Transition of Solid $C_{60}$. *Europhys. Lett.* **1995**, 31, 525-530.

[22] Tycko, R.; Dabbagh, G.; Fleming, R.M.; Haddon, R.C.; Makhija, A.V.; Zahurak, S.M. Molecular Dynamics and the Phase Transition in Solid $C_{60}$. *Phys. Rev. Lett.* **1991**, 67, 1886.

[23] David, W.I.F.; Ibberson, R.M.; Matthewman, J.C.; Prassides, K.; Dennis, T.J.; Hare, J.P.; Kroto, H.W.; Taylor, R.; Walton, D.R.M. Crystal Structure and Bonding of Ordered $C_{60.}$ *Nature* **1991**, 353, 147–149.

[24] Gunnarsson, O. Superconductivity in Fullerides. *Rev. Mod. Phys.* **1997**, 69, 575–606.

[25] Riccò, M.; Belli, M.; Mazzani, M.; Pontiroli, D.; Quintavalle, D.; Janossy, A.; Csanyi, G. Superionic Conductivity in the $Li_4C_{60}$ Fulleride Polymer, *Phys. Rev. Lett.* **2009**, 102 145901.

[26] Mitsari, E.; Romanini, M.; Zachariah, M.; Macovez, R. Solid State Physicochemical Properties and Applications of Organic and Metallo-Organic Fullerene Derivatives. *Curr. Org. Chem.* **2016**, 20, 645–661.

[27] Alarco, P.-J.; Abu-Lebdeh, Y.; Abouimrane, A. and Armand, M. The plastic-crystalline Phase of Succinonitrile as a Universal Matrix for Solid State Ionic Conductors. *Nat. Mater.* **2004**, 3, 476-481.

[28] Derollez, P.; Lefebvre, J.; Descamps, M.; Press, W.; Fontaine, H. Structure of Succinonitrile in its Plastic Phase. *J. Phys. Condens. Matter* **1990**, 2, 6893-6903.

[29] Tamarit, J.Ll.; Rietveld, I.B.; Barrio, M.; Céolin, R. The Relationship between Orientational Disorder and Pressure: The Case Study of Succinonitrile. *J. Molecular Structure* **2014**, 1078, 3-9.

[30] Geirhos, K.; Lunkenheimer, P.; Michl, M.; Reuter, D; Loidl, A. Conductivity Enhancement in Plastic-Crystalline Solid-State Electrolytes. *J. Chem. Phys.* **2015**, 143, 081101.

[31] MacFarlane, D.R.; Forsyth, M. Plastic Crystal Electrolyte Materials: New Perspectives on Solid State Ionics. *Adv. Mater.* **2001**, 13, 957-966.

[32] Bauer, Th.; Köhler, M.; Lunkenheimer, P.; Loidl, A.; Angell, C. A. Relaxation Dynamics and Ionic Conductivity in a Fragile Plastic Crystal. *J. Chem. Phys.* **2010**, 133, 144509.

[33] Kremer, F. and Schönhals, A. Broad Band Dielectric Spectroscopy, Springer Berlin **2003**.

**[34]** Capaccioli, S.; Lucchesi, M.; Rolla, P. A.; Ruggeri, G. Dielectric Response Analysis of a Conducting Polymer Dominated by the Hopping Charge Transport. *J. Phys.: Condens. Matter.* **1998**, 10, 5595–5617.

[35] Lunkenheimer, P. and Lloid, A. Response of Disordered Matter to Electromagnetic Fields. *Phys. Rev. Lett.* **2003**, 91, 207601.

# Chapter 2

# Models of Dielectric Relaxation and Charge Transport in Disordered Systems

## 2.1 Introduction

The history of dielectric theory can be traced back to the pioneering work of Faraday and Maxwell [1] and to later work by Clausius, Mossotti, and Lorentz.[2,3,4] The way in which electromagnetic fields interact with a dielectric medium is described, on a macroscopic level, by Maxwell's equations.[5] Relaxation phenomena related to molecular fluctuations of dipoles and the motion of mobile charge carriers which causes conductivity contributions to the dielectric response may be described in Maxwell's formalism by including them using suitable choices for the permittivity and conductivity of the medium, choices that reflect assumption on the microscopic structure of the material. The present interpretation of the dielectric relaxation correlated to the molecular structure is based on the theory of Debye[6] and subsequent

refinements. In this chapter we discuss the dielectric relaxation theory and charge transport mechanism in disordered organic solids.

The permittivity or dielectric function[7] is a measure of the ability of a material to store a charge from an applied electric field, and can be defined as the ratio of the field strength in vacuum to that in the material for the same distribution of charge. Consider two parallel conducting plates in vacuum, each of area A, separated by a distance d. When a voltage V is applied across the plates, they acquire (free) charges $+Q_f$ and $-Q_f$ per unit area, corresponding to a surface (free) charge density $\sigma_f = \pm Q/A$. The capacitor in vacuum has then capacitance given by:

$$C_0 = \frac{Q_f}{V} = \frac{\varepsilon_0 A}{d} \quad (2.1)$$

$C_0$ is called the empty capacitance, and $\varepsilon_0$ is the vacuum permittivity (or dielectric constant of vacuum, $\varepsilon_0 = 8.854 \times 10^{-12}$ F.m$^{-1}$).

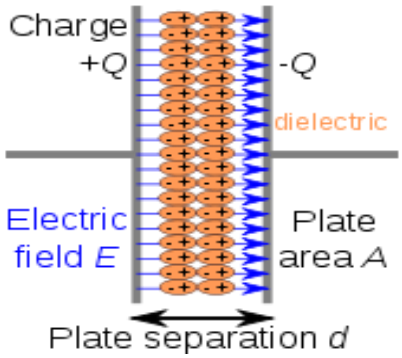


Figure 2.1: Schematic representation of a dielectric material inside a capacitor.

By filling the space between two plates with a dielectric material, under the same potential difference V a larger free charge $Q_f$' will deposit on the metal plates, due to the fact that polarization charges at the surface of the dielectric will screen the electric field inside it. The new capacitance will be given by:

$$C = \frac{Q_f'}{V} = \frac{\varepsilon_0 \varepsilon_r A}{d} \quad (2.2)$$

Here $\varepsilon_r$ is the dimensionless dielectric constant or the relative permittivity, defined by:

(2.3) $$\varepsilon_r = \frac{C}{C_0}$$

When an electric field is applied to a dielectric material, the atomic and/or molecular charges in the dielectric are displaced from their equilibrium position and the material becomes polarized (see Figure 2.1). The macroscopic polarization P is defined as the number of microscopic dipole moment per unit volume and quantifies how the material reacts to an applied electric field. At the surface of the dielectric, the polarization results in bound surface charges which effectively lower the value of the macroscopic field inside the dielectric with respect to the magnitude of the applied field. If the dielectric medium is lineal and isotropic (as it occurs for most liquids, glasses, or disordered solids under not too large applied fields), the polarization P and the macroscopic field E inside the dielectric can be related as:

(2.4) $$P = (\varepsilon_r - 1)\varepsilon_0 E = \chi\varepsilon_0 E$$

where $\chi = \varepsilon_r - 1$ is called susceptibility of the material. $\varepsilon_r$ (or equivalently $\chi$) is a material-dependent and dimensionless quantity that describes the linear response reaction of a material to an electric field.

## 2.2 Polarization Mechanisms

The polarization mechanism can be classified based on the type of material and the constituents that undergo polarization[8].

For very high (i.e., above optical/UV) frequencies even electrons cannot keep up with the changing field, resulting in a relative permittivity $\varepsilon_r = 1$.

When placing a non-polar medium into a capacitor, under the influence of the electric field two types of polarization may arise, known as electronic and atomic polarizations, which are dominant at relatively high frequencies (in the UV, visible, and IR ranges). Electronic polarization takes place on a time scale of $10^{-15}$ s, which lies in the visible or near UV region of the electromagnetic spectrum, while the atomic polarization takes place at a longer time scale of $10^{-12}$ s (IR region).

The electronic polarization ($P_e$) occurs due to the displacement of the negatively charged electron cloud relative to the positive nuclei in the atom and the electron cloud, which can be easily displaced under an applied electric field due to the low mass of the electron. In this way, induced dipole moments arise, producing the electronic polarization.

The atomic polarization ($P_a$) is due to the relative displacement of ions in ionic materials and to molecular vibrations in molecules made up of different atoms. In heteronuclear molecules, the electron shells are distorted and point in the direction of more electronegative atoms. Application of electric field causes the equilibrium position of charges to change, with the inter-atomic separation increasing or decreasing, which leads to a modification of the molecular dipole moment.

If a material contains permanent dipoles, another polarization mechanism may be present in the radiofrequency range or for quasi-static fields, known as “orientational” or “dipolar polarization” (Figure 2.2). When the polar molecule is subjected to an electric field of frequency between 1 Hz and 100 MHz, the permanent dipoles will tend to orient parallel to the applied field,

causing a net polarization in the field direction. The tendency of orientation of permanent dipoles with the applied field is called orientational polarization[9] ($P_o$), and contrary to the previous two cases, it is strongly temperature dependent. As the temperature increases, the thermal motion and thus the characteristic frequency of molecular orientations increases; at the same time, the overall alignment of permanent dipoles decreases since the tendency of the dipoles to align along the applied field is disturbed by their thermal motion.

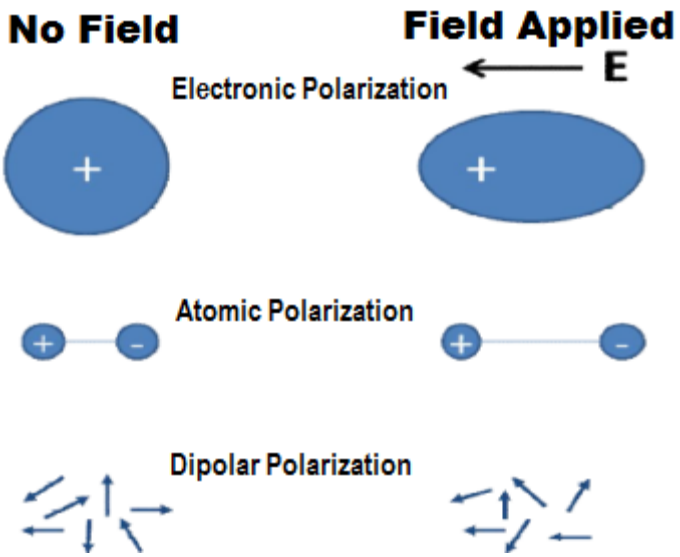


Figure 2.2: Schematic representation of electronic, atomic and dipolar polarization mechanisms.

At yet lower frequencies, interfacial or space charge polarization effects and dc conductivity contributions dominate the linear response. Interfacial or space charge polarization ($P_{sc}$) occurs when there is an accumulation of charge at the boundary between different media, i.e., at the electrode surface or at the interphase in multi-phase materials. It is different from orientational and atomic polarization because instead of arising only from bound charges (i.e. ionic and covalently bonded structures), interfacial polarization also stems from free charges. At the electrode surface, a quasi-static field will

cause a charge imbalance (accumulation of free charge from the metal side) because of the dielectric material's insulating properties. However, the mobile charges in the dielectric will also tend to migrate, in order to maintain charge neutrality. Both effects are responsible for interfacial polarization (Figure 2.3).

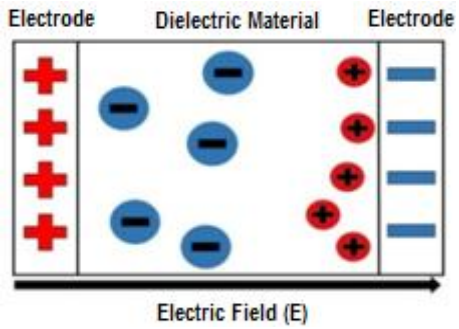


Figure 2.3: Schematic representation of interfacial electrode polarization which shows how the free positive (resp. negative) charges inside the dielectric material migrate towards the negative (resp. positive) charge build-up on the right (resp. left), caused by the external electric field.

Finally, the dc conductivity gives rise to ohmic losses that show up in the conductivity response of dielectric materials, which will be further discussed in Section 2.5. The conductivity contribution in a dielectric is especially visible at higher temperatures, where the conductivity strongly increases. In the rest of this Section we will deal with the polarization effects listed earlier.

Neglecting the ohmic losses due to the dc conductivity, the total polarization can be written as:

$$P = P_e + P_a + P_o + P_{sc} \quad (2.5)$$

where $P_e$ is the electronic polarization, $P_a$ the atomic polarization, $P_o$ the orientational polarization and $P_{sc}$ the space charge polarization. Both $P_e$ and $P_a$ are due to induced local dipoles, i.e., they are due to dipole moments that are absent in the absence of the applied field. Such induced dipoles are

linearly proportional to the local field $E_{loc}$ = E+P/3$\varepsilon_0$, which is the field present at a particular molecular site, and can thus be expressed as:

$$(2.6) \quad p_{induced} = \alpha_{id} \boldsymbol{E}_{loc} = \alpha_{id} \left( \mathbf{E} + \frac{\mathrm{P}}{3\varepsilon_0} \right),$$

where $\alpha_{id}$ is the molecular polarizability of each molecule (which is measure of mobility of negative and positive bound charges). In non-dipolar media where permanent dipoles are absent, the relation between the macroscopic electric field and the polarization due to N induced dipoles per unit volume V is given by the theory of Mosotti and Clausius[2] as:

$$(2.7) \quad \boldsymbol{P}_{id} = \frac{N}{V} \boldsymbol{p}_{induced} = \frac{N}{V} \alpha_{id} \boldsymbol{E}_{loc} = \frac{\frac{N}{V}\alpha_{id}}{1 - \frac{N\alpha_{id}}{3V\varepsilon_0}} \boldsymbol{E}$$

Eq. (2.8) can be readily derived combining Eq. (2.4) with Eq. (2.7) as well as the definition P = (N/V)$p_{induced}$. The Clausius-Mosotti formula Eq.2.7 can also be rewritten as:

$$(2.8) \quad \frac{\varepsilon_{\mathrm{r}}-1}{\varepsilon_{\mathrm{r}}+2} = \frac{\mathrm{N}\alpha_{\mathrm{id}}}{3\mathrm{V}\varepsilon_0}$$

While in non-dipolar media equations (2.7) and (2.8) are valid for the static permittivity, in media with mobile permanent dipoles they are correct only at frequencies above the characteristic frequency of molecular orientations, and below the characteristic frequency of atomic ($10^{12}$ Hz) and electronic polarization ($10^{15}$ Hz). In this latter case, the relative permittivity $\varepsilon_r$ must be replaced with the constant value $\varepsilon_\infty$ at frequencies intermediate between radiofrequency and IR, and the Clausius-Mosotti equation (2.8) must be rewritten as:

(2.9) $$\frac{\varepsilon_{\infty}-1}{\varepsilon_{\infty}+2} = \frac{N}{V}\frac{\alpha_{id}}{3\varepsilon_0}$$

At the beginning of 20th century Debye generalized equation (2.9) by adding the effect of orientation polarization, i.e. the contribution of permanent dipoles. The orientational polarization can be expressed as the macroscopic volume density of the vectorial sum over all N permanent dipoles contained in the unit volume V in a form reminiscent of Eq. (2.6), as:

(2.10) $$\mathbf{P}_0 = \frac{N}{V}\alpha_o \boldsymbol{E}_{loc} = \frac{\mu^2}{3k_B T}\frac{N}{V}\boldsymbol{E}_{loc}$$

where $\alpha_o$ the orientational polarizability, which Debye found using an argument based on statistical physics, and $\mu^2$ is the mean square dipole for non-interacting dipoles.

The total polarization due to both the permanent and the induced molecular dipoles is the sum of equations (2.7) and (2.10):

(2.11) $$\mathbf{P} = \frac{N}{V}(\alpha_{id} + \alpha_o)\boldsymbol{E}_{loc}$$

From the expression for the local field $\mathbf{E}_{loc} = \mathbf{E} + \mathbf{P}/3\varepsilon_0$ and the linear constitutive relation $\mathbf{P} = \varepsilon_0 (\varepsilon_r\text{-}1)\,\mathbf{E}$, equations (2.11) can be rewritten as:

(2.12) $$\frac{\varepsilon_s-1}{\varepsilon_s+2} = \frac{N}{V3\varepsilon_0}(\alpha_{id} + \alpha_o)$$

where $\varepsilon_s$ is now the static permittivity that takes into account the polarization due to both permanent and induced dipoles. By means of equation (2.9), equation (2.12) can finally be written as:

(2.13) $$\frac{\varepsilon_s-1}{\varepsilon_s+2} - \frac{\varepsilon_{\infty}-1}{\varepsilon_{\infty}+2} = \frac{N}{V}\frac{\mu^2}{9\varepsilon_0 k_B T}.$$

Equation (2.13) is known as Debye formula[6]. Onsager[10] extended the Debye-formula by considering the enhancement of the permanent dipole moment of a molecule μ by the polarization of the environment (reaction field) as given below:

$$\varepsilon_s - \varepsilon_\infty = \frac{1}{3\varepsilon_0} \frac{\varepsilon_s(\varepsilon_\infty+2)^2}{3(2\varepsilon_s+\varepsilon_\infty)} \frac{\mu^2 N}{k_B T V} \quad (2.14)$$

and the quantity $\Delta\varepsilon = \varepsilon_s - \varepsilon_\infty$ appearing in Eq. (2.14) is called "dielectric strength" of the dipolar relaxation.

The drawback of both Debye and Onsager formulas is that these equations are only valid for systems where dipole-dipole interactions are negligible such as dipolar gases and certain dipolar non-associating liquids, while they are not actually valid for most condensed phases containing permanent dipoles interacting through dipolar interaction or steric inter-dipole interactions. Onsager's extension fails in polar associating liquids because it does not consider the static orientational correlations between molecules. Later Kirkwood[11] and Frohlich[7] introduced a phenomenological correlation factor (symbol $g_K$) to model the local interaction between dipoles and rewrote the Onsager formula as:

$$\Delta\varepsilon = \varepsilon_s - \varepsilon_\infty = \frac{1}{3\varepsilon_0} \frac{\varepsilon_s(\varepsilon_\infty+2)^2}{3(2\varepsilon_s+\varepsilon_\infty)} g_K \frac{\mu^2 N}{k_B T V} \quad (2.15)$$

If we consider only the nearest neighbours of a dipole, the $g_K$ factor can be approximated as:

$$gK = 1 + z\langle \cos\psi \rangle \quad (2.16)$$

where z is the coordination number and ψ is the angle between a test dipole and one of its neighbors, and the bracket denote the time average. If there is a correlation

between the orientations of the neighbouring dipoles, $g_K$ will differ from 1 (since then $\langle \cos\psi \rangle \neq 1$). When the value of $g_K > 1$ which gives the parallel alignment of dipoles, $g_K < 1$ correspond to an anti-parallel alignment and $g_K = 1$ for non-interacting dipoles. In practice $g_K$ is complicated to calculate theoretically[12], but it can be estimated from the experimental value of the dielectric strength $\Delta\varepsilon$ using Eq. (2.15).

## 2.3 Detailed Frequency-Dependent Response

The values of the dielectric permittivity discussed so far are only those in the static and high-frequency (relative to orientational polarization processes) limits. Much dielectric studies are, however, concerned with the detailed knowledge of frequency-dependent phenomena, where dielectric dispersion occurs, because from such knowledge dynamic information can be obtained. When a harmonic alternating electric field $E(t) = E_0 \exp(i\omega t)$, of angular frequency $\omega = 2\pi f$, is applied to a sample containing permanent dipoles, all polarization mechanisms described earlier take place. The polarization due to induced dipoles has very fast response times (between $10^{-17}$ and $10^{-14}$ seconds for the electronic polarization and between $10^{-13}$ and $10^{-12}$ seconds for the atomic polarization), so that this contribution to the polarization may be considered, in dielectric experiments, to rise instantaneously with the change in electric field. In contrast, orientational polarization has relatively long response time (between $10^{3}$ and $10^{-10}$ seconds, depending on temperature) and therefore lags behind the rise in the electric field, which results in the phase shift between electric field E and the polarization P. This lag is commonly referred to relaxation, which is defined as the delay in the response of a system to changes in the forces to which it is subjected. Similarly, if the applied electric field is suddenly switched off, the polarization does not go to zero instantaneously. The time delay necessary for a dielectric to respond to a change in the applied electric field is called characteristic relaxation time. These phenomena occur because the molecular reorientation motions take much longer time than electronic transitions or molecular vibrations.

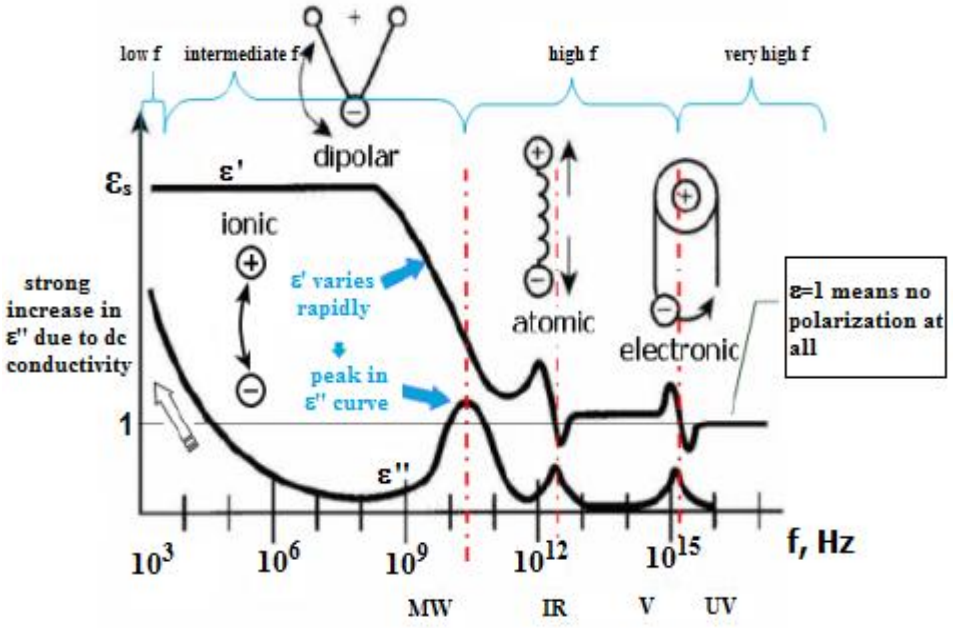


Figure 2.4: Different polarization mechanism in both real and imaginary part of relative permittivity as a function of frequency.

Under such conditions, the dielectric permittivity has to be treated as a complex dielectric function of the form $\varepsilon^* = \varepsilon'(\omega) - i\varepsilon''(\omega)$ where ε'(ω) and ε''(ω) are the real and imaginary parts of the permittivity, respectively. The real part is related to the reversible energy stored in the material, while the imaginary part is proportional to the dissipated energy. Both provide quantitative information about the relaxation processes associated with the reorientation of the dipoles (see Figure 2.4). Dielectric spectroscopy, which is one of the main experimental techniques employed in this thesis, and which is described in detail in Chapter 3, allows simultaneous measure of both the real and imaginary parts of the complex permittivity. The imaginary part of the permittivity contains information about Joule losses due to the dc conductivity, as explained later in Section 2.5.

In the imaginary part (see Figure 2.5), a dielectric relaxation appears as a (usually asymmetric) peak, named dielectric loss peak, whose maximum defines the characteristic relaxation frequency $\omega_{max}$ and the corresponding relaxation time $\tau = 1/\omega_{max}$. In the real part, a step-like decrease is observed with increasing frequency

across $\omega_{max}$, whose height is the dielectric strength $\Delta\varepsilon$ of the relaxation process. At low frequency, the real part of the permittivity reaches its static value. At high frequency, the orientation polarization is unable to follow the time variation of the field; hence this contribution to the overall polarization (Eq. 2.5) drops out and the real part of the dielectric function reaches the value $\varepsilon_\infty$. For example, for small-molecule polar liquids of low viscosity, the time required for the dipole or orientation polarization process is about $10^{-11}$ to $10^{-10}$ seconds, corresponding to frequencies in the microwave region. The orientation polarization contributes at lower frequency, but it does not show up in the IR response, since the typical required time for vibrational processes is about $10^{-12}$ to $10^{-14}$ s, corresponding to the frequency of infrared light (the electronic polarization is the most rapid process and the time required is about $10^{-15}$ s, which corresponds to the frequency of ultraviolet light).

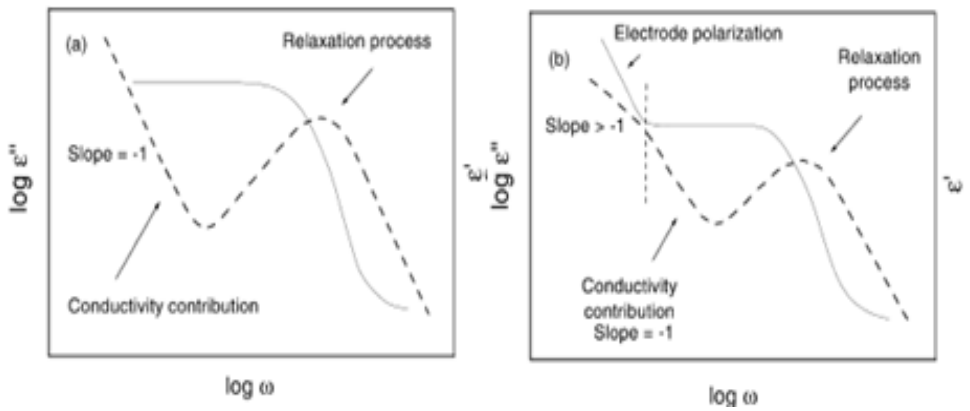


Figure 2.5: Scheme of the real ε'(ω) (*solid line*) and the imaginary ε''(ω) (*dashed line*) part of the complex dielectric function for system displaying a single relaxation process and ohmic (*a*) or non-ohmic (*b*) conductivity. In the latter case, an electrode polarization effect is also observed at low frequency.

The dynamic processes that contribute to the orientational polarization in the complex permittivity may be inter- or intra-molecular, i.e. involve the motion of whole molecules or else of a subunit of a larger molecule, and they can be more or less cooperative. In glass-forming system, for example, the most important dynamic

process is the so-called primary (α) relaxation process, which corresponds to the cooperative, collective rearrangement of the constituent molecules that is directly associated with the viscosity of the system.[13] The frequency of the α process (as well as the viscosity) decreases with decreasing temperature, and displays in fact a continuous, dramatic slow-down by several decades in a short temperature interval upon approaching the glass transition temperature $T_g$.

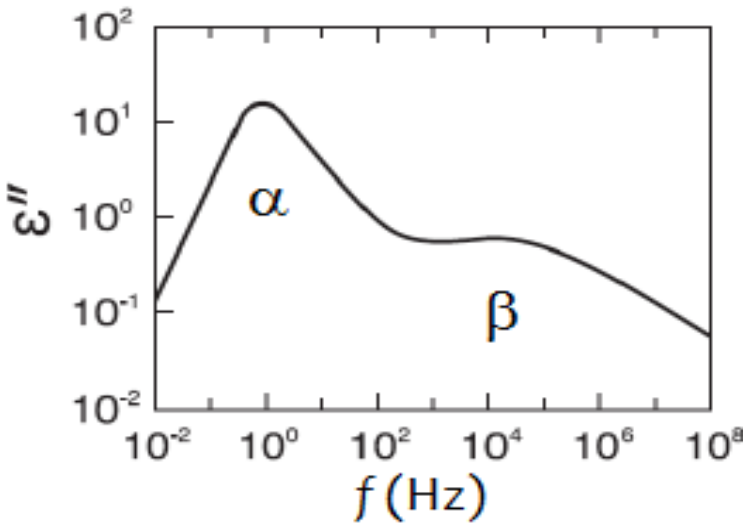


Figure 2.6: Schematic representation of the frequency dependent dielectric loss of a dynamically disordered material. Two distinct features are shown; (*a*) primary α-relaxation and (*b*) secondary relaxation.

Other (usually less cooperative) molecular dynamic processes can occur in addition to the primary relaxation. These molecular motions occur at longer frequency than the α relaxation, and are called secondary relaxations as they are less cooperative in character. These secondary relaxations may be in some cases single-molecule motions,[14] or else correspond to the reorientational motion of mobile side groups or larger parts of the constituent molecule. The typical spectral lineshape of a material displaying both a primary and a secondary relaxation is shown in Figure 2.6. The temperature dependence of the characteristic relaxation time of the α process deviates from a thermally activated behavior (Arrhenius) and follows instead a

Vogel-Fulcher-Tammann (VFT) temperature dependence (see chapter 3). The reorientational processes studied in this thesis correspond either to cooperative primary processes or to non-cooperative intramolecular motions.

The Kramers–Kronig relations, which stem from the causality of response and stimulus, describe how the real and imaginary part of ε''(ω) are related to each other. The consequence of the existence of such relations, which are formulated in Eq. (2.17) below, is that it suffices to know the imaginary part ε''(ω) for getting the full complex ε*(ω) since the real part can be calculated from the imaginary part, and vice-versa.

(2.17a) $$\varepsilon'(\omega_0) = \varepsilon_\infty + \frac{2}{\pi}\int_0^\infty \varepsilon''(\omega)\frac{\omega}{\omega^2-\omega^2{}_0}d\omega$$

(2.17b) $$\varepsilon''(\omega_0) = \frac{2}{\pi}\int_0^\infty \varepsilon'(\omega)\frac{\omega}{\omega^2-\omega^2{}_0}d\omega$$

The mutual dependence between both magnitudes can be useful for testing the existence of a relaxation process. For example, polarization processes at low frequencies and high enough temperatures are sometimes obscured by the effect of the dc conductivity. Wübbenhorst and van Turnhout [15] have proposed an approximation of ε'', Eq. (2.18), based on the Kramers-Kronig relations (2.17), which can be used to remove the effect of the conductivity.

(2.18) $$\varepsilon''_{cond}(\omega) = \frac{\sigma_{dc}}{\omega\varepsilon_0} + \varepsilon''_{pol}(\omega)\text{ , where }\varepsilon''_{pol}(\omega) = -\frac{\pi}{2}\frac{\partial\varepsilon'(\omega)}{\partial ln(\omega)}$$

## 2.4 Dielectric Relaxation Models

### 2.4.1 Debye Model

Debye proposed a microscopic relaxation model for the complex dielectric function based on the assumption that identical dipolar non-interacting molecules undergoing thermal reorientations will tend to align with the applied field with a single, common relaxation time $\tau_D$. According to Debye's model, the rate of increase of material's

polarization is proportional to the instantaneous value of the polarization; this can be described by the following first-order differential equation:

(2.19) $$\frac{dP(t)}{d(t)} = -\frac{P(t)}{\tau_D}$$

Equation (2.19) leads to an exponential decay of the correlation function, as $\phi(t) \sim \exp\left(-\frac{t}{\tau_D}\right)$.

In Debye's model, the dipoles are no interacting and the equilibrium is reached with only one type of process, whereby all dipoles reorient with the same characteristic time ($\tau_D$). The complex permittivity in the frequency domain has the following form, known as Debye function:

(2.20) $$\varepsilon^*_D(\omega) = \varepsilon_\infty + \frac{(\varepsilon_s - \varepsilon_\infty)}{1 + i\omega\tau_D}$$

It is found that if ε*(ω) is described by a Debye function, the corresponding complex modulus M* = 1/ε* is also a Debye function:

(2.21) $$M^*(\omega) = \varepsilon_\infty + \frac{(M_s - M_\infty)}{1 + i\omega\tau_{D-M}},$$

where the modulus relaxation time is $\tau_{D-M} = (\varepsilon_\infty/\varepsilon_S)\tau_D$ whence $\tau_{D-M} < \tau_D$ (since $\varepsilon_\infty < \varepsilon_S$). Therefore, a relaxation process appears in the modulus representation at a higher frequency than for the corresponding permittivity representation ε*(ω). The imaginary parts of both the complex modulus and complex permittivity in Debye's model display a symmetric loss peak with half width of 1:14 decades (as shown for the permittivity by the continuous line in Figure 2.7).

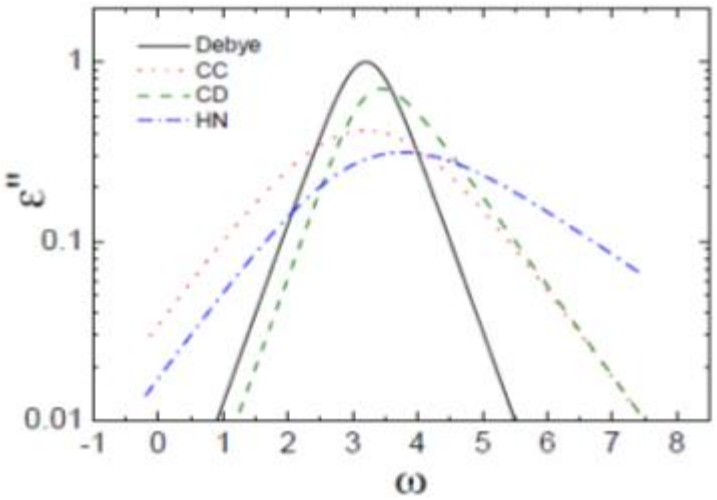


Figure 2.7: Imaginary part of the dielectric permittivity for Debye, Cole-Cole (CC), Cole-Davidson (CD) and Havriliak-Negami (HN) equations.

### 2.4.2 The Havriliak-Negami Function

Debye relaxation is not really suited to describe the dielectric response of disordered materials. In real systems, the dielectric loss peak is broader or less symmetric than that corresponding to a Debye process, indicating that there is no single relaxation time as in the Debye model, but rather a continuous distribution of relaxation times centered about a central, characteristic value. For the representation of experimental dispersion curves, empirical fitting functions were suggested, based on modifications to Debye's Eq. (2.20), such as the Cole and Cole function[16], the Fuos and Kirkwood function[17], the Cole and Davidson function[18], or the Jonscher function[19]. The common characteristic of all of them is the power-law dependences at high and low frequencies (see Figure 2.7). The Havriliak and Negami[20] (HN) function is the most extensively used in literature. It is defined by the following equation:

$$\varepsilon^*_{HN}(\omega) = \varepsilon_\infty + \frac{\Delta\varepsilon}{(1+(i\omega\tau_{HN})^\alpha)^\beta}\,, \tag{2.22}$$

where α and β are shape parameters with values between 0 and 1, which depend on the distribution of relaxation times. For α =β=1, the Debye function is obtained.

The inverse of $\tau_{HN}$ is not the frequency of maximal loss, rather it depends on the α and β exponents and is given by:

$$(2.23) \quad \omega_{max} = \frac{1}{\tau_{HN}} \left[\sin\frac{\alpha\pi}{2\beta+2}\right]^{1/\alpha} \left[\sin\frac{\alpha\beta\pi}{2\beta+2}\right]^{-1/\alpha}$$

Usually, only the HN function is able to describe the experimental data in the whole frequency range of BDS. This means that for a complete description of the frequency behaviour of a relaxation process, at least a set of four parameters is needed. If several relaxation processes are observed in the measured frequency window, a combination of several HN functions can be used to describe and separate the different processes. Provided that the different relaxation regions are independent and hence that the contribution of each process to the complex dielectric function is additive, the total dielectric function will be given by $\sum_k \varepsilon^*_{HN,k}(\omega_i)$ where k runs over all the relaxation processes.

### 2.4.3 Cole-Cole and the Cole-Davidson Functions

For e.g. polymeric materials, a symmetric broadening of the loss peak is usually visible which can be described by the Cole-Cole (CC) function[16] (obtained by setting $\beta = 1$ in the HN function):

$$(2.24) \quad \varepsilon^*_{CC}(\omega) = \varepsilon_\infty + \frac{(\varepsilon_s - \varepsilon_\infty)}{1+(i\omega\tau_{CC})^\alpha}$$

The position of maximal loss is related to the Cole-Cole relaxation time by the relation $\omega_{max} = 1/\tau_{CC}$. For α = 1 the Debye function is again obtained. In the case of liquids or molecular glass forming materials, an asymmetric broadening of the loss peak is often observed. This behavior is better described by the HN function or by the Cole-Davidson (CD) function[18] (obtained by setting α =1 in the HN function) as:

(2.25) $\varepsilon^*_{CD}(\omega) = \varepsilon_\infty + \frac{(\varepsilon_s - \varepsilon_\infty)}{(1+i\omega\tau_{CD})^\beta}$

The CD function gives a power-law proportional with ω on the low frequency side and another proportional with $\omega^{-\beta}$ on the high frequency side. The position of maximal loss is related to the Cole-Davidson relaxation time by the relation $\omega_{max} = \frac{1}{\tau_{CD}} tan\left[\frac{\pi}{2\beta+2}\right]$. When β = 1 the Debye function is obtained.

### 2.4.4 The Kohlrausch-Williams-Watts Function

Although all our discussion focused here on the frequency representation of the permittivity, this quantity can also be measured or computed in the time domain (frequency- and time-domain representations are related by Frourier transformation). In the time domain, the decay function ϕ(t) is more stretched than the simple exponential function corresponding to a Debye process (Eq. 2.19). To model this non-exponential character it is possible to use the Kohlrausch-Williams-Watts (KWW) function[21], which can be written as:

(2.26) $\varepsilon_{KWW}(t) = \varepsilon_\infty + \Delta\varepsilon\left[1 - exp\left(-\frac{t}{\tau_{KWW}}\right)^{\beta_{KWW}}\right]$

Here $\tau_{KWW}$ is the characteristic relaxation time and $\beta_{KWW}$ is the so-called stretching exponent, which has values between 0 and 1. The KWW function has no analytic Fourier transform in the frequency domain, but there exists an approximate connection between the HN function and the KWW function as given by the following choice of parameters[22]:

(2.27) $\ln\left(\frac{\tau_{HN}}{\tau_{kww}}\right) = 2.6\left(1 - \beta_{KWW}\right)^{1/2}\exp\left(-3\beta_{KWW}\right)$

(2.28) $\beta_{KWW} = (\alpha\beta)^{1/1.23}$

## 2.5 Charge Transport Mechanism and Conductivity-Induced Dielectric Losses

In disordered systems without long-range order, but also in molecular solids and polymers, charge carriers are localized at specific sites (rather than being delocalized as Bloch electrons in atomic crystals), and charge transport occurs by a hopping process. In molecular systems, polarization effects are very important. A hop of a charge carrier to a new site can only lead to a successful charge transport if the polarization cloud follows; otherwise the charge carrier will jump back with a high probability. This mutual movement of the charge carrier and the surrounding polarization cloud leads to a space-charge relaxation process requiring an electrical relaxation time $\tau_\sigma$. If the frequency of the outer electrical field is higher than $1/\tau_\sigma$, its effect on the charge transport averages out. For frequencies lower than $1/\tau_\sigma$, the relaxation of the polarization cloud is in phase with the outer electrical field and the field supports the propagation of the charges. Hence the polarization relaxation gives rise to a contribution in the real part of the dielectric function which increases with decreasing frequency.

The disordered materials investigated in this thesis have characteristic responses in the real and imaginary parts of the conductivity σ*, permittivity ε* or electrical modulus M*. All these representations are completely equivalent but they emphasize different aspects of the underlying mechanisms of charge transport[23]. In this section, we discuss the conductivity induced losses and the basic mechanisms that describe charge transport in disordered materials.

From Ohm's law and Maxwell's equations the relationship between the complex dielectric permittivity and the complex conductivity can be derived as follows:

$$\sigma*(\omega) = \sigma'(\omega) + \sigma''(\omega) = i\omega\varepsilon_0\,\varepsilon*(\omega) \tag{2.29}$$

By adding the conductivity contribution, the imaginary part of dielectric permittivity ε''(ω) can be written as:

(2.30) $\varepsilon''(\omega) = \varepsilon_{or}(\omega) + \left(\frac{\sigma_0}{\varepsilon_0 \omega}\right)^s$

where $\varepsilon_{or}$ describes the orientational polarization, $\sigma_0$ is a phenomenological parameter, and *s* is a phenomenological exponent that has a value of one in the case of pure ohmic conduction[24] (Figure 2.8(*a*)). In this latter case no conductivity contribution is present in $\varepsilon'$, $\sigma_0$ is equal to the dc electrical conductivity $\sigma_{dc}$, and increases linearly with decreasing frequency ($\varepsilon''(\omega) \sim \frac{\sigma_{dc}}{\varepsilon_0 \omega}$). In the conductivity representation the real part $\sigma'(\omega)$ is then constant ($\sigma_{dc}$), and the imaginary part $\sigma''(\omega)$ increases linearly with frequency. In experiments the slope is often not one because of the not perfectly ohmic character of the conductivity, in which case $\sigma_0$ is just a fitting parameter.

The dielectric properties can also be expressed in the modulus representation $M^*(\omega) = M'(\omega) + iM''(\omega)$. A conductivity relaxation time[9] can be calculated from the imaginary part of modulus by fitting it as:

(2.31) $M''(\omega) = M_\infty \frac{\omega\tau_{cond}}{1+(\omega\tau_{cond})^2}$

Eq. (2.31) is similar to the imaginary part of $M^*(\omega)$ for a Debye-like relaxation process, and exhibits a peak for $\omega_M\tau_{Cond} = 1$ with $\tau_{Cond} = \varepsilon_0\varepsilon_\infty/\sigma_{dc}$. Therefore the dc conductivity can in principle be estimated from the position of modulus maximum loss ($\omega_M$) (Figure 2.8). In practice, the dc conductivity contribution to the dielectric response may be masked by non-ohmic conduction, dipolar relaxation peaks, or by electrode polarization or other space-charge effects.

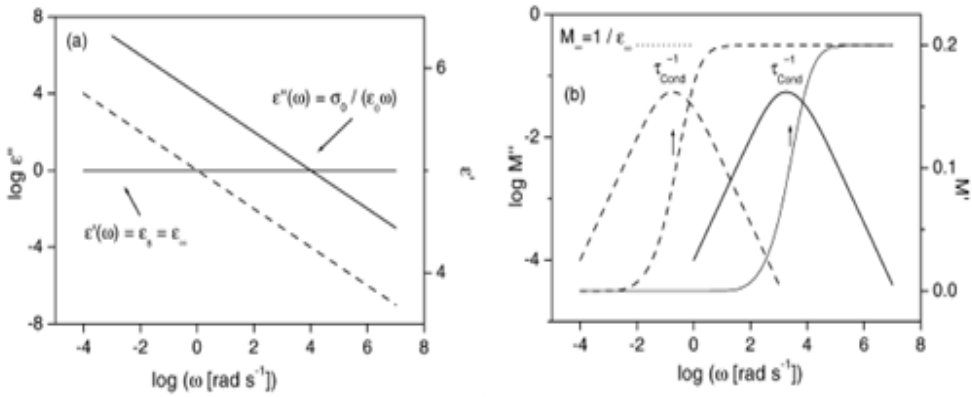


Figure 2.8: (*a*) Theoretical example for a complex dielectric function with a pure ohmic contribution: $\sigma_0/\varepsilon_0 = 1$ *(dashed line)*, $\sigma_0/\varepsilon_0 = 10^4$ *(solid line)*, ε' = 5. (*b***)** Real part M' and imaginary part M'' of the complex electric modulus according to the complex dielectric function given in (a):$\sigma_0/\varepsilon_0 = 1$ *(dashed line)*,$\sigma_0/\varepsilon_0 = 10^4$ *(solid line)*

### 2.5.1 Dc Transport

Theoretical and experimental studies of the steady state or dc conductivity ($\sigma_{dc}$) in hopping electronic systems began in the 1950's[25,26] with the discovery of impurity hopping conduction in compensated semiconductors such as germanium and silicon. The theoretical analysis by Miller and Abrahams[25] postulated that the hopping probability $W_{ij}$ for the electronic charge carrier to hop from a site *i* to an unoccupied site *j* is given by:

$$W_{ij} = f_0 \exp\left(-2\alpha R_{ij} - \frac{\Delta E_{ij}}{k_B T}\right) \quad (2.32)$$

Here $f_0$ represents the number of hop attempts per unit of time at high temperature and small distances, which is of the order of magnitude of the optical phonon frequency; $R_{ij}$ is hopping the distance between site *i* and site *j* (see Figure 2.9); $\Delta E_{ij}$ is the energy difference between site *i* and site *j*; and $\alpha$ is the inverse of the decay length of the (localized) electronic wave function. If $R_{ij}$ and $\Delta E_{ij}$ refer only to nearest neighbor hopping sites, Eq. (2.32) leads to a simply-activated form of

the nearest- neighbor hopping (NNH) dc conductivity (since $R_{ij}$ and $\Delta E_{ij}$ are then the same for all hopping processes):

$$\sigma_{dc} = A\exp\left(-\frac{\Delta E}{k_B T}\right) \quad (2.33)$$

where A is a constant. The concept of variable range hopping (VRH) was introduced by Mott to cover the situation where the energy between (non-nearest-neighbor) hopping sites is a function of their spatial separation.

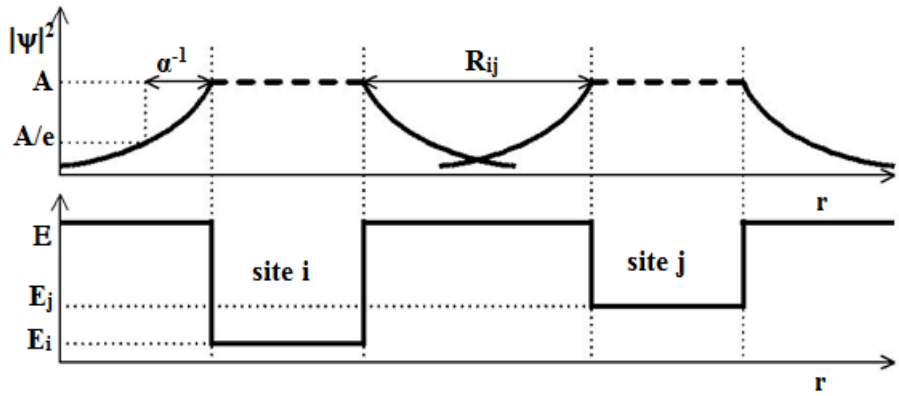


Figure 2.9: Illustration of a disordered material with localized wave functions and energies that differ from site to site. Two sites (*i* and *j*) are shown. $\alpha^{-1}$ is the localization length and $R_{ij}$ is the distance between the sites.

Mott [27, 28] used the expression for the hopping probability $W_{ij}$ to derive an expression for the (low-)temperature dependence of the dc conductivity of a disordered material with a constant density of states (DOS) around the Fermi level. From Mott's law the temperature dependence of the dc conductivity can be represented as:

$$\sigma_{dc}(T) = \frac{A}{T^b}\exp\left(-\frac{T_0}{T}\right)^n \approx \sigma_0\exp\left(-\frac{T_0}{T}\right)^n \quad (2.34)$$

The constants A and $T_0$ depend on the overlap and number density of the electronic states involved. The exponents b and n depend on the distribution of states around the Fermi level; the value of n is related to the dimensions of the transport process and usual values of n are ½ and ¼. Mott's calculation assumed that the density of localized states near the Fermi level does not depend on energy; under this assumption n = ¼. However, Efros and Shklovskii[29] pointed out that in some disordered systems, the DOS is not constant but rather displays a gap at the Fermi level. This occurs because, when an electron hops from one site to another, it leaves behind a hole and the system must have enough energy to overcome the resulting electron-hole Coulomb interaction. The resulting DOS vanishes near the Fermi level (Coulomb gap), and such Coulomb-type correlation leads to a value n = 1/2.[29,30,31] Compared to the NNH model, the VRH model accounts for the contribution, at low temperature, of charge carriers hopping not to first neighbor molecules, but to more distant states, energetically more favorable. A key quantity of the hopping mechanism is the critical rate $W_c$, i.e., the fastest rate at which a macroscopic continuous path across the material can exist. Such a path consists of all the *i*–*j* pairs of states with a transition rate $W_{ij} > W_c$. The rate $W_c$ determines the dc conductivity value so that $\sigma_{dc}$ and $W_c$ are proportional and exhibit the same temperature dependence.

In the case of ionic conductors, such as salt solutions, ionic liquids and some plastic crystals, the temperature dependence of dc conductivity can be modeled with empirical Vogel-Fulcher-Tammann (VFT) equation (see chapter 3 for more details).

### 2.5.2 Ac Transport

A typical example of ac conductivity spectrum (real part of $\sigma'(\omega)$) is shown in Figure 2.10. The conductivity spectrum displays three distinct frequency regions with distinct behavior, namely: a characteristic bending at low frequency called electrode polarization effect, a frequency-independent plateau at low or intermediate frequencies, called dc conductivity which bends off at a certain critical frequency $\omega_c$ marking the onset of a third region in which the conductivity increases with frequency, showing power law dependence for $\omega >> \omega_c$. The critical frequency can be

determined by calculating the maximum in the second derivative of σ′ with respect to ω. Electrode polarization[9,32] is caused by the (partial) blocking of charge carriers at the electrode/sample interface which lead to the separation of positive and negative charges when a slowly varying electric field is applied. EP occurs mainly for moderately to highly conducting samples and masks the dielectric response of the sample for slowly varying fields. This effect, giving rise to giant values of the dielectric constant and a strong drop of conductivity towards low frequencies, arises when the charge carriers arrive at the metallic electrodes and accumulate in thin layers immediately beneath the sample surface forming a so-called space-charge region.

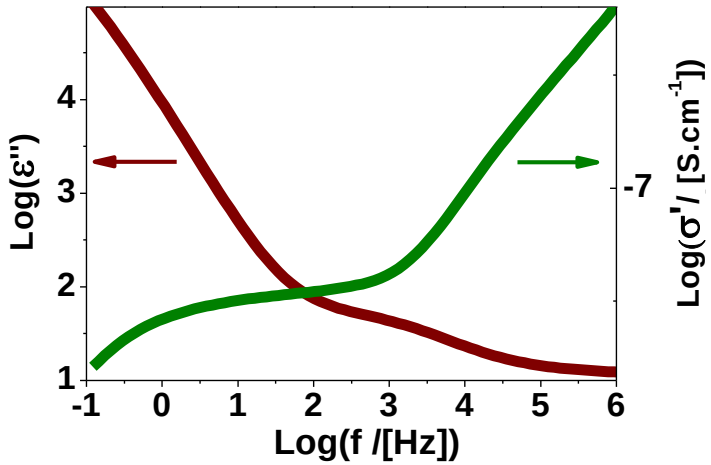


Figure 2.10: Logarithmic plot of dielectric loss with corresponding ac conductivity for a specific temperature in solid $C_{60}(ONa)_{24}$.

Apart from the electrode polarization effect, which will not be analyzed in detail in this thesis, the variation of the real part of conductivity with frequency is empirically expressed by Jonscher's universal dielectric response (UDR)[33] as:

$$\sigma'(\omega) = \sigma_{dc} + A\omega^{s} \quad (2.35)$$

Here $\sigma_{dc}$ is the dc conductivity, A is constant for a particular temperature, and *s* is the dimensionless frequency exponent. In this model the ac response in the high

frequency limit is considered as the sum of individual (not correlated) responses of pairs of sites randomly distributed through the material, as described by the pair approximation model introduced by Pollak and Geballe[34]. Eq. (2.35) is a common feature for amorphous semiconductors and some other disordered systems.[33] The values of *s* in an ideal Debye-dielectric and ideal ionic-type crystals are one and zero respectively. Typically, it is understood that a value of *s* closer to zero indicates that charge carriers are free to move (delocalized) through the material, while an *s* value between 0.5 and 0.8 is observed in materials with more localized charge carriers. In some disordered solids, ac conductivity measurement at sufficiently high frequency results in a crossover from power law to a linear increase with frequency, called 'second universality.'[35,36]

The movement or hopping of the charge carriers is influenced by their neighborhood, and the exponent *s* is a measure of the degree of interaction. The behavior of the frequency exponent as a function of temperature can be used to determine the origin of ac conduction mechanism. Besides the VRH theory, various other models have been proposed in the scientific literature[37,38] to account for the ac conductivity line shape, such as quantum mechanical tunneling (QMT) model, the correlated barrier hopping (CBH) model, the overlapping large-polaron tunneling (OLPT) model and the non-overlapping small-polaron tunneling (NSPT) model, to name a few. In the QMT model, *s* depends upon frequency but is independent of temperature. If the exponent *s* depends on both frequency and temperature, and it, increases with increase in temperature then it is in agreement with the predictions of the NSPT model, whereas if *s* decreases at first, reaching a minimum and increases thereafter with increase temperature, such behavior can be rationalized within the OLPT model. In the CBH model, the exponent *s* always decreases with increasing temperature.

The frequency dependence of ac conductivity does not seem to follow the simple Jonscher's power law in glassy materials. Instead, they sometimes follow the so-called jump relaxation model (JRM), introduced by Funke[39,40,41] to account for the ionic conduction in solids, in which the full conductivity spectrum can be described by the double power law[42]:

(2.36) $\sigma'(\omega) = \sigma_{dc} + A\omega^{s1} + B\omega^{s2}$

Here A and B are constants, the power-law term with $s_1 < 1$ corresponds to the grain-boundary conductivity arising from the translational hopping motion, while the last term with exponent $s_2$ corresponds to well localized relaxation/reorientational motions.

### 2.5.3 Relation between Dc and Ac Conductivities

The UDR line shape is observed in samples that do not exhibit, at least close to $\omega_c$, any relaxations due to permanent molecular dipoles. In such case, when the dielectric data are plotted as loss spectra rather than as ac conductivity, a bump-like feature is observed at $\omega_c$, as in the spectra of Figure 2.10. This loss feature originates from localized hopping motions of charge carriers, but it can be described in a quite similar way as for dipolar relaxations, albeit with parameters having a different meaning and temperature dependence. In particular, the shape parameters, as well as the relaxation strength ($\Delta\varepsilon$) and the dielectric loss peak ($\omega_{max}$) actually depend on the dc conductivity value. An empirical relation introduced by Barton, Nakajima and Namikawa and thereby known as BNN relation [43] correlates the electrical conductivity to the dielectric strength $\Delta\varepsilon$ of the corresponding dielectric loss:

(2.37) $\sigma_{dc} = p\varepsilon_0\Delta\varepsilon\omega_{max}$

In the BNN relation, $p$ is a loosely defined parameter, expected to be of order 1, and $\Delta\varepsilon$ is only weakly dependent on temperature, so that the frequency position of the loss peak ($\omega_{max}$) is linearly correlated with dc conductivity ($\sigma_{dc}$). [44] The conductivity-induced relaxation, which we will refer to also as BNN relaxation is, in general, quite broad and asymmetric, and thus far from a Debye-like relaxation. The corresponding dielectric strength $\Delta\varepsilon$ may arise entirely from mobile charge effects and not involve bulk dielectric effects at all.

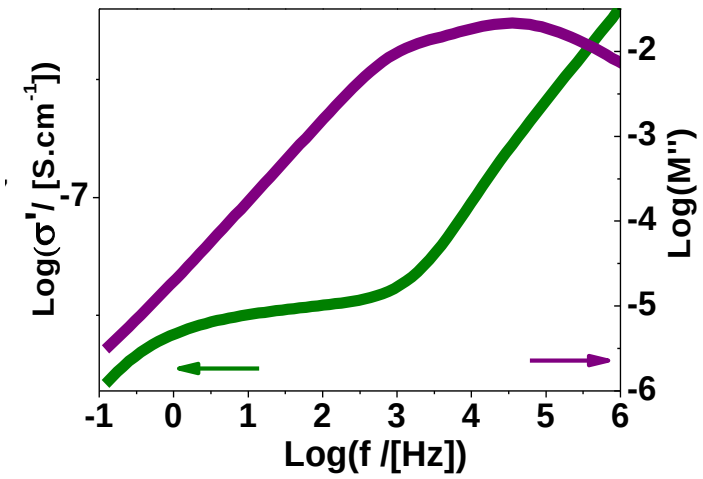


Figure 2.11: Logarithmic plot of modulus M'' with corresponding ac conductivity, for a specific temperature in solid $C_{60}(ONa)_{24}$.

Figure 2.11 shows the comparison between an ac conductivity spectrum and the corresponding imaginary part of the modulus. The latter displays a peak; often called "conductivity relaxation", [45] which in the case of Figure 2.11 it has actually two components. The low-frequency component of the M'' feature lies in the range of frequencies in which charge carriers can perform successful hopping from one site to the neighboring sites (leading to effective charge transport). The high-frequency component in M'' lies in the range of frequencies in which the charge carriers are spatially confined to their potential wells and the charge can make only localized motions within the well. The spectral position of the modulus feature marks roughly the transition from long-range to short-range mobility with increasing frequency.

When equation (2.37) is satisfied, it entails that both ac and dc conductivity are closely related to each other, and therefore that the charge transport is based on the same mechanism, regardless of the frequency at which it is studied.

Also ionic charge conduction (due e.g. to cations diffusing through a disordered matrix) occurs by hopping, only not between molecules but rather between empty interstitial sites. In order to effectively model the conductivity spectrum in

disordered ionic materials such as liquids or glasses, Dyre [9,46,47,48] has developed an analytical model known as the symmetric hopping model or random free energy barrier model that ascribes both ac and dc conductivity to the same underlying physical process, in which charge carriers in a disordered matrix experience random, spatially varying potential energy barriers which prevent or allow their hopping to new sites in the matrix. In this model, jump rate (jump probability per unit time) is assumed symmetric i.e., the same for the charge carrier to jumps forwards and backwards across the barrier. According to this model, the complex conductivity can be expressed as:

$$\sigma^*(\omega) = \sigma_0 \left[\frac{i\omega\tau_e}{ln(1+i\omega\tau_e)}\right], \quad (2.38)$$

where $\tau_e$ is the attempt frequency to overcome the largest barrier, determining the dc conductivity. The frequency which characterizes the onset of dc conductivity $\sigma_0$, is related to the BNN relation and if $\sigma_0 = 1/\tau_e$ which implies that they are due to same charge transport process.

### 2.5.4 Scaling of the Ac Conductivity

Many dynamical processes in disordered materials exhibit what is often referred to as 'thermorheological simplicity' (TRS), also known as 'time-temperature superposition'.[48,49] This means that, while the characteristic frequency or time scale governing the process varies with temperature, the inherent spectral features of the relaxation remain in the same proportion. Consequently, the frequency-dependent line shapes of the relaxation spectra are undistorted by changing temperature and are only shifted in frequency by virtue of the temperature dependence of the characteristic frequency. The scaling of the ac conductivity spectra requires both division by the dc conductivity ($\sigma_{dc}$) and shifting by some characteristic frequency $f_0$'

$$\frac{\sigma(f)}{\sigma_{dc}} = G\left(\frac{f}{f_0'}\right). \quad (2.39)$$

Here the characteristic frequency $f_0$' refers to a temperature-dependent reference frequency which may be chosen for example as the onset frequency $f_c = \omega_c/2\pi$ of the dispersive part of the conductivity spectra, or in some cases as $f_0' = 2\sigma_{dc}$, as shown by Kahnt.[50] In this scaled representation, the data collapse onto a single, common curve, a so-called "master curve", whose line shape is given by the function G(x) in equation (2.39). The validity of such scaling arises from the fact that the horizontal and vertical scales are generally related by the Nernst-Einstein relation,[51] so that the macroscopic quantity $\sigma_{dc}T$ is proportional to a microscopic quantity such as the characteristic frequency of hopping. When a scaling of the vertical and horizontal scales is obtained by setting $\sigma_{dc}T = f_c$, the resulting scaling is referred to as Summerfield scaling.[52,53] This type of scaling is most often observed in temperature-dependent measurements of disordered samples with fixed (temperature-independent) charge-carrier concentration, provided the disordered matrix remains isostructural. An example is provided in Chapter 4 of this thesis.

# References


[1] Faraday, M**.** Supplementary Note to Experimental Researches in Electricity. Eleventh Series. *Phil. Trans. R. Soc. Lond.* **1837**, 128, 79-81: Maxwell, J. C. A Dynamical Theory of Electromagnetic Field. *Phil. Trans. R. Soc. Lond.* **1865**, 155, 459-512.

[2] Clausius, R. *Die Mechanische Wärmetheorie*. vol II. Brauschweig 1879: Mossotti, P.F. Bibl. Univ. Modena, **1847**, 6,193.

[3] Maxwell, J. C. On a Method of Making a Direct Comparison of Electrostatic with Electromagnetic Force; With a Note on the Electromagnetic Theory of Light. *Phil. Trans. R. Soc. Lond.* **1868**,158, 643-657.

[4] Lorentz, H.A. Über die Beziehungzwischen der Fortpflanzungsgeschwindigkeit des Lichtes und der Körperdichte. *Ann. Phys.* **1880**, 9, 641-665.

[5] Maxwell, J. C. *Electricity and Magnetism, vol. 1* Clarendon: Oxford **1892**.

[6] Debye, P. Polar Molecules; Dover: New York **1929**.

[7] Fröhlich, H. *Theory of Dielectrics*; Clarendon Press: Oxford **1958**.

[8] Böttcher, C. F. J. and Bordewijk, P. *Theory of Electric Polarisation*, Vol II (2nd edition), Elsevier: Amsterdam **1978**.

[9] Kremer, F and Schönhals, A. *Broad Band Dielectric Spectroscopy*, Springer Berlin **2003**.

[10] Onsager, L. Electric Moments of Molecules in Liquids. *J. Am. Chem. Soc.* **1938**, 58, 1486-1493.

[11] Kirkwood, J. G. The Dielectric Polarization of Polar Liquids. *J. Chem. Phys.* **1939**, 58, 911-919.

[12] Chao, Z.; Jürg, H. and Michiel, S. Computing the Kirkwood *g*-Factor by Combining Constant Maxwell Electric Field and Electric Displacement Simulations: Application to the Dielectric Constant of Liquid Water. *J. Phys. Chem. Lett.* **2016**, 7, 2696–2701.

[13] Angell, C. A.; Ngai, K. L.; McKenna, G. B.; McMillan, P. F.; Martin, S. F. Relaxation in Glassforming Liquids and Amorphous Solids. *J. Appl. Phys.* **2000**, 88, 3113-3115.

[14] Johari, G.P. and Goldstein, M. Viscous Liquids and the Glass Transition. II. Secondary Relaxations in Glasses of Rigid Molecules. *J. Chem. Phys.* **1970**, 53, 2372.

**[15]**Wubbenhorst, M. and Turnhout, J. van. Analysis of Complex Dielectric Spectr. I. One-Dimensional Derivative Techniques and Three-Dimensional Modeling. *J. Non. Cryst. Solids* **2002**,305, 40–49.

[16] Cole, K. S. and Cole, R. H. Dispersion and Absorption in Dielectrics I. Alternating Current Characteristics *J. Chem. Phys.* **1949**, 9, 341.

[17] Fuoss, R.M. and Kirkwood, J.G. Electrical Properties of Solids. VIII. Dipole Moments in Polyvinyl Chloride-Diphenyl Systems. *J. Am. Chem. Soc*. **1941**, 63, 385-394.

[18] Davidson, D.W. and Cole, R. H. Dielectric Relaxation in Glycerine. *J. Chem. Phys.* **1951**, 18, 1417.

[19] Jonscher, A. K. A New Model of Dielectric Loss in Polymers. *Colloid and Polymer. Sci.* **1975**, 253, 231-250.

[20] Havriliak S.; Negami, S. A complex Plane Analysis of α-Dispersions in Some Polymer Systems. *J. Polym. Sci. C* **1966**, 16, 99−117.

[21] Kohlrausch, R. Nachtrag ueber die elastische Nachwirkung beim Cocon und Glasfaden etc. *Pogg*. *Ann*. *Phys*. **1847**, 12, 393-399.

[22] Alvarez, F.; Alegría, A.; Colmenero, J. Relationship between the Time-Domain Kohlrausch-Williams-Watts and Frequency-Domain Havriliak-Negami Relaxation Functions. *Phys. Rev. B* **1991**, 44, 7306.

[23] Baranovski, S. *Charge Transport in Disordered Solids with Applications in Electronics.* Wiley **2006**.

[24] Barsoukov, E. and Macdonald, J. R. *Impedance Spectroscopy Experiment, and Applications.* Wiley **2005**.

[25] Miller, A and Abraham, E. Impurity Conduction at Low Concentration. *Phys.Rev.* **1960**, 120, 745.

[26] Hill, R.M and Jonscher, A.K. Dc and Ac Conductivity in Hopping Electronic Systems. *J. Non. Cryst. Solids* **1979**, 32, 53-59.

[27] Mott, N. F. and Davis, E. A. Electronic Processes in Noncrystalline Materials, Clarendon, Oxford **1979**.

[28] van Staveren, M. P. J.; Brom, H. B.; de Jongh, L. J. Metal-Cluster Compounds and Universal Features of the Hopping Conductivity of Solids. *Phys. Rep.* **1991**, 208, 1-96 and references therein.

[29] Efros, A.L. and Shklovskii, B.I. *Electronic Properties of Doped Semiconductors*, Springer, Heidelberg **1984**.

[30] Efros, A.L. and Shklovskii, B.I. Coulomb Gap and Low-Temperature Conductivity of Disordered Systems. *J. Phys. C. Solid St. Phys.* **1975**, 8, L49.

[31] Capaccioli, S.; Lucchesi, M.; Rolla, P. A.; Ruggeri, G. Dielectric Response Analysis of a Conducting Polymer Dominated by the Hopping Charge Transport. *J. Phys.: Condens. Matter.* **1998**, 10, 5595–5617.

[32] Emmert, S. Wolf, M. Gulich, R. Krohns, S. Kastner, S. Lunkenheimer, P. Loidl, A. Electrode Polarization Effects in Broadband Dielectric Spectroscopy. *Eur. Phys. J. B* **2011**, 83, 157-165.

[33] Jonscher, A. K. The 'Universal' Dielectric Response. *Nature* **1977**, 267, 673-679.

[34] Pollak, M. and Geballe,T.H. Low-Frequency Conductivity Due to Hopping Processes in Silicon. *Phys. Rev.* **1961**, 122, 1742.

[35] Lee, W. K.; Liu, J. F. and Nowick, A. S. Limiting Behavior of Ac Conductivity in Ionically Conducting Crystals and Glasses: A New Universality. *Phys. Rev. Lett.* **1991**, 67, 1559.

[36] Nowick, A.S. Vaysleyb, A.V.and Lim, B.S. Further Evidence for a Second Universality in Alternating Current Conductivity Relaxation *J. Appl. Phys.* **1994**, 76, 4429-4431.

[37] Elliott, S.R. Ac Conduction in Amorphous Chalcogenide and pnictide Semiconductors. *Adv. Phys.* **1987**, 36, 135-218.

[38] Macdonald, J. R. Comparison of the Universal Dynamic Response Power-Law Fitting Model for Conducting Systems with Superior Alternative Models. *Solid State Ion*. **2000**, 133, 79–97.

[39] Funke, K. Jump Relaxation in Solid Electrolytes. *Prog. Solid State Chem.* **1993**, 22, 111–195.

[40] K Funke, Solid electrolytes: Jump relaxation and Universal Dynamic Response. *Radiat. Eff. Defect. S.* **1991**, 119-121, 463-468.

[41] Cutroni, M.; Mandanici , A. ; Piccolo A.; Tomasi, C. Dielectric Response of Some Solid Electrolytes at Low and high Frequencies. *Philos. Mag.* **1995**, 71, 843-850.

[42] Almond, D.P. and Bowen, C.R. Anomalous Power Law Dispersions in Ac Conductivity and Permittivity Shown to be Characteristic of Microstructural Electrical Networks. *Phys. Rev. Lett.* **2004**, 92, 157601.

[43] (a) Barton, J.L. La Relaxation Diélectrique de Quelques Verres Ternaries Silice Oxyde Alcalin Oxyde Alcalino-Terreux. *Verres et Refr.* **1971**, 20, 324-328. (b) Nakajima, T. Correlations between Electrical Conduction and Dielectric Polarization in Inorganic Glasses. *Ann. Rep. Conf. on Electric Insulation and Dielectric Phenomena, National Academy of Sciences, Washington DC*. **1971**, 168-176. (c) Namikawa, H. Characterization of the Diffusion Process in Oxide Glasses Based on the Correlation between Electric Conduction and Dielectric Relaxation. *J . Non. Cryst. Solids* **1975**, 18, 173-195.

[44] Tsonos, C.; Kanapitsas, A.; Kechriniotis, A.; Petropoulos, N. Ac and Dc Conductivity Correlation: The Coefficient of Barton–Nakajima–Namikawa relation. *J. Non. Cryst. Solids* **2012**, 358, 1638–1643.

[45] Köhler, M.; Lunkenheimer, P.; and Loidl A. Dielectric and Conductivity Relaxation in Mixtures of Glycerol with LiCl. *Eur. Phys. J. E* **2008**, 27, 115–122.

[46] Dyre, J.C. Universal Low-Temperature Ac Conductivity of Macroscopically Disordered Nonmetals. *Phys. Rev. B* **1993**, 48, 12511.

[47] Griffin, P.J.; Cosby, T.; Holt, A.P.; Benson, R. S. and Sangoro, J. R. Charge Transport and Structural Dynamics in Carboxylic-Acid-Based Deep Eutectic Mixtures. *J. Phys. Chem. B* **2014**, 118, 9378−9385.

[48] Dyre, J. C.; Schroder, T. B. Universality of Ac Conduction in Disordered Solids. *Rev. Mod. Phys.* **2000,** 72, 873−892.

[49] Leon, C.; Lunkenheimer, P.; Ngai, K. L. Test of Universal Scaling of Ac Conductivity in Ionic Conductors. *Phys. Rev. B* **2001,** 64, 184304.

[50] Kahnt, H. Ionic Transport in Oxide Glasses and Frequency Dependence of Conductivity. *Ber. Bunsenges. Phys. Chem.* **1991**, 95, 1021-1025.

[51] Sidebottom, D. L. Colloquium: Understanding Ion Motion in Disordered Solids from Impedance Spectroscopy Scaling. *Rev. Mod. Phys.* **2009**, *81*, 999-1014.

[52] Summerfield, S and Butcher, P.N. Universal Behaviour of Ac Hopping Conductivity in Disordered systems. *J. Non. Cryst. Solids* **1985**, 77 & 78, 135-138.

[53] Imre, A. W.; Schonhoff, M.; Cramer, C. Unconventional Scaling of Electrical Conductivity Spectra for PSS-PDADMAC Polyelectrolyte Complexes. *Phys. Rev. Lett.* **2009**, 102, 255901.

# Chapter 3

# Experimental Techniques and Data Analysis

## 3.1 Basic Characterization Techniques

### 3.1.1 Thermogravimetric Analysis

Thermogravimetric analysis (TGA) is a method of thermal analysis in which changes in physico-chemical properties of materials are measured as a function of increasing temperature with constant heating rate, or as a function of time with constant temperature and/or constant mass loss. In this thesis TGA is employed to measure the mass loss of a sample as a function of temperature. Such mass loss may occur as result of decomposition, evaporation of volatile impurities attached to sample such as water vapor, carbon dioxide, or by desorption of adsorbed molecules, among others. TGA can provide information about physical phenomena such as phase transitions, vaporization/sublimation, absorption, and adsorption and desorption, and decomposition.

The TGA experiments presented in thesis were performed with a Q50 thermo-balance from TA-instruments. The instrument is equipped with a titanium sample-holder supported by a precision balance and residing in a furnace for heating or cooling the sample. In a typical experiment, a sample of initial mass between 0.5 to 10 mg was placed in an aluminum pan (TA-instruments) and the mass was monitored while heating the sample under nitrogen flow. Typically, the temperature was varied between room temperature (300 K) and 600 K, at a rate of 2 to 10 K per minute. The use of nitrogen flow ensures that no oxidation takes place during heating. The plot of mass value versus temperature is referred to as the thermogravimetric curve (TG curve). The mass is usually normalized to the initial mass, and the TG curve is shown as percentage, as shown in the example of Figure 3.1. The derivative thermogravimetric (DTG) curve is shown as dotted line. Such curve represents the rate of mass change as a function of temperature when substance is heated at uniform rate.[1]

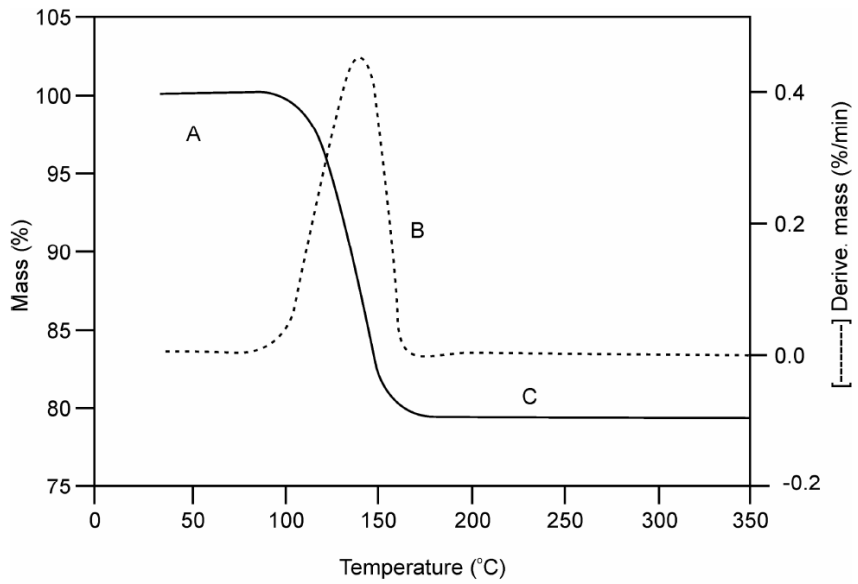


Figure 3.1: A percent TG curve, referenced to the sample's initial mass, exhibiting a low-temperature plateau of constant mass (A), the mass loss region (B), and another plateau of constant mass (C). The dotted line shows the first derivative of the percent mass loss with respect temperature (DTG Curve).

### 3.1.2 Differential Scanning Calorimetry

Differential scanning calorimetry (DSC) is a thermoanalytical technique used for measuring the characteristic phase-change properties of a sample such as melting and crystallization as well as the glass transition. The enthalpy of transition is determined by measuring the difference in the amount of heat required to increase the temperature of a sample and that of a known reference as a function of temperature. The reference used for DSC has a heat capacity that varies slowly over the range of temperatures measured; indium is normally used as a standard for calibration of temperature and enthalpy changes due to its well-defined melting point and heat of fusion. Both sample and reference are maintained at nearly the same temperature throughout the experiment. When the sample undergoes a physical transformation such as a phase transition, it requires either a larger or lower heat flow, compared to the reference, to remain at the same temperature as the reference. Whether less or more heat must flow into the sample depends on whether the transformation process is exothermic or endothermic, respectively. For example, as a solid sample melts to a liquid it will require an extra heat flow corresponding to the latent heat of transformation, because the phase transition from solid to liquid is an endothermic process. On the other hand, if the sample undergoes an exothermic process such as crystallization it will release energy in the form of heat. By analyzing the difference in heat flow between the sample and reference, DSC is able to measure the amount of heat absorbed or released during such transitions.[2,3]

The DSC experiments were performed with a Q100 analyser from TA instruments equipped with a refrigerated cooling system, yielding a wide operating range of temperatures from 190 to 600 K, with cooling/heating rates between 2 and 10 K per minute. In order to carry out DSC measurements at temperatures below 190 K, we employed a different calorimeter equipped with a liquid nitrogen dewar, namely a TA-2920-MDSC analyser (also from TA-instruments). The sample atmosphere during DSC experiments is controlled by connecting purge gases (nitrogen or helium) to the setup and the flow rate of the gas is monitored by a mass

flow controller. A sample of size between 1 and 30 mg is placed in an aluminum pan (TA instruments) or in a high-pressure stainless steel pan with gold plated seal (Perkin-Elmer). The last one is used for samples that can react readily with the aluminium sample holder or in the case of materials with high vapour pressure. Figure 3.2 shows an example of DSC thermogram, acquired upon heating a molecular glass. The glass transition temperature ($T_g$) is signaled by a small bump in the baseline which marks the corresponding change in the heat capacity of the sample (more visible in the inset). Above the glass transition temperature, the material is in a metastable supercooled liquid state. As the temperature increases further, heat is released in the crystallization process, as the entropy of the sample decreases, leading to an exothermic (downward) feature. Upon further heating this crystal phase, an intense endothermic (upward) peak appears which signals the melting temperature ($T_m$).

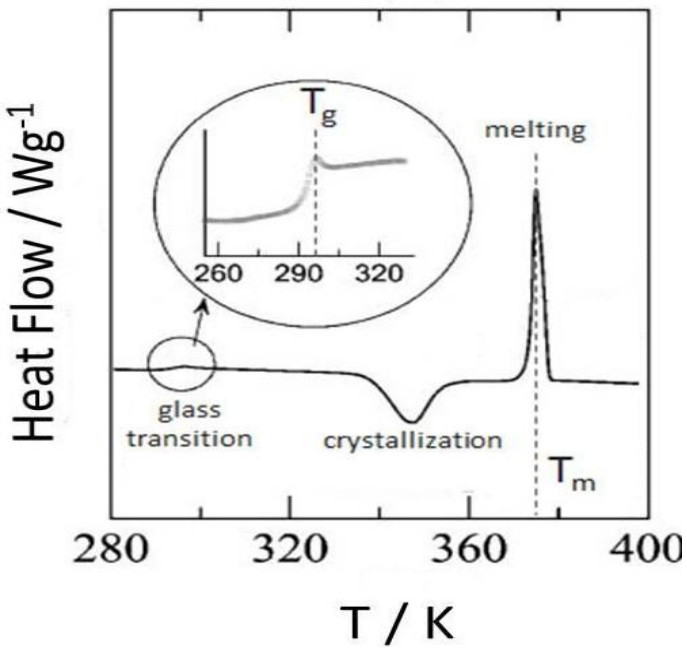


Figure 3.2: A DSC thermogram of a glass forming material. The main peak corresponds to the melting of the solid phase ($T_m$), which is formed by crystallization of the supercooled liquid obtained by heating the glass above the glass transition temperature ($T_g$).

### 3.1.3 Fourier-Transform Infrared Spectroscopy

Fourier-transform infrared spectroscopy (FTIR) is an optical absorption spectroscopy technique that allows detecting the dipolar inter-atomic vibrations of individual molecules of a sample. When infrared radiation is passed through a sample, some of the radiation is absorbed by the sample. The absorbed IR radiation is resonant with a specific vibration of the inter-atomic bonds about their equilibrium distance. Only vibrations resulting in the change in the local dipole moment can be excited in IR spectroscopy. Because each molecule is a unique combination of atoms, the IR spectrum is like a molecular fingerprint, as no two molecular structures produce the same infrared spectrum. Infrared spectroscopy can thus be used to identify the chemical composition of unknown material; the intensity of the peaks in the spectrum is a direct indication of the amount of each molecule present. It can also be employed to investigate the presence of impurities or of specific intermolecular bonds and supermolecular structures.[4] For the measurements presented in this thesis we used a Thermo Scientific Nicolet$^{TM}$ 6700 FT-IR spectrometer equipped with a He/Ne laser source, a CsI beamsplitter and DTGS-CsI detector with a spectral range between 4000 and 400 $cm^{-1}$ and wave number resolution of 1 $cm^{-1}$. The measurements are carried out in transmission mode, using free-standing pellets made by mixing a sufficient amount of powder sample with KBr powder, which is transparent in the probed wavenumber range.

### 3.1.4 X-ray Powder Diffraction

X-ray powder diffraction (XRPD) is an analytical technique used for structural characterization and phase identification of polycrystalline materials. X-ray diffractometers consist of three basic elements: an x-ray tube, a sample holder and an X-ray detector. X-ray diffraction is based on the constructive interference of monochromatic X-rays diffracted by a crystalline sample. The X-rays are generated by a cathode ray tube, filtered to obtain monochromatic radiation and collimated to

achieve a beam with a well-defined direction, which impinges on the sample. The scattering of the incident rays from the sample yields constructive interference (and thus a diffraction peak) when Bragg's Law ($n\lambda = 2d\sin\theta$) is satisfied. Bragg's law provides the correlation between the diffraction angle θ and the lattice spacing d along a particular crystallographic direction in the sample, for a given wavelength λ of the impinging electromagnetic radiation. The diffracted X-rays are then detected at different scattering angles. While a single crystal sample provides diffraction spots in well-defined 3D directions, in a polycrystalline powder sample the crystalline domains have random orientations, which results in a series of diffraction 'cones', each one at a different scattering angle. In typical powder diffraction experiment, the X-ray tube (and thus the direction of the incoming X-rays) is maintained fixed, and the detector is moved (Bragg-Brentano geometry). By varying the scattering angle, i.e., by moving the detector along an arc of circumference covering a sufficiently large angle, all possible diffraction directions of the lattice should be obtained due to the random orientation and large number of crystalline grains. Consider the scattered intensity from crystallographic planes oriented at an angle θ with respect to the incoming X-rays. The Bragg-scattered beam will emerge at an angle equal to θ with respect to the same planes, that is, at an angle 2θ with respect to the incident beam. Therefore, when a scattering maximum is detected by the detector, the angle between the X-ray tube and the detector at that moment is equal to 2θ. From the conversion of the angular position θ of the Bragg-planes to d-spacings by means of Bragg's law, it is possible to identify the material's lattice symmetry as well as the lattice parameters.

The high-resolution XRPD profiles used in this thesis were recorded by means of a vertically mounted INEL cylindrical position sensitive detector (CPS120). The detector was used in the Debye-Scherrer geometry (transmission mode), enabling simultaneous recording of the diffraction profile over a 2θ- range between 4˚ and 120˚ (angular step ca. 0.029˚ (2θ)). Monochromatic Cu Kα1 radiation (λ= 1.54059 A) was selected by means of an asymmetrically focusing curved quartz monochromator. Temperature control was achieved with a liquid nitrogen 700 series Cryostream Cooler from Oxford Cryosystems operating from 500K to 90 K with a

temperature accuracy of 0.1 K. The generator power was commonly set to 35 kV and 35 mA. External calibration with cubic phase $Na_2Ca_2Al_2F_4$ was performed for converting measured 4096 channels into 2θ-degrees, using cubic spline fittings.[5] For the measurements, the samples are introduced into typically 0.5-mm-diameter Lindemann glass capillaries in the liquid or in the solid state at room temperature and are continuously rotated perpendicularly to the X-ray beam during data collection to improve averaging of the crystallites. The peak positions are determined by pseudo-Voigt fits performed with DIFFRACTINEL software.

## 3.2 Broadband Dielectric Spectroscopy

The main experimental technique used in this thesis to investigate the dielectric and charge transport properties of the studied materials is broadband dielectric spectroscopy (BDS), also known as impedance spectroscopy. It is called "broadband" as it allows probing the interaction of matter with electromagnetic waves in the frequency regime between $10^{-6}$ and $10^{12}$ Hz. In this extraordinarily extended dynamic range, molecular and collective dipolar fluctuations, charge transport and polarization effects at inner and outer boundaries take place, and determine the dielectric properties of the material under investigation. BDS enables studying the dynamics of permanent dipoles and induced mesoscopic dipoles, and the conduction properties of materials, in a single experiment.[6]

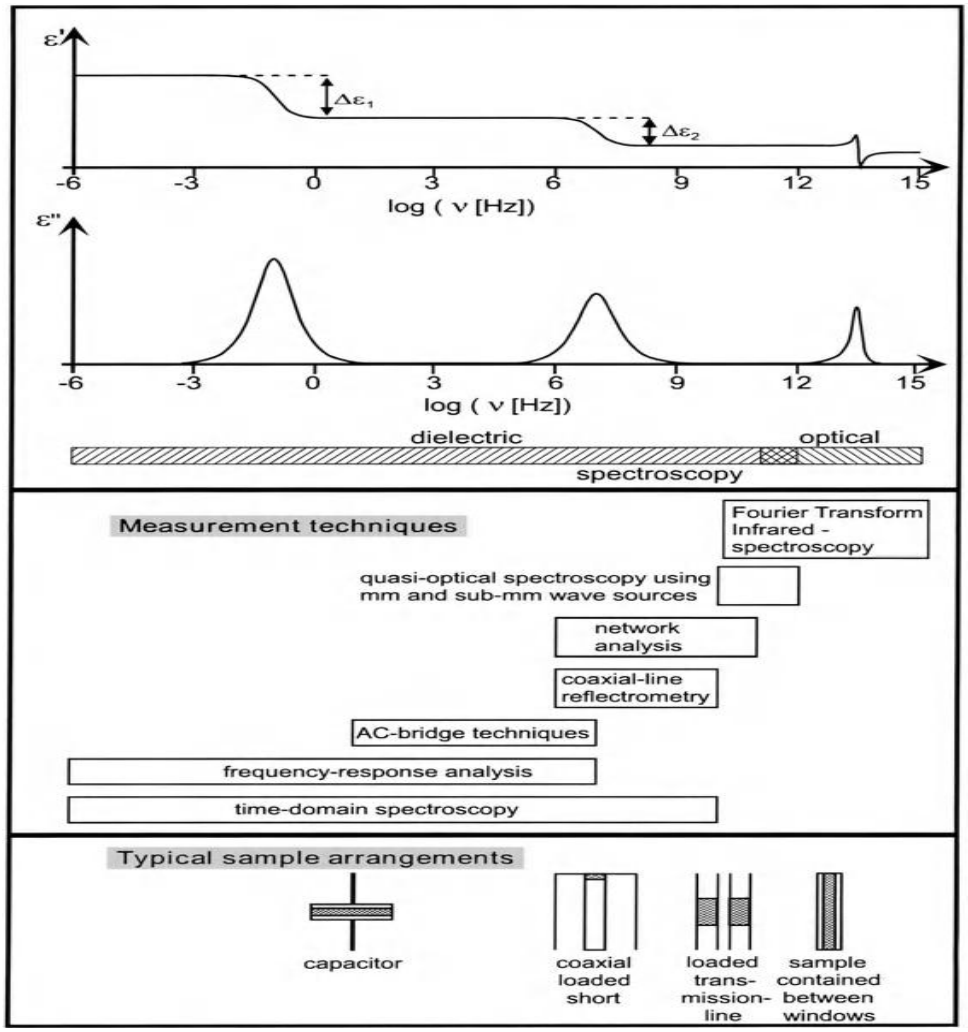


Figure 3.3: Survey of measurements techniques used in the frequency range between $10^{-6}$ Hz and $10^{15}$ Hz.[6]

BDS experiments can be performed either in time or frequency domain. In this work, dielectric spectroscopy is performed in the frequency domain; the measurements are carried out by varying directly the frequency of the applied AC field. No single BDS setup allows measuring in the whole range between $10^{-6}$ and $10^{12}$ Hz; rather, depending on the electromagnetic spectral range, different setups based on different measurement principles have to be used (Figure 3.3). In this thesis, the low-frequency range between $10^{-2}$ Hz and $10^{7}$ Hz was probed using a

Novocontrol Alpha analyzer and the range from $10^6$ Hz to $1.8 \times 10^9$ Hz by using the Agilent HP4291 impedance analyzer. In both setups the sample is placed in a capacitor cell of empty capacitance equal to $C_0$, and from the experimentally measured complex capacitance $C^*$ of the capacitor filled with the material under study, the material's complex dielectric function is obtained as:

$$\varepsilon*(\omega) = \varepsilon'(\omega) - i\varepsilon''(\omega) = \frac{C^*(\omega)}{C_0} \quad (3.1)$$

Here $\omega$ is the angular frequency with $\omega = 2\pi f = 2\pi T^{-1}$ (T is the period, or time for a complete oscillation of the field), and $\varepsilon'(\omega)$ and $\varepsilon''(\omega)$ describe the real and imaginary part of the complex dielectric function. To measure C*, a sinusoidal electric field $E^*(\omega) = E_0 \exp(i\omega t)$ at angular frequency $\omega$ is applied inside the capacitor by applying an ac voltage $V^*(\omega) = V_0 \exp(i\omega t)$, chosen so that the field strength $E_0 = V_0/d$ (where d is the sample thickness, i.e. the distance between plates) is within the linear response range (the upper limit for most materials is taken to be $E_0 \leq 10^6$ V $cm^{-1}$). The dielectric function can be obtained by measuring the amplitude of the current through the capacitor and its relative phase with respect to the voltage, thereby measuring the complex impedance $Z^*(\omega) = V^*(\omega)/I^*(\omega)$ of the sample. Since for a capacitor of capacitance $C$ the complex impedance is $Z^* = 1/i\omega C$, the frequency-dependent complex dielectric function is then given, using Eq. (3.1), as:

$$\varepsilon*(\omega) = \frac{1}{i\omega z^*(\omega) C_0} \quad (3.2)$$

The value for $C_0$ can be obtained from a measurement of the empty cell or directly from the knowledge of the geometry of the cell. At high (microwave) frequency the geometrical dimensions of the sample capacitor become important and different cells have to be used in the two different experimental setups.

With the Alpha analyzer, a parallel plate capacitor configuration is used. In order to measure low dielectric loss ($\varepsilon''$), small plate distances and large areas of the

capacitor plate are necessary. To measure a polycrystalline powder sample, the powdered material is sandwiched between two metallic discs made up of stainless steel or brass (gold coated brass is used in case of reactive material), and the capacitor is made by pressing the material between two electrode plates by using a hydraulic press. A Teflon ring is used to cover the lateral surface of the discs and sample to prevent a signal contribution from stray electric fields formed at the exterior edge of the pellet. The separation between both electrodes is determined by the pellet thickness d and thus by the quantity of material which is being compressed. For measuring liquid samples, a special home-built capacitor with a reservoir is employed that is filled directly with the liquid (see the schematics in Figure 3.4). Glass-fiber spacers are used to fix the distance between the plates at 50 μm or 100 μm. For both cases (powder and liquid dielectric), the capacitor filled with the sample is placed in a sample holder between the two electrodes of the holder (photographed in Figure 3.4) and the whole set up is then inserted inside the cryostat.

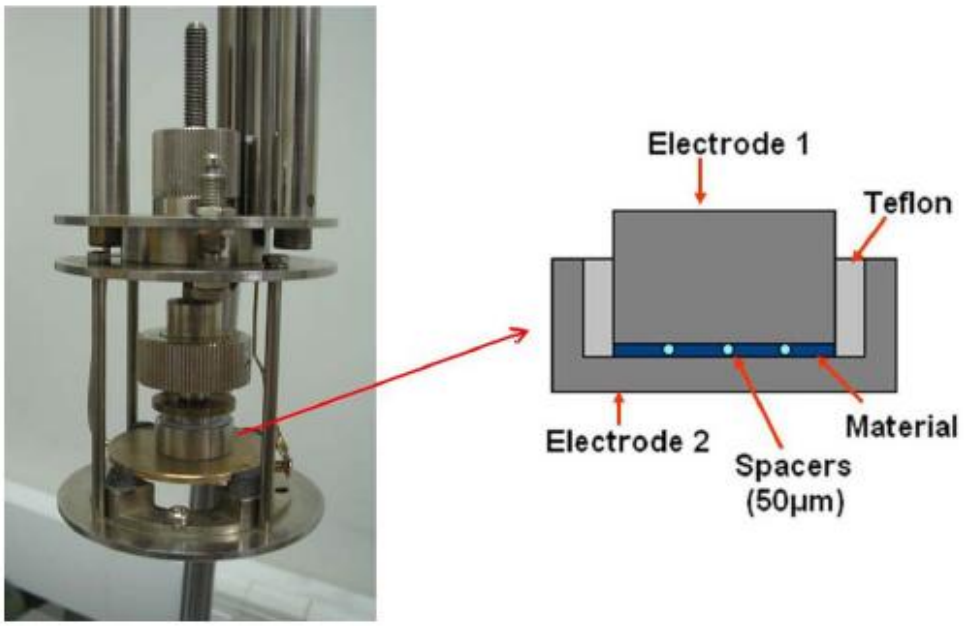


Figure 3.4: Picture of the sample holder with a scheme of the capacitor used for liquid samples.

High-frequency range measurements between $10^6$ Hz to$10^9$ Hz are performed by using a coaxial reflection technique. The sample under investigation is loaded in a small capacitor that is placed at the end of a home-made coaxial line (Figure 3.5), which is then connected to the test head of the HP4291 impedance analyzer.

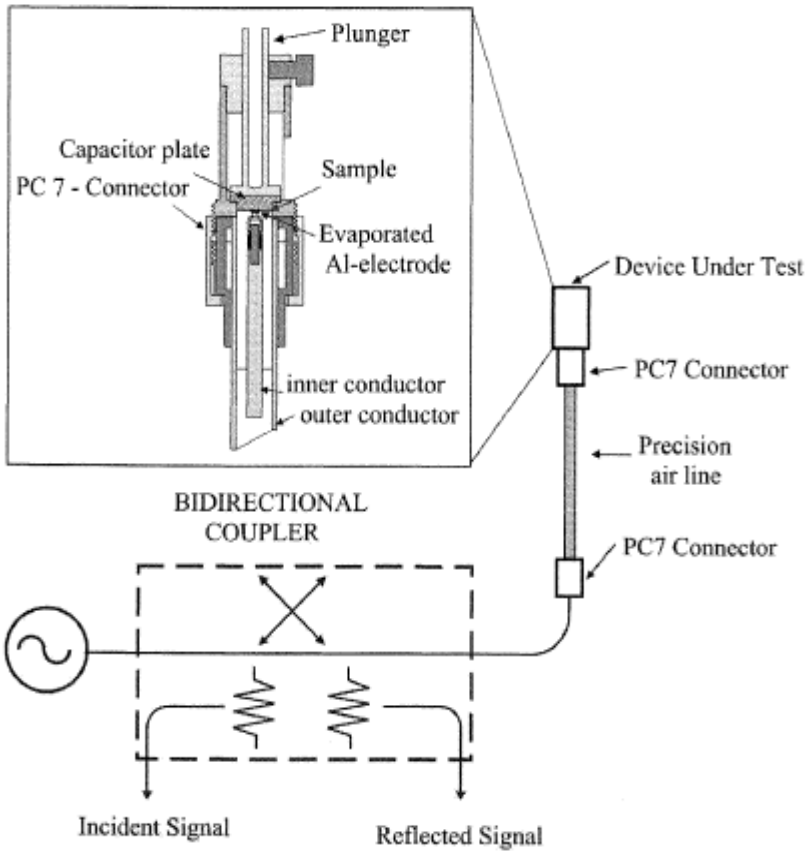


Figure 3.5: Scheme of the coaxial line reflectometer used for high-frequency dielectric measurements.[6]

The electromagnetic wave travelling along the line is reflected by the sample, and the properties of the reflected signal depend on the nature of the sample. The real part of the parallel capacitance $C_p$' and the real part of the conductance G' are obtained by current-voltage measurements. The relation between $C_p$' and the real part of the complex dielectric permittivity of the sample is given by:

(3.3) $\varepsilon' = \frac{C_P}{C_0}$.

Similarly the relation between G' and the imaginary part of the complex dielectric permittivity is given by:

(3.4) $\varepsilon'' = \frac{G'}{C_0 2\pi f}$.

Here $C_0 = \varepsilon_0 A/d$ is the capacitance of the empty capacitor with electrodes of surface area A separated by a distance d; $\varepsilon_0$ is the vacuum permittivity and f is the frequency.

In this technique the perfect construction of the coaxial line and the proper mounting of the sample are essential, and a careful calibration of the system is required to correct any contributions of the coaxial line itself and of the sample holder.

A scheme of the experimental station common to both setups is shown in Figure 3.6. The station allows controlling the sample temperature by means of a nitrogen-gas heating/cooling stage. The variation of dielectric spectra with temperature is investigated with the help of Novocontrol Quatro Cryosystem, consisting of a cryostat in which the sample holder or cell is placed, equipped with a gas heating unit and connected to a liquid nitrogen Dewar with pressure sensor (Figure 3.6). The sample temperature is measured by a platinum resistor sensor (PT100) in thermal contact with one of the capacitor plates. The system can work in the temperature range from 116 K to773 K with a nominal precision of 0.01 K.

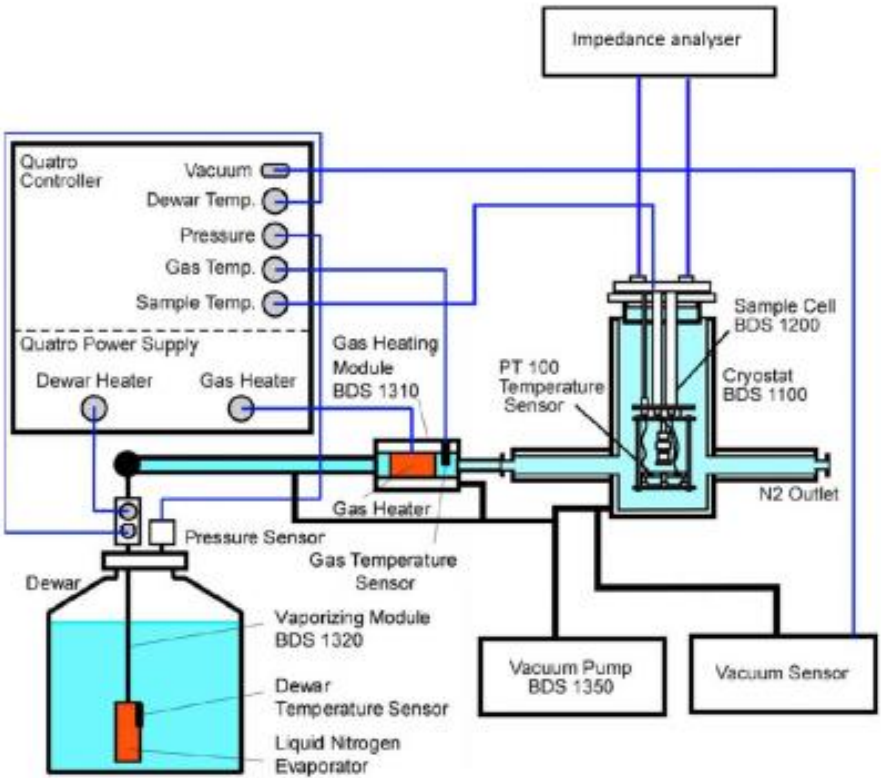


Figure 3.6: Experimental setup for temperature-dependent broadband dielectric measurements.[7]

## 3.3 Dielectric Data Analysis

The complex, frequency-dependent dielectric function $\varepsilon^*(\omega)$ represents the response of a sample to an applied AC electric field, which originates from different processes: (i) microscopic fluctuations of molecular dipoles (orientational relaxation), (ii) the propagation of mobile charge carriers (translational diffusion of electrons, holes or ions), and (iii) the separation/accumulation of charges at interfaces. The latter gives rise to an additional polarization and can take place at inner dielectric boundaries (e.g. grain boundaries), and is then referred to as a "space-charge relaxation", and/or at the external electrodes contacting the sample, and is then referred to as "electrode polarization effect". Its contribution to the dielectric loss can be orders of magnitude larger than the dielectric response due to molecular fluctuations. Each of the above mentioned processes exhibits specific

features in the frequency and temperature dependence of the real and imaginary part of the complex dielectric function.

Here we discuss the methods to analyze, to separate, and to quantify the different contributions to the dielectric spectra. Depending on whether the dielectric response of the sample under study is dominated by mobile charge carriers or permanent molecular dipoles, i.e., whether the conductivity contribution or molecular relaxation processes preponderates, dielectric data is more usefully represented as $\varepsilon^*(\omega)$, $\sigma^*(\omega)$, or $M^*(\omega)$ (all three representations are inter-related and equivalent in terms of the total information they carry).

### 3.3.1 Complex Permittivity and Dielectric Relaxations

All dielectric relaxation processes are characterized by a relatively broad peak in the imaginary part $\varepsilon''$, and a corresponding step-like decrease of the real part $\varepsilon'$ of the complex dielectric function $\varepsilon^*(\omega) = \varepsilon'(\omega) - i\varepsilon''(\omega)$ with increasing frequency. The imaginary part of the permittivity $\varepsilon''(\omega)$, called loss spectrum, is related to the real part of the ac conductivity $\sigma'(\omega)$ as $\varepsilon''(\omega) = \sigma'(\omega)/(2\pi f\varepsilon_0)$. The dc conductivity contribution to the imaginary part of the dielectric function is a background proportional to reciprocal frequency, visible in logarithmic spectra as a straight line with negative slope (vertical height increasing with decreasing frequency). The loss spectrum contains information about the characteristic frequency of dielectric losses such as molecular reorientational motions, and about conductivity-induced losses.[8] As to the real permittivity $\varepsilon'(\omega)$, for pure ohmic conduction the real part of $\varepsilon^*(f)$ is independent of frequency while for non-ohmic conduction or polarization effects (at inner boundaries or external electrodes) the real part of $\varepsilon^*(\omega)$ increases with decreasing frequency. A schematic representation of the frequency dependence of $\varepsilon^*(\omega)$ (for both real and imaginary parts) is given in Figure 3.7.

Dielectric relaxation processes appear in the imaginary part of the permittivity as very broad, sometimes asymmetric, bump-like features covering more than one decade in frequency, and are therefore best displayed in logarithmic spectra as a function of frequency. The line shape of a relaxation loss feature can be numerically

accounted for using the empirical formula given by Havriliak and Negami, and usually referred to as HN function.[9,6] The analytic expression of the HN function is (in terms of linear or angular frequencies):

$$\varepsilon_{HN} = \varepsilon_{\infty} + \frac{\Delta\varepsilon}{(1+(if/f_{HN})^{\alpha})^{\beta}} = \varepsilon_{\infty} + \frac{\Delta\varepsilon}{(1+(i\omega\tau_{HN})^{\alpha})^{\beta}} \quad (3.5)$$

Here $\Delta\varepsilon = \varepsilon_s - \varepsilon_\infty$ is the so-called dielectric strength of the dielectric feature, $\varepsilon_\infty$ and $\varepsilon_s$ being the high-frequency and static low-frequency limits of the real permittivity. The constants $\alpha$ and $\beta$ are shape parameters in the range from 0 to 1, and $f_{HN} = 1/2\pi\tau_{HN}$ is a fitting parameter from which the frequency $f_{max}$ at which the dielectric loss is maximum is obtained as:

$$f_{max} = f_{HN}\left(\sin\frac{\alpha\pi}{2+2\beta}\right)^{1/\alpha}\left(\sin\frac{\alpha\beta\pi}{2+2\beta}\right)^{-1/\alpha} \quad (3.6)$$

A sample may display more than one relaxation process; each fitted or modeled with a separate HN function with different coefficients. In the case of materials having also a conductivity contribution, a dc-conductivity term has to be included in the fitting function used to model the loss spectra, so that the total contribution to the dielectric permittivity can be written as a superposition of, say, a total of *k* Havriliak Negami functions plus a conductivity term, yielding the following equation in terms of the angular frequency:

$$\varepsilon*(\omega) = -i\left(\frac{\sigma_0}{\varepsilon_0\omega}\right)^{N} + \sum_k\left[\frac{\Delta\varepsilon_k}{(1+(i\omega\tau_k)^{\alpha_k})^{\beta_k}}\right] + \mathrm{i}\varepsilon_\infty \quad (3.7)$$

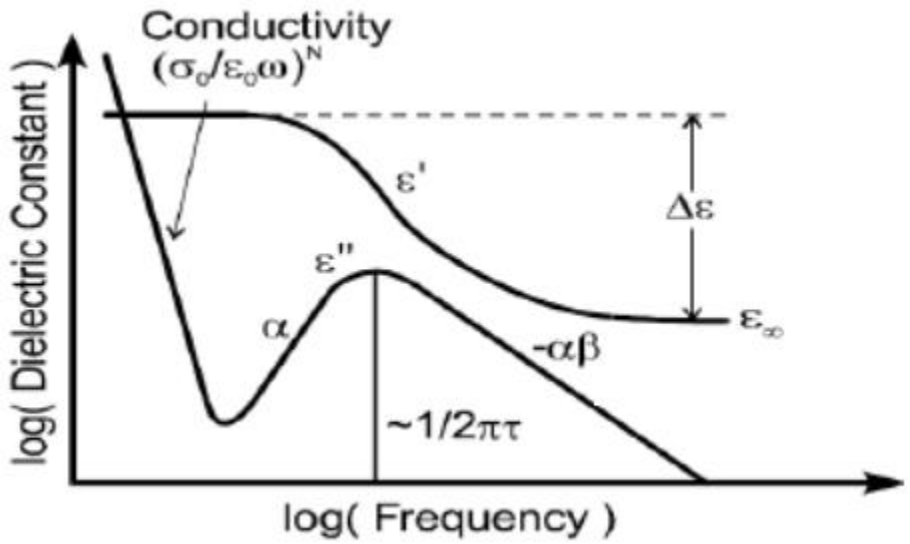


Figure 3.7: Schematic representation of the real and imaginary dielectric permittivity parts of equation (3.7) with only one Havriliak-Negami function.

For ohmic contacts and no space-charge or Maxwell-Wagner-Sillars-polarization effects (see subsection 3.3.2), the exponent N is equal to 1, but in most cases 0.5 < N < 1 is obtained. For each relaxation process, the dielectric strength $\Delta\varepsilon = \varepsilon_{sk} - \varepsilon_{\infty k}$ gives the step-like difference in ε′ at frequencies lower and higher than the frequency of loss maximum, being also proportional to the area below the corresponding ε″ relaxation peak. The value ε′ at infinite frequency is determined by $\varepsilon_\infty$. For common values of the Havriliak Negami shape parameters α and β, the maximum of the relaxation peak in ε″ is approximately situated at $f_{HN} = 1/(2\pi\tau_{HN})$. The width parameter α specifies the slope of the low frequency side whereas −αβ gives the slope of the high frequency side of the relaxation in ε″. The HN function contains as special cases the Cole-Cole (β = 1) and Cole-Davidson (α = 1) functions, and if α = β = 1 it reproduces the Debye behavior. The Debye behavior is particularly simple as it corresponds to the dielectric response of a sample with a unique relaxation time; compared to it, all other functions are said to represent a material displaying a continuous distribution of relaxation times.

The dielectric loss peaks of dipolar origin, in particular at low frequencies may obscured by the (ionic or electronic) dc conductivity, so that the ohmic conduction term should be eliminated to elucidate low-frequency relaxation processes. In order to remove frequency independent conduction from measured loss spectra an approximate logarithmic derivative approach is used[10]:

$$\varepsilon''_{der} = -\frac{\pi}{2}\frac{\partial \varepsilon'(\omega)}{\partial ln(\omega)} \approx \varepsilon''_{pol} \quad (3.8)$$

Equation 3.8 approximately equals the ohmic-conduction-free dielectric loss $\varepsilon''_{pol}$ for rather broad peaks, like those of primary or secondary relaxations in molecular glass formers.

In this thesis we have fitted only the imaginary part of the dielectric permittivity (loss spectra), or equivalently the ac conductivity spectra, without fitting simultaneously the real permittivity spectra. To this aim, we employed the standard software package WinFIT, which is especially designed for dielectric and impedance fits. It gives a fast routine for the optimization of the imaginary part of equation (3.7), allowing an analytical evaluation of dielectric spectra. The main feature of WinFIT is nonlinear curve fitting of the measured data in the frequency and time domains. The measured data can be imported in several binary and flexible ASCII formats, displaying the data and fit function in an online window.

### 3.3.2 Ac Conductivity and Space-Charge Losses

Figure 3.8 shows the typical ac conductivity spectrum σ'(ω) of a disordered material without any relaxation due to permanent dipoles (if such a relaxation were present, it would be visible as a bump-like feature in the ac conductivity, just as in the ε″(ω) spectra, only on top of a non-horizontal background). The ac conductivity in such disordered materials is mediated by hopping (rather than band-like) processes, and it displays a flat response at low frequency corresponding to the dc limit, and a temperature-dependent power-law-like increase at high frequency. This behavior is characteristics of the charge transport in disordered materials and is

known after Jonscher as "universal dynamic response" (UDR).[11,12] The frequency behavior of the dispersive part of the ac conductivity can be described roughly by:

$$\sigma'(\omega) = \sigma_{dc}\left[1 + \left(\frac{\omega}{\omega_c}\right)^s\right], \quad (3.9)$$

where $\sigma_{dc}$ is the (frequency-independent) dc conductivity and $s$ is the power-law exponent, in the range $0 < s \leq 1$. In several cases, $s$ is not constant but actually depends on frequency (and temperature).

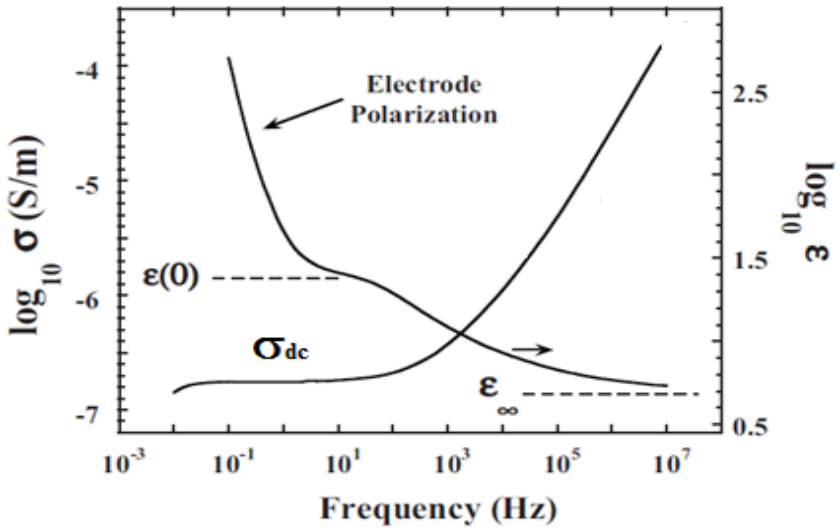


Figure 3.8: Schematic representation of real part of ac conductivity and dielectric constant in a disordered material.

In the UDR, the dc conductivity corresponds to long-range hopping processes, while the ac conductivity stems from local processes that have limited extent or restricted range (for example, electronic hopping between two next neighbor molecules with low-lying energy levels from where the electronic charges have nowhere to hop to). The change from dc to ac regimes is marked by a so-called onset frequency or crossover frequency ($\omega_c$), which represents the typical hop frequency of restricted-range hopping of charge carriers between sites. If the hopping mechanism underlying the dc conductivity is the same as that of the ac

conductivity (except for the larger possible hopping range), the temperature dependence of the cross-over frequency $\omega_c$ is virtually identical to that of the dc conductivity $\sigma_{dc}$. In some cases, at the onset frequency of the ac conduction regime a dielectric loss peak is visible, associated with accumulation of free charge carriers at spatial inhomogeneities of the sample such as grain boundaries. Such loss peak is referred to as conductivity-induced (or space-charge) relaxation and is usually described by the Barton–Nakajima–Namikawa (BNN) relation[13]:

$$\sigma_{dc} = p\varepsilon_0 \Delta\varepsilon\omega_c \quad (3.10)$$

where $p$ is a constant of order 1, $\Delta\varepsilon$ is the dielectric strength of the space-charge relaxation, and $\varepsilon_0$ is the permittivity of free space. Since $\Delta\varepsilon$ has only weak temperature dependence, while $\sigma_{dc}$ and $\omega_c$ are thermally activated, eq. (3.10) implies that the temperature behaviors of the two quantities are strongly correlated, as stated above (see Subsection 3.3.3 for a discussion of the typical temperature dependence). The ac conductivity spectrum can also display a characteristic "bending" at low frequency (Figure 3.8) with a large increase in dielectric constant, which is due to the electrode polarization effect, i.e., the accumulation of charge at the sample/electrode interface. The dc value of the conductivity is usually assigned in such case to the plateau value observable at intermediate frequency. Experimentally, since the plateau is not perfectly horizontal, in the absence of an electrode polarization effect the value of $\sigma_{dc}$ can be taken to be the low-frequency value of the $\sigma'$ spectrum. In spectra exhibiting a more pronounced electrode polarization effect, $\sigma_{dc}$ was taken to be the value of $\sigma'$ in the middle of the plateau or at the point of inflection, that is, at the frequency for which $d\sigma'/df$ was minimum.

It is worth noticing that the ac conductivity obeys a *time-temperature superposition principle*, which means that the shape of $\sigma'(\omega)$ in a log-log plot is temperature independent. This makes it possible to construct a master curve. The shape of the master curve is roughly the same for all disordered solids (universality).[12]

In heterogeneous media made up of distinct phases, these display usually distinct static permittivity (and possibly different dc conductivity). When an ac electric field is applied, this heterogeneity results in the build-up of space charges (both free and bound ones) near the interfaces between the various phases. Such an interfacial polarization may result in a characteristic dipolar loss, referred to as Maxwell-Wagner-Sillars polarization[14,15] which usually occurs at frequencies lower than the time scales typical of molecular orientational polarization contributions. The accumulation of charges at internal phase boundaries causes a strong increase in $\varepsilon'$ with decreasing frequency, just as in the electrode polarization effect. The simplest models to characterize the dielectric properties of a inhomogeneous media is a layered structure of two materials with frequency independent dielectric constants $\varepsilon_1$ and $\varepsilon_2$, in which only one medium is electrically conductive or else a spherical intrusion of one phase in an otherwise uniform background of the other phase. In these models, each region is characterized by a different relative permittivity and dc conductivity. Experimentally, it is found that if the phase boundaries are well defined, the Maxwell-Wagner-Sillars polarization has a single, well-defined relaxation time and can be fitted accordingly by the Debye model function (special case of HN function, Eq. 3.5, with $\alpha = \beta = 1$). The more complicated case in which both media are electrically conductive and have dc conductivities $\sigma_1$ and $\sigma_2$, respectively, as sketched in Figure 3.9, the complex dielectric function can be written as:

$$\tilde{\varepsilon}^*(\omega) = \tilde{\varepsilon}_\infty + \frac{\widetilde{\Delta\varepsilon}}{1+\omega\tau_{MW}} \qquad (3.11)$$

Equation (3.11) is similar to Debye formula but the parameters have a completely different meaning and physical origin. The relaxation time $\tau_{MW}$ of the interfacial polarization can be computed as:

$$\tau_{MW} = \varepsilon_0 \frac{\varepsilon_1+\varepsilon_2}{\sigma_{r1}+\sigma_{r2}} \qquad (3.12)$$

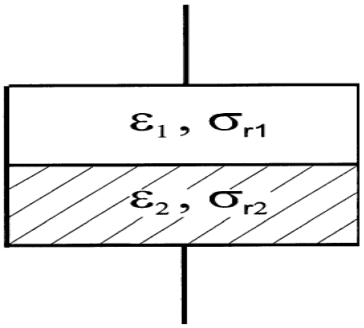


Figure 3.9: Two dielectric layers in series. $\varepsilon_i$ and $\sigma_{ri}$ are the corresponding dielectric permittivities and dc conductivities. [6]

We conclude this subsection with a short discussion of the modulus formulism. In the complex modulus representation, an increase in ε″ or a decrease in σ′ with decreasing frequency is transformed into a step-like change in the real part of the modulus and as a peak in the imaginary part of modulus. Hence a modulus peak is often observed which is associated with the conduction process.[16,17] In materials exhibiting a relaxation due to the motion of permanent dipoles, such dipolar relaxation is also visible as a (separate, higher-frequency) peak in the imaginary part of *M*. The advantage of representing dielectric data in modulus formalism is that the electrode polarization effects are suppressed in this representation. This is primarily because of the insensitiveness of the frequency dependence of the imaginary part of the modulus to the polarization processes, provided these are characterized by capacitances that are much larger than the bulk capacitance.[18]

An HN function can be defined in the modulus formalism, and used to fit relaxation or conductivity losses visible in the modulus spectrum. The phenomenological HN function used to analyze the frequency dependence of the complex modulus is given by [6]:

$$M_{\mathrm{HN}}{}^{*}(f) = M_{\infty} + \frac{\Delta M}{(1+(-i(\omega\tau_{HN-M})^{-1})^{\alpha_M})^{\beta_{HN-M}}} \qquad (3.13)$$

As in the permittivity HN function, $\tau_{HN\text{-}M}$ is a characteristic relaxation time, and α and β are shape parameters describing the distribution of relaxation times.[19]

### 3.3.3 Temperature Dependence of the Relaxation Times and Dc Conductivity

Once the relaxation times and dc conductivity have been determined with the procedures described in the previous sections, the temperature dependence of the relaxation times and dc conductivity can be analyzed. In practice two expressions are commonly used to express the temperature dependence of the dipolar relaxation and ionic motion. The first one is the Arrhenius equation, originally introduced to describe chemical reactions. The second one is the Vogel–Fulcher–Tamman (VFT) equation[20], introduced to describe the non-Arrhenius dependence in many glass-forming systems.[21]

***Arrhenius and Vogel-Fulcher-Tammann Temperature Dependence***

The mathematical expression characterizing the temperature dependence of the rate *R* of a simply activated process is the Arrhenius law:

$$R = Aexp\left(-\frac{E_a}{k_B T}\right) \tag{3.14}$$

Here A is an independent factor, $E_a$ is the activation energy and $k_B$ is the Boltzmann constant. Linearization of this equation shows that an Arrhenius process shows up as a straight line when the rate *R* (relaxation time or dc conductivity) is plotted versus the inverse temperature (the so-called Arrhenius plot), and the slope of this line is proportional to the activation energy. Thus, Arrhenius plots are commonly used to display the temperature dependence of the dynamics.

If the temperature dependence of a process is only approximately described by the Arrhenius Eq. (3.14), it is convenient to define effective or apparent, activation energy, as:

(3.15) $$E_a(R(T)) = -k_B \frac{d(Ln(R))}{d(1/T)}$$

In the case of perfect Arrhenius dependence, $E_a$ as calculated from Eq. (3.15) is exactly constant, while for sub- or super-Arrhenius dependence $E_a$ increases or decreases with increasing temperature.

The variation with temperature of the primary relaxation time of glass formers and so-called rotator phases (phases in which the average molecular centers of mass occupy lattice points, as in an atomic crystal, but where the molecules display rotational motions) is generally non-Arrhenius (Figure 3.10). In particular, upon cooling the relaxation time almost always increases faster than predicted by the Arrhenius equation (3.14). One of most commonly accepted models to mimic such behavior is the Vogel-Fulcher-Tammann (VFT) equation[20], which was introduced as a fitting function for the relaxation time of glass-forming liquids. The VFT equation is usually given in the form:

(3.16) $$\tau = \tau_0 \exp\left(\frac{DT_{VF}}{T - T_{VF}}\right),$$

where $\tau_0$ is the high temperature limit of the relaxation time, D is strength coefficient which related to the fragility of the material and $T_{VF}$ is the Vogel temperature, associated by some authors with a would-be "ideal" glass transition temperature.

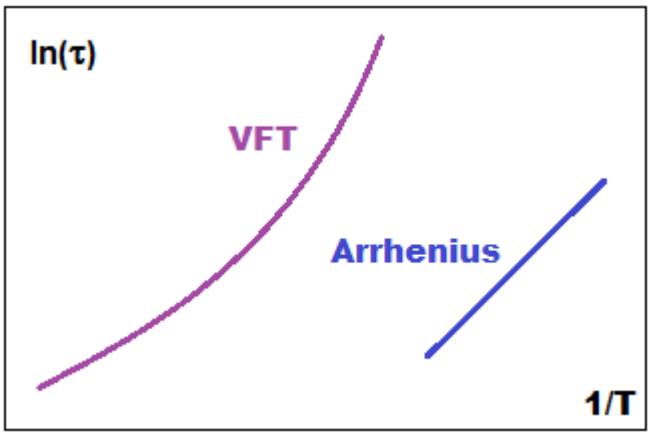


Figure 3.10: Schematic representation of VFT behavior and the Arrhenius dependence of relaxation process.

***Sub-Arrhrenius and Super-Arrhenius Dependence of the dc Conductivity***

In the case of Arrhenius plot of dc conductivity, several systems display non-Arrhenius dependence. Interestingly, depending on the sign of the variation of effective activation energy with a change in temperature, different conduction mechanism can be distinguished (Figure 3.11). In the case of electronic or polaronic charge carriers moving by hopping, the dc conductivity may either follow or deviate from the Arrhenius behavior. For example, the so-called nearest-neighbor hopping (NNH) model, in which an electronic charge carrier may only jump from an initial molecule to a first neighbor molecule, the predicted temperature behavior is a perfect Arrhenius law:

(3.17) $\sigma_{dc} = \sigma_0 \exp(-T_0/T)$.

Many semiconducting materials, however, follow the prediction of the so-called variable-range hopping (VRH) theory,[22,23] first introduced by Mott, according to which the temperature dependence of the dc conductivity is given by:

(3.18) $\sigma_{dc} = \sigma_0 \exp[-(T_0/T)^n]$,

entailing that the Arrhenius plot of $\sigma_{dc}$ follows a power-law dependence of the type $Log(\sigma_{dc}) = A - B/T^n$. The result of the fit for different samples gives values of n close to ½ or ¼.[24,25]

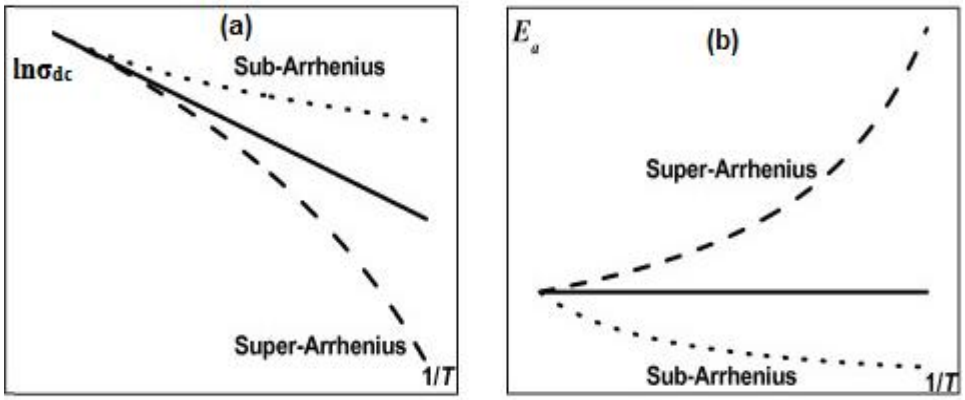


Figure: 3.11 Schematic representation of the Arrhenius plot for the (*a*) dc conductivity and (*b*) its activation energy.

While in the NNH hopping conduction always occurs via neighboring sites, and hence the hopping range (typical hopping distance) are independent of temperature, according to the theory proposed by Mott, the hopping range may vary as temperature decreases. The basic idea is the following: while in the NNH model it is assumed that all sites are equivalent so that the activation energy (typical energy barrier) between all possible pairs of molecules is always the same, in real materials hops between different sites and energy levels will also have different activation energy. While at high enough temperature the thermal energy is sufficiently high that next-neighbor hops will always be the most likely to occur, at low temperature the charge carriers might find it more efficient to hop (tunnel) through larger distances if this allows finding a new site characterized by a smaller energy barrier (the hopping rate decays exponentially the longer the hopping distance, but also the higher the barrier). As a result, the typical hopping range will increase as the temperature is decreased, whence the name variable-hopping range. While Mott

original theory assumed an energy-independent density of states, and predicted a power-law exponent n = ¼, the more commonly found n = ½ value is determined by electron-electron correlation leading to a weak Coulomb gap near the Fermi level and to a square dependence of the local state density on energy. In both cases, the apparent activation energy is observed to increase with increasing temperature, and the Arrhenius plot of $\sigma_{dc}$ exhibits a positive curvature.

In the case of ionic charge carriers, different behaviors are observed. In disordered materials such as glass formers, the Arrhenius plot of $\sigma_{dc}$ exhibits a negative curvature; in other words a decrease in effective activation energy with increasing temperature is usually observed. The temperature dependence of $\sigma_{dc}$ in (partially) disordered ionic conductors has been often represented by the empirical VFT equation, in the form:

$$\sigma_{dc} = \sigma_0 \exp\left(\frac{DT_{VF}}{T-T_{VF}}\right). \quad (3.19)$$

***Walden rule and Debye-Stokes-Einstein relation***

In salt solutions, ionic liquids and glass formers, a correlation between the dc conductivity $\sigma_{dc}$ and the self-diffusion relaxation time $\tau$ is often found, described by the Debye–Stokes–Einstein (DSE) relation:

$$\sigma_{dc}\tau = \text{constant}. \quad (3.20)$$

The DSE relation implies that the plot of Log ($\sigma_{dc}$) *versus* Log ($\tau$) has a slope equal to minus one, an empirical relation known as Walden rule and verified in many liquid electrolytes.[26] In the case of glass formers, near the glass transition temperature a decoupling is sometimes observed between the dc conductivity and the structural relaxation time. In such case, the relation between $\tau$ and $\sigma_{dc}$ can be described using an empirical equation known as fractional DSE relation:

(3.21) $\sigma_{dc}\,\tau^{s} = \text{constant},$

where the exponent *s* is less than 1. This equation is a phenomenological correction of the DSE law.[27]

# References


[1] Brown, M.E. *Introduction to Thermal Analysis*, Kluwer Academic Publisher, London **2001**.

[2] Pungor, E. *A Practical Guide to Instrumental Analysis.* Boca Raton, CRC Press Florida **1995**.

[3] Skoog, D. A. Holler, F. J. and Crouch, S. R. *Principles of Instrumental Analysis,* 6th Ed. Thomson Brooks, Belmont, CA **2007**.

[4] Griffiths, P. R. and De Haseth, J. A. *Fourier Transform Infrared Spectrometry,* 2nd Ed. Wiley New York **2007**.

[5] Evain, M.; Deniard, P.; Jouanneaux, A. and Brec, R. Potential of the INEL X-ray Position-sensitive detector: A General Study of the Debye–Scherrer Setting. *J. Appl. Cryst.* **1993**, 26, 563-569.

[6] Kremer, F.; Schönhals, A. *Broad Band Dielectric Spectroscopy*, Springer: Berlin **2003**.

[7] http://www.novocontrol.de/.

[8] Lunkenheimer, P and Loidl, A. Response of Disordered Matter to Electromagnetic Fields. *Phys. Rev. Lett.* **2003**, 91, 207601.

[9] Havriliak S.; Negami, S. A complex Plane Analysis of α-Dispersions in Some Polymer Systems. *J. Polym. Sci. C* **1966**, 16, 99−117.

[10] Wubbenhorst, M. and Turnhout, J. van. Analysis of Complex Dielectric Spectr. I. One-Dimensional Derivative Techniques and Three-Dimensional Modeling. *J. Non. Cryst. Solids* **2002**, 305, 40–49.

[11] Jonscher, A. K. The 'Universal' Dielectric Response. *Nature* **1977**, 267, 673-679.

[12] Dyre, J. C. and Schrøder, T.B. Universality of Ac Conduction in Disordered Solids. *Rev. Mod. Phys.* **2000**, 72, 873-892.

[13] (a) Barton, J.L. La Relaxation Diélectrique de Quelques *Verres* Ternaries Silice Oxyde Alcalin Oxyde Alcalino-Terreux. *Verres et Refr.* **1971**, 20, 324-328. (b) Nakajima, T. Correlations between Electrical Conduction and Dielectric Polarization in Inorganic Glasses. *Ann. Rep. Conf. on Electric Insulation and Dielectric Phenomena, National Academy of Sciences, Washington DC*. **1971**, 168-176. (c) Namikawa, H. Characterization of the Diffusion Process in Oxide Glasses Based on the Correlation between Electric Conduction and Dielectric Relaxation. *J . Non. Cryst. Solids* **1975**, 18, 173-195.

[14] Wagner, R.W. Erklärung der dielektrischen Nachwirkungsvorgänge auf Grund Maxwellscher Vorstellungen. *Archiv. Elektrotech.* **1914**, 2, 371.

[15] Sillars, R.W. The Properties of A Dielectric Containing Semiconducting Particles of Various Shapes. *J. lnst. Elect. Eng.* **1937**, 80, 378-394.

[16] Köhler, M.; Lunkenheimer, P.; and Loidl A. Dielectric and Conductivity Relaxation in Mixtures of Glycerol with LiCl. *Eur. Phys. J. E* **2008**, 27, 115–122.

[17] Baskaran, N. Conductivity Relaxation and Ion Transport Processes in Glassy Electrolytes. *J. Appl. Phys.* **2002**, 92, 825.

[18] Molak, A.; Paluch, M.; Pawlus, S.; Klimontko, J.; Ujma, Z. and Gruszka, I. Electric Modulus Approach to the Analysis of Electric Relaxation in Highly Conducting $(Na_{0.75}\ Bi_{0.25})(Mn_{0.25}Nb_{0.75})O_3$ Ceramics. *J. Phys. D: Appl. Phys*. **2005**, 38, 1450–1460.

[19] Wojnarowska, Z.; Wang, Y.; Paluch, K. J.; Sokolov, A. P.; Paluch, M. Observation of Highly Decoupled Conductivity in Protic Ionic Conductors. *Phys. Chem. Chem. Phys.* **2014**, 16, 9123-9127.

[20] Vogel, H. Temperature Dependence of Viscosity of Melts. *Physik. Z.* **1921**, 22, 645-646.

[21] Lunkenheimer, P.; Schneider, U.; Brand, R and Loidl, A. Glassy Dynamics. *Contemporany Physics* **2000**, 41, 15-36.

[22] Mott, N. F. and Davis, E. A. Electronic Processes in Noncrystalline Materials, Clarendon, Oxford, **1979.**

[23] Capaccioli, S.; Lucchesi, M.; Rolla, P. A.; Ruggeri, G. Dielectric Response Analysis of a Conducting Polymer Dominated by the Hopping Charge Transport. *J. Phys.: Condens. Matter.* **1998**, 10, 5595–5617.

[24] Efros, A.L.; Shklovskii, B.I. Coulomb Gap and Low Temperature Conductivity of Disordered Systems. *J. Phys. C: Solid State Phys.* **1975**, 8, L49–L51.

[25] van Staveren, M. P. J.; Brom, H. B.; de Jongh, L. J. Metal-Cluster Compounds and Universal Features of the Hopping Conductivity of Solids. *Phys. Rep.* **1991**, 208, 1-96 and references therein.

[26] Walden, P. Z. Organic solvents and Ionization Media. III. Interior Friction and its Relation to Conductivity. *Phys. Chem.* 1**906**, 55, 207-246.

[27] Wang, Y.; Lane, N. A.; Sun, C-N.; Fan, F. Zawodzinski, T. A. and Sokolov, A. P. Ionic Conductivity and Glass Transition of Phosphoric Acids. *J. Phys. Chem. B* **2013**, 117, 8003−8009.

# Chapter 4

# Water-Triggered Conduction and Polarization Effects in a Hygroscopic Fullerene

## 4.1 Introduction

Fullerenes and their derivatives display interesting charge conduction properties that are very promising for opto-electronic and slow-electronics applications,[1,2] or even, in the case of some fullerene-metal charge transfer compounds, for electrochemical applications such as batteries.[3,4,5] For what concerns charge transport mediated by electronic charge carriers, electrical conduction in organic molecular materials (such as fullerenes) results from the interplay between hopping, which favors electron and hole transport, and local interactions such as Coulomb repulsion, polarization effects, trapping at defects, or coupling to molecular vibrations, all of which tend to localize charge carriers. As a consequence, most small-molecule organic materials are insulating or behave as disordered

semiconductors in which the main conduction mechanism is electron (or hole) hopping.[6] Localization and polarization effects are especially important:[7] charge carriers are localized on single molecules and are surrounded by a polarization cloud, hence hopping of a charge carrier to a neighboring site is hindered by inter-electron Coulomb repulsion,[8] and it leads to charge transport only if the polarization cloud follows, since otherwise the charge carrier jumps back attracted by the excess bound polarization charge.[9] While this general framework is widely accepted, the mechanism of charge transport in organic molecular materials is subject of debate, and in particular the observation of metallic-like behaviour and superconductivity in some alkali fullerene salts (fullerides), is surprising, since most other organic materials behave as semiconductors.[10]

Many organic materials containing metals or oxygen groups are hygroscopic. The presence of water has in general a strong impact on the conduction properties both in the case of the ionic and electronic transport, introducing in particular new mechanisms for charge generation and conduction and thus boosting the overall dc conductivity.[11,12,13,14,15] This well-known effect is exploited in many kinds of humidity sensors, based both on inorganic materials such as ceramics and on organic materials such as polymers.[16,17] The presence of water can also have an important effect on the dielectric response of materials, leading to an increase of the dielectric constant due to the high orientational polarizability of the dipolar $H_2O$ molecules. Determining the impact of water adsorption or intake on charge conduction properties is not only interesting from a fundamental point of view but it is also crucial for the implementation of organic materials in electronic or sensing devices.[18] Since the value of the conductivity of organic semiconductors in their pure form is usually quite low, the introduction of new charge carriers or conduction paths through adsorption of water leads generally to an increase of the material's conductivity even by several orders of magnitude. The exact origin of such effect, both in organic and inorganic materials, has been the subject of debate.

To shed some light on these issues, we have investigated the intrinsic and water-induced charge transport in a relatively simple organic system, namely the ordered solid phases of a highly symmetric organic fullerene derivative, $C_{60}(ONa)_{24}$, which

is synthesized as a polycrystalline hydrate and which can be obtained as a pure material by heating to sufficiently high temperature. The pure form is hygroscopic, which allows studying the effect on conductivity of water molecules captured from the atmosphere surrounding the sample. The existence of two well-defined phases (pure material and hydrate) allows investigating the impact on the electric conduction of two distinct types of water molecules exhibiting different interactions with the organic matrix: namely, structural water – which is an integral part of the hydrate's crystal structure – and surface hydration water – which is present at the surface of crystalline domains.

## 4.2 Synthesis and Experimental Methods

Sodium oxofulleride ($C_{60}(ONa)_{24}$) was synthesized in the last step of a synthetic route starting from Buckminster fullerene $C_{60}$ (Aldrich, 99.8 %). The route involves first the synthesis of fullerol (chemical formula $C_{60}(OH)_{24}$), as detailed in refs 19, 20 and 21. $C_{60}(ONa)_{24}$ was then obtained by neutralizing $C_{60}(OH)_{24}$ (80 mg) with an aqueous NaOH 1 M solution (~1.7 ml). The salt was precipitated with acetone, centrifuged, washed with acetone and dried at room temperature. The product was a hygroscopic polycrystalline brown powder, soluble in water, which was stored in air prior to measurements (Figure 4.1). The material was characterized by thermogravimetric analysis (TGA), differential scanning calorimetry (DSC), Fourier-transform infrared (FTIR) spectroscopy, X-ray powder diffraction (XRPD), and broadband dielectric spectroscopy (BDS). For both infrared and dielectric spectroscopy the powders were mechanically pressed into pellets of submillimeter thickness.

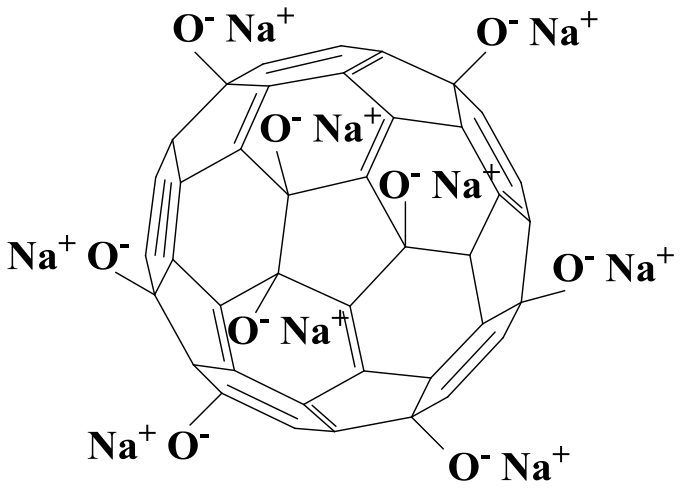


Figure 4.1: Molecular structure of the Sodium oxofulleride $C_{60}(ONa)_{24}$

For the FTIR measurements it was necessary to add KBr powder to the organic material to achieve free standing pellets, and the spectrum of a pure KBr pellet was used as baseline. FTIR spectra were measured in the mid-infrared range (4000 – 400 $cm^{-1}$) using a Nicolet 6700 spectrophotometer equipped with a He/Ne laser source and DTGS-CsI detector. Each spectrum was the average of 32 scans collected with 1 $cm^{-1}$ resolution. TGA scans were acquired while heating the sample under $N_2$ flow between room temperature (300 K) and 600 K at a rate of 2 K $min^{-1}$, by means of a Q50 thermobalance from TA-Instruments. DSC measurements were carried out in an open vessel between 300 K and 600 K, at a rate of 2 K $min^{-1}$, using of a Q100 calorimeter from TA-Instruments. High-resolution X-ray powder diffraction (XRPD) profiles were recorded with a vertically mounted INEL cylindrical position-sensitive detector (CPS120). The peak positions were determined by fits with pseudo-Voigt functions using the DIFFRACTINEL software (see chapter 3 for more details).

Dielectric measurements were carried out in the frequency ($f$) range from $10^{-2}$ to $10^6$ Hz with a Novocontrol Alpha analyzer, using stainless steel electrodes in a parallel-plate capacitor configuration. Isothermal frequency scans were acquired in the temperature range between 200 and 550 K (with a temperature stability of 0.3 K) in a $N_2$ flow Quatro cryostat. The complex impedance data are displayed in four

representations: real and imaginary part of the permittivity (ε' and ε"), real part of the conductivity (σ'), and imaginary part of the modulus (M", where M is defined as the inverse of the complex permittivity, $M = 1/\varepsilon$). The frequency-dependent complex conductivity and the complex relative permittivity are related by the equation $\sigma = 2\pi f\, \varepsilon_0\, \varepsilon$ (see chapter 3 section 3.3). All these quantities are displayed as function of the frequency *f* of the applied electric voltage.

## 4.3 Preliminary Characterization

As mentioned in the introduction, sodium oxofullerene ($C_{60}(ONa)_{24}$) is a hygroscopic material that is synthesized as a polycrystalline hydrate. Figure 4.2(*a*) displays the room temperature FTIR spectra of the as-stored hydrate powder and of the powder heated to 423 K, which no longer contains the structural water. The spectra are normalized to the height of the most intense band at 1458 $cm^{-1}$, which corresponds to the bending mode of the covalent C–O bonds of the $C_{60}(ONa)_{24}$ molecules. Such normalization is equivalent to rescaling the spectra to the relative fullerene content. The presence of water in the as-stored powder is confirmed by the observation of intense bands (indicated by arrows in Figure 4.2(*a*)) at 3465 $cm^{-1}$ (stretching vibration of the O–H bonds of water) and 1690 $cm^{-1}$ (bending mode), whose intensity is significantly reduced after heating to 423 K.

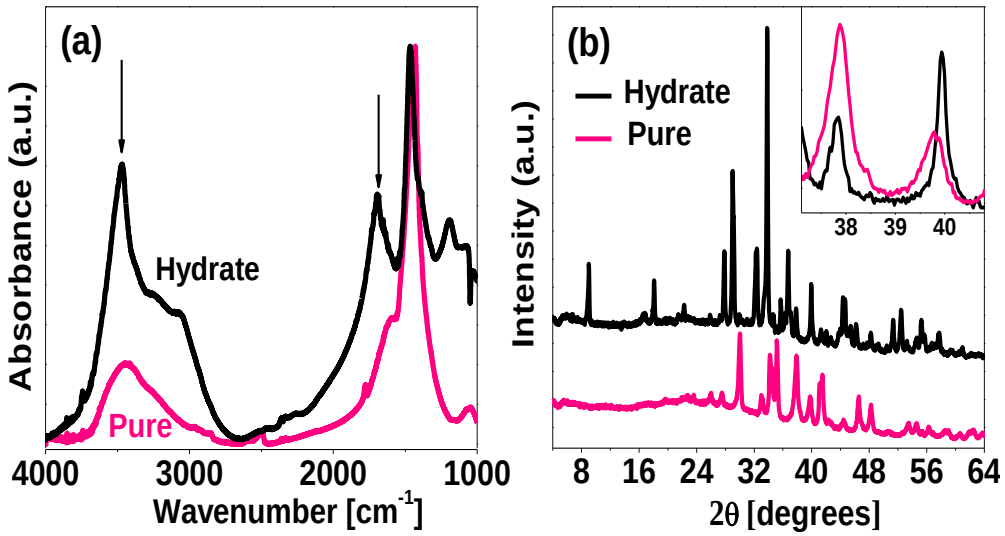


Figure 4.2: Room-temperature FTIR spectra (*a*) and XRPD patterns (*b*) of the as-stored hydrate and of the pure material (after heating to 423 K). The XRPD patterns are normalized to acquisition time and displayed with an offset for clarity. Inset to panel *b*: close-up of the XRPD pattern in the 2θ range between 37 and 41 degrees.

The crystalline nature of both the as-stored and pure materials is revealed by the XRPD patterns of Figure 4.2(*b*). The diffraction pattern of the pure material, obtained by heating the hydrate, exhibits a much higher scattering background and significantly broader peaks, suggesting only partial order and smaller grain size in the pure material than in the hydrate. The average grain size was estimated in both phases from the angular width of non-overlapping diffraction peaks using the Scherrer equation,[22,23] and found to be 32 ± 4 nm for the pure material and 50 ± 10 nm for the hydrate. A smaller linear dimension of the pure grains may be expected considering both the loss of water volume and the possible formation of defects upon the structural change. The structure obtained after heating to 500 K exhibits no clear peaks below 2θ = 20° and displays main peaks at much higher scattering angles than the hydrate. This indicates that the pure material is characterized by a smaller first-neighbor distance, as expected due to the loss of structural water.

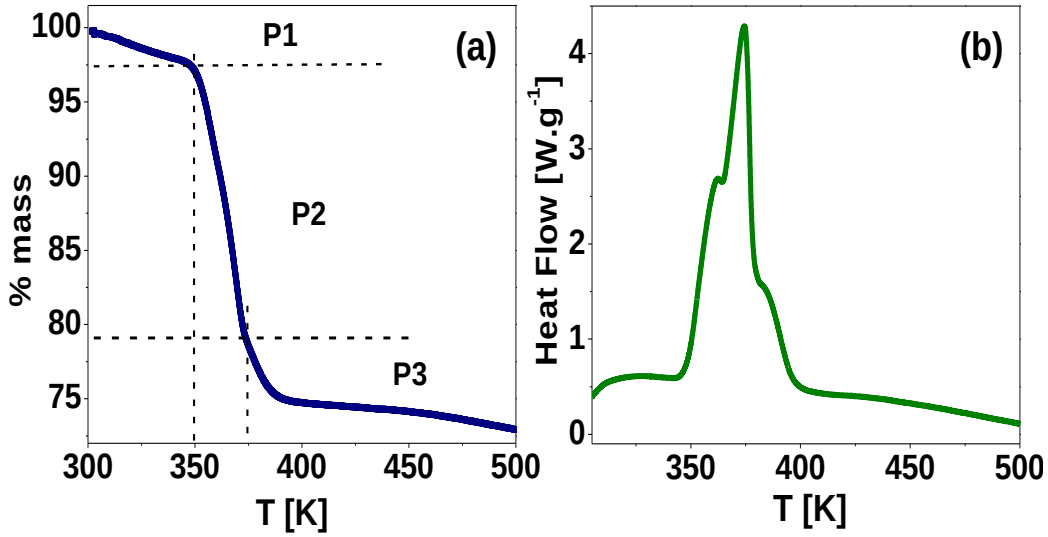


Figure 4.3: TGA (*a*) and DSC (*b*) curves measured on the as-stored hydrate powder. Three different processes associated with the loss of water may be identified: P1 - desorption of surface water; P2 - dehydration of structural water accompanied by phase change; P3 - desorption of migrated water.

Figure 4.3(*a*) displays the TGA scan acquired while heating the hydrate. The curve displays an initially slow decrease of mass (marked in the Figure as P1) starting at room temperature up to approximately 350 K, the temperature that marks the onset of the main water loss (marked as P2). The clear step in the TGA curve indicates a sharp transition from a hydrated to a dehydrated phase upon heating to 370 K which is 15.6% mass loss corresponding to roughly 16 water molecules per fullerene unit, whose stoichiometry can be represented as $C_{60}(ONa)_{24} \cdot 16\ H_2O$ . The temperature of maximum mass loss (obtained by taking the first derivative of the TGA curve) is approximately 370 K, i.e. roughly the boiling point of pure water, which moreover coincides with the crystallographic transition between the hydrate and pure material (see below). We assign the initial mass loss between room temperature and 350 K to desorption of $H_2O$ molecules adsorbed onto the outer surface of the crystalline grains, which are less tightly bound than the structural (interstitial) ones. The main loss corresponds instead to the decomposition of the hydrate. Both assignments will be further corroborated in Section 4.4.

It may be observed that the TGA graph (Figure 4.3(*a*)) does not exhibit the same slope throughout the main water loss. Similarly, the DSC curve (Figure 4.3(*b*)) exhibits a structured peak with weak shoulders on both sides. All observed DSC features correspond to endothermic processes. Such multiple-component spectra are reminiscent of those of other $C_{60}$-derived systems,[24] and result from the different processes accompanying the loss of water, namely the breaking of hydrogen bonds between water and fullerene units, the re-crystallization into a new lattice structure, the migration of water to the outer surface and its final desorption, which is the last process that takes place (we label it as P3 in Figure 4.3(*a*)). The temperature range of each process and the corresponding mass loss are highlighted with dashed lines (see caption of Figure 4.3(*a*)).

The powder diffraction spectra measured near the transition temperature of 370 K (not shown) reveal a single structural change between a crystalline hydrate and a partially ordered pure phase which is obtained irreversibly by heating to high temperature. The structural change therefore occurs simultaneously with the main water loss. The XRPD pattern of the hydrated phase could be indexed by pattern-matching as a monoclinic P2/m phase (Figure 4.4). The indexation was carried out using the DICVOL91 program implemented in the FullProf Suite.[25] The monoclinic P2/m was the only solution obtained in the range of values of unit cell volume between 1000 and 2000 $Å^3$, which is typical of other fullerene derivatives such as $C_{60}Br_{24}(Br_2)_2$, $C_{60}F_{36}$ or $C_{60}F_{48}$.[26,27] Taking as a starting point this solution, the lattice parameters were refined using the Pattern Matching option of the FullProf program. After the last step the following parameters were obtained: $a$ = 19.554(1), $b$ = 9.287(1), $c$ = 6.208(4), $\beta$ = 92.27(5), corresponding to a unit cell volume of 1126.5(1) $Å^3$. The reliability factors were $R_p$ = 3.57, $R_{wp}$ = 4.73, $R_{exp}$ = 2.75 and $\chi^2$ = 2.96. It was not possible to obtain a reliable indexing for the pure material, perhaps due to the low intensity and relatively large width of the low-angle diffraction features in the corresponding pattern (upper curve in Figure 4.2(*b*)). As it occurs for $C_{60}$ powders obtained from solutions and $C_{60}$ solvates in which solvent molecules remain trapped into the re-built lattice,[28] the pure material resulting from the dehydration process may contain structural defects (such as the well-known solvent-

induced stacking faults) which produce broadening, shift or asymmetry of diffraction peaks that vary for different Miller indexes.[24]

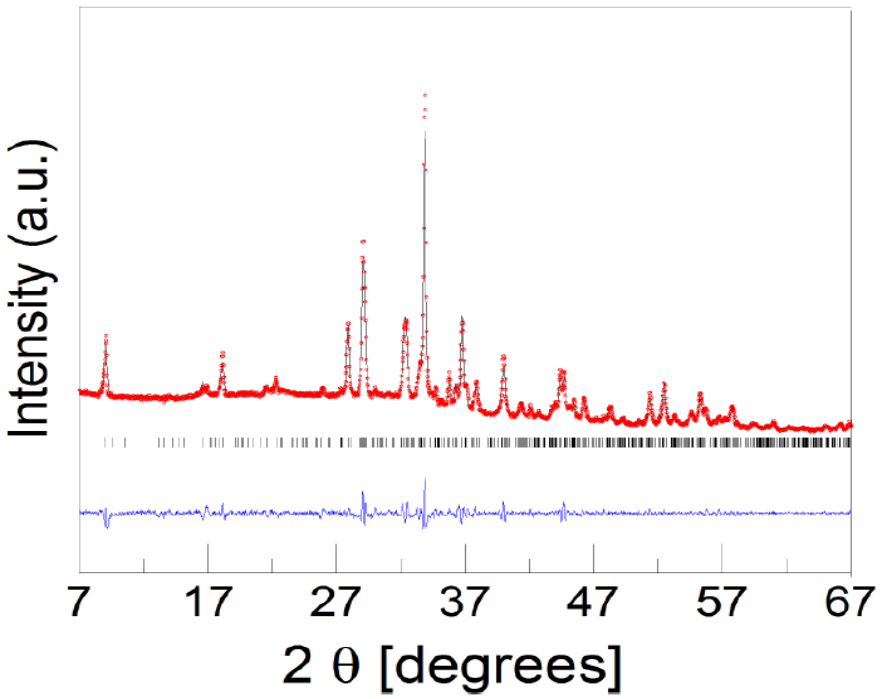


Figure 4.4: Experimental (red circles) and calculated (black line) XRPD patterns along with the difference profile (blue line) and Bragg reflections (vertical sticks) for the pattern matching refinement of the P2/m monoclinic phase of the hydrate at room temperature (same data as those of Figure 4.2(*b*)).

Figure 4.5 shows the frequency-dependent dielectric spectra acquired on the as-stored material (hydrate) during heating from room temperature to 433 K. The data are shown both in the dielectric loss (left-hand panels) and ac conductivity (right-hand panels) representations, and displayed in separate temperature ranges to highlight the observed changes in line shape. The high-temperature spectra shown in Figure 4.5(*d*) (and partially in Figure 4.5(*c*)) represents the pure $C_{60}(ONa)_{24}$ salt, which will be discussed later in this chapter.

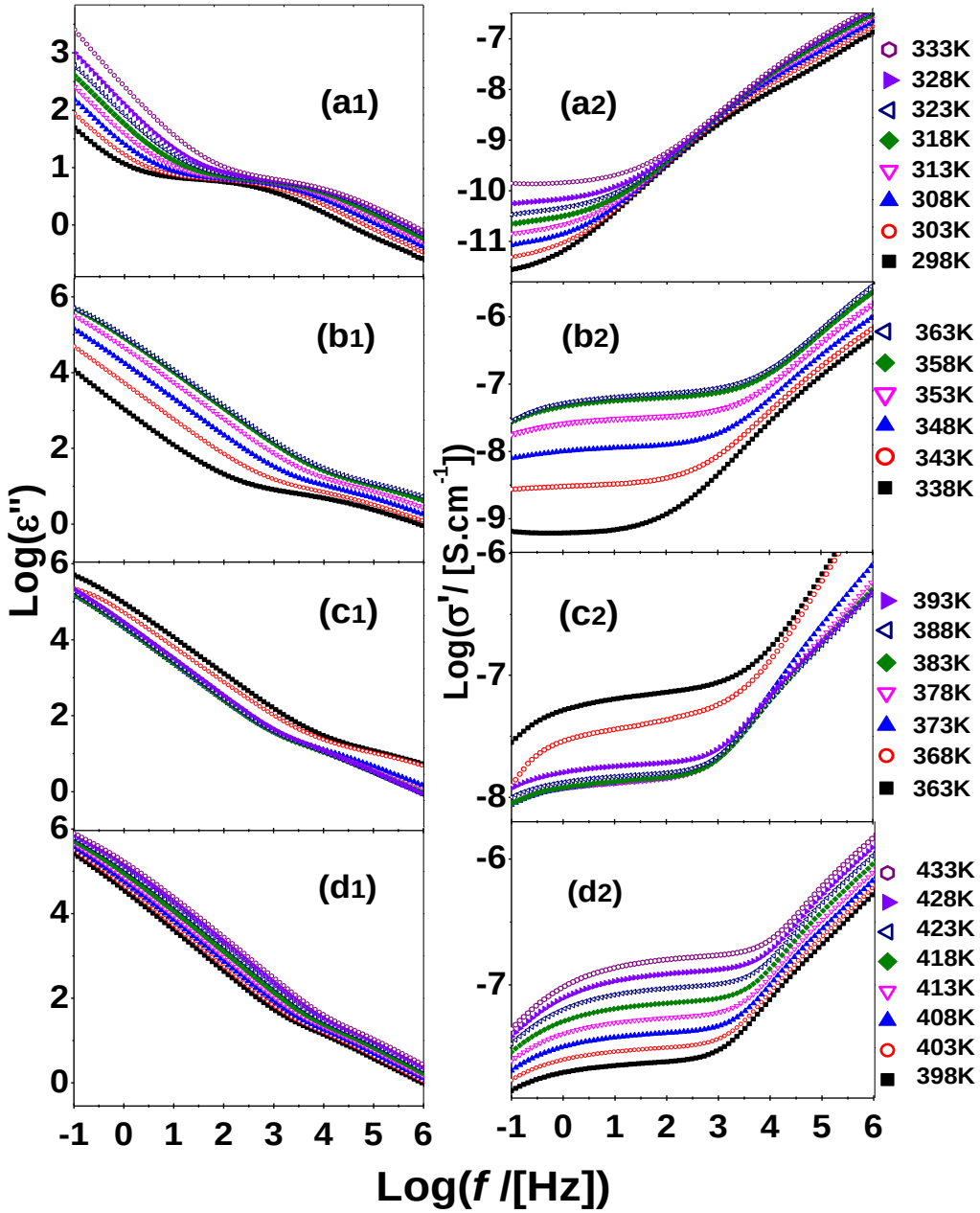


Figure 4.5: Dielectric loss (left panels, 1) and ac conductivity (right panels, 2) spectra acquired on heating the as-stored hydrate, in separate temperature ranges: (*a*) 298 to 333 K; (*b*) 338 to 363 K; (*c*) 368 to 393 K; (*d*) 398 to 433 K.

The dielectric loss (ε") is characterized, both in the hydrate and in the pure material, and at almost all investigated temperatures, by a conductivity background proportional to reciprocal frequency at low frequency[9] and a single loss feature at radiofrequency. As is visible in Figure 4.5(*a1*), in the as-stored hydrate the loss feature is particularly intense and broad, indicating a wide distribution of relaxation times. The relaxation feature in the pure material (Figure 4.5(*d1*)) is characterized by a much lower intensity and is observed in a different frequency range. The origin of this spectral feature is ascribed to charge-carrier-related loss associated with the accumulation of charge at crystalline grain boundaries which will be discussed in the section 4.4.1 in detail. Given the high water content of the as-stored material, it is tempting to ascribe the loss feature in Figure 4.5(*a1*) to the dielectric relaxation of water molecules present in the sample, as was proposed for other organic systems.[29] We will show in the next Section that the origin of the dielectric loss in the hydrate is likely charge accumulation at grain boundaries, although the presence of water molecules affects its spectral intensity. The conductivity spectra exhibit an almost constant value at low frequency, corresponding to $\sigma_{dc}$, and a temperature-dependent increase at high temperature (the so-called dispersive region). As seen in panels *c* and *d* of Figure 4.5, at higher temperatures the conductivity displays a characteristic low-frequency "bending" (also visible, although less pronounced, in the corresponding dielectric loss spectra) due to the electrode polarization effect.

The dielectric response of the hydrate exhibits a complex dependence on temperature. Below approximately 315 K (Figure 4.5(*a*)), both the frequency of the relaxation maximum and the dc conductivity are temperature-activated, as seen from the quasi-rigid shifts (in logarithmic frequency scale) of both the permittivity and conductivity spectra. Between 315 and 333 K, the shift of the relaxation frequency slows down, until it appears to stop at 333 K (Figure 4.5(*a1*)). Between 338 and 363 K (Figure 4.5(*b*)), both the relaxation frequency and $\sigma_{dc}$ are observed to shift much faster with temperature than they do at lower temperatures. Finally, in the range between 368 and 393 K, that is, in the temperature interval of the main mass loss and structural change, a dramatic change of spectral profile is observed in the

dielectric loss spectrum (Figure 4.5(*c1*)), accompanied by a decrease of the dc conductivity by one order of magnitude (Figure 4.5(*c2*)).

The loss peak exhibits a sudden jump to lower frequency around 370 K. We may take this temperature, which lies in the temperature interval of the main dehydration process (Figure 4.3(*a*)) and is very close to the boiling point of pure water at standard pressure, to mark the structural change from hydrate to pure material. The changes observed in Figure 4.5(*c*) signal the transition to the pure phase, which exhibits a smooth temperature-dependence of both the conductivity and the relaxation frequency. As all water has left the sample above 380 K (Figure 4.3(*a*)), the loss peak observed at higher temperatures (Figure 4.5(*d1*)) cannot be associated with a dipolar relaxation of $H_2O$ molecules. This confirms the identification of the dielectric loss in the pure phase as a conductivity-related feature associated with the accumulation of charge at spatial heterogeneities in the sample.

The non-monotonic temperature-dependence of $\sigma_{dc}$ and of the frequency of the loss maximum observable in Figure 4.5 may be at first surprising, as one expects both the conductivity and the characteristic loss frequency to increase with temperature. However, such behavior is not uncommon in water containing porous systems near the water desorption temperature.[30,31,32,33] Given the complexity of the results and the presence of two modalities of hydration in the as-stored powder (Figure 4.3(*a*)), we have probed separately the effect of the structural and surface hydration water. This was achieved by subjecting the as-stored material to different temperature treatments prior to measuring, as explained in the next section.

## 4.4 Detailed Characterization by BDS

The rest of the chapter is organized in three separate sections. In Section 4.4.1 we focus on the charge transport mechanism and related dipolar loss of the pristine material (i.e., the pure $C_{60}(ONa)_{24}$ compound as obtained by annealing to high temperature under nitrogen atmosphere). In Section 4.4.2 we focus on the effect of surface hydration water on the same material. In Section 4.4.3 we present the

conduction and relaxation properties of the $C_{60}(ONa)_{24} \cdot 16\ H_2O$ hydrate, and analyze the effect of the loss of structural water.

### 4.4.1 Pure $C_{60}(ONa)_{24}$

Given that the transition from the hydrate to the pure material is accompanied by a significant mass loss and a change in structure and unit cell volume, heating a pellet made with the hydrate powder (as in Figure 4.5) likely results in a sample with pronounced inhomogeneity due to the loss of the water volume. Therefore, in order to probe the pure material by dielectric spectroscopy, we preheated the as-stored powder to 430 K prior to pressing it into the pellet form necessary for dielectric characterization. The pellet was then heated to 500 K to remove any remaining water. Figure 4.6 shows four representations of the frequency-dependent complex impedance data acquired on pure (water-less) $C_{60}(ONa)_{24}$, at various measuring temperatures while cooling from 500 K. The data are plotted as imaginary part of the complex relative permittivity (dielectric loss) (*a*), real part of the relative permittivity (*b*), real part of the ac conductivity (*c*), and imaginary part of the modulus (*d*).

The isothermal loss spectra (panel *a*) display a conductivity background visible as linear decrease at low frequencies, followed by a loss feature at radiofrequencies. The permittivity spectra (logarithmic plot of ε'(*f*), panel *b*) exhibit a steep decrease at low frequency, followed by a step-like feature at intermediate frequency, whose height is observed to vary slightly with temperature (see also below). Due to the Kramers–Kronig relations, the height of the step in ε' is equal to the dielectric strength Δε of the loss feature. The ac conductivity spectra (panel *c*) display an almost constant plateau value at low frequency, corresponding to the dc limit, and a temperature-dependent power-law-like increase at high frequency (usually termed dispersive region). In the measurements performed at higher temperatures, the conductivity displays a characteristic "bending" at low frequency; the same bending is also visible, although less evident, in the dielectric loss and permittivity spectra at low frequency (panels *a* and *b*). The low-frequency deviation from the dc value of

the conductivity (or equivalently the deviation from linearity in the loss and permittivity spectra) is indicative of accumulation of charge at the sample/electrode interface (electrode polarization). The dc value of the conductivity is usually assigned in such case to the plateau value observable at intermediate frequency. At lower temperatures, the value of $\sigma_{dc}$ can be taken to be the low-frequency value of σ'. In the high-temperature spectra exhibiting a more pronounced electrode polarization effect, $\sigma_{dc}$ was taken to be the value of σ' at the point of inflection, that is, at the frequency for which $d\sigma'/df$ was minimum. The two methods gave consistent results when applied to the low-temperature spectra.

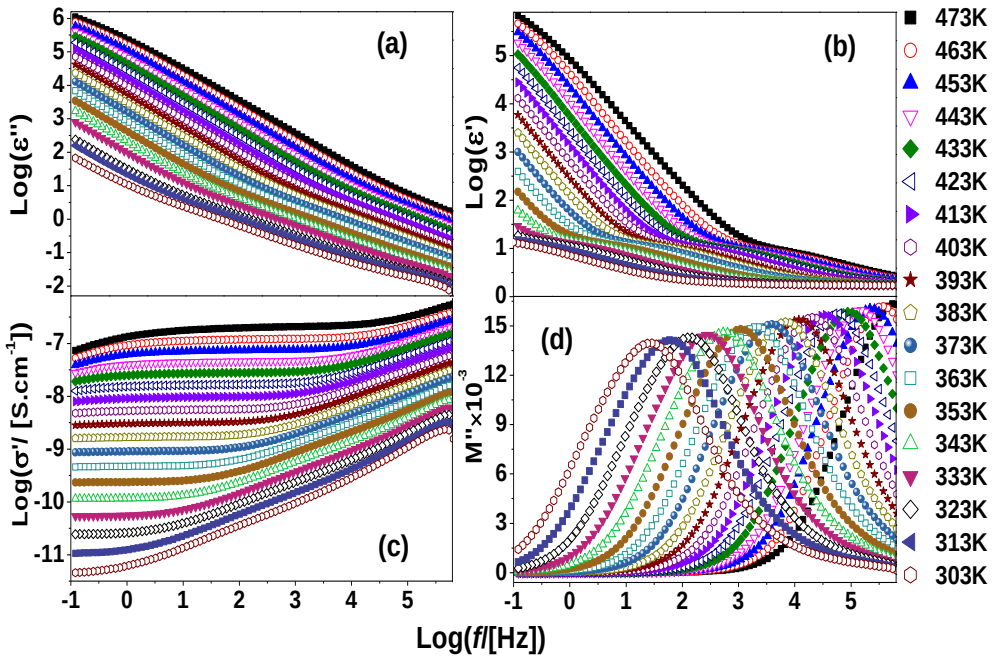


Figure 4.6: Logarithmic plot of the dielectric loss ε" (*a*), permittivity ε' (*b*), and ac conductivity σ' (*c*) spectra, and semilogarithmic plot of the modulus spectra M" (*d*), measured at the indicated temperatures.

The modulus spectra (semilogarithmic plot of M"(*f*), panel *d*) display a main peak, usually termed conductivity relaxation.[9] The spectral position $f_{M"max}$ of the modulus maximum, which was obtained by fitting the spectrum with a HN function in the

modulus representation (see chapter 3 section 3.3.2) coincides with the change of the conductivity between the frequency-independent (dc) plateau value and the dispersive regime characterized by the power-law-like increase. The modulus spectra are slightly asymmetric due to the contribution at high frequency of the dielectric loss feature.

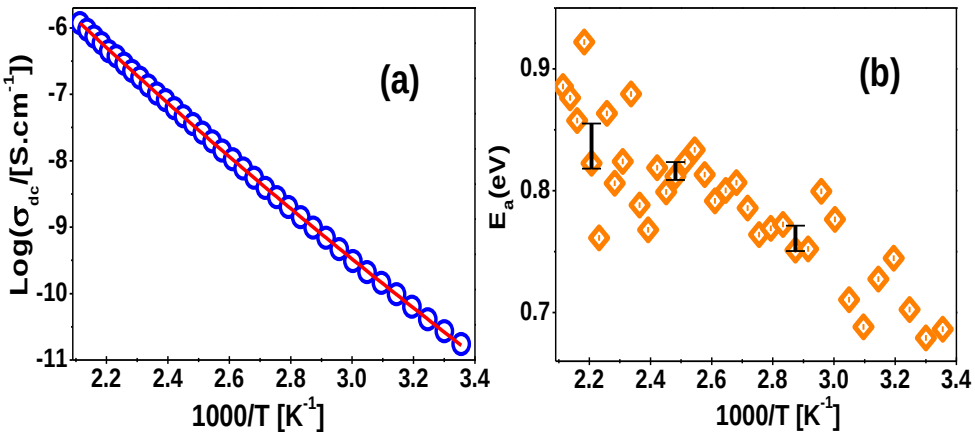


Figure 4.7: Dc conductivity data of pure $C_{60}(ONa)_{24}$, as extracted from Figure 4.6(*c*). (*a*) Arrhenius plot of $\sigma_{dc}$ and corresponding power-law fit (line) (see Eq.(4.2)). (*b*) Apparent activation energy $E_a$ of $\sigma_{dc}$. Bars represent typical uncertainties.

Figure 4.7(*a*) displays the dependence upon temperature of the dc conductivity of the pure material. The variation of the dc conductivity with temperature does not follow a simply-activated Arrhenius behavior with constant activation energy.

Rather, an apparent, temperature-dependent activation energy ($E_a$) can be defined for $\sigma_{dc}$ as:

$$E_a(\sigma_{dc}(T)) = -k_B \frac{d(Ln(\sigma_{dc}))}{d(1/T)} . \quad (4.1)$$

This allows analyzing the temperature-activated behavior of the dc conductivity and of the dielectric response in general.[34]

Figure 4.7(*b*) exhibits the apparent activation energy of $\sigma_{dc}$, as a function of the inverse temperature. It is observed that the apparent activation energies increase slowly with increasing temperature. In fact, the Arrhenius plots of $\sigma_{dc}$ (panel *a*) has a slight positive curvature in the whole temperature range probed. The experimental $\sigma_{dc}$ points were fitted assuming a power-law dependence of the type;

(4.2*a*) $\sigma_{dc} = \sigma_0 \exp [-(T_0/T)^n]$

or equivalently:

(4.2*b*) $\text{Log}(\sigma_{dc}) = A - B/T^n$.

The result of the fit for different samples gave a value of *n* equal to 0.55 ± 0.05, a result which is virtually the same as the value of ½ observed in many systems characterized by variable-range hopping electronic conduction[34] (VRH, see chapter 3 section 3.3.3). The apparent activation energy of $\sigma_{dc}$ is close to 0.7 eV at room temperature and reaches approximately 0.9 eV at 475 K. We can thus take the average activation energy to be 0.8 eV for dc conductivity; such value represents the effective average energy barrier for hopping of charge carriers (barrier which includes Coulomb repulsion and polarization effects).

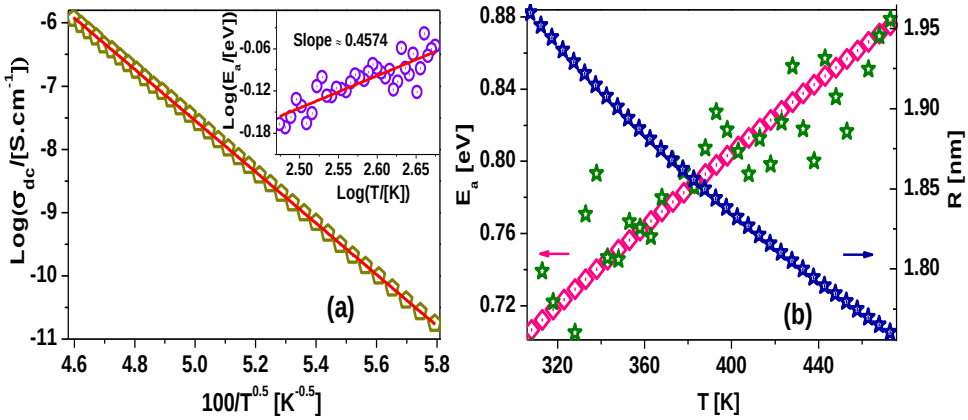


Figure 4.8: Dc conductivity data of pure $C_{60}(ONa)_{24}$, as extracted from Figure 4.6(*c*). (*a*) Plot of Log($\sigma_{dc}$) *vs* $100/\sqrt{T}$. Inset: Logarithmic plot of the apparent activation energy *vs* temperature. Both in the main panel and in the inset the continuous lines are linear fits. (*b*) Activation energy and hopping distance R as a function of temperature for VRH conduction in pure $C_{60}(ONa)_{24}$ (see the text for more details).

To further analyze electrical conduction in pure $C_{60}(ONa)_{24}$ in terms of the VRH model, Figure 4.8(*a*) shows the logarithmic plot of $\sigma_{dc}$ vs $100/T^{0.5}$ from 313 K to 473 K, and the inset to this panel depicts the apparent activation energy calculated by means of Eq. (4.1), this time plotted as a function of temperature. Applying the definition of activation energy for $\sigma_{dc}$ (Eq. (4.1)) to Eq. (4.2), one finds that in the VRH model $E_a$ is supposed to vary as a function of temperature, and in particular that the slope of the logarithmic plot of $E_a$ *vs* $T$ plot should be equal to $1 - n$.[35] The slope of 0.46±0.04 obtained from the linear fit of the data of the inset to Figure 4.8(*a*) gives a value of $n$ of 0.54±0.04, which is consistent with the value of $n$ obtained by direct fit of the experimental data points of Figure 4.7(*a*). Such value is compatible with and very close to the theoretical value of 1/2 of the VRH model, observed in many systems characterized by hopping electronic conduction, ranging from metal-cluster compounds to granular and ceramic metals or to doped or amorphous organic and inorganic semiconductors.[36,37,38,39] The value $n$ = 1/2 is determined by electron-electron correlation leading to a weak Coulomb gap near the Fermi level and to a square dependence of the localized state density on energy.[40,41]

It is important to note that, compared to the nearest-neighbor hopping model which predicts a simple Arrhenius behavior (see Chapter 3 section 3.3.3), the VRH model can more satisfactorily describe the experimental results for $\sigma_{dc}$ in the whole probed range of temperatures. Figure 4.8(*b*) shows the typical hopping distance $R$ in the whole temperature range. The typical hopping distance is given by[35]

(4.3) $$R = \xi\,(T_0/192T)^{0.25}$$

Here $\xi$ is the decay length of the localized electronic wavefunction, which is assumed to be equal to 1 nm, *i.e.* equal to the van der Waals radius of the $C_{60}$ molecule., while $T_0 = 8.72 \pm 1.26 \cdot 10^5$ K is the parameter entering in Eq. 4.2(*a*), which was determined from the fit of the $\sigma_{dc}$ values. The value of $R$ varies from 1.96 to 1.75 nm as the temperature increases from 313 K to 473 K. The apparent activation energy shown in the same plot was calculated both using Eq. (4.1) and according to the formula:

(4.4) $$E_a = 0.5 k_B T_0^{0.5} T^{0.5}$$

which is valid for the case of VRH with $n = 0.5$. As visible from Figure 4.8(*b*), Eq. (4.4) gives values more or less consistent with those obtained directly from the raw data using Eq. (4.1). These results therefore indicate that the charge conduction mechanism in pure material is due to variable-range hopping of localized electronic states. We suggest that the charge carriers are electrons, rather than holes, based on the known electron affinity and *n*-channel behavior of pure $C_{60}$ and of many of its derivatives.[5,2,3,42]

Figure 4.9(*a*) shows the Arrhenius plot of the relaxation frequency $f_{max}$ of the loss peak of the pure material. Just as the dc conductivity, also the relaxation frequency does not obey a simply-activated Arrhenius behavior. The apparent activation energy for $f_{max}$ is defined, in line with Eq. 4.1, as:

(4.5) $$E_a(f_{max}(T)) = -k_B \frac{d(Ln(f_{max}))}{d(1/T)}$$

As visible in panel Figure 4.9(*b*), despite its noisier profile the apparent activation energy of $f_{max}$ displays the same mild temperature dependence as $\sigma_{dc}$, increasing with increasing temperature. The Arrhenius plot of $f_{max}$ (panel *a*) could be fitted with a power law of the same form as for the dc conductivity, with a slightly higher exponent equal to 0.62 ± 0.08.

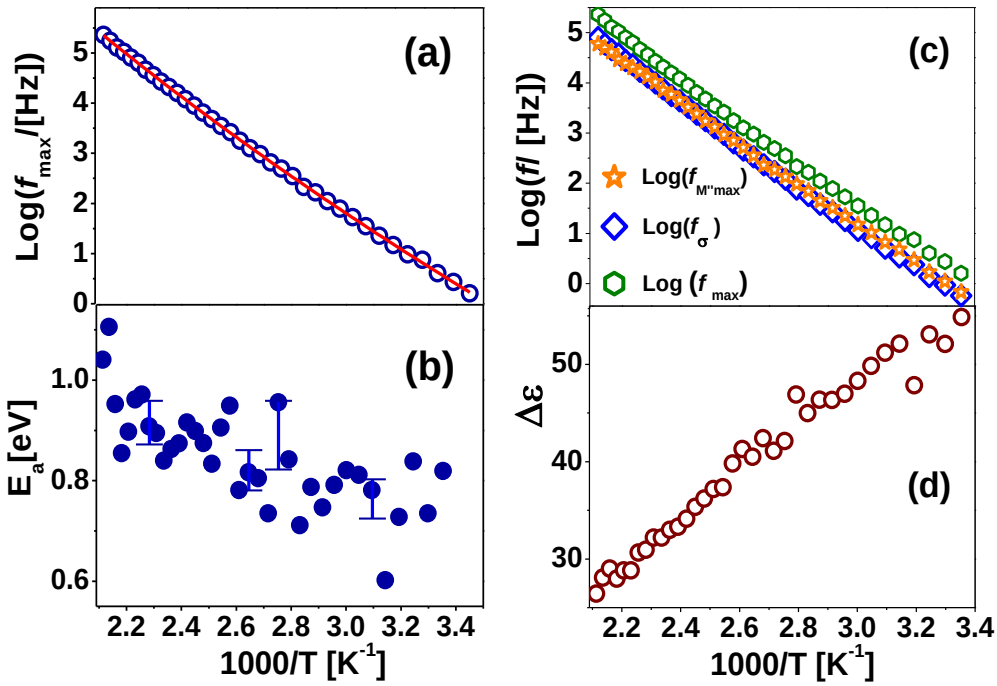


Figure 4.9: Dielectric relaxation data of pure $C_{60}(ONa)_{24}$. (*a*) Arrhenius plot of the frequency $f_{max}$ of the loss maximum and corresponding power-law fit (line). (*b*) Apparent activation energy of $f_{max}$ as function of the inverse temperature. Bars represent typical uncertainties. (*c*) Arrhenius plot of the frequency $f_{M"max}$ of the conductivity relaxation peak of the modulus spectra and of $f_\sigma$ (see text). The Arrhenius plot of $f_{max}$ is also shown for comparison. (*d*) Arrhenius plot of the dielectric strength Δε, as extracted from the fits to the loss spectra.

A loss feature with these characteristics cannot correspond to the dipolar relaxation of polar impurities (e.g. water). In fact, the same feature was observed even after annealing at 575 K (the highest temperature reached in our experiments) in nitrogen atmosphere, where no volatile dipolar impurity such as water can be present in the sample. Moreover, the positive curvature of the Arrhenius plot of $f_{max}$ is incompatible with a dipolar relaxation peak. The strong similarity between the temperature variation of the loss frequency and the dc conductivity indicates instead that the loss feature is associated with the hopping of charge carriers. As may be gathered by visual inspection of Figure 4.9(*c*), the Arrhenius plot of the loss feature $f_{max}$ has a temperature dependence that is very similar to that of $\sigma_{dc}$. This confirms that the dielectric loss is associated with the electrical conduction (namely, with hopping processes of electronic charge carriers), as already suggested in the second part of Section 4.3. The interpretation of the loss peak as being a conductivity-induced effect is further corroborated by the scaling behavior of the spectra (see below).

As mentioned in Section 4.3, the simplest explanation of the conductivity-induced loss feature is the accumulation of (free) charges due to the spatial variation (inhomogeneity) of the conductivity, the so-called space-charge effect. The frequency of the loss feature marks the onset of the dispersive conductivity regime dominated by back-and-forth hops of charges between first-neighbor sites, whereas the dc value is determined by long-range correlated hopping processes.[43,44] Given that the grain size is quite small (roughly 30 nm, see the discussion of Figure 4.2(*b*)), it is natural to ascribe the observation of a space-charge effect to dissipative processes accompanying electron accumulation at grain boundaries.

It is convenient for our analysis of the Arrhenius behavior to introduce another characteristic frequency, the so-called space-charge relaxation frequency $f_\sigma$, which represents the characteristic relaxation frequency of spatial charge fluctuations in a conducting medium,[45,46] and which is defined as $f_\sigma = \sigma_{dc}/(2\pi\varepsilon_0\Delta\varepsilon)$. Figure 4.9(*c*) displays the Arrhenius plot of $f_{max}$, $f_\sigma$ and of the frequency $f_{M''max}$ of the modulus peak. The values of Log ($f_{M''max}$) overlap almost perfectly with those of Log ($f_\sigma$). Since usually the dielectric strength $\Delta\varepsilon$ is at most a slowly varying function of

temperature, Log ($f_\sigma$) is basically proportional to Log($\sigma_{dc}$). On the other hand, the frequency of the conductivity peak in the modulus spectra basically represents the frequency $f^*$ which marks the onset of the dispersive part of the conductivity,[47] defined as the frequency at which $\sigma'(f^*) = 2\sigma_{dc}$.[48] The fact that Log ($f_{M''max}$) and Log ($f_\sigma$) coincide therefore implies that the activated behavior of $\sigma_{dc}$, a quantity that is related to the long-range charge transport, is identical to that of the onset frequency $f^*$ above which the conductivity is dominated by hopping processes between nearest-neighbor molecules. This entails that the mechanism behind the long-range charge transport is the same as for the dispersive regime, namely hopping processes between neighboring molecules, as may be expected.

Panel *d* of Figure 4.9 shows the temperature dependence of the strength $\Delta\varepsilon$ of the dielectric loss as obtained from fits to the $\varepsilon''$ spectra. The slow decrease of $\Delta\varepsilon$ may be expected in the case of a conductivity-related dielectric loss in a molecular material, since the thermal motions limit the extent and dynamics of the polarization clouds surrounding the charge carriers. It should be pointed out however that several distinct microscopic models predict an inverse proportionality between $\Delta\varepsilon$ and T (see e.g. Ref. 49).

Figure 4.10 shows the results of the scaling analysis of the dielectric spectra acquired upon cooling from 473 to 313 K. As visible in panel *a*, the ac conductivity ($\sigma'$) spectra display the same line shape at all temperatures and may be superposed to the same master curve. The spectra are found to obey a time-temperature superposition principle following in particular the prescription of the so-called Summerfield scaling relationship $\sigma'(f)/\sigma_{dc} = G(f/\sigma_{dc}T)$ (see *e.g.* Ref 50). In this expression, G is the shape function (master curve) of the normalized conductivity spectra, common to all temperatures, and *f* is the frequency in Hertz.

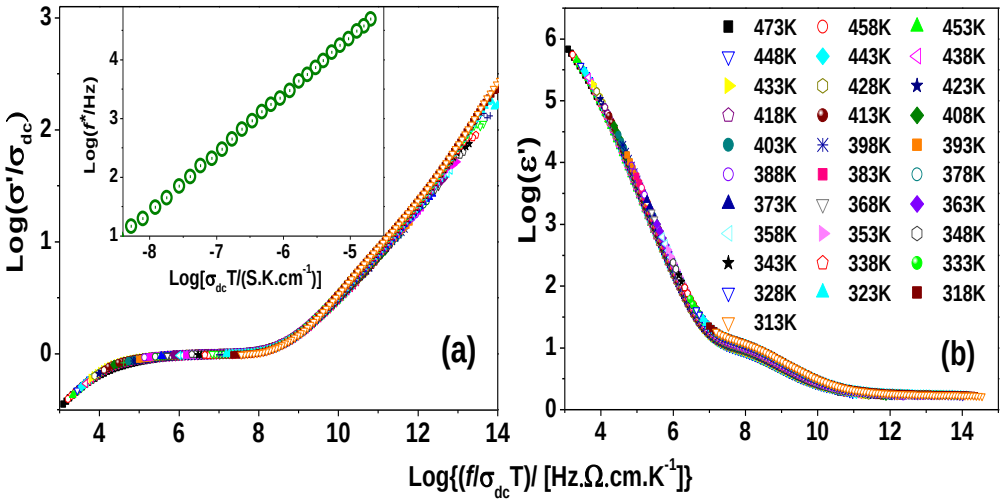


Figure 4.10: Summerfield scaling analysis of the normalized ac conductivity $\sigma'/\sigma_{dc}$ (*a*) and of the permittivity ε' (*b*) between 473 and 313 K. Inset to panel *a*: logarithmic plot of the onset frequency *f** (defined in the text) versus $\sigma_{dc}T$.

As shown in the inset to Figure 4.10(*a*), the onset frequency *f** of the dispersive part of the conductivity spectra, defined as the frequency *f** at which $\sigma'(f^*) = 2\sigma_{dc}$,[48] is directly proportional to the product $\sigma_{dc}T$. This is further proof that the same mechanism involved in the long range charge transport (dc conductivity) is responsible for the transition to the dispersive part of σ'. The conductivity is the product of the charge carrier density N, the mobility μ, and the charge *e* of the carriers. The mobility has activated behavior scaling with the same activation energy as *f**, while the charge carrier is constant or only weakly dependent on temperature.[45,51]The real part of the permittivity (Figure 4.10(*b*)) also obeys the Summerfield scaling. The height of the step-like bump in the ε' spectrum, which as mentioned is equal to the strength Δε of the loss feature in ε", is observed to decrease slowly with increasing temperature, in agreement with Figure 4.9(*d*).

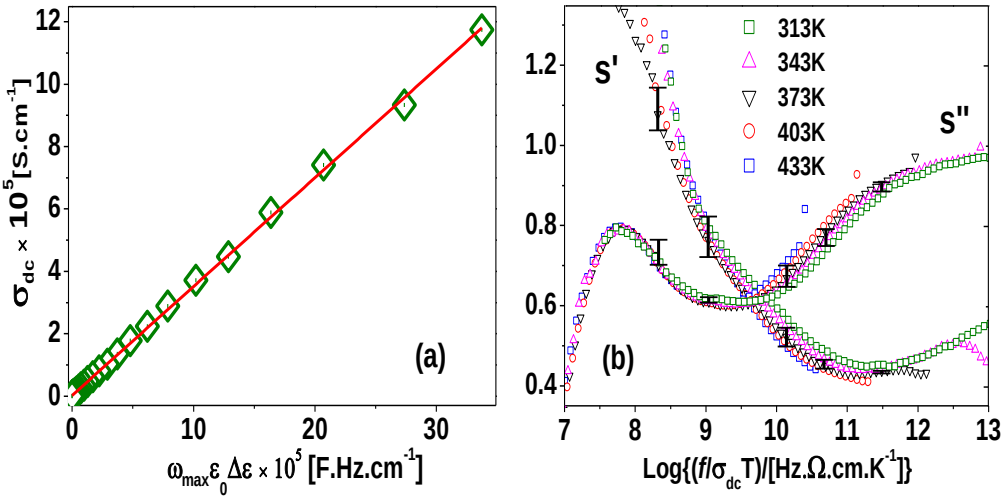


Figure 4.11: (*a*) Plot of $\sigma_{dc}$ versus $2\pi\varepsilon_0\Delta\varepsilon\, f_{max}$ to verify the validity of the Barton-Nakajima-Namikawa relationship (see text). (*b*) Summerfield scaling analysis of the exponents *s*' and *s*" characterizing the complex ac conductivity (see text). Error bars are relative to the data acquired at 373 K but represent the typical uncertainty of all spectra.

Figure 4.11(*a*) displays the linear relationship between the dc value of the conductivity and the quantity $2\pi\varepsilon_0\Delta\varepsilon\, f_{max}$. The slope of the linear fit is of the order of unity (the actual value is 0.35), which shows that $\sigma_{dc} \sim 2\pi\varepsilon_0\Delta\varepsilon\, f_{max}$, or $f_{max} \sim f_{\sigma}$. This relationship, known as Barton-Nakajima-Namikawa (BNN) condition,[52] is further confirmation that the frequency position $f_{max}$ of the loss peak is determined by the dc conductivity. The validity of the time-temperature superposition principle and the fulfillment of the BNN relationship together entail.[34] that the mechanism driving conduction is basically the same at all temperatures and that the high-temperature relaxation feature is associated with the motion of the charge carriers that contribute the dc conductivity, a situation encountered in many inhomogeneous or disordered materials and even in organic and inorganic ionic conductors.[34, 53]

If the sample exhibited two equally important contributions to the conductivity coming respectively from the electronic and ionic mobility, one would expect that the temperature-dependence of both would differ; hence the observation of Summerfield scaling implies that the electronic contribution is the dominant mechanism, and that ionic contribution, if present, plays only a minor role, despite

the high density of sodium moieties in the material. An electrode polarization effect is observed only at the highest temperatures probed (see Figure 4.6), confirming that the ionic displacements are negligible at low temperature. These observations imply that the $Na^+$ ions are relatively tightly bound to the oxygen atoms of the fullerene cages.

The real and imaginary parts of the complex conductivity in the dispersive regime, that is, above the onset frequency $f^*$, are usually analyzed in terms of a power-law-like dependence of the type $\sigma' \sim f^{s'}$ and $\sigma'' \sim f^{s''}$.[34] Figure 4.11(*b*) shows the frequency-dependent exponents *s*' and *s*" characterizing the conductivity spectra of the material at the indicated temperatures. As may be expected from the scaling analysis carried out so far, the Summerfield scaling is found to apply also to both exponents, except for *s*' at low frequency. The discrepancy is due to the different extent of the electrode polarization at different temperatures. Such polarization effects also lead to the observed decrease of the *s*" exponent as the frequency is lowered (left-hand portion of panel *b* of Figure 4.11). At intermediate frequencies, the *s*' exponent displays a small bump indicative of the presence of the dielectric loss, which as discussed is centered near $f^*$, in correspondence with which *s*" exhibits a broad local minimum. The values of both exponents coincide near $f^*$, where $s' \approx s'' \approx 0.6$. At higher frequencies (right-hand portion of Figure 4.11(*b*)) the frequency-dependence of both exponents matches the behavior observed in other systems,[9] with *s*" becoming larger than *s*' above $f^*$.

It is interesting to compare the origin and character of induced polarization in the oxofullerene sodium derivative with those of Buckminster fullerene. Compared to the pristine $C_{60}$ molecule, the formation of covalent C–O bonds in $C_{60}(ONa)_{24}$ reduces the aromaticity and conjugation of the carbon-carbon bonds of the fullerene cages. Since the locations of the remaining fewer double bonds in $C_{60}(ONa)_{24}$ are fixed with respect to the positions of the oxygen moieties, a much lower molecular orbital polarizability results, compared with that of the molecular orbitals of $C_{60}$ and its anions. In other words, contrary to solid $C_{60}$ and to solid phases containing $(C_{60})^{n-}$ anions, in which the molecular polarizability is due to the $\pi$ electrons in the

molecular orbitals of the carbon cage,[7,54,55,56] the molecular polarizability of $C_{60}(ONa)_{24}$ is likely to be due mainly to the distortion of the polar C–O···Na bonds.

### 4.4.2 Effect of the Surface Hydration Water on Pure $C_{60}(ONa)_{24}$

As mentioned at the beginning of subsection 4.4.1, to measure the pure material we preheated the hydrate powder to dehydrate it, getting rid of the structural water. However, between this preheating and the measurements, i.e., during preparation of the pellet, the sample was exposed to ambient air. Due to the hygroscopic nature of $C_{60}(ONa)_{24}$, this resulted in formation of a surface hydration-water layer on the powder grains, as we describe in this subsection.

The spectra acquired on one such quasi-pure pellet obtained by exposure of the pure material to air are displayed in panels *a* and *b* of Figure 4.12. As visible from comparison of Figure 4.12 with Figure 4.5, it is seen that the only partially hydrated powder does not exhibit the phase change observed in the hydrate upon heating, but rather a single, non-reversible spectral modification as the temperature increases from room temperature to 360 K. The dc conductivity of the partially hydrated powder (Figure 4.12(*c*)) was initially much higher than that of the fully dehydrated material, and only dropped to a value comparable with the latter upon heating to 325 K. Above this temperature, the temperature-dependence of the conductivity was the same as in pristine (water-less) $C_{60}(ONa)_{24}$, and the spectra obtained in subsequent heating-cooling cycles under constant nitrogen flow overlapped with the first cool-down data, confirming that all surface water leaves the sample in the first heating to 325 K. A single, broad permittivity feature is observed in all dielectric spectra of Figure 4.12(*a*). The Arrhenius plot of the characteristic frequency $f_{max}$ (respectively, dielectric strength $\Delta\varepsilon$) of such feature is shown in the main panel of Figure 4.12(*d*) (respectively, in the inset). In the same temperature range of the conductivity change, the loss feature undergoes a non-monotonous frequency shift and a significant decrease in strength (by a factor of three).

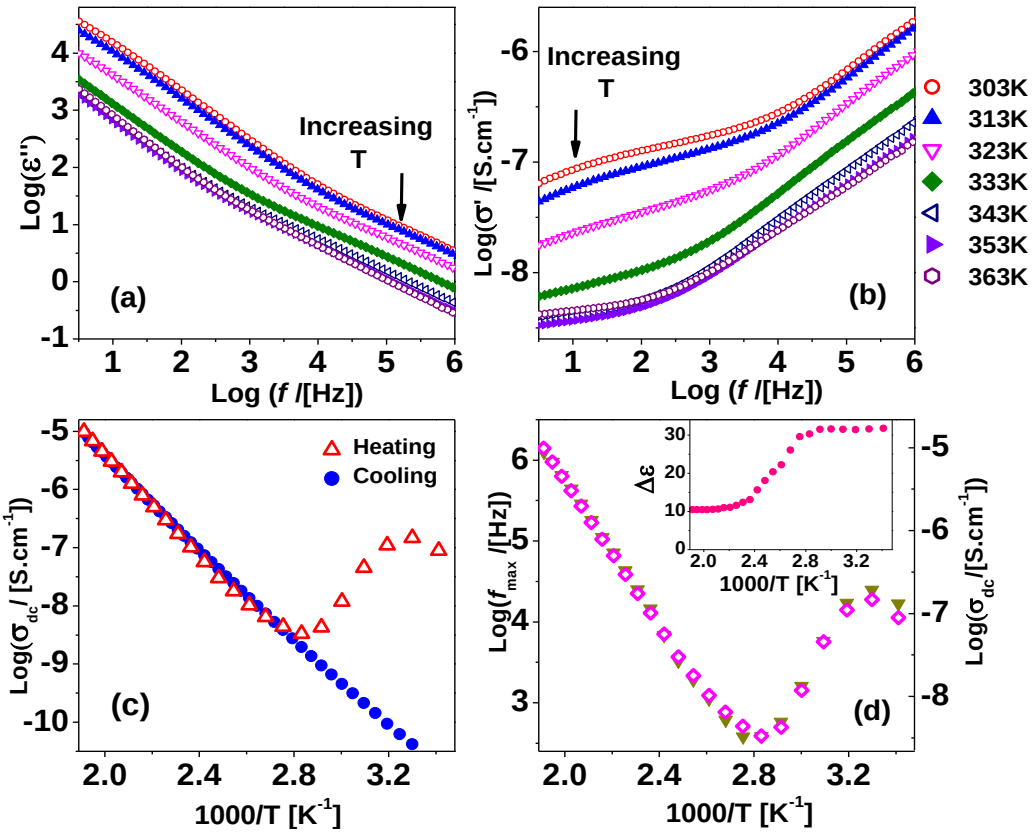


Figure 4.12: Dielectric loss (*a*) and ac conductivity (*b*) spectra acquired on a pellet made with powder preheated to 430 K and then exposed to ambient air, in the temperature range between 293 and 373 K. The arrows highlight the spectral variation with increasing temperature. (*c*) Arrhenius plot of $\sigma_{dc}$ for the same data. For comparison, the $\sigma_{dc}$ values extracted from measurements performed cooling down from 500 K is also shown (same data as Figure 4.6(*b*)). (*d*) Arrhenius plot of the relaxation frequency, compared with that of $\sigma_{dc}$. Inset: dielectric strength $\Delta\varepsilon$ as a function of the reciprocal temperature.

The observed decrease of $\sigma_{dc}$ upon desorption of water is reminiscent of the behavior of many insulating and semiconducting porous inorganic materials[11-13] in which a conductivity enhancement is observed after exposure to humidity. It may be gathered from Figure 4.12(*c*) that the conductivity variation is approximately of four orders of magnitude, a dramatic effect which is in line with reported conductivity enhancements in inorganic systems.[11-13] The recovery of the conductivity value of

the pristine material at relatively low temperatures and the absence of the other changes visible in the hydrate (Figure 4.5) together indicate that, in the short exposure to air prior to measurement, the material did not have time to form a stable hydrate phase containing structural water. We thus conclude that air exposure led to condensation of (loosely bound) hydration water onto the surface of pure $C_{60}(ONa)_{24}$ grains. In what follows, we will refer to this water contribution as "surface hydration water" to distinguish it from the structural water. Such surface hydration water is responsible for the observed conductivity enhancement. As we discussed in the section 4.4.1, pure $C_{60}(ONa)_{24}$ is a polycrystalline powder with rather low conductivity ($10^{-11}$ S/cm at room temperature) and relatively large surface area, considering the size of the crystalline grains (~30 nm). The large surface area rationalizes the observed dramatic (surface) conductivity increase upon air exposure. The conductivity enhancement is responsible also for the more prominent electrode polarization effect visible in the room-temperature spectra (Figure 4.12(*b*)).

Water-induced conductivity enhancements are known to occur in inorganic metals and oxides, and it is generally accepted that they arise from small-ion transport through chemisorbed and physisorbed water layers.[11,14,33] In fact, the conductivity enhancement in these materials is purely a surface effect, as water cannot penetrate inside their tight lattice structure of inorganic materials. The exact nature of the underlying conduction mechanism is debated,[30] but the most likely candidates are ion diffusion and proton exchange, the latter being a "shuttle" mechanism by which O–H bonds are interchanged between adjacent water molecules. The proton exchange mechanism is responsible for the electrical conductivity of a wide range of systems such as pure water, ice, phosphoric acid, pharmaceutical phosphate salts, as well as some hydrated organic compounds.[57,58,59,60,61] This mechanism, known in water as "Grotthuss shuttling," is sometimes accompanied by rearrangements of the molecular orientations and of the solvation shells.[57] Contrary to what has been proposed for some inorganic materials, where the protons responsible for the surface conductivity enhancement have been suggested to stem from the chemisorption of water onto activation sites,[59] the surface effect reported here is unlikely to arise from a chemisorption process, as the extra surface-conductivity contribution vanishes

upon heating to moderate temperatures (lower than 350 K), indicating that the surface water molecules maintain their integrity (the desorption of chemisorbed water from e.g. metal oxide surfaces takes instead place at 473 K).[62] Similarly, we can exclude that the surface conductivity is due to the motion of the sodium species, as it has been shown in the section 4.4.1 that the sodium atoms remain tightly bound to the fullerene molecules up to at least 575 K. A more likely explanation is that the surface-enhanced conductivity is due to charge propagation by hydrogen-bond exchange (proton-shuttling) between intact, physisorbed water molecules in higher hydration layers.

As visible in Figure 4.12(*a*), a loss feature is initially visible at room temperature above $10^5$ Hz, that is, at a significantly higher frequency than the relaxation feature of the bulk hydrate (see Figure 4.5(*a*)). Upon raising the temperature, the loss feature is observed to shift to lower frequencies while the conductivity decreases (Figures 4.12(*a*) and 4.5(*b*)). Such temperature dependence of the loss feature is anomalous (the characteristic frequency should increase with temperature due to the higher thermal energy), and resembles that observed in other hydrated systems such as organic[30] and inorganic[31-33] porous materials. The origin of this effect has been the object of controversy, and has been related either to a reduction of the available free volume per defect in the hydrogen-bond network of interstitial water upon heating, [32,63,64] or to a Maxwell-Wagner-Sillar polarization effect due to the strong increase of the static permittivity of a porous sample when water adsorbs onto inner surfaces. The data of Figure 4.12 reveal that a different mechanism is responsible for the anomalous shift of the loss feature in $C_{60}(ONa)_{24}$. In fact, as seen in Figure 4.12(*d*), the variation with temperature of the loss frequency is identical to that of the conductivity (both vertical scales in Figure 4.12(*d*) span the same number of decades). This situation, analogous to the pure $C_{60}(ONa)_{24}$, indicates that the origin of the loss feature is the accumulation of charge carriers at the sample's heterogeneities such as grain boundaries. In other words, the observed relaxation feature is a space-charge loss. While in the fully dehydrated material the charge carriers responsible for the space-charge loss are only electrons, it may be that also protons take part in the space-charge relaxation of the surface-hydrated material.

Our results demonstrate that the strong decrease in the sample's conductivity upon desorption of hydration water can lead to a non-monotonic temperature dependence of the loss feature, although by itself it is not sufficient to explain the simultaneous observation of anomalous temperature dependencies of distinct loss features reported in some samples.[29]

Below 348 K the loss spectrum does not exhibit any change in line shape but rather undergoes a rigid shift to lower frequency as the temperature is raised with no loss of spectral intensity. The line shape variation and the decrease in strength of the loss feature (by a factor of three) occur only above 348 K (inset to Figure 4.12(*d*)). Notice that the dielectric strength does not go to zero, but to a constant value corresponding to that of the pure material. Because in the case of the preheated powder no structural changes occur during the measurements, the observed three-fold enhancement of the dielectric strength is due solely to the presence of physisorbed water. The fact that a decrease in dielectric strength in the loss feature occurs only after the conductivity has dropped to its value in the pure material is worth noticing. Water adsorbed onto hygroscopic or hydrophilic surfaces is organized in different hydration layers, the first (interfacial) hydration layer being the most strongly bound and the last to desorb upon heating. The dielectric strength is observed to decrease only at the highest temperatures (i.e., at the very last stages) of the desorption, indicating that the intensity of the loss feature is determined by the first (interfacial) hydration layer. This may be expected for a loss originating from charge-carrier accumulation at crystalline grain boundaries, as the presence of interfacial water molecules with their large orientational polarizability is likely to affect the overall dipolar character of such charge accumulations. At the same time, the fact that the $\sigma_{dc}$ value starts dropping already at the initial stages of $H_2O$ desorption indicates that the conductivity enhancement is due to conduction through higher hydration layers, in agreement with previous studies.[14,15,33]

To summarize, while pure $C_{60}(ONa)_{24}$ exhibits low conductivity due to hopping of electronic charge carriers between crystalline grains, physisorption of water on the surface of $C_{60}(ONa)_{24}$ grains leads to a four-decade enhancement of the overall conductivity due to the introduction of new charge carriers and new conduction

paths through the hydration layers. It is the water in higher hydration layers that is responsible for the conductivity enhancement and for the frequency shift of the (conductivity-induced) space-charge dielectric loss feature. The shape and intensity of such loss feature are determined by the interfacial water molecules that are directly adsorbed onto the organic matrix (first hydration layer). Indeed, the dielectric strength of the permittivity feature does not vary with the conductivity (which is strongly temperature-dependent), but rather only depends on whether water is present (or absent) at the very surface of the crystalline grains. This may be rationalized, since the loss feature is related to accumulation of free charge at spatial heterogeneities such as grain surfaces and boundaries, and the presence of interfacial water molecules with their large dipole moment and orientational and hydrogen-bond polarizability is likely to affect the overall dipolar character of such charge accumulations. The higher dielectric strength (by a factor of three) of the loss feature in the presence of an interfacial hydration layer might reflect a partial contribution to the loss feature from protons or from interfacial water dipoles.

### 4.4.3 $C_{60}(ONa)_{24} \cdot 16H_2O$ Hydrate

Given that pellets made from the as-stored powder (Section 4.3) contain both structural and surface hydration water, and since the latter affects not only the shape of the loss spectrum but also the magnitude of the dc conductivity (Subsection 4.4.2), in order to obtain a more reliable characterization of the bulk hydrate we preheated the pellets to 323 K in nitrogen atmosphere, so as to minimize the amount of surface hydration water.

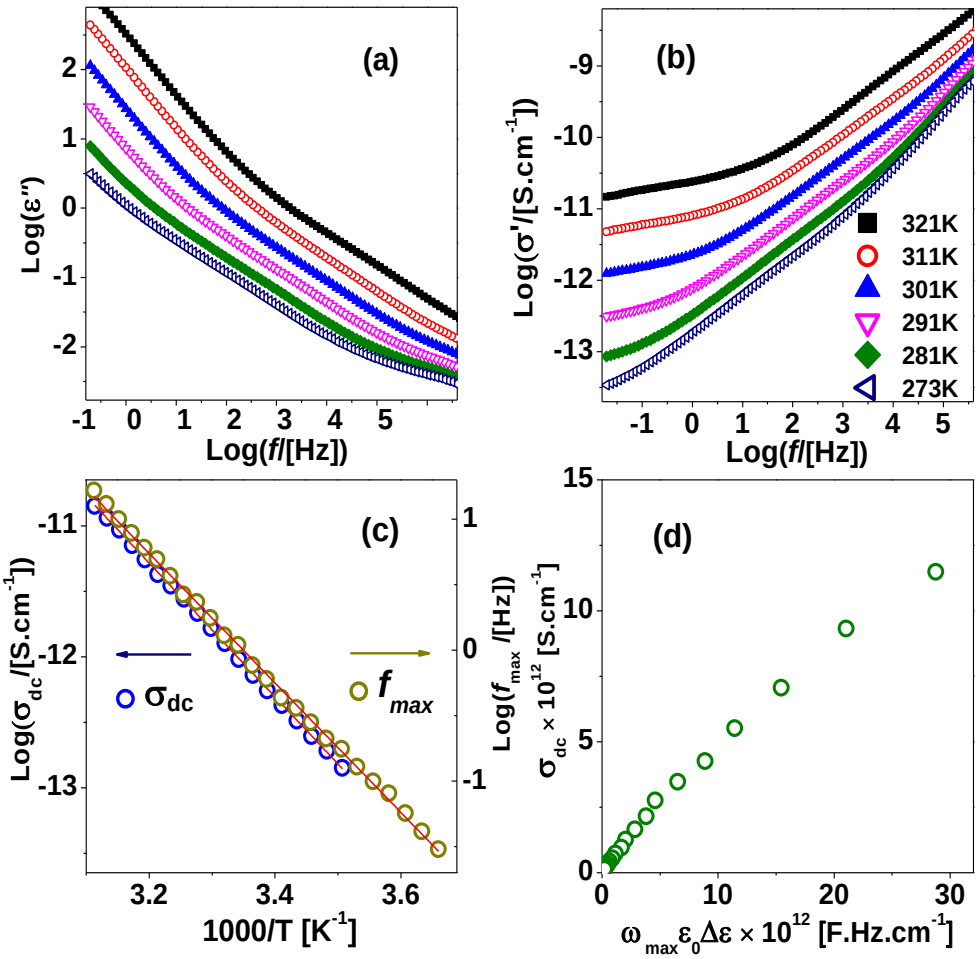


Figure 4.13: Dielectric loss (*a*) and ac conductivity (*b*) spectra acquired on the hydrate preheated to 323 K. (*c*) Arrhenius plots of $\sigma_{dc}$ between 285 and 320 K (filled markers) and $f_{max}$ between 273 and 320 K (open markers) and respective linear fits (continuous lines). The two temperature ranges are different as no reliable estimate of $\sigma_{dc}$ could be obtained from the dielectric data down to $10^{-2}$ Hz. (*d*) Plot of $\sigma_{dc}$ versus $2\pi\varepsilon_0\Delta\varepsilon\ f_{max}$ between 285 and 320 K to test the validity of the BNN relation (see text).

The results of the characterization of the $C_{60}(ONa)_{24}\cdot 16H_2O$ hydrate preheated to 323 K are displayed in Figures 4.13 and 4.14. The low-temperature data, prior to the loss of structural water, are shown in Figure 4.13. As visible in Figure 4.13(*c*), in the hydrate without surface water, the dc conductivity between 285 and 320 K follows a simply-activated (Arrhenius) temperature dependence. This contrasts with the case

of the pure compound, which displays instead a dependence of the dc conductivity on temperature of the form $\mathrm{Log}(\sigma_{dc}) \sim -1/T^{n}$ (Eq. 4.2) with *n* close to ½, typical of variable-range electronic hopping (section 4.4.1). The simply activated behavior observed in the hydrate suggests instead that conduction is not purely electronic, as might be expected due to the massive presence of structural water, which may result in partially protonic or ionic conductivity mechanism (see also below). The activation energy of the dc conductivity of the bulk hydrate is slightly above 1 eV, and it is higher than the effective activation energy observed in the pure material, which in this temperature range varies between 0.7 and 0.8 eV. This may be rationalized considering that the electronic contribution to the conductivity is hindered in the hydrate by the larger intermolecular spacing (Section 4.3) and by the presence of the water molecules. As visible in Figure 4.13(*a*), the loss spectra contain at least one main relaxation feature. The Arrhenius plot of the frequency $f_{max}$ of this main relaxation feature (Figure 4.13(*c*)) exhibits a simply activated behavior with an activation energy that is very similar to that of the dc conductivity, which would suggest a correlation between this main dielectric feature and the long-range charge transport. In Figure 4.13(*d*) we have plotted $\sigma_{dc}$ versus the quantity $2\pi\varepsilon_0\Delta\varepsilon f_{max}$ to test the validity of the BNN [38] condition. Although the ratio of these two quantities is expected to be the of the order of unity (in fact, between 0.4 and 0.5), they do not display the perfect linear correlation predicted by the BNN theory (according to which $\sigma_{dc} \sim 2\pi\varepsilon_0\Delta\varepsilon f_{max}$). This implies that the loss feature is not a pure space-charge effect, contrary to the case of the pure material.

Figure 4.14 displays the dielectric spectra acquired on the preheated hydrate, this time in the temperature range corresponding to the loss of structural water. The data are plotted in separated temperature intervals, similarly to what has been done in Figure 4.5. The sample's dc conductivity and loss feature display initially weak temperature dependence up to 323 K (Figure 4.14(*a*)). Starting from this temperature, the variation with temperature is more pronounced, as may be gathered at a glance by the larger spacing between consecutive spectra in Figure 4.14(*b*). This behavior continues up to 363 K, close to the boiling point of water under standard conditions. Between 368 and 383 K, in the temperature interval of the main loss of

mass (Figure 4.14(*c*)), the conductivity is observed to decrease while the dielectric loss feature undergoes a shift to lower frequency (arrows in Figure 4.14(*c*)). Above 388 K, after all structural water has left the sample; the spectra resume their initial weak temperature dependence (Figure 4.14(*d*)). Neither the pronounced slowing-down observed around 333 K in Figure 4.5(*a*) nor the anomalous behavior below 350 K reported in Figure 4.12 are observed in Figure 4.14, which indicates that the anomalous relaxation behavior below 350 K in the as-stored hydrate is due exclusively to the surface hydration water.

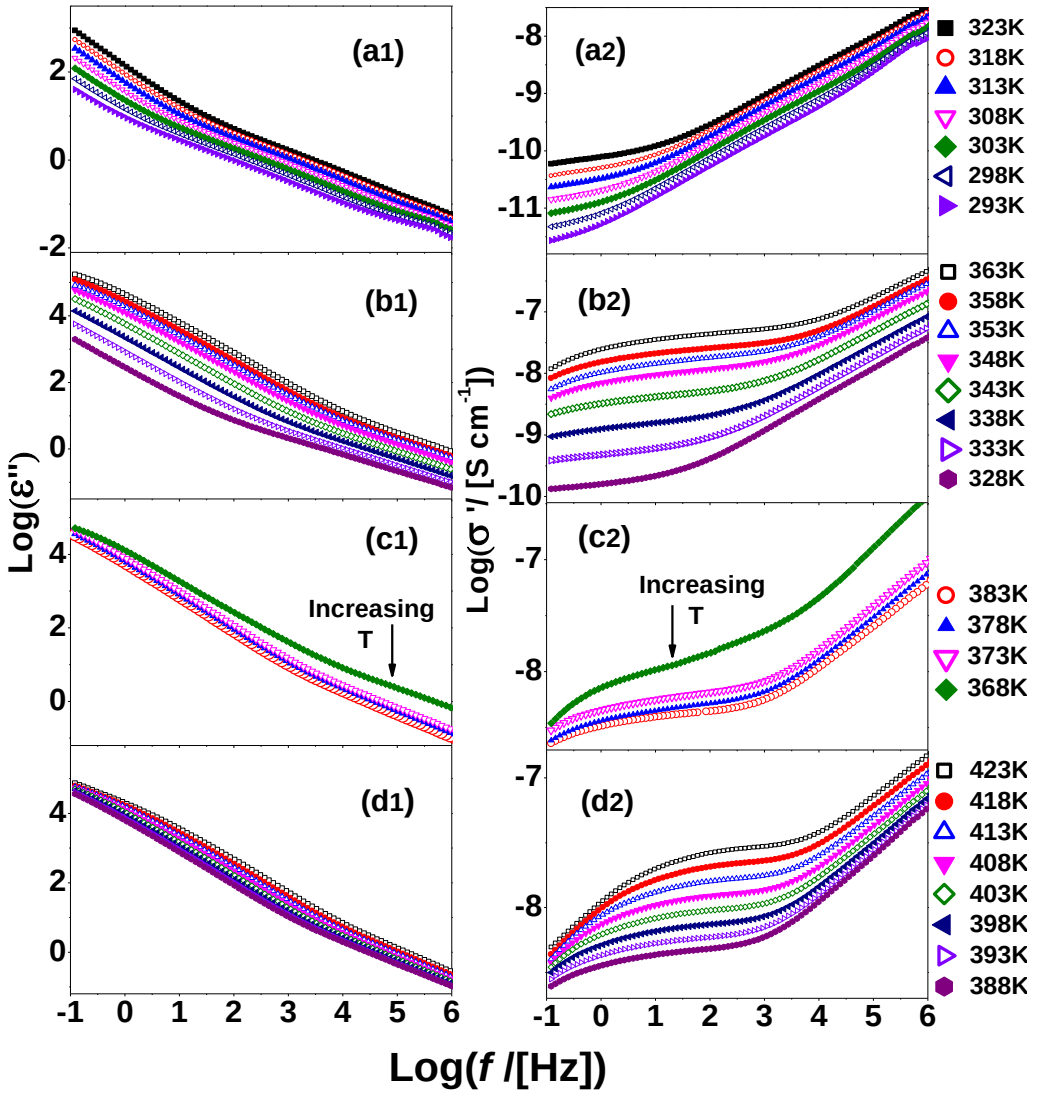


Figure 4.14: Dielectric loss (left panels, 1) and ac conductivity (right panels, 2) spectra acquired on heating the $C_{60}(ONa)_{24} \cdot 16H_2O$ hydrate preheated under nitrogen atmosphere to 323 K, in different temperature intervals: (*a*) 293 to 323 K; (*b*) 328 to 363 K; (*c*) 368 to 383 K; (*d*) 388 to 423 K.

It may be gathered from Figure 4.14(*a*) that, prior to the loss of structural water, the permittivity spectra are actually characterized by two loss features, one in the same frequency range of the conduction-related feature of the pure material, and a second one at higher frequency, visible only below room temperature in our

experimental frequency range. Both relaxation features exhibit simply activated behavior. While the lower-frequency feature appears to be associated with charge accumulation at grain boundaries, as mentioned above, the low-temperature feature visible at high frequency, which displays activation energy of 0.9 eV (not shown), might have a dipolar origin. As this faster feature is observed only in the hydrate and has no analog in the pure material, we associate it with the dipolar relaxation of structural $H_2O$ molecules, which, given the crystalline nature of the hydrate, may only exhibit reorientational motions (e.g., as in a plastic crystal). The activation energy of such fast relaxation is significantly higher (by almost a factor of two) than that observed in supercooled or confined water,[61-64] which may result from the much stronger interactions and orientational correlations (steric hindrance) between the structural $H_2O$ molecules in the crystal lattice of the hydrate.

Figure 4.15 shows the Arrhenius plots of the main (slower) relaxation (panel *a*) and of the conductivity (panel *b*) in the whole temperature range of the spectra of Figure 4.14. For comparison purposes, in Figure 4.15(*b*) we also show $\sigma_{dc}$ for the pure material (same data as those of Figure 4.7(*a*)). In Figure 4.15(*a*), together with the maximum loss frequency $f_{max}$ we show also the space-charge relaxation frequency defined as $f_\sigma = \sigma_{dc}/(2\pi\varepsilon_0\Delta\varepsilon)$ (see Section 4.4.1), where $\Delta\varepsilon$ is the dielectric strength of the slower relaxation in the hydrate. The correspondence between the line shapes of all three Arrhenius plots ($\sigma_{dc}$, $f_{max}$ and $f_\sigma$) upon heating is remarkable. Both $f_{max}$ and $\sigma_{dc}$ display a crossover to steeper temperature dependence above 323 K. This more pronounced variation with temperature slows down at 350 K, until its trend is reversed at around 370 K (the temperature of the structural transition), with both $\sigma_{dc}$ and $f_{max}$ decreasing with increasing temperature. The non-monotonic behavior of the dc conductivity is simultaneous with that of the loss feature, and both exhibit a maximum at 365 K. The Arrhenius plot of $f_\sigma$ displays a similar behavior. All these similarities and the continuous evolution of the main loss feature of the hydrate into that of the pure material (which arise from a space-charge accumulation effect as shown in Subsection 4.4.1) are all strong indications that the main loss feature in the bulk hydrate has a space-charge origin.

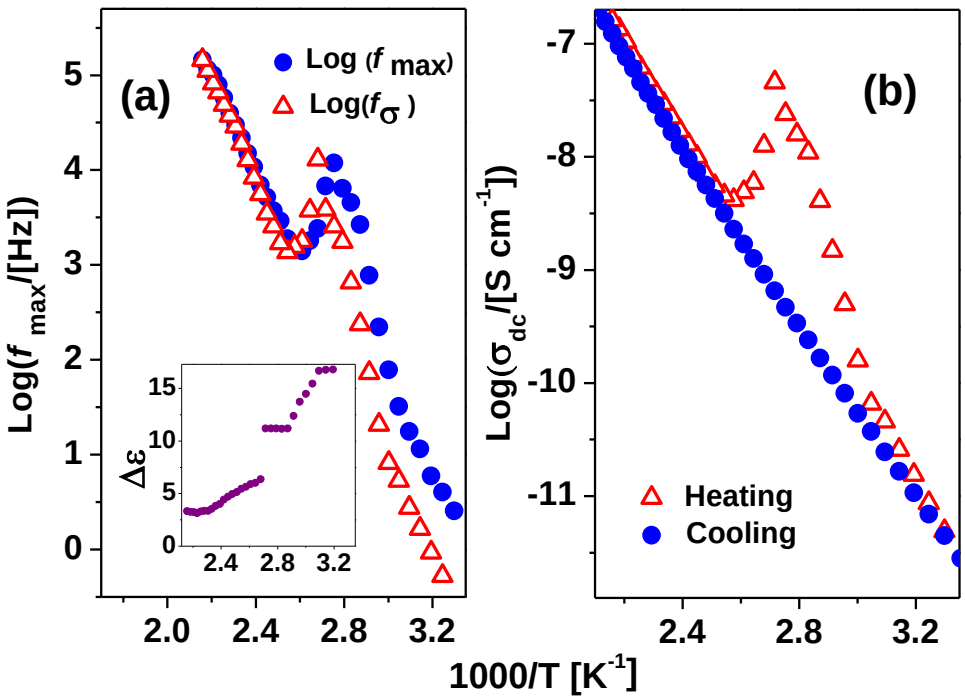


Figure 4.15: Change in the dielectric properties of the $C_{60}(ONa)_{24}\cdot 16H_2O$ hydrate preheated to 323 K upon the structural dehydration: (*a*) frequency $f_{max}$ of the main loss feature, and corresponding space-charge relaxation frequency $f_\sigma$ ; (*b*) Dc conductivity upon heating (red markers) and cooling (blue markers). Inset to panel a: dielectric strength Δε of the data acquired upon heating, as a function of reciprocal temperature. The data upon heating correspond to the spectra of Figure 4.14.

As visible in the inset to Figure 4.15(*a*), the dielectric strength of the loss feature decreases with increasing temperature, in line with the results presented in Figure 4.5 in Section 4.3. As it can be inferred from a visual comparison between the permittivity spectra of panels *a1* and *d1* of Figure 4.5 or 4.14, and as clearly visible in the insets to Figure 4.12(*d*) and Figure 4.15(*a*), the strength Δε of the loss feature is always higher in the (even partially) hydrated samples than in the pure material. In particular, upon heating the structural hydrate the dielectric strength shows two abrupt changes to lower values, the first around 323 K, in coincidence with the crossover to steeper Arrhenius dependence, and the second one at 370 K, in correspondence with the structural transition. There is an overall decrease of

strength by a factor of 7 between the hydrate and pure material. The higher value of $\Delta\varepsilon$ in the presence of water and the fact that at low temperature the Arrhenius plots for $f_{max}$ and of $f_\sigma$ do not overlap (Figure 4.15(*a*)), as well as the only approximate validity of the BNN condition and the slight difference between the activation energies of the dc conductivity and of the permittivity feature (Figure 4.13), are all clear indications that, while the loss feature and the conductivity are correlated, the origin of the loss cannot be a pure space-charge effect as in the pure material. In particular, it appears evident that the structural/interfacial water molecules contribute directly to the strength of the permittivity feature. To rationalize our findings, we suggest that the fundamental origin of the main loss feature in the hydrate is accumulation of charge at the sample's inhomogeneities, as in the pure material; however, such dielectric feature also contains in the surface-hydrated material and in the structural hydrate a partial dipolar contribution associated with the reorientational motions of the structural $H_2O$ dipoles which accompany the oscillation of the interfacial dipole associated with the accumulation of charge carriers. Notice in fact that the strength of the space-charge feature is always higher in the presence of water (both in the case of structural water and surface hydration water).

We finally analyze the effect of the structural dehydration on the dc conduction properties. The observation of a local maximum of conductivity close to the maximum water loss (Figure 4.15(*b*)) and the fact that the inter-fullerene spacing is higher in the hydrate than in the pure material, suggest that the hydrate's $\sigma_{dc}$ is dominated in this temperature range by a non-electronic charge transport mechanism associated with water. The charge carriers associated with the hydrogen-bonded network of structural water molecules are probably protons moving by hydrogen-bond shuttling, which as mentioned in Subsection 4.4.2, is the main conductivity mechanism in several hydrogen-bonded and hydrated systems.[57-64] Indeed, the abrupt changes in the value of the dielectric strength and activation energies are observed around 323 K, where the temperature dependence becomes steeper; this temperature is well below the onset of the loss of structural water, which takes place at 350 K (Figure 4.2(*a*)): hence, the conductivity enhancement cannot be ascribed to

the formation of internal voids in the hydrate, which makes it unlikely that it can be explained by means of a vehicle mechanism (i.e., diffusion of $H_3O^+$ or $OH^-$ ions).

The observation of a conductivity maximum entails that the density of charge carriers is not constant. In fact, in a series of spectra taken at the fixed temperature of 350 K under constant $N_2$ gas flow (in a different experimental run than that of Figure 4.16) the dc conductivity was observed to decrease with time. These data, displayed in Figure 4.16, clearly show that, in the temperature window where water starts leaving the sample, the measured $\sigma_{dc}$ value is not an equilibrium value, so that no true activation energy can be extracted from the heat-up data of Figure 4.15(*b*).

The fact that the conductivity drops in time further proves that the conductivity enhancement cannot be due to hydronium or hydroxyl ions that start diffusing through the voids left in the lattice by the departing water, for in such case one would expect the conductivity to increase (or, at least, to remain constant) as more water leaves the sample. Having thus discarded an electronic or a vehicle charge transport mechanisms in the hydrate, and given that the surface conductivity enhancement is due to proton shuttling (section 4.4.2), we propose that the proton-exchange scenario applies also to the $\sigma_{dc}$ enhancement preceding the dehydration process.

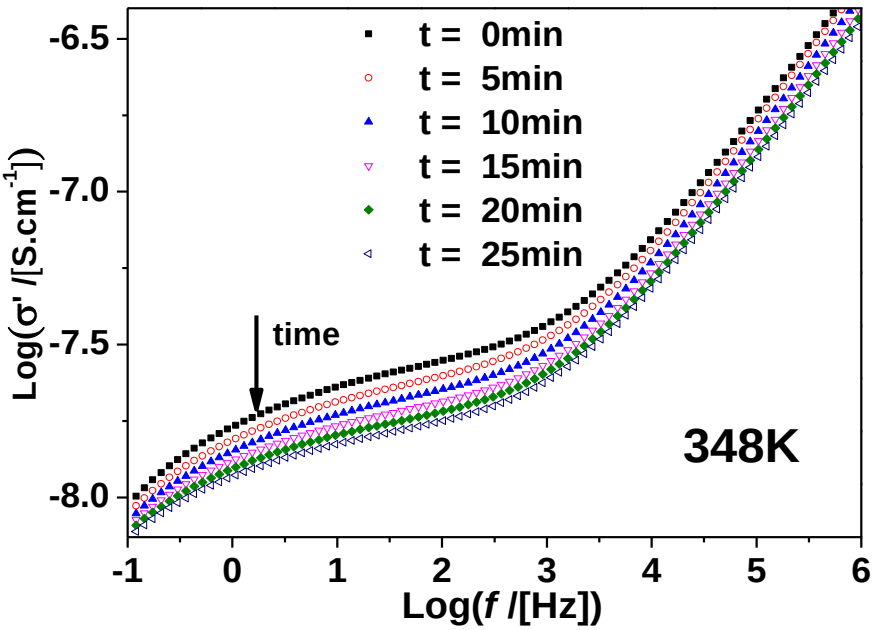


Figure 4.16: Series of conductivity spectra acquired at 348 K after heating for the first time a hydrate pellet to this temperature.

To summarize, the $C_{60}(ONa)_{24} \cdot 16H_2O$ hydrate exhibits two dielectric relaxations. The fastest one (at higher frequency) may stem from reorientational motions of the structural $H_2O$ molecules. The slower and more prominent loss (larger dielectric strength) is observed to evolve, upon dehydration, into the conductivity-induced relaxation feature of the pure $C_{60}(ONa)_{24}$ salt. While this suggests a common origin associated with charge-carrier accumulation at the sample's heterogeneities, the dielectric strength and temperature-dependence of this main relaxation indicate that it involves also the reorientational motion of water dipoles at the same heterogeneities. Several conductivity anomalies are reported below and at the temperature of structural dehydration. A decrease of conductivity is observed at the structural transition, obviously related to the phase change, which indicates a direct involvement of water molecules in charge transport through the hydrate. At temperatures below the structural dehydration we observe a cross-over of the conductivity to a more pronounced temperature dependence, which we ascribe to the onset of a water-induced conduction mechanism likely involving hydrogen-bond

exchange. The effects of water on conduction and dielectric properties appear to be closely inter-correlated: on one hand, water reorientations accompany the space-charge relaxation of carriers at heterogeneities; on the other, the onset of proton exchange is likely accompanied by the onset of reorientational motions of the water molecules.

## 4.5 Conclusions

We have analyzed the conduction and dielectric properties of the recently synthesized polycrystalline $C_{60}(ONa)_{24}$ powder and of its hydrate, of chemical formula $C_{60}(ONa)_{24} \cdot 16\ H_2O$. In the pure material charge conduction is electronic and well described by Mott's variable-range polaron hopping model. The effective hopping activation energy $E_a$ and most probable hopping range vary between 0.72 eV and 0.88 eV and 1.95 to 1.76 nm, respectively, as the temperature increases from 313 K to 473 K. The imaginary permittivity spectra display a single loss feature which is associated with polarization effects accompanying the hopping of polaronic charge carriers, as demonstrated by the validity of the Barton-Nakajima-Namikawa condition and of the time-temperature superposition principle based on the Summerfield scaling.

While the fully dehydrated, pure material exhibits low conductivity, exposing it to humid atmosphere leads to a four-decade conductivity enhancement below 325 K, due to charge transport through the hydration layers present on the surface of the crystalline grains. Such charge transport is due to proton exchange through second or higher molecular hydration layers.

In the hydrate, the dc conductivity is strongly temperature-dependent, and it is higher than that of the pure material by almost two orders of magnitude around 350 K. A cross-over of the conductivity to a more pronounced temperature dependence is observed in the hydrate at a temperature substantially lower than the structural dehydration temperature. We argue that both the higher conductivity in the hydrate, and the cross-over in temperature dependence arise most likely from a proton exchange majority contribution to the long-range charge transport.

A space-charge loss associated with charge accumulation at grain boundaries is observed in all spectra. Its dielectric strength is strongly affected by the presence of water at the grains' surface: it drops by a factor of approximately three upon desorption of the surface hydration water, and by a slightly lower factor upon loss of the structural water. Our results indicate that interfacial water has a strong impact not only on the long-range charge transport but also on energy dissipation processes that accompany the accumulation of charge at crystalline grain boundaries.

Our study sheds light on two well-known but not fully understood phenomena, namely, the surface conductivity enhancement in porous materials upon adsorption of water vapour, and the change in conductivity across the structural dehydration of crystalline hydrates. In particular, we have shown that the extra surface conduction takes place through secondary hydration layers and involves proton hopping between whole water molecules; and that the conductivity change actually occurs at lower temperature than that of structural decomposition. Our results also imply that the anomalous non-monotonic behavior of relaxations observed in porous water-containing systems may arise simply as a result of the change of conductivity induced by the desorption of water. Finally, we have shown that it is the presence of water around the fullerene derivatives which results in proton drift, while the water-free material does not exhibit protonic conduction, a result which rationalizes earlier findings.[11-14]

# References


[1] Lai, Y.-Y.; Cheng, Y.-J.; Hsu, C.-S. Applications of Functional Fullerene Materials in Polymer Solar Cells. *Energy Environ. Sci.* **2014,** 7, 1866–1883.

[2] Anthopoulos, T.D.; Singh, B.; Marjanovic, N.; Sariciftci, N.S.; Ramil, A.M.; Sitter, H.; Cölle, M.; de Leeuw, D.M. High performance N-Channel Organic Field-Effect Transistors and Ring Oscillators Based on $C_{60}$ Fullerene Films. *Appl. Phys. Lett.* **2006**, 89, 213504.

[3] Riccò, M.; Belli, M.; Mazzani, M.; Pontiroli, D.; Quintavalle, D.; Janossy, A.; Csanyi, G. Superionic Conductivity in the $Li_4C_{60}$ Fulleride Polymer, *Phys. Rev. Lett.* **2009**, 102, 145901.

**[4]** Pontiroli, D.; Aramini, M.; Gaboardi, M.; Mazzani, M.; Gorreri, A.; Riccò, M.; Belli, M. Ionic Conductivity in the Mg Intercalated Fullerene Polymer $Mg_2$ $C_{60}$ *Carbon* **2013**, 51, 143-147.

**[5]** Quintavalle, D.; Márkus, B. G.; Jánossy, A.; Simon, F.; Klupp, G.; Győri, M.; AKamarás, K.; Magnani, G.; Pontiroli, D. and Riccò, M. Electronic and Ionic Conductivities in Superionic $Li_4C_{60.}$ *Phys. Rev. B* **2016**, 93, 205103.

[6] Brutting, W.; Adachi, Ch. (Ed.s). *Physics of Organic Semiconductors,* 2nd Ed. Wiley **2012.**

[7] Macovez, R.; Hunt, M. R. C.; Goldoni, A.; Pedio, M.; Rudolf, P. Surface Hubbard U of Alkali Fullerides. *J. Electron Spectr. Relat. Phenom.* **2011**, 183, 94–100.

[8] Fazekas, P. *Lecture Notes on Electron Correlation and Magnetism.* World Scientific Publishing: Singapore **2003.**

[9] Kremer, F.; Schönhals, A. *Broad Band Dielectric Spectroscopy*. Springer: Berlin **2003**.

[10] Gunnarsson, O. Superconductivity in Fullerides. *Rev. Mod. Phys.* **1997**, 69, 575-606.

[11] Haspel, H.; Bugris, V.; Kukovecz, Á. Water Sorption Induced Dielectric Changes in Titanate Nanowires. *J. Phys. Chem. C.* **2013**, 117, 16686–16697.

[12] Aragoneses, A.; Tamayo, I.; Lebrato, A.; Cañadas, J.C.; Diego, J.A. Arencón, D.; Belana, J. Effect of Humidity in Charge Formation and Transport in LDPE. *J. Electrostatics.* **2013**, 71, 611-617.

[13] Cramer, C.; De, S.; Schönhoff, M. Time-Humidity-Superposition Principle in Electrical Conductivity Spectra of Ion-Conducting Polymers. *Phys. Rev. Lett.* **2011**, 107, 028301.

[14] Ahmad, M. M.; Makhlouf, S. A.; Khalil, K. M. S. Dielectric Behavior and Ac Conductivity Study of Ni*O*/$Al_2O_3$ Nanocomposites in Humid Atmosphere. *J. Appl. Phys.* **2006,** 100, 094323.

[15] Faia, P. M.; Furtado, C. S.; Ferreira, A. J. AC Impedance Spectroscopy: A New Equivalent Circuit for Titania Thick Film Humidity Sensors. *Sensors and Actuators B.***2005**, 107, 353–359.

[16] Bernard. M, Kulwicki. Humidity Sensors. *J. Am. Ceram. Soc.* **1991,** 74, 697–708

[17] Yamazoe, N. and Shimizu, Y. Humidity Sensors: Principles and Applications. *Sensors and Actuators.* **1986**, 10, 379–398.

[18] Coropceanu, V.; Cornil, J.; da Silva Filho, D. A.; Olivier, Y.; Silbey, R.; Bredas, J.-L. Charge Transport in Organic Semiconductors. *Chem. Rev.* **2007**, 107, 926-952.

[19] Djordjevic, A.; Vojinovic-Miloradov, M.; Petranovic, N.; Devecerski, A.; Lazar, D.; Ribar, B. Catalytic Preparation and Characterization of $C_{60}Br_{24}$. *Fullerene Sci. Technol.* **1998**, 6, 689-694.

[20] Bogdanovi, G.; Kojic, V.; Djordevic, A.; Canadanovic-Brunet, J.; Vojinovic-Miloradov, M.; Vit. Baltic, V. Modulating Activity of Fullerol $C_{60}(OH)_{22}$ on Doxorubicin-Induced Cytotoxicity. *Toxicology In Vitro* **2004**, 18, 629–637.

[21] Macovez R.; Mitsari, E.; Zachariah M.; Romanini, M.; Zygouri, P.; Gournis D.; Tamarit, J. Ll. Ultraslow Dynamics of Water in Organic Molecular Solids. *J. Phys. Chem. C* **2014**, 118, 4941–4950.

[22] Scherrer, P. Bestimmung der Grösse und der Inneren Struktur von Kolloidteilchen mittels Röntgenstrahlen. *Göttinger Nachrichten Gesell.* **1918**, 2, 98.

[23] Patterson, A. The Scherrer Formula for X-Ray Particle Size Determination. Phys. *Rev.* **1939**, 56, 978–982.

[24] Michaud, F.; Barrio, M.; Toscani, S.; López, D. O.; Tamarit, J. L.; Agafonov, V.; Szwarc, H.; Céolin, R. Solid-State Studies on Single and Decagonal Crystals of $C_{60}$ Grown from 1,2-Dichloroethane. *Phys.Rev. B* **1998**, 57, 10351−10358.

[25] Rodríguez-Carvajal, J. FullProf Suite: Crystallographic Tools for Rietveld, Profile Matching and Integrated Intensity Refinements of X-ray and/or Neutron Data. Available at http://www.ill.eu/sites/fullprof/

[26] Dinnebier, R. E.; Stephens, P. W.; Carter, J. K.; Lommen, A. N.; Heiney P. A.; McGhie, A. R.; Brard, L.; Smith III, A. B. X-ray Powder Diffraction Structure of Triclinic $C_{60}Br_{24}(Br_2)_2$. *J. Appl. Cryst.* **1995**, 28, 327-334.

[27] Kawasaki, S.; Aketa, T.; Touhara, H.; Okino, F.; Boltalina, O. V.; Gol'dt, I. V.; Troyanov, S. I.; Taylor, R. Crystal Structures of the Fluorinated Fullerenes $C_{60}F_{36}$ and $C_{60}F_{48}$. *J. Phys. Chem. B* **1999**, 103, 1223-1225.

[28] Vaughan, G. B. M.; Chabre, Y.; Dubois, D. Effect of Stacking Disorder on the Orientational Ordering Transition of Solid $C_{60}$. *Europhys. Lett*. **1995**, 31, 525.

[29] Frunza, L.; Kosslick, H.; Pitsch, I.; Frunza, S.; Schönhals, A. Rotational Fluctuations of Water Inside the Nanopores of SBA–Type Molecular Sieves. *J. Phys. Chem. B* **2005**, 109, 9154–9159.

[30] Haspel, H.; Laufer, N.; Bugris, V.; Ambrus, R.; Szabó-Révész, P.; Kukovecz, Á. Water-Induced Charge Transport Processes in Titanate Nanowires: An Electrodynamic and Calorimetric Investigation. *J. Phys. Chem. C* **2012**, 116, 18999–19009.

[31] Frunza, L.; Kosslick, H.; Frunza, S.; Schönhals, A. Unusual Relaxation Behavior of Water Inside the Sodalite Cages of Faujasite–Type Molecular Sieves. *J. Phys. Chem. B* **2002**, *106*, 9191–9194.

[32] Sjöström, J.; Swenson, J.; Bergman, R.; Kittaka, S. Investigating Hydration Dependence of Dynamics of Confined Water: Monolayer, Hydration Water and Maxwell–Wagner Processes. *J. Chem. Phys.* **2008**, 128, 154503.

[33] Anderson, J. H.; Parks, G. A. Electrical Conductivity of Silica Gel in the Presence of Adsorbed Water. *J. Phys. Chem.* **1968**, 72, 3662**–**3668.

[34] Capaccioli, S.; Lucchesi, M.; Rolla, P. A.; Ruggeri, G. Dielectric Response Analysis of a Conducting Polymer Dominated by the Hopping Charge Transport. *J. Phys.: Condens. Matter.* **1998,** 10, 5595− 5617 and references therein

[35] Han, H.; Davis, C.; Nino, J.C. Variable Range Hopping Conduction in $BaTiO_3$ Ceramics Exhibiting Colossal Permittivity. *J. Phys. Chem. C* **2014**, 118, 9137−9142.

[36] Huijbregts, L. J.; Brom, H. B.; Brokken-Zijp, J. C. M.; Kemerink, M.; Chen, Z.; de Goeje, M. P.; Yuan, M.; Michels, M. A. J. The Optimal Structure-Conductivity Relation in Epoxy-Phthalocyanine Nanocomposites. *J. Phys. Chem. B* **2006,** 110, 23115-23122.

[37] van Staveren, M. P. J.; Brom, H. B.; de Jongh, L. J. Metal-Cluster Compounds and Universal Features of the Hopping Conductivity of Solids. *Phys. Rep.* **1991**, 208, 1-96 and references therein

[38] Tran, T. B.; Beloborodov, I. S.; Lin, X. M.; Bigioni, T. P.; Vinokur, V. M.; Jaeger, H. M. Multiple Cotunneling in Large Quantum Dot Arrays. *Phys. Rev. Lett.* **2005**, 95, 076806.

[39] Yu, D.; Wang, C.; Wehrenberg, B. L.; Guyot-Sionnest, P. Variable Range Hopping Conduction in Semiconductor Nanocrystal Solids. *Phys. Rev. Lett.* **2004**, 92, 216802.

[40] Efros, A.L.; Shklovskii, B.I. Coulomb Gap and Low Temperature Conductivity of Disordered Systems. *J. Phys. C: Solid State Phys.* **1975**, 8, L49–L51.

[41] Shklovskii, B. I.; Efros, A. L. Electronic Properties of Doped Semiconductors. Springer: Berlin **1984**.

[42] Mitsari, E.; Romanini, M.; Zachariah, M.; Macovez, R. Solid State Physicochemical Properties and Applications of Organic and Metallo-Organic Fullerene Derivatives, *Curr. Org. Chem.* **2016**, 20, 645–661.

[43] Jonscher, A. K. The 'Universal' Dielectric Response. *Nature* **1977**, 267, 673−679.

[44] Dyre, J. C.; Schroder, T. B. Universality of Ac Conduction in Disordered Solids. *Rev. Mod. Phys.* **2000,** 72, 873−892.

[45] Sidebottom, D. L. Universal Approach for Scaling the Ac Conductivity in Ionic Glasses, *Phys. Rev. Lett.* **1999**, 82, 3653-3656.

[46] Neagu, R. M.; Neagu, E.; Bonanos, N.; Pissis, P. Electrical Conductivity Studies in Nylon 11. *J. Appl. Phys.* **2000**, 88, 6669–6677.

[47] Rim, Y. H.; Lee, B. S.; Choi, H. W.; Cho, J. H.; Yang, Y. S. Electrical Relaxation of Bismuth Germanate Silicate Glasses. *J. Phys. Chem. B* **2006,** 110, 8094-8099.

[48] Kahnt, H. Ionic Transport in Oxide Glasses and Frequency Dependence of Conductivity. *Ber. Bunsenges. Phys. Chem.* **1991**, 95, 1021-1025.

[49] Sidebottom, D. L. Colloquium: Understanding Ion Motion in Disordered Solids from Impedance Spectroscopy Scaling. *Rev. Mod. Phys.* **2009**, 81, 999-1014.

[50] Imre, A. W.; Schonhoff, M.; Cramer, C. Unconventional Scaling of Electrical Conductivity Spectra for PSS-PDADMAC Polyelectrolyte Complexes. *Phys. Rev. Lett.* **2009**, 102, 255901.

[51] Das, S. and Bhattacharyya, A. J. Time–Temperature Scaling of Conductivity Spectra of Organic Plastic Crystalline Conductors. *J. Phys. Chem. Lett.* **2012**, 3, 3550–3554.

[52] Namikawa, H. Characterization of the Diffusion Process in Oxide Glasses Based on the Correlation between Electric Conduction and Dielectric Relaxation. *J. Non. Cryst. Solids* **1975**, 18, 173-.

[53] Riccò, M.; Belli, M.; Mazzani, M.; Pontiroli, D.; Quintavalle, D.; Janossy, A.; Csanyi, G. Superionic Conductivity in the $Li_4C_{60}$ Fulleride Polymer. *Phys. Rev. Lett.* **2009**, 102, 145901.

[54] Hebard, A.F.; Haddon, R.C.; Fleming, R.M.; Kortan, A.R. Deposition and Characterization of Fullerene Films. *Appl. Phys. Lett.* **1991**, 59, 2109.

[55] Pederson, M. R.; Quong, A. A. Polarizabilities, Charge States, and Vibrational Modes of Isolated Fullerene Molecules. *Phys. Rev. B* **1992**, 46, 1358.

[56] Guinea, F.; Gonzalez, J.; Vozmediano, M. A. H. Shake-Up Effects and Intermolecular Tunneling in $C_{60}$ Ions. *Phys. Rev. B* **1994**, 50, 5752.

[57] Knight, C. and Voth, G. A. The Curious Case of the Hydrated Proton. *Acc. Chem. Res.* **2012**, 45, 101–109.

[58] Vilčiauskas, L.; Tuckerman, M. E.; Bester, G.; Paddison, S. J.; Kreuer, K. D. The Mechanism of Proton Conduction in Phosphoric Acid. *Nat. Chem.* **2012**, 4, 461–466.

[59] Charalampopoulos, V. G.; Papaioannou, J. C. Dipole Relaxation and Proton Transport in Polycrystalline γ-Cyclodextrin Hydrate: A Dielectric Spectroscopy Study. *Solid State Ionics* **2011**, 191, 1–11.

[60] Wojnarowska, Z.; Wang, Y.; Paluch, K. J.; Sokolov, A. P.; Paluch, M. Observation of Highly Decoupled Conductivity in Protic Ionic Conductors. *Phys. Chem. Chem. Phys.* **2014**, 16, 9123-9127.

[61] Gränicher, H.; Jaccard, C.; Scherrer, P.; Steinemann, A. Dielectric Relaxation and the Electrical Conductivity of Ice Crystals. *Discuss. Faraday Soc.* **1957**, 23, 50–62.

[62] Egashira, M.; Nakashima, M.; Kawasumi, S.; Selyama, T. Temperature Programmed Desorption Study of Water Adsorbed on Metal Oxides. 2. Tin Oxide Surfaces. *J. Phys. Chem.* **1981**, 85, 4125–4130.

[63] Ryabov, Y. E.; Puzenko, A.; Feldman, Y. Nonmonotonic Relaxation Kinetics of Confined Systems. *Phys. Rev. B* **2004**, 69, 014204.

[64] Ryabov, Y.; Gutina, A.; Arkhipov, V.; Feldman, Y. Dielectric Relaxation of Water Absorbed in Porous Glass. *J. Phys. Chem. B* **2001**, 105, 1845–1850.

# Chapter 5

# Hopping Conduction and Conductivity Cross-Over in Bromofullerene

## 5.1 Introduction

Fullerenes, the fourth known allotrope of carbon after diamond, graphite and amorphous carbon, display intriguing conduction and molecular dynamic properties.[1,2] Thanks to their relatively high electron affinity, fullerenes and their derivatives usually behave as electron-transporting (*n*-channel) materials and as such they have been successfully implemented in electrical and optoelectronic devices such as high-efficiency fullerene-polymer-blend heterojunction solar cells,[3,4] high-mobility vacuum $C_{60}$ field-effect transistors,[5] and air-stable *n*-channel organic transistors.[6,7] Understanding the charge transport properties of fullerene-based systems is of crucial importance for the design of novel carbon materials with improved performance. Most small-molecule organic materials such as fullerenes behave as disordered inorganic semiconductors, where the main conduction

mechanism is by polaronic (electron or hole) hopping.[8] The hopping-mediated conductivity is a consequence of strong local interactions that tend to localize charge carriers, such as inter-electron Coulomb repulsion and polarization screening,[9] coupling to molecular vibrations,[10] or trapping at defects.

Due to their globular shape, $C_{60}$ and some of its derivatives display rotational motions and orientational phase transformations in the solid state. For example, solid $C_{60}$ displays a face-centered cubic (*fcc*) rotator phase of freely spinning molecules at room temperature, while below 260 K the free-rotor motion is reduced to a ratcheting motion between two preferred orientations.[11,12] This merohedral reorientational motion finally freezes out at a glass transition taking place 90 K, below which the lattice structure is simple cubic with four non-equivalent orientations.[13,14] Similar transitions are observed at very similar temperatures in simple derivatives such as $C_{60}O$ and the annulene isomer of $C_{61}H_2$,[15,16] albeit in the room-temperature *fcc* phase of the latter compounds the molecules do not behave as free rotors due to the fact that the adducts occupy interstitial sites of the fullerene lattice. The cyclopropane isomer of $C_{61}H_2$ displays instead a different phase diagram than its annulene isomer, exhibiting in particular an orientational melting occurring through a two-step transition around 198–213 K.[17]

In pristine $C_{60}$, orientational ordering strongly favors electronic charge transport: across the transition at 260 K, the dc conductivity of $C_{60}$ raises by more than one order of magnitude,[18] and a similar behavior was observed in $C_{60}$ salts across the *fcc* to simple cubic transition.[1] This would indicate that molecular reorientations in crystalline fullerenes hinder electron hopping, possibly because they favor coupling to intermolecular vibrations and because the disorder induced by molecular reorientational motions leads to even stronger electron localization on single fullerene molecules and yet smaller electronic bandwidth.[9] Less is known on the effect of molecular motions in fullerene derivatives or polycrystalline and disordered fullerene systems. In this chapter we employ dielectric spectroscopy BDS to investigate electrical conduction and dipolar molecular dynamics in the solid phase of the halofullerene $C_{60}Br_6$ derivative.

## 5.2 Synthesis and Experimental Methods

For the preparation of $C_{60}Br_6$, a procedure based on Troshin et al.[19] was followed. In a typical synthesis, 79 mg of pristine fullerene ($C_{60}$, Aldrich, 99.8% pure) were dissolved in a mixture of 2 mL of elementary bromine and 10 mL of carbon disulfide. The resulting mixture was allowed to stand without stirring and heating for 10 days. The precipitate was filtered off, washed with hexane and dried at room temperature. Figure 5.1 shows the molecular structure of $C_{60}Br_6$.

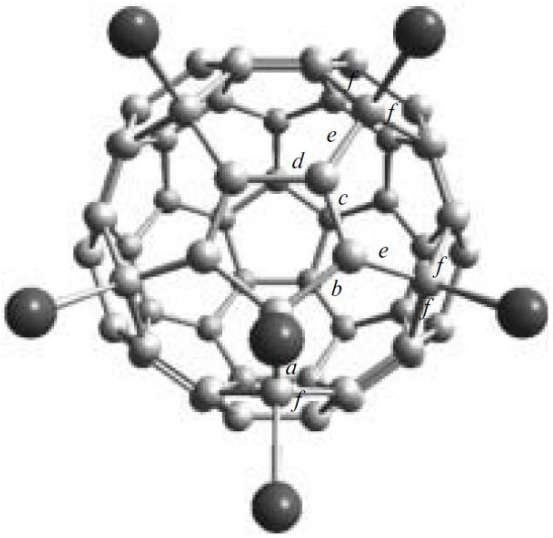


Figure 5.1: Molecular structure of $C_{60}Br_6$

The as-synthesized powder was characterized by thermogravimetry analysis (TGA) and scanning calorimetry (DSC). TGA curves were acquired while heating the sample under $N_2$ flow between room temperature (300 K) and 450 K by means of a Q50 thermobalance from TA-Instruments. DSC measurements were carried out between 200 K and 450 K using a Q100 calorimeter from TA-Instruments. In both experiments the heating rate was set to 10 K $min^{-1}$, and the powder was placed in an open vessel to allow evaporation of volatile species.

For broadband dielectric spectroscopy measurements, the powder was mechanically pressed into pellets of submillimeter thickness between 7 mm-

diameter stainless steel electrode disks in parallel-plate capacitor geometry. Dielectric spectra were acquired in the frequency range from $10^{-2}$ to $10^{7}$ Hz using a Novocontrol Alpha analyzer. Isothermal frequency scans were acquired between 125 and 360 K (with a temperature stability of ±0.3 K) in a $N_2$ flow Quatro cryostat (the sample was in a nitrogen flux during all measurements). Dielectric spectroscopy yields the complex conductivity and permittivity of a sample as a function of frequency (*f*). As mentioned in Chapter 3, the imaginary part of the permittivity ε"(*f*), or loss spectrum, is related to the real part of the ac conductivity σ'(*f*) as ε"(*f*) = σ'(*f*)/(2π*f*ε$_0$). The σ'(*f*) spectra (real part of the ac conductivity) displayed a plateau value at low frequency, corresponding to the dc value of the conductivity, $\sigma_{dc}$. In order to study the temperature dependence of $\sigma_{dc}$, an effective activation energy of the conductivity is computed as

$$E_a(\sigma_{dc}) = -\frac{d\left(Ln(\sigma_{dc})\right)}{d(1/k_B T)}. \quad (5.1)$$

Each ac conductivity spectrum and corresponding loss spectrum were fitted as the sum of one or more relaxation processes, modeled with the Havriliak–Negami function,[20,21] on top of a background representing the dc conductivity contribution (see chapter 3 section 3.3).

## 5.3 Thermodynamic Characterization

Figure 5.2 shows a typical TGA curve of the as-synthesized powder, both as mass percent and as its first derivative. The main mass loss observed approximately up to 425-450 K corresponds to slightly above 35% in weight, which is in agreement with the expected mass decrease upon loss of all bromine atoms in $C_{60}Br_6$ (the theoretical value is 479.4/1200.1 = 40%). The final product after heating to 450 K is polycrystalline $C_{60}$, as determined from powder X-ray diffraction experiments (not shown). At lower temperature, a smaller mass loss is observed in the range between room temperature and 340 K due to volatile impurities, likely $Br_2$ or carbon disulfide, both of which are employed in the synthesis (see Experimental Section).

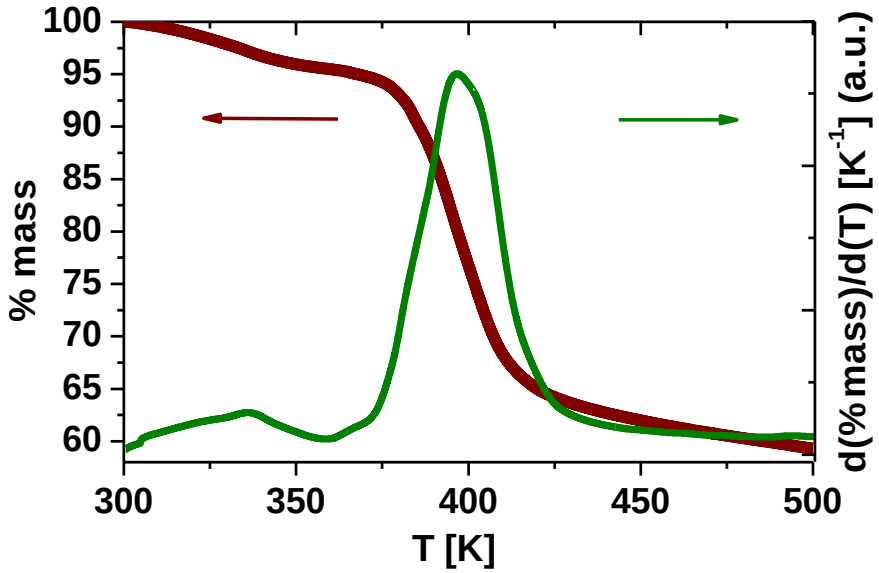


Figure 5.2: TGA curve measured on the as-synthesized $C_{60}Br_6$ powder upon heating. Here the thin line is the first derivative of the percent mass loss (thick line).

Molecules of bromine and/or of organic solvents are known to remain trapped in the solid matrix during the synthesis process of brominated fullerenes and $C_{60}Br_6$ in particular, sometimes even leading to the formation of solvates.[19,22,23] As visible in Figure 5.3, the DSC thermogram exhibits two endothermic features, each occurring in correspondence with a mass loss.

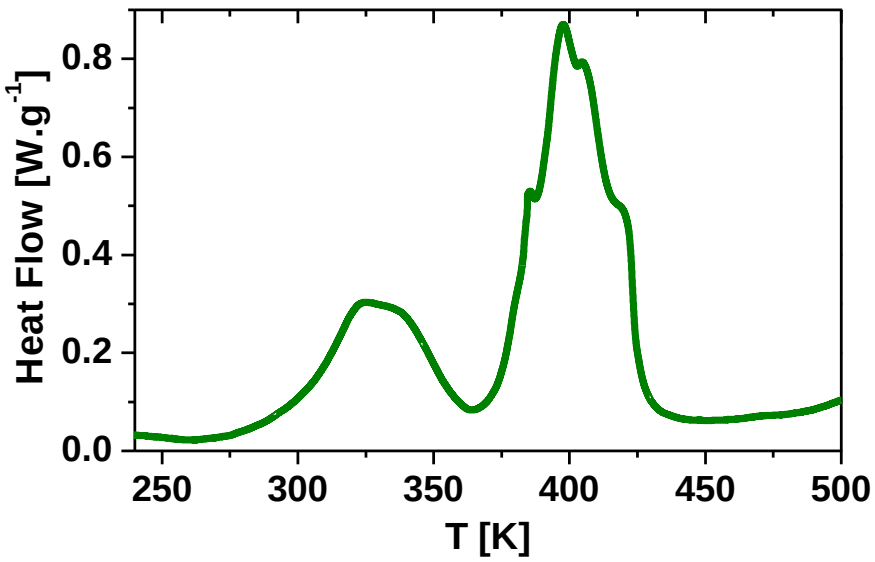


Figure 5.3: DSC curves measured on the as-synthesized $C_{60}Br_6$ powder upon heating.

In light of these results, for the characterization of $C_{60}Br_6$ by dielectric spectroscopy, the powder was pre-heated to 323 K prior to acquisition of the spectra in order to remove all volatile impurities present in the powder[24] (heating to 343 K did not further modify the spectral response).

## 5.4 BDS Results and Discussion

Figure 5.4 shows the frequency-dependent ac conductivity spectra (*a*) and loss spectra (*b*) of a typical (pre-heated) $C_{60}Br_6$ pellet, as measured upon heating from 125 K. Similar data were obtained by measuring while subsequently cooling the sample from room temperature.

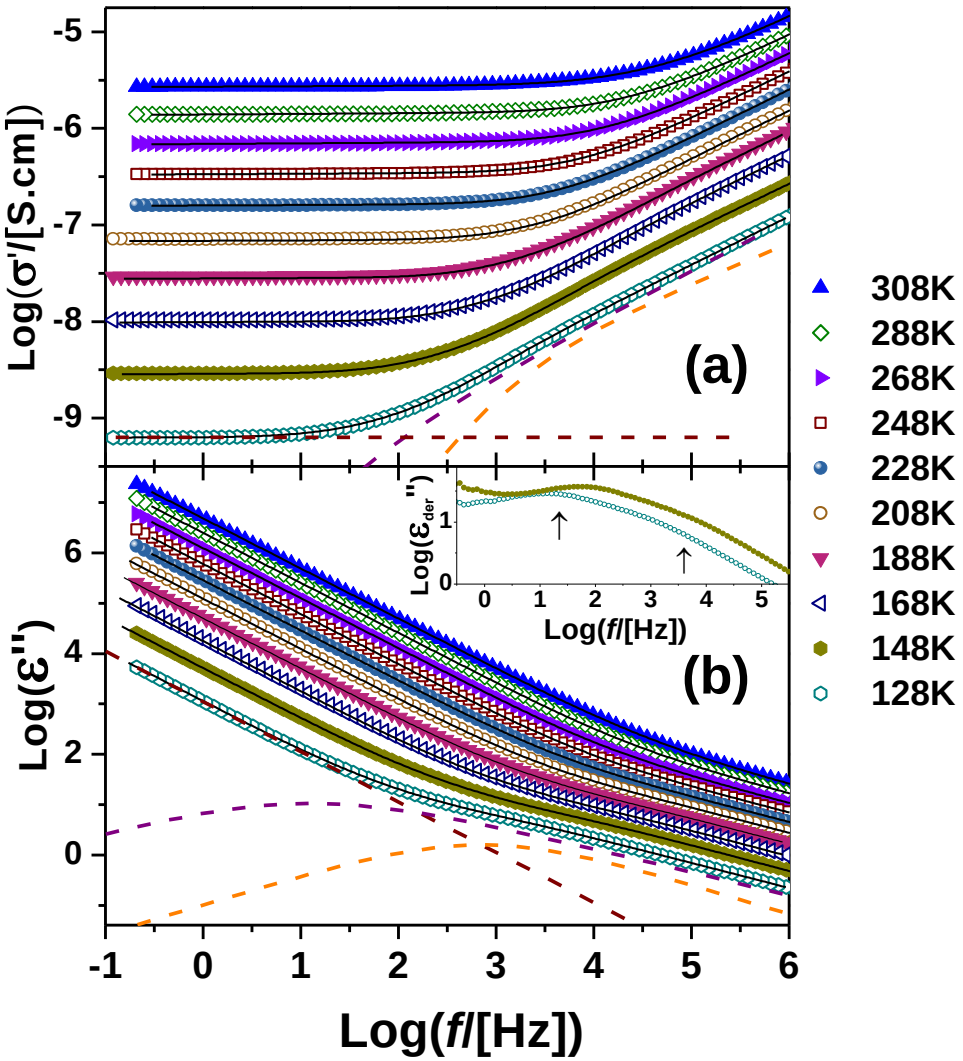


Figure 5.4: Logarithmic plot of the ac conductivity σ' (*a*) and dielectric loss ε" (*b*) spectra of $C_{60}Br_6$, shown for selected temperatures (between 308 and 128 K, every 20 K). Continuous lines are fits with Havriliak-Negami components on top of a background representing the dc conductivity limit. The fit components are shown as dashed lines for the spectrum acquired a 128 K. Inset to (*b*): logarithmic derivative spectrum $\varepsilon''_{pol}$ shown for two selected temperatures (128 and 148 K; see Eq. (5.6) in the text for the definition). The arrows indicate the position of the two components present in the spectrum.

The lineshape of the ac conductivity spectra σ'(*f*) is similar to that of a very wide range of disordered systems ranging from amorphous semiconductors and glasses to

metal-cluster compounds to polymers and polymer composites. In all these materials the conductivity is frequency-independent at low frequencies, reaching a plateau value corresponding to the dc value ($\sigma_{dc}$), and then, above a temperature-dependent onset frequency, exhibits a power-law-like dependence on *f*, described approximately by:

$$\sigma'(f) = \sigma_{dc} + \sigma_0 f^{s} . \quad (5.2)$$

Eq. (5.2) is known as the universal dielectric response.[25,26,27,28,29] In the case of $C_{60}Br_6$, the universal ac conduction law gives an only rough fit to the experimental spectra, which in logarithmic scale exhibit a curved rather than linear lineshape for frequencies above the onset of the ac response. A fit of the spectra with Eq. (5.2) gives values of the exponent *s* in the range of 0.6-0.7, which is consistent with hopping of localized (polaronic) states.[30] The only approximate validity of the universal Eq. (5.2) is due to the presence of a dielectric loss, which is clearly visible in Figure 5.4(*b*) as a broad bump-like feature above the low-temperature linear dc-conductivity background. Many disordered conductors have similar ac conductivity spectra, in which the separation between the dc and ac regimes of the conductivity is signaled by a dielectric loss in the radiofrequency range.[25] In most cases such loss is associated with charge accumulation due to spatial inhomogeneities of the dc conductivity.[31] The origin of the loss feature in the case of $C_{60}Br_6$ is discussed later.

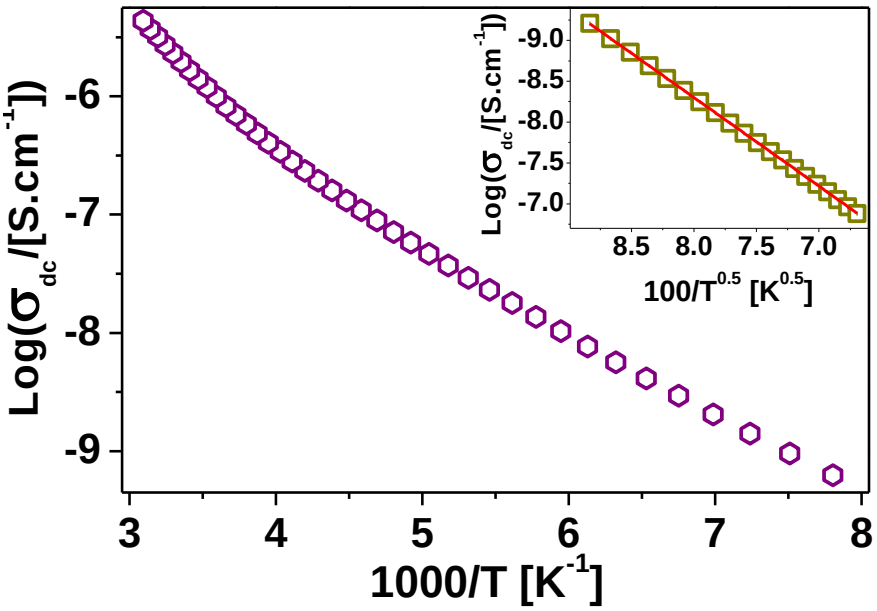


Figure 5.5: Semilogarithmic plot of the dc conductivity $\sigma_{dc}$ of $C_{60}Br_6$ *vs* 1000/*T* (Arrhenius plot) between 125 and 330 K. Inset: plot of Log($\sigma_{dc}$) *vs* $100/\sqrt{T}$ below 220 K, for the same data as in the main panel.

Figure 5.5 depicts the Arrhenius plot of the dc conductivity ($\sigma_{dc}$), extracted directly as the plateau value in the σ' spectra of Figure 5.4 (*a*). It may be observed that $\sigma_{dc}$ does not exhibit a simply activated (Arrhenius) behavior, but rather displays a negative curvature in the whole probed temperature range (125-330 K).

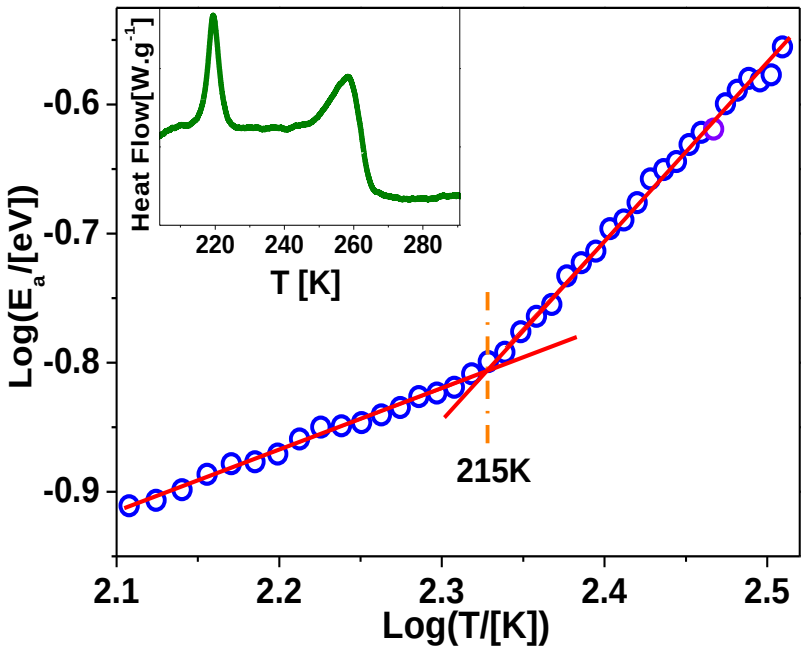


Figure 5.6: Logarithmic plot of the activation energy $E_a$ (in eV) of the dc conductivity, *versus* temperature. The continuous lines are linear fits of the data below and above 215 K, respectively. The dashed vertical line indicates the cross-over temperature-between the two regimes, as determined by the intersection of both linear fits. Inset: DSC scan acquired on the same sample upon heating from 200 K.

To study the temperature dependence of the conductivity in more detail, we have calculated the effective (temperature-dependent) activation energy $E_a$ of the dc conductivity using Eq. (5.1), and represented this quantity as a function of temperature in the logarithmic plot shown in Figure 5.6. Although the effective activation energy is a monotonic function of temperature (always increasing with increasing temperature), it may be observed that it exhibits markedly different temperature dependences above and below approximately 215 K. The logarithmic plot of Figure 5.6 clearly highlights the existence of two conduction regimes, one characterized by a slope of 0.49±0.02 and the other with a slope of 1.36±0.02 in the logarithmic representation. It is interesting to notice that a small endothermic feature is detected at the same temperature in the DSC thermogram, as shown in the inset to

Figure 5.6. The onset of the new conduction mechanism therefore accompanies a fundamental change in the material.

### 5.4.1 Variable Range Hopping Conduction in $C_{60}Br_6$

The data below 215 K are consistent with an electronic charge transport described by Mott's variable range hopping (VRH) model.[32] According to this model, the logarithm of the dc conductivity should follow a fractional power-law dependence, given by:

$$\sigma_{dc} = \sigma_0 \exp[-(T_0/T)^n]. \quad (5.3)$$

Here $\sigma_0$ and $T_0$ are constants and the exponent $n$ is usually equal to 1/2 or 1/4. Applying the definition of activation energy (Eq. (5.1)) to Eq. (5.3), one finds that the slope of the logarithmic plot of $E_a$ *vs* $T$ plot should be equal to $1 - n$.[30] The slope of 0.49±0.02 obtained below 215 K gives a value of $n$ of 0.51±0.02, which is virtually identical to the theoretical value of 1/2 of the VRH model, observed in many systems characterized by hopping electronic conduction, ranging from metal-cluster compounds to granular and ceramic metals, to doped or amorphous organic and inorganic semiconductors.[26,27,29, 33 , 34] The value $n$ = 1/2 is determined by electron-electron correlation[27] leading to a weak Coulomb gap near the Fermi level [29] and to a square dependence of the localized state density on energy.[35,36] The inset to Figure 5.5 shows the logarithmic plot of $\sigma_{dc}$ vs $1/T^{0.5}$ below 220 K to highlight the consistency with the VRH model.

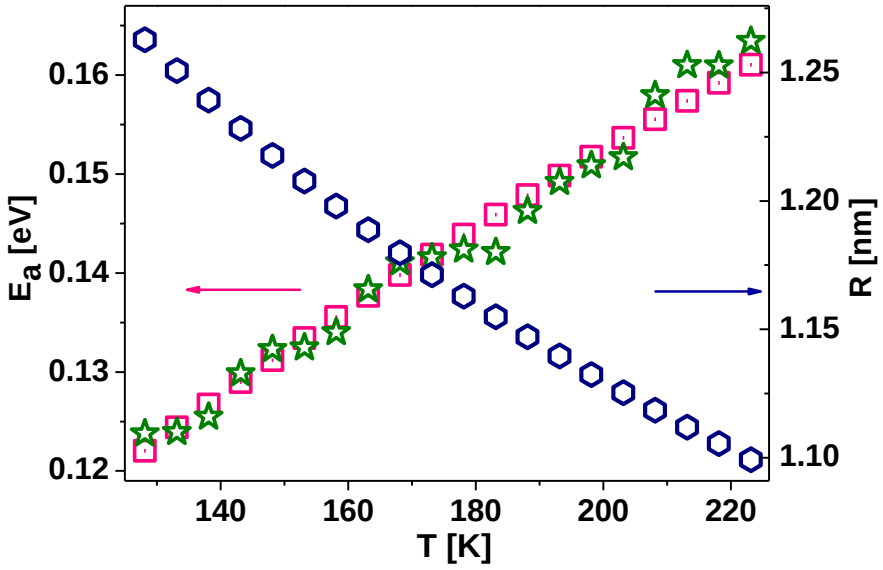


Figure 5.7: Activation energy $E_a$ and hopping distance R as a function of temperature for VRH conduction in $C_{60}Br_6$ below 220 K (see the text for more details).

Figure 5.7 shows the activation energy $E_a$ and typical hopping distance $R$, in the same temperature range. The typical hopping distance is given by [30]

(5.4) $R = \xi\,(T_0/192T)^{0.25}$

Here $\xi$ is the decay length of the localized electronic wavefunction, and $T_0$ = 6.25±0.05 · $10^4$ K is the temperature parameter in Eq. 5.3, as determined from the fit of the $\sigma_{dc}$ values below 215 K. From Eq. (5.4) it is found that the value of $R$ decreases from 1.27$\xi$ to 1.08$\xi$ as the temperature is raised from 125 to 215 K. Figure 5.7 shows a plot of the hopping distance $R$ assuming that $\xi$ = 1 nm, *i.e.* equal to the van der Waals radius of the $C_{60}$ molecule.[37] The activation energy shown as a function of temperature in the same inset was calculated both using Eq. (5.1) and according to the formula

(5.5) $E_a = 0.5k_B T_0^{0.5} T^{0.5}$

which is valid for the case of VRH with $n = 0.5$. As visible from the Figure 5.7, Eq. (5.5) gives values consistent with those obtained directly from the raw data using Eq. (5.1).

The results discussed so far show that charge conduction in $C_{60}Br_6$ has a dominant contribution below 215 K due to variable-range hopping of localized electronic states (or holes), as expected from the known electron affinity and *n*-channel behavior of $C_{60}$ derivatives.[2] The value of the slope of the Log($E_a$) *vs* Log($T$) plot above 215 K is inconsistent with the variable-range hopping model, as such theory predicts a slope between zero and one (a slope close to zero would correspond to a simply-activated Arrhenius behavior). The fact that the activation energy increases with increasing temperature might suggest that the conduction is still electronic in nature above 215 K. On the other hand, the fact that a new dominant charge conduction mechanism starts being effective only above the threshold temperature of 215 K is reminiscent of the behavior of another fullerene derivative, namely the polymeric salt $Li_4C_{60}$.[38, 39] In this material, the conductivity above 130 K is dominated by the contribution of $Li^+$ ions,[40] which become mobile only above this temperature.[41] A possible ion-conduction mechanism in $C_{60}Br_6$ could be associated with the diffusion of ionic impurities or, less likely, to the intermolecular exchange of $Br^-$ ions.

The nature of the transition at 215 K is at present unclear. The shape of the DSC feature in the inset to Figure 5.6 as well as the lack of a clear relaxation feature in the spectra of Figure 5.4 above this temperature (see below) indicate that it is not an orientational glass transition as the one of pure $C_{60}$ at 90 K,[13,14] but rather it might be a solid-solid transition between phases with different orientational order. The associated enthalpy of transition is 0.5±0.2 J/mol, which indicates that the degree of disorder might be similar in both the phases above and below 215 K. Since we do not observe any new dielectric relaxation at 215 K, if an orientational transition takes place in $C_{60}Br_6$ then either both phases are crystalline, with no orientational dynamics, or else the molecular dynamics in the high-temperature phase corresponds to a rotation about the molecule's symmetry axis, which does not modify the direction of the molecular dipole moment. It is seen in the inset to Figure

5.6 that a second, rather broad, endothermic feature is present at higher temperature, between 250 and 260 K. It might be that the solid-solid phase transition is not a single-step transition. Such behavior is for example observed for the orientational melting transition in the solid phase of the cyclopropane isomer of $C_{61}H_2$, which as mentioned in the introduction occurs in two steps between 198 and 125 K.[17]

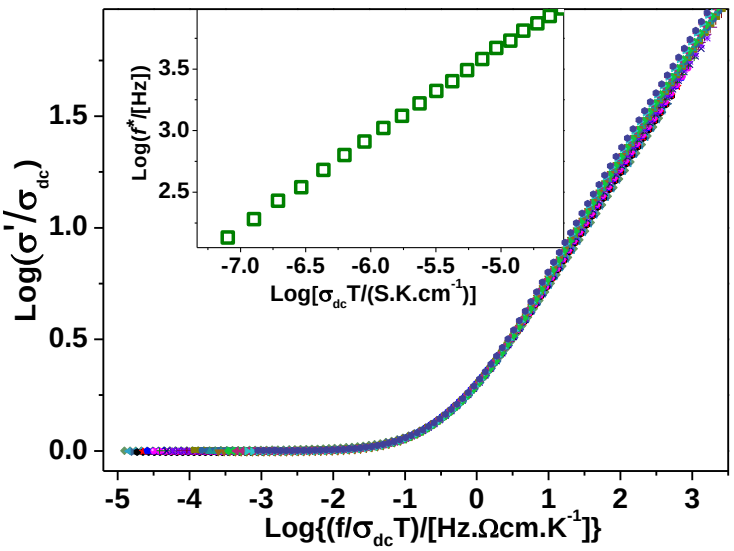


Figure 5.8: Summerfield scaling analysis of the normalized ac conductivity $\sigma'/\sigma_{dc}$ below 220 K. Inset to panel: logarithmic plot of the onset frequency $f^*$ (defined in the text) versus $\sigma_{dc}T$.

Figure 5.8 shows the results of the scaling analysis of the ac conductivity ($\sigma'$) spectra acquired below 220 K (from 128 K). The spectra are found to obey a time-temperature superposition principle, following in particular the equation of the Summerfield scaling [42] illustrated in chapter 2, and may thus be superposed to the same master curve. As shown in the inset to Figure 5.8, in fact, the onset frequency $f^*$ of the dispersive part of the conductivity spectra, defined as the frequency $f^*$ at which $\sigma'(f^*) = 2\sigma_{dc}$, is directly proportional to the product $\sigma_{dc}T$. Above 220 K, the scaling breaks down and a different conduction mechanism emerges, with the plot depicted in the inset exhibiting a deviation from linear dependence.

### 5.4.2 Dielectric Relaxation in $C_{60}Br_6$

We finally discuss the dielectric losses in the material. Albeit the $C_{60}Br_6$ molecules possess a non-zero permanent dipole moment, given that solid $C_{60}Br_6$ is a crystalline material [19] we do not expect to observe dipolar relaxations (especially below 215 K). A different possible origin for the wide radiofrequency feature visible at low temperature in the isothermal ε"(*f*) spectra of Figure. 5.4(*b*) might be a conductivity-induced relaxation, *i.e.*, a space-charge loss feature associated with the accumulation of (free) electronic charge carriers at spatial heterogeneities of the sample such as grain boundaries. A loss feature of this kind is also reported in chapter 4 in the case of fullerene derivative, $C_{60}(NaO)_{24}$ A quantitative fitting analysis was carried out to corroborate this assignment in $C_{60}Br_6$. We found that the loss feature on Figure. 5.4(*b*) could not be fitted with a single Havriliak-Negami (HN) function, but actually contained two contributions. The presence of two loss features may be best observed in the logarithmic derivative of the imaginary permittivity, defined as:

$$\varepsilon''_{pol} = -\frac{\pi}{2}\frac{\partial \varepsilon'(\omega)}{\partial ln\,(\omega)}. \quad (5.6)$$

Here, $\omega = 2\pi f$ and ε' is the real part of the permittivity (which is measured simultaneously with the imaginary part). The logarithmic derivative is a good approximation to the dielectric loss without the ohmic-conduction contribution, and can be employed to better visualize ac losses.[43] The logarithmic derivative spectra are shown in the inset to Figure 5.4(*b*) for two temperatures (128 and 148 K). It may be seen that the ohmic-conduction-free loss indeed contains two contributions, whose spectral positions are indicated by arrows, both of which shift to higher frequency with increasing temperature. Each dielectric spectrum (both in the ac conductivity and permittivity representations) was therefore fitted as the sum of a dc conductivity background proportional to reciprocal frequency plus the imaginary part of two HN functions, each representing a distinct loss feature. The obtained fits are displayed as continuous lines in Figure 5.4. The fit components are shown

explicitly for the spectrum acquired at the lowest temperature (128 K), in both representations.

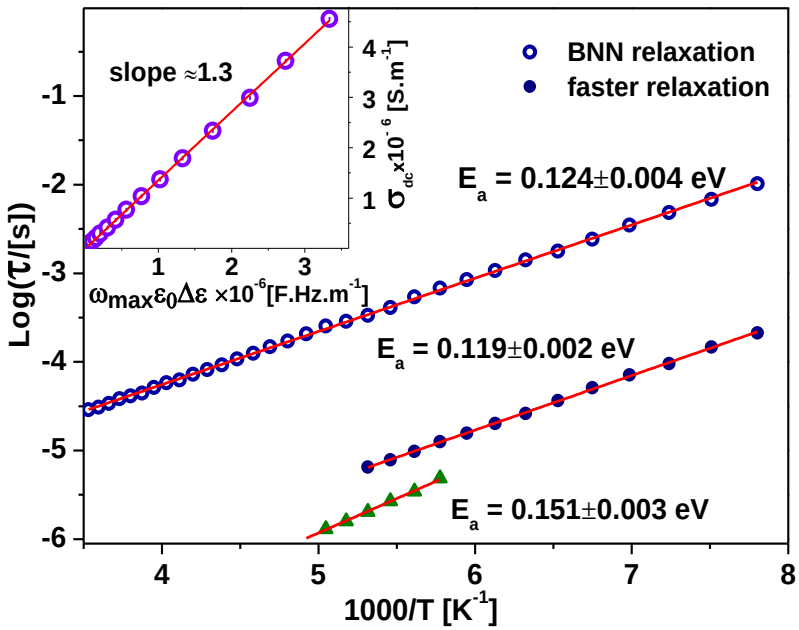


Figure 5.9: Arrhenius plot of the characteristic times τ of both dielectric loss features in $C_{60}Br_6$ (blue circles), and of the low-temperature dielectric loss of partially brominated $C_{60}$ (green triangles), all shown together with the corresponding Arrhenius fits (continuous lines). Inset: plot of $\sigma_{dc}$ *versus* the quantity $2\pi\varepsilon_0\Delta\varepsilon/\tau$ calculated for the most prominent dielectric loss in $C_{60}Br_6$. The continuous line is a linear fit to verify the validity of the BNN relation below 220 K (see the text).

Figure 5.9 shows the temperature dependence of the relaxation times τ of the two loss features in $C_{60}Br_6$. Both relaxations roughly follow an Arrhenius behavior, with similar slopes. The inset to Figure 5.9 is a linear plot, for temperatures below 220 K, of the dc conductivity $\sigma_{dc}$ as a function of the quantity $2\pi\varepsilon_0\Delta\varepsilon/\tau$ calculated for the slower and most prominent dielectric loss, *i.e.*, the one with longer relaxation times ($\Delta\varepsilon$ is the dielectric strength and τ is the relaxation time, see chapter 3 section 3.3). It is seen that both quantities are linearly correlated (with a slope close to unity, namely of 1.3) in the temperature range where the conductivity is electronic in

character (T < 220 K). This correlation, known as Barton-Nakajima-Namikawa (BNN) relation,[44] is typical of the conductivity-induced loss observed in many samples at the onset of the ac regime of the conductivity. This result shows that the most prominent (slower) component in the loss spectrum is indeed a conductivity-related loss associated with the hopping of polaronic species.[27] Above 220 K, the validity of the BNN relation breaks down, with the plot depicted in the inset to Figure 5.9 exhibiting a sublinear dependence. This is a consequence of the onset of the new conduction mechanism and the breakdown of the VRH model.

As to the origin of the faster relaxation feature, we carried out further experiments on a partially brominated $C_{60}$ sample, which also contained unreacted fullerite . The corresponding dielectric loss data are shown in Figure 5.10.

It may be seen that the loss spectra exhibit, besides a prominent loss feature (again likely due to a conductivity effect), a faster feature at lower temperature. The Arrhenius plot of the relaxation time of this feature is shown in Figure 5.10 together with those of the two relaxations in $C_{60}Br_6$. The activation energy and range of characteristic times of the faster relaxation match rather closely between both samples. The freezing temperatures of the two processes, defined as the temperature at which the corresponding relaxation time equals 100 seconds, were extrapolated assuming a perfect Arrhenius dependence and found to be equal to 70 and 61 K for $C_{60}Br_6$ and partially brominated $C_{60}$, respectively. These values represent lower limits for the actual freezing temperatures, as we cannot exclude a Vogel-Fulchert-Tamman temperature dependence of the relaxation features, especially close to their freezing point.

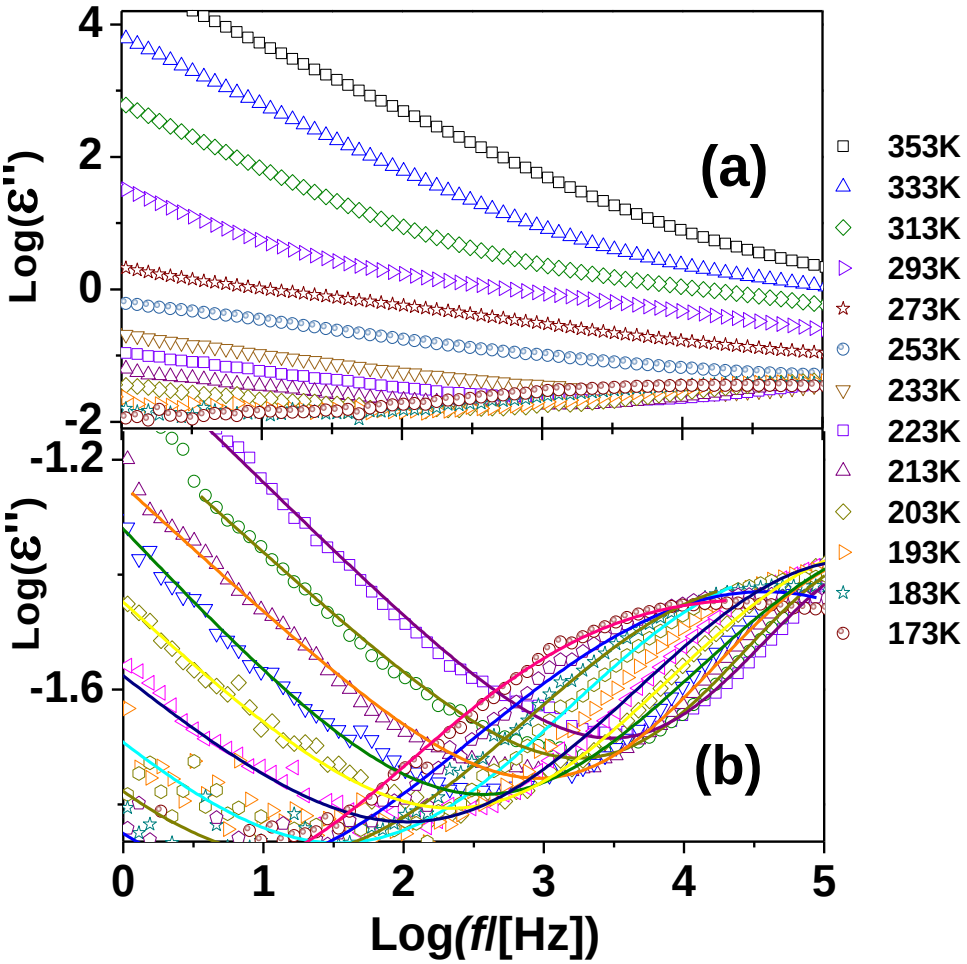


Figure 5.10: Dielectric loss ε" spectra of partially brominated $C_{60}$ between 353 and 173 K (*a*), and between 233 and 173 K (*b*). The continuous lines in panel (b) are fits.

It may therefore be concluded that the freezing temperature of the fast dynamic process in partially brominated $C_{60}$ is close to the glass transition temperature of pure $C_{60}$ (90 K)[11,12,13,14] or simple derivatives such as $C_{60}O$ (100 K) and $C_{61}H_2$ (130 K).[16] This suggests that this dynamic process is in fact associated with the glass transition of dipolar brominated species in partially brominated $C_{60}$, perhaps due to $C_{60}Br_6$ molecules in an amorphous arrangement or lower-stoichiometry halofullerene species such as $C_{60}Br_1$. The same relaxation appears to be present in the $C_{60}Br_6$ sample, where it could originate from the presence of labile $C_{60}Br_x$ molecular impurities with $x < 6$ or from less tightly bound $C_{60}Br_6$ moieties at defects

or grain boundaries. The lower visibility of the fast relaxation in $C_{60}Br_6$ could then be ascribed to the larger variety of local environments of labile species, leading to a wider distribution of relaxation times and thus to a flatter lineshape.

## 5.5 Conclusions

We have analyzed the conduction and dielectric properties of the fullerene derivative $C_{60}Br_6$ by means of temperature-dependent dielectric spectroscopy and the concomitant help of other techniques. Electrical conduction below 220 K is due to hopping processes of electronic charge carriers and it is well-described by Mott's variable-range hopping model, with effective hopping activation energy $E_a$ varying between 0.12 and 0.16 eV between 120 and 220 K, and most probable hopping range $R$ ranging between 100 and 125% of the decay length of the localized polaron's wavefunction. Above 215 K a new conduction mechanism, likely also electronic in character, sets in accompanied by a weak endothermic feature in the calorimetry thermogram, which might signal an orientational solid-solid transition. Two dielectric loss features are observed. The main loss is a conductivity-related loss associated with polaron hopping, as confirmed by the validity of the Barton-Nakajima-Namikawa condition. By means of comparison with an only partially brominated $C_{60}$ sample, the second loss feature is ascribed to the reorientational motions of labile dipolar $C_{60}Br_x$ moieties with $x \leq 6$. The temperature at which such motions freeze is found to be close to the glass transition temperature of pure $C_{60}$ and of simple derivatives such as $C_{60}O$.

# References


[1] Macovez, R.; Goldoni, A.; Petaccia, L.; Brühwiler, P.A.; Rudolf, P. Reversible Phase Transformation and Doubly Charged Anions at the Surface of Simple Cubic $RbC_{60}$. *Phys. Rev. Lett.* **2008**, 101, 236403.

[2] Mitsari, E.; Romanini, M.; Zachariah, M.; Macovez, R. Solid State Physicochemical Properties and Applications of Organic and Metallo-Organic Fullerene Derivatives. *Curr. Org. Chem.* **2016**, 20, 645-661.

[3] He, Z.; Zhong, C.; Su, S.; Xu, M.; Wu, H.; Cao, Y. Enhanced Power-Conversion Efficiency in Polymer Solar Cells Using an Inverted Device Structure. *Nat. Photonics* **2012**, 6, 591–595.

[4] Lai, Y.-Y.; Cheng, Y.-J.; Hsu, C.-S. Applications of Functional Fullerene Materials in Polymer Solar Cells. *Energy Environ. Sci.* **2014**, 7, 1866–1883.

[5] Anthopoulos, T.D.; Singh, B.; Marjanovic, N.; Sariciftci, N.S.; Ramil, A.M.; Sitter, H.; Cölle, M.; de Leeuw, D.M. High Performance N-channel Organic Field-Effect Transistors and Ring Oscillators based on $C_{60}$ Fullerene Films. *Appl. Phys. Lett.* **2006**, 89, 213504.

[6] Jones, B. A.; Facchetti, A.; Wasielewski, M. R.; Marks, T. J. Tuning Orbital Energetics in Arylene Diimide Semiconductors. Materials Design for Ambient Stability of N-Type Charge Transport. *J. Am. Chem. Soc.* **2007**, 129, 15259–15278.

[7] Usta, H.; Risko, C.; Wang, Z.; Huang, H.; Deliomeroglu, M. K.; Zhukovitskiy, A.; Facchetti, A.; Marks, T. J. Design, Synthesis, and Characterization of Ladder-Type Molecules and Polymers. Air-Stable, Solution-Processable N-Channel and Ambipolar Semiconductors for Thin-Film Transistors via Experiment and Theory. *J. Am. Chem. Soc.* **2009**, 131, 5586–5608.

[8] Brutting, W.; Adachi, Ch. (Ed.s). Physics of Organic Semiconductors, 2nd Ed. Wiley **2012.**

[9] Macovez, R.; Hunt, M. R. C.; Goldoni, A.; Pedio, M.; Rudolf, P. Surface Hubbard U of Alkali Fullerides. *J. Electron Spectr. Relat. Phenom.* **2011**, 183, 94–100.

[10] Gunnarsson, O. Superconductivity in Fullerides. *Rev. Mod. Phys.* **1997**, 69, 575-606.

[11] Tycko, R.; Dabbagh, G.; Fleming, R.M.; Haddon, R.C.; Makhija, A.V.; Zahurak, S.M. Molecular Dynamics and the Phase Transition in Solid $C_{60}$. *Phys. Rev. Lett.* **1991**, 67, 1886.

[12] David, W.I.F.; Ibberson, R.M.; Matthewman, J.C.; Prassides, K.; Dennis, T.J.; Hare, J.P.; Kroto, H.W.; Taylor, R.; Walton, D.R.M. Crystal Structure and Bonding of Ordered $C_{60}$. *Nature* **1991**, 353, 147–149.

[13] Gugenberger, F.; Heid, R.; Meingast, C.; Adelmann, P.; Braun, M.; Wühl, H.; Haluska, M.; Kuzmany, H. Glass Transition in Single-Crystal $C_{60}$ Studied by High-Resolution Dilatometry. *Phys. Rev. Lett.* **1992**, 69, 3774.

[14] Heiney, P.A.; Fischer, J. E.; McGhie, A.R.; Romanow, W.J.; Denenstein, A.M.; Jr. McCauley, J.P.; Smith, A.B.; Cox, D.E. Orientational Ordering Transition in Solid $C_{60}$. *Phys. Rev. Lett.* **1991**, 66, 2911.

[15] Lommen, A.N.; Heiney, P.A.; Vaughan, G.B.M.; Stephens, P.W.; Liu, D.; Li, D.; Smith, A.L.; McGhie, A.R.; Strongin, R.M.; Brard, L.; Smith III, A.B. Structure and Phase Transition of the 6,5-Annulene Isomer of $C_{61}H_2$. *Phys. Rev. B* **1994**, 49, 12572.

[16] Meingast, C.; Roth, G.; Pintschovius, L.; Michel, R.H.; Stoermer, C.; Kappes, M.M.; Heiney, P.A.; Brard, L.; Strongin, R.M.; Smith III, A.B. Structure, Dynamics, and

Phase Transitions in the Fullerene Derivatives $C_{60}O$ and $C_{61}H_2$. *Phys. Rev. B* **1996**, 54, 124.

[17] Stetzer, M.R.; Heiney, P.A.; Stephens, P.W.; Dinnebier, R. E.; Zhu, Q.; McGhie, A.R.; Strongin, R.M.; Brandt, B.M.; Smith III, A.B. Structure and Phase Transitions of the 6,6-Cyclopropane Isomer of $C_{61}H_2$. *Phys. Rev. B* **2000**, 62, 9305.

[18] Katz, E. A.; Faiman, D.; Iakoubovskii, K.; Isakina, A.; Yagotintsev, K. A.; Strzhemechny, M. A.; Balberg, I. Effect of the Disorder/Order Phase Transition on the Electrical and Photoelectrical Properties of $C_{60}$ Thin Films. *J. Appl. Phys.* **2003**, 93, 3401.

[19] Troshin, P. A.; Kemnitz, E.; Troyanov, S. I. Characterization of Reactions of Fullerene $C_{60}$ with Bromine. Crystal structures of Bromofullerenes $C_{60}Br_6$, $C_{60}Br_6 \bullet CS_2$, $C_{60}Br_8 \bullet CHBr_3 \bullet 2Br_2$, and $C_{60}Br_{24} \bullet C_6H_4Cl_2 \bullet Br_2$. *Russian Chemical Bulletin, International Edition* **2004**, 53, 2787 –2792.

[20] Havriliak S.; Negami, S. A complex Plane Analysis of α-Dispersions in Some Polymer Systems. *J. Polym. Sci.-Pt. C* **1966**, 16, 99−117.

[21] Havriliak S. and Negami, S. A complex Plane Representation of Dielectric and Mechanical Relaxation Processes in Some Polymers. *Polymer* **1967**, 8, 161−210.

[22] Birkett, P.R.; Hitchcock, P.B.; Kroto, H.W.; Taylor, R.; Walton, D.R.M. Preparation and characterization of $C_{60}Br_6$ and $C_{60}Br_8$. *Nature* **1992**, 357, 479-481.

[23] Birkett, P.R.; Crane, J.D.; Hitchcock, P.B.; Kroto, H.W.; Meidine, M.F.; Taylor, R.; Walton, D.R.M. The structural characterization of buckminsterfullerene compounds. *J. Mol. Struct.* **1993**, 292, 1-8.

[24] Macovez, R.; Mitsari, E.; Zachariah, M.; Romanini, M.; Zygouri, P.; Gournis, D.; Tamarit, J. Ll. Ultraslow Dynamics of Water in Organic Molecular Solids. *J. Phys. Chem. C* **2014**, 118, 4941−4950.

[25] Jonscher, A. K. The 'Universal' Dielectric Response. *Nature* **1977**, 267, 673-679.

[26] van Staveren, M. P. J.; Brom, H. B.; de Jongh, L. J. Metal-Cluster Compounds and Universal Features of the Hopping Conductivity of Solids. *Phys. Rep.* **1991**, 208, 1-96.

[27] Capaccioli, S.; Lucchesi, M.; Rolla, P. A.; Ruggeri, G. Dielectric Response Analysis of a Conducting Polymer Dominated by the Hopping Charge Transport. *J. Phys.: Condens. Matter.* **1998**, 10, 5595–5617.

[28] Lunkenheimer, P.; Lloid, A. Response of Disordered Matter to Electromagnetic Fields. *Phys. Rev. Lett.* **2003**, 91, 207601.

[29] Huijbregts, L. J.; Brom, H. B.; Brokken-Zijp, J. C. M.; Kemerink, M.; Chen, Z.; de Goeje, M. P.; Yuan, M.; Michels, M. A. J. The Optimal Structure-Conductivity Relation in Epoxy-Phthalocyanine Nanocomposites. *J. Phys. Chem. B* **2006,** 110, 23115-23122.

[30] Han, H.; Davis, C.; Nino, J.C. Variable Range Hopping Conduction in $BaTiO_3$ Ceramics Exhibiting Colossal Permittivity. *J. Phys. Chem. C* **2014**, 118, 9137−9142.

[31] Yamamoto K.; Namikawa, H. Conduction Current Relaxation of Inhomogeneous Conductor I. *Jpn. J. Appl. Phys. Part 1* **1988**, 27, 1845.

[32] Mott, N. F.; Davis, E. A. Electronic Processes in Noncrystalline Materials,Clarendon, Oxford, **1979**.

[33] Tran, T. B.; Beloborodov, I. S.; Lin, X. M.; Bigioni, T. P.; Vinokur, V. M.; Jaeger, H. M. Multiple Cotunneling in Large Quantum Dot Arrays. *Phys. Rev. Lett.* **2005**, 95, 076806.

[34] Yu, D.; Wang, C.; Wehrenberg, B. L.; Guyot-Sionnest, P. Variable Range Hopping Conduction in Semiconductor Nanocrystal Solids. *Phys. Rev. Lett.* **2004**, 92, 216802.

[35] Efros, A.L.; Shklovskii, B.I. Coulomb Gap and Low Temperature Conductivity of Disordered Systems. *J. Phys. C: Solid State Phys.* **1975**, 8, L49–L51.

[36] Shklovskii, B. I.; Efros, A. L. Electronic Properties of Doped Semiconductors. Springer: Berlin **1984**.

[37] Saito, S.; Oshiyama, A. Cohesive Mechanism and Energy Bands Of Solid $C_{60}$. *Phys. Rev. Lett.* **1991**, 66, 2637-2640.

[38] Margadonna, S.; Pontiroli, D.; Belli, M.; Shiroka, T.; Riccò, M.; Brunelli, M. $Li_4C_{60}$: A Polymeric Fulleride with a Two-Dimensional Architecture and Mixed Interfullerene Bonding Motifs. *J. Am. Chem. Soc.* **2004**, 126, 15032 –15033.

[39] Riccò, M.; Shiroka, T.; Belli, M.; Pontiroli, D.; Pagliari, M.; Ruani, G.; Palles, D.; Margadonna, S.; Tomaselli, M. Unusual Polymerization in the $Li_4C_{60}$ Fulleride. *Phys. Rev. B* **2005**, 72, 155437.

[40] Macovez, R..; Savage, R.; Venema, L.; Schiessling, J.; Kamaras, K.; Rudolf, P. Low Band Gap and Ionic Bonding with Charge Transfer Threshold in the Polymeric Lithium Fulleride $Li_4C_{60}$. *J. Chem. Phys. C* **2008**, 112, 2988–2996.

[41] Riccò, M.; Belli, M.; Mazzani, M.; Pontiroli, D.; Quintavalle, D., Janossy, A.; Csanyi, G. Superionic Conductivity in the $Li_4C_{60}$ Fulleride Polymer. *Phys. Rev. Lett.* **2009**, 102, 145901.

[42] Imre, A. W.; Schonhoff, M.; Cramer, C. Unconventional Scaling of Electrical Conductivity Spectra for PSS-PDADMAC Polyelectrolyte Complexes. *Phys. Rev. Lett.* **2009**, 102, 255901.

[43] Wübbenhorst, M.; van Turnhout, J. Analysis of Complex Dielectric Spectr. I. One-Dimensional Derivative Techniques and Three-Dimensional Modelling. *J. Non-Cryst. Solids* **2002**, 305, 40–49.

[44] Namikawa, H. Characterization of the Diffusion Process in Oxide Glasses Based on the Correlation between Electric Conduction and Dielectric Relaxation. *J. Non.Cryst. Solids* **1975**, 18, 173-195.

# Chapter 6

# Self-Diffusion and $Li^+$-Ion Conduction in Succinonitrile-Based Plastic-Crystal Electrolytes

## 6.1 Introduction

Organic plastic-crystalline ionic conductors have been the subject of intensive research due to their applications in power sources and other electrochemical devices such as fuel cells, batteries, supercapacitors, and solar cells.[1,2] Several organic plastic crystalline materials have excellent solvating properties, giving rise to high ionic conductivities in the solid state at ambient temperature.[3,4,5] In plastic crystals, the average centers of mass of the molecules occupy the sites of a crystalline lattice with translational symmetry, but the molecules themselves exhibit dynamic orientational disorder, undergoing on-site tumbling motions.[6,7] The term "plastic crystal" reflects the plasticity of most of these orientationally disordered phases, which arises from the presence of lattice defects near which the molecules exhibit also translational (diffusion) dynamics. Plastic crystals exhibit a

phenomenology similar to that of glass-forming materials, displaying in particular a continuous dramatic slow-down of collective rotational motions (the so-called α relaxation, see Chapter 2) upon cooling,[8] which in some cases even leads to a glass-like transition associated with the rotational freezing.[9] Plastic-crystalline ionic conductors are very interesting as electrolytes for electrochemical devices, because their mechanical flexibility reduces the problem of poor electrical contact with the electrodes caused by volume changes of solid electrolytes, while eliminating the leakage problems associated with liquid ones.[10,11]

The molecules of most plastic crystals have roughly globular shape and relatively weak mutual interactions, providing little hindrance for reorientational processes. The reorientations may generate a (transient) free volume within the lattice enabling ionic motion. In some molecular ionic conductors with orientational disorder, charge transport has been suggested to be boosted by the molecular reorientational dynamics, and several efforts have been directed in the past years to investigate a possible connection between molecular dynamics and ion transport.[5,12,13] In at least two cases ion conduction was found to be enhanced by the molecular dynamics: in the plastic-crystal phase of a phosphonium hexaphosphate by the rotational motion of the phosphonium ions,[14] and in lithium-salt doped polyethylene oxide by the segmental motions of the polymer chains.[15,16,17] In some organic plastic-crystalline electrolytes it has been proposed that the ionic motion may be boosted via a so-called "paddling wheel" (or "revolving door") mechanism.[13,18,19]

In this light, an important ionically conducting plastic crystal is succinonitrile ($N{\equiv}C{-}(CH_2)_2{-}C{\equiv}N$). The versatile physical properties of succinonitrile (SN) make it a suitable organic solid solvent for dissolution of a wide range of monovalent and higher-valence salts. The succinonitrile molecule forms a plastic-crystal phase that behaves as a solid ion or proton conductor in the presence of ionic impurities or when doped with acids or lithium salts, suggesting a possible application of this material as plastic electrolyte.[20,21,22,23] Even undoped, "pure" succinonitrile exhibits non negligible ionic conductivity, most likely due to small-ion impurities trapped in the proximity of the highly polar nitrile ($C{\equiv}N$) triple bonds. A lot of effort has been made to optimize the conductivity in succinonitrile by varying the type and quantity

of salts added and SN also was suggested to be used in composites with polymer electrolytes.[24,25] Since the plastic phase of succinonitrile melts already at 331 K while higher temperatures are generally needed for electrochemical applications, mixed polymer-succinonitrile electrolytes have been implemented to achieve higher mechanical stability and enhance the dc conductivity. Indeed, when mixed with polymers such as polyacrylonitrile or polyethylene terephthalate, Li-salt doped succinonitrile exhibits mobilities that are up to a factor of 50 higher with respect to that of pure succinonitrile.[1,16,26]

The plastic-crystalline phase of pure succinonitrile has body-centered cubic (*bcc*) structure of space group *Im3m*.[27,28] In this phase the succinonitrile molecules exist in three isomeric conformations, namely two *gauche* isomers of $C_2$ molecular symmetry and a less abundant *trans* isomer of $C_{2h}$ symmetry, which are interrelated by 120º-rotation about the central C–C bond.[23,27,29] The *trans* isomer has a quasi-linear centrosymmetric structure, while the *gauche* isomers display a twisted-U shape and differ between one another in their chirality. In the *bcc* cell there are two nonequivalent molecules, both with their C–C bond oriented along the diagonals of the cube.[26,29,30,31,32] At temperature lower than 233 K, a fully ordered monoclinic phase with all molecules in the *gauche* conformation becomes stable.[30,33,34]

The disorder in plastic succinonitrile is associated to *trans-gauche* isomeric fluctuations involving a rotation about the central C–C bond of the molecules and to molecular jumps from one diagonal position of the *bcc* cell to another.[23,32] This leads to a significantly lower density of the *bcc* plastic phase compared to the fully ordered monoclinic structure.[28] It has been proposed that the *trans* isomers act as 'impurities' that favor charge transport, creating vacancies that enhance molecular and small-ion diffusivity.[31] Similarly, the higher conductivity observed in succinonitrile-polymer mixtures was ascribed to the enhanced molecular dynamics of SN in the looser environment of the polymer matrix.[16] In spite of these suggestions and of the widespread belief that the orientational dynamic processes in plastic SN are beneficial to its high ionic mobility, however, the correlation between the molecular dynamics and the ionic mobility in succinonitrile systems is still controversial.[35,36]

To reach a fuller understanding of charge conduction and molecular dynamics in succinonitrile-based plastic materials, we have performed dielectric spectroscopy experiments[37] on pure and lithium-salt doped binary mixtures of succinonitrile with two other nitriles (glutaronitrile, acetonitrile) at high succinonitrile concentration. Together with calorimetry, we employ dielectric spectroscopy to study the dc conductivity, relaxation motions and phase behavior of the binary mixtures with the other nitrile species. Glutaronitrile ($N{\equiv}C{-}(CH_2)_3{-}C{\equiv}N$) is chemically very similar to succinonitrile (both are alkane-dinitriles), yielding a relatively good miscibility even in the solid state.[35,36] Moreover, the addition of glutaronitrile in sufficient amount effectively enlarges the temperature range in which the plastic phase can be supercooled and thus the available experimental range. On the other hand, acetonitrile ($N{\equiv}C{-}CH_3$) is a universal solvent, and mixing it with succinonitrile allows exploring the effect of the reduction of the density of nitrile groups.

## 6.2 Experimental Methods

Succinonitrile (SN, 99%), glutaronitrile (GN, 99%), acetonitrile (AN, 99.7%) and three lithium salts ($LiBF_4$ 98%, $LiCF_3SO_3$ 99.995% and $LiN(CF_3SO_2)_2$ (abbreviated as LiTFSI, from "lithium *bis*-trifluoromethanesulphonimide") 99.95%) (Sigma Aldrich; the percentage in parenthesis is the molar purity) were weighted and mixed in the correct proportions to obtain the desired stoichiometries (Figure 6.1). The undoped mixtures were obtained by dissolving the succinonitrile powder in liquid glutaronitrile or acetonitrile. A small amount of a lithium salt, preheated to 400 K to avoid the presence of water, was added in some cases. Sonication at 330 K (above the melting point of the mixtures) was used to favor homogeneous mixing prior to calorimetric and dielectric measurements. To check for the influence of GN on the relaxation dynamics and ionic conductivity, we investigated $SN_{1-x}GN_x$ samples at different GN molar contents (x = 0, 0.07, 0.11, 0.13). Differential-scanning calorimetry measurements were carried out in an open vessel between 200 K and 350 K at a rate of 5 K $min^{-1}$, using a Q100 calorimeter from TA-Instruments.

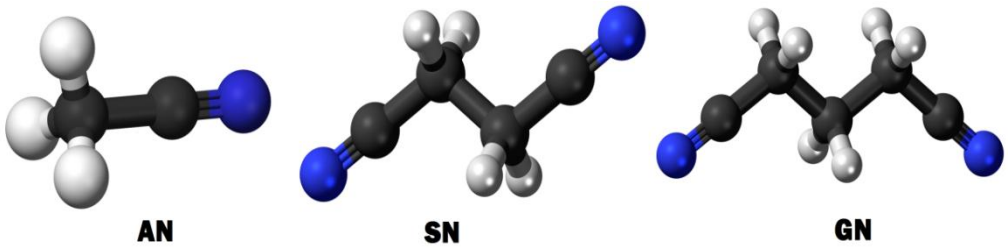


Figure 6.1: Molecular structure of acetonitrile, glutaronitrile and succinonitrile.

For dielectric measurements, carried out in the frequency ($f$) range from $10^{-2}$ to $10^{9}$ Hz, the sample was placed in liquid form inside a home-made stainless steel capacitor specially designed for liquid samples, and loaded inside a nitrogen-gas flow cryostat to achieve sample temperature control. Isothermal frequency scans were acquired in the range between 350 and 130 K (with a stability of ±0.3 K) upon cooling from the liquid phase to ensure the maximum sample homogeneity. The isothermal dielectric spectra are complex functions of frequency displayed in several representations, as complex permittivity ε (consisting of the dielectric function ε'($f$) and the loss spectrum ε"($f$)), as complex conductivity $\sigma = i\,2\pi f\,\varepsilon_0\,\varepsilon$ (of which the real part σ'($f$),) or as modulus M = 1/ε (of which the imaginary part M"($f$) contains information on both dielectric and conductivity loss processes). The studied samples exhibited several dipolar dynamic processes, which gave rise to broad features in the loss spectra ε"($f$).

## 6.3 Thermodynamic Characterization

Figure 6.2 shows the phase diagram of the mixture of SN and GN as determined by the DSC measurements by the group of P. Lunkenheimer and coworkers (Ref. 35). For GN concentrations less than 10%, a plastic phase appears, which cannot however be supercooled and always transforms (at least partially) into the fully ordered low-temperature phase of SN. Between 15% and 95% of GN concentrations, supercooling of plastic phase is possible, leading to an orienational glass state. The pure GN ($x$=100%) has only one (perfectly crystalline) solid phase

below its melting point at 244 K, in which both its *trans* and *gauche* conformations are present and the sample is translationally and orientationally ordered (pure GN does not form any plastic crystalline phase). The phase diagram of Figure 6.2 shows that, while the plastic phase of pure SN crystallizes at 233 K, the addition of GN in sufficient amount suppresses the transition to the fully ordered monoclinic phase, thus effectively enlarging the temperature range in which the plastic phase can be experimentally observed.

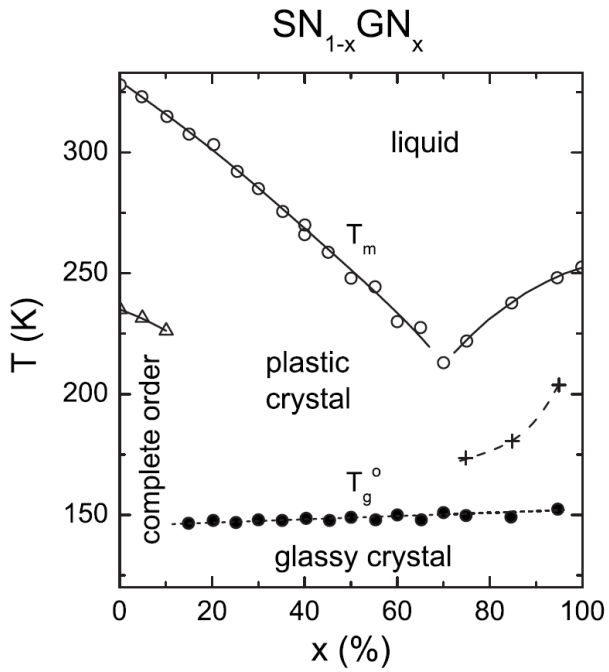


Figure 6.2: Phase diagram of the system $SN_{1-x}GN_x$ as determined from DSC measurements under heating.[35] The open and closed circles denote the melting and the orientational-glass transition temperatures, respectively. The triangles indicate the transitions from the completely ordered (i.e., both translationally and orientationally) to the plastic-crystalline state. The crosses correspond to the occurrence of complete order under heating occurring at high *x* values.

Figure 6.3 shows the DSC curves of the $SN_{0.93}GN_{0.07}$ and $SN_{0.85}GN_{0.15}$ mixtures acquired upon heating from low temperature after cooling the homogeneous liquid phases. Both thermograms display, besides an endothermic feature above room

temperature, also a weaker endothermic feature well below it. This entails that the transition between the liquid and the plastic phase does not occur at once; rather, solidification starts slightly above room temperature and is only complete below 273 K. These line shapes are typical of the eutectic equilibrium of binary mixtures, where liquid-to-solid transitions normally occur in two steps: upon cooling, nucleation of the solid phase takes place across the higher-temperature endothermic peak, followed by a temperature interval in which the sample coexists in a liquid and solid phase; solidification is only completed in correspondence with the second peak at lower temperature. The same behavior was reported in SN doped with lithium salts.[20]

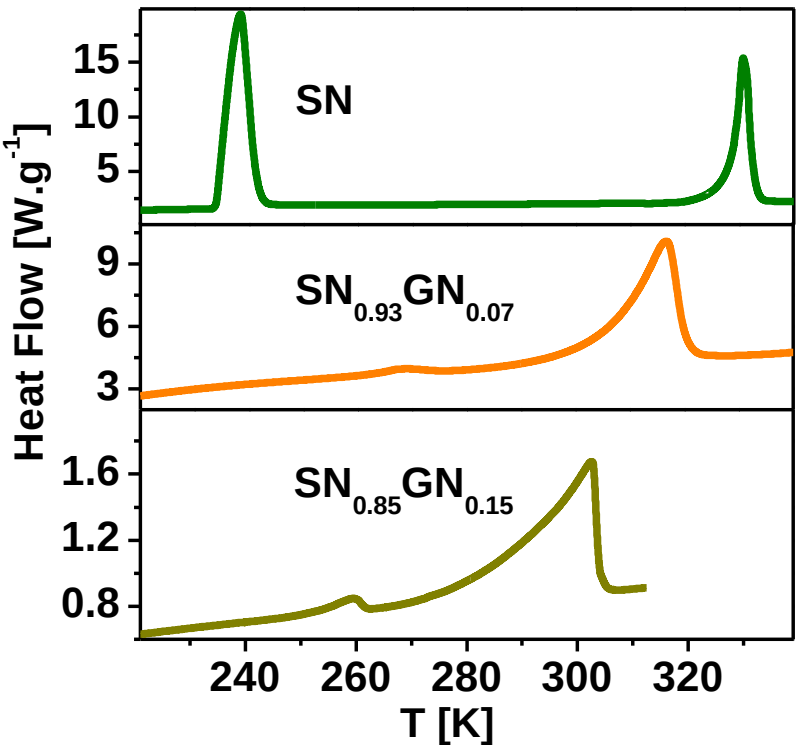


Figure 6.3: DSC thermograms of pure SN, $SN_{0.93}GN_{0.07}$ and $SN_{0.85}GN_{0.15}$, acquired upon heating.

It may be observed from Figure 6.3 that, with respect to pure SN, the onset of solidification is shifted to lower temperature the higher the GN doping level, as

expected and in agreement with previous studies.[35,36] moreover, the width and asymmetry of the higher-temperature DSC feature increase with increasing GN content. In the temperature interval between the two DSC peaks of Figure 6.3 the sample is in a mixed phase (liquid plus plastic-crystal, each in a different amount and with distinct GN stoichiometry). This entails in particular that SN mixtures are partially liquid at room temperature, a fact that prevents their application as solid-state ion electrolytes.

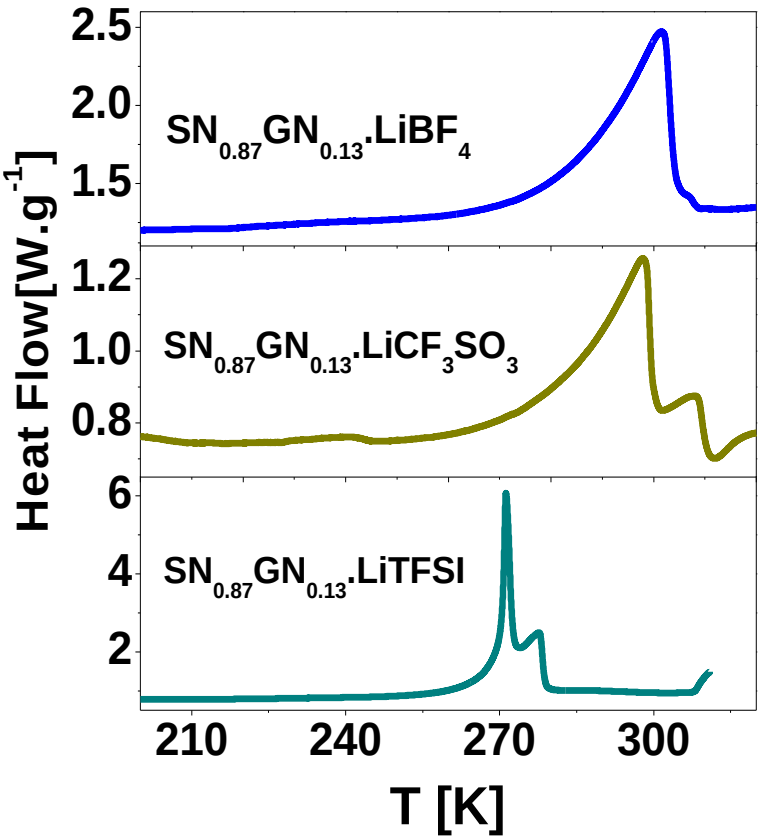


Figure 6.4: DSC thermograms of $SN_{0.87}$ $GN_{0.13}$ doped with three distinct lithium salts acquired upon heating.

Figure 6.4 shows the DSC heat flow of SN-GN sample doped with three lithium salts as measured under heating from the low temperature after cooling the liquid phases. It is clear from the thermograms that the plastic phase of all three doped

samples can be supercooled to below 233 K. For the $LiBF_4$ doped SN-GN mixture, the main endothermic peak at about 300 K indicates the melting of the plastic-crystalline phase into the liquid. This endothermic peak shifted slightly to lower temperatures in the SN-GN mixture doped with $LiCF_3SO_3$. It may be seen that in the $LiCF_3SO_3$ doped sample, the melting of the plastic crystal phase takes place in several steps, as visible by the presence of smaller peaks around the main endothermic peak. This strongly suggests the occurrence of mixed phases. In the case of the sample doped with $LiN(CF_3SO_2)_2$, the stability of the liquid phase is extended to lower temperature, and the melting of the plastic crystalline phase takes place well below room temperature, around 270 K. Also in this case the transition temperature is not unique, indicating phase segregation in the sample. In view of the above results, we have mainly focused our study on pure and $LiBF_4$ doped mixtures.

## 6.4 BDS Results and Discussion

Figure 6.5 shows the dielectric function $\varepsilon'(f)$, dielectric loss $\varepsilon''(f)$, ac conductivity $\sigma'(f)$ and imaginary modulus spectra $M''(f)$ of the plastic phase of the $SN_{0.87}$ $GN_{0.13}$ mixture between 140 and 250 K. Similar results were obtained also at other GN stoichiometries, and also in the plastic-crystal phase of pure SN and of SN-AN mixtures, albeit in a smaller temperature range than that of Figure 6.5 since SN and SN-AN mixtures crystallized between 220 and 230 K upon cooling. At temperatures above 300 K (not shown) the spectra exhibited a clear change of line shape signaling the transition from the plastic crystal to the liquid. This confirms that the data shown in Figure 6.5 are relative to the plastic phase and not to a possible supercooled liquid phase.[35,36] Analogous liquid-to-plastic transitions were observed in pure SN and in SN-AN mixtures, as also discussed in the following.

The dielectric function (Figure 6.5(*a*)) exhibits a plateau at low frequency, corresponding to the static relative permittivity $\varepsilon_s$ of the sample. This is followed at higher frequency by a drop in the value of $\varepsilon'$, which takes place at the characteristic frequency ($f_\alpha$) of the collective reorientational motion of the molecular dipoles. Above $f_\alpha$, the dipolar nitrile molecules are no longer able to follow the applied field,

so that the molecular reorientational motion no longer contributes to the dielectric permittivity. The loss spectra (Figure 6.5(*b*)) exhibit at lowest frequency a background proportional to inverse frequency (not shown), which stems from the dc conductivity of the sample, followed by a prominent loss feature peaked at $f_\alpha$. This loss feature (α relaxation) is the spectral signature of the collective orientational motions of the molecules, and its frequency position $f_\alpha$, called α-relaxation frequency, coincides with the step-like decrease in ε'(*f*) (as expected from the Kramers-Kronig causality relations).[37] As visible in both panels of Figure 6.5(*a*) and Figure 6.5(*b*), $f_\alpha$ shifts to smaller values as the temperature is decreased, as expected since a lower thermal energy entails slower molecular dynamics. In SN-GN plastic co-crystals, the main loss (α peak) is observed at roughly the same frequency position independent of the stoichiometry.[35,36] It may be observed from Figure 6.5(*b*) that the α process reaches a frequency of $10^{-2}$ Hz at around 143 K, which corresponds to the glassy transition temperature measured by calorimetry (between 143 and 150 K depending on the stoichiometry). At the same time, the width of the α relaxation feature increases upon cooling, indicating a wider distribution of relaxation times which reflects the higher cooperativity of this dynamic process at low temperature.

Dielectric spectroscopy is only sensitive to the change in the dipole moment of the sample, hence to changes of the molecular orientation (rotations or rototranslations). Although (as mentioned in Section 6.1) in plastic crystalline phases there is in general a contribution to the molecular dynamics from rototranslational processes due to a minority of molecules diffusing through or near lattice defects,[38,39] the α relaxation feature stems mainly from pure-rotation motion of the majority molecules at a fixed position in the *bcc* lattice.

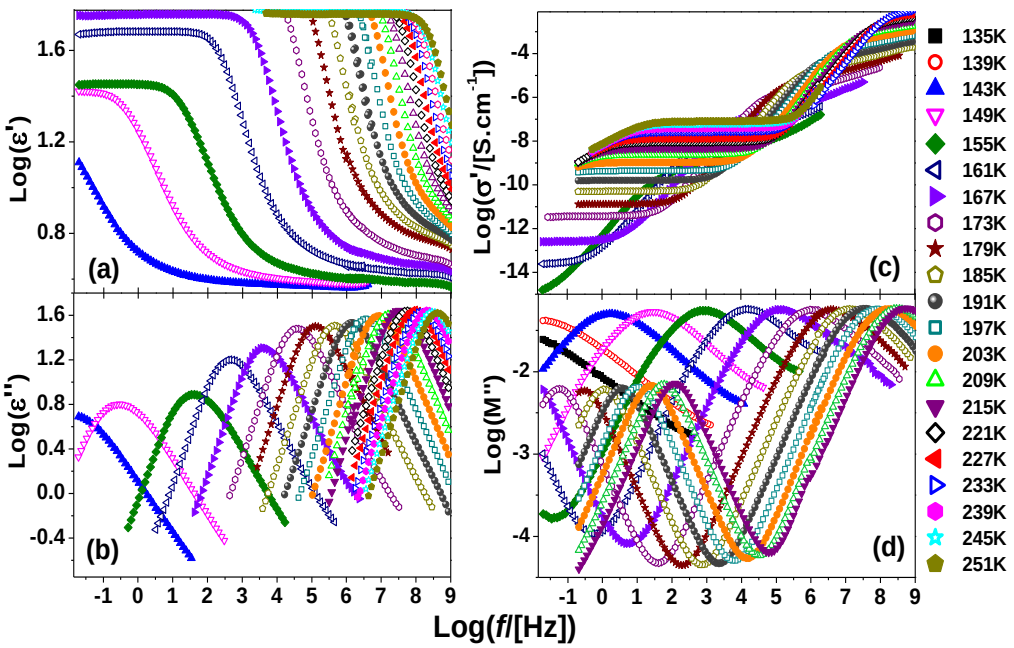


Figure 6.5 Log-log plot of the spectra of the dielectric function ε'(*f*) (*a*), dielectric loss ε"(*f*) (*b*), ac conductivity σ'(*f*) (*c*) and modulus M"(*f*) (*d*) spectra of the plastic-crystal phase of $SN_{0.87}GN_{0.13}$, at the indicated temperatures.

The ac conductivity spectra (Figure 6.5(*c*)) are characterized by a horizontal plateau at intermediate or low frequencies, corresponding to the dc conductivity regime. Especially at high temperature, the spectra exhibit a decrease of conductivity (spectral bending) at the lowest frequencies which is due to the accumulation of ions at the electrode-sample interface (electrode polarization effect). At high frequency, the σ' spectra exhibit a bump-like feature in correspondence with the α relaxation (as expected because $\sigma' = 2\pi f\ \varepsilon_0\varepsilon''$). Finally, Figure 6.5(*d*) displays the modulus spectra M"(*f*). These are characterized by two peaks of quite different shape and intensity, a more intense peak at high frequency, corresponding to the dielectric α relaxation loss, and a weaker one at low frequency, referred to as conductivity peak. It may be observed that the conductivity peak in the modulus representation is centered at a frequency $f_\sigma$ which lies approximately in the middle of the plateau corresponding to the dc conductivity in the σ' spectra.

From dielectric data such as those presented in Figure 6.5 one may obtain, for each measurement temperature, the value of the static permittivity, the dc conductivity $\sigma_{dc}$, the characteristic frequency $f_\alpha$ of the collective α process, and the characteristic frequency $f_\sigma$ of the conductivity loss (lower-frequency modulus peak). In order to obtain $f_\alpha$ and $f_\sigma$, the α feature in the dielectric loss spectra Figure 6.5(*b*) and the conductivity peak in the modulus spectra Figure 6.5(*d*) were fitted assuming a Havriliak-Negami profile (see chapter 3 section 3.3.1). The value of $\sigma_{dc}$ was taken to be value of the ac conductivity spectra σ'(*f*) (panel *b*) in the middle of the plateau.

## 6.5 Relaxation Dynamics and Dc Conductivity in Undoped Plastic Co-crystals

Figure 6.6 shows the Arrhenius plots of $f_\alpha$ and $\sigma_{dc}$ obtained for the plastic phases of pure SN and of two mixtures, respectively with GN and AN. The pure SN and $SN_{0.92}$ $AN_{0.08}$ samples display a phase transition to a (fully-ordered) crystalline phase below approximately 230 K. This is visible by the sudden decrease of the dc conductivity around this temperature (Figure 6.6(*b*)), and by the fact that only the SN-GN mixture displays a relaxation frequency down to low *T* (Figure 6.6(*a*)). In the case of pure SN, the conductivity drops by almost three orders of magnitude in the fully-ordered phase compared to its value in the plastic phase. Such conductivity drop is expected because the ionic mobility is lower in the perfectly ordered crystal phase than in the plastic one, due both to the higher density of the former and the beneficial effect of molecular rotations in the latter. For $SN_{0.92}$ $AN_{0.08}$ the drop in $\sigma_{dc}$ is only of one decade, possibly due to an only partial crystallization or to the increased disorder of the crystal phase due to the different size and end-groups of SN and AN moieties. It may be observed from Figure 6.6(*a*,*b*) that a partial crystallization (accompanied by phase separation) is taking place, albeit at lower temperature (for $T < 170$ K), also in $SN_{0.87}$ $GN_{0.13}$, where it is visible as a decrease of the static permittivity $\varepsilon_s$ and of the dielectric strength of the α relaxation at and below 170 K.

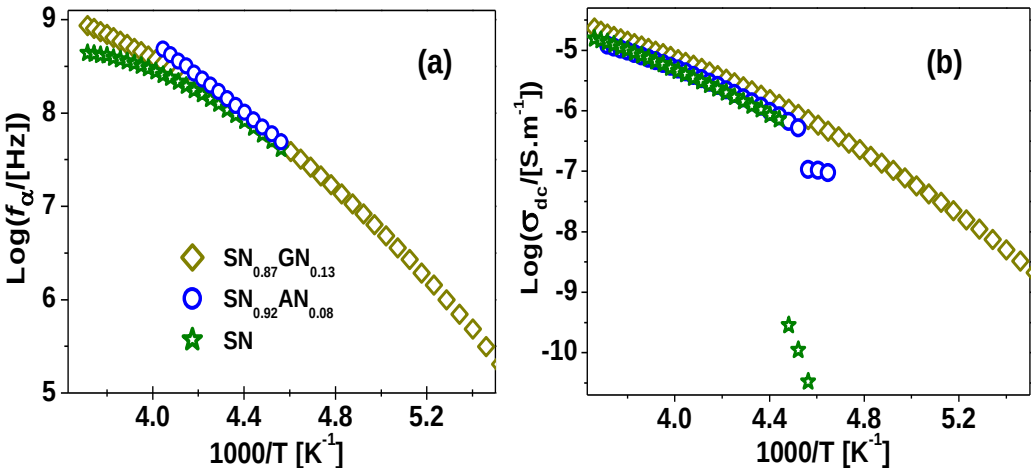


Figure 6.6: Semilogarithmic plot of $f_\alpha$ (*a*) and of $\sigma_{dc}$ (*b*) *vs* 1000/*T*, for pure SN and for the $SN_{0.87}GN_{0.13}$ and $SN_{0.92}AN_{0.08}$ plastic cocrystals.

It is worth noticing that the value of the dc conductivity in the plastic-crystal phase of pure SN and of the binary mixtures is remarkably high, considering that all nitrile molecules are neutral closed-shell molecules, so that no intrinsic electronic or ionic conduction is expected to take place. The negative curvature in the Arrhenius plot of $\sigma_{dc}$ is characteristic of ionic conduction in disordered systems,[35] while electronic conduction leads to a positive curvature. The relatively high conductivity value in succinonitrile systems is therefore indicative of a relatively high mobility of ionic impurities in the system. Such ionic impurities may be due to the presence of small-ion contaminants, or else to charged molecular species. With respect to pure SN and to the mixtures of SN with AN, the SN-GN system displays yet higher conductivity (by a factor between 2 and 3 depending on the concentration, as visible in Figure 6.6(*b*)).

It may be observed from Figure 6.6(*a*) that the α relaxation frequency of the SN-GN mixtures at a given (high) temperature is virtually identical to those of pure SN. This is consistent with the fact that the glass transition temperature of SN-GN mixtures is almost constant regardless of the stoichiometry,[35] indicating that the molecular dynamics in the presence of GN is identical (or only slightly slower than) that in pure SN. Also the SN-AN mixture displays similar collective dynamics, as

visible in Figure 6.6(*a*). Concerning the temperature dependence of the molecular dynamics and of the conductivity, in all plastic-crystal phases it is observed that neither the logarithm of the maximum loss frequency nor that of the dc conductivity follow a linear scaling with the inverse temperature (simply-activated Arrhenius behavior); instead, both quantities display a more pronounced temperature dependence, giving rise to a curved line shape, as mentioned above for the dc conductivity. A non-Arrhenius behavior of the relaxation frequency is rather common feature in glass forming materials and plastic phases,[40,41] and it is consistent with recent studies on the SN-GN binary system,[35,36] where it was shown that the temperature dependence of $f_\alpha$ (a) and $\sigma_{dc}$ can be described by the so called Vogel-Fulcher-Tammann (VFT) equation,[37] a phenomenological modification of the Arrhenius law which will be discussed later.

### 6.5.1 Walden Rule and Stokes-Einstein Relation in Undoped Plastic Co-crystals

Diffusion processes are responsible for many properties such as viscosity, plasticity, or heat and charge transport. In liquids, the diffusion of the constituent molecules accounts for the fluidity and viscosity of the medium, while diffusion of dissolved charged species results in electrical conductivity.

In liquids, the dipolar relaxation frequency $f_\alpha$ corresponds to the characteristic frequency at which (rototranslational) molecular diffusion takes place, and it is directly proportional to the viscosity $\eta$ of the medium. If (some of) the molecular species in the liquid carry a net charge, then molecular diffusion also results in charge transport. The empirical Walden rule states that the product of the limiting molar conductivity and the solvent's viscosity $\eta$ (or equivalently the diffusional $f_\alpha$) is constant for diluted electrolyte solutions, so that a slope of one is obtained in the Walden plot. The Walden rule, fulfilled in ideal electrolyte solutions, is essentially a consequence of the Stokes-Einstein relation[42], according to which two diffusion processes are mutually coupled because the motion of bulky ions in a viscous liquid is limited by the viscosity of the medium, so that $\frac{D}{k_B T\,\eta} \simeq const$, where $k_B T$ is the

thermal energy, $D$ is the diffusivity of the (charged) species, proportional to the conductivity $\sigma_{dc}$, and $\eta$ is the viscosity (proportional to the characteristic diffusion frequency). This relation is valid for solutions of large, weakly coordinating ions in solvents with nonspecific ion-solvent interactions.[43]

Also in the solid state the diffusion of ions gives rise to charge transport, but since usually the concepts of viscosity and of molecular diffusion are not useful to describe crystalline solids, no equivalent of the Stokes-Einstein or Walden relations exist. The validity of the Walden rule was only reported in disordered condensed systems such as glass-forming supercooled liquids or polymers.[15]

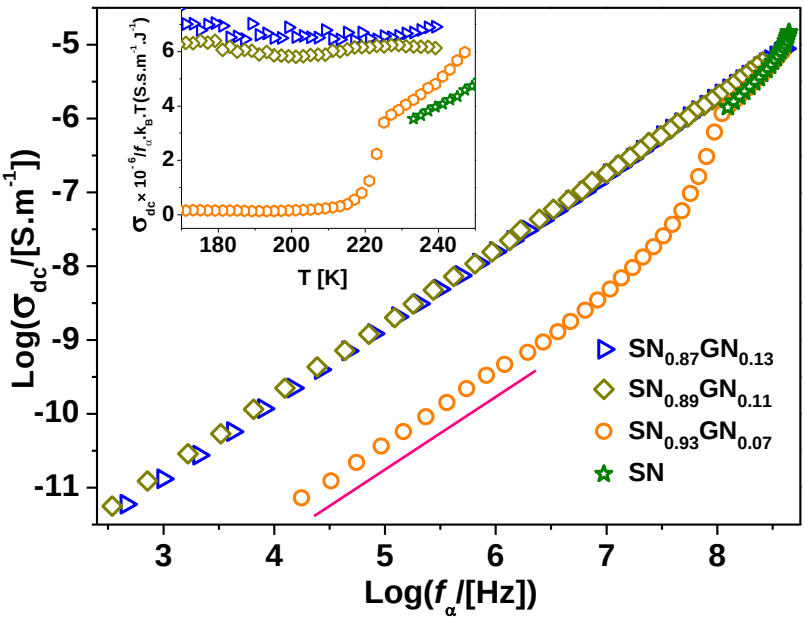


Figure 6.7: Walden plots of Log ($\sigma_{dc}$) vs Log($f_\alpha$) of $SN_{1-x}GN_x$ samples at different GN content ($x$ = 0, 0.07, 0.11, 0.13). The continuous line has slope equal to 1 (Walden rule). Inset: Plot of $\sigma_{dc} / (f_\alpha \cdot k_B T)$ versus temperature for the same sample to verify the validity of the Stokes-Einstein relation.

Figure 6.7 shows the plot of Log($\sigma_{dc}$) *vs* Log($f_\alpha$) for a series of $SN_{1-x}GN_x$ samples ($x$ = 0.07, 0.11, 0.13) and for pure SN. Since in a liquid $f_\alpha$ correlates with the viscosity, the plot of Figure 6.7 is analogous to the Walden plot for liquid

electrolytes. It is observed that, at least at low temperatures, the plot of all SN-GN plastic co-crystals exhibit a slope close to one, *i.e.*, they follow the Walden rule characteristic of ideal electrolyte solutions. The connection between ion diffusion and molecular reorientations in plastic SN can be best corroborated by looking at the behavior of the quantity $\sigma_{dc}/ (k_B T.f_\alpha)$, defined in analogy to the Stokes-Einstein relation, and shown as a function of $T$ in the inset to Figure 6.7. It may be observed that the numerical value of $\sigma_{dc} / (k_B T.f_\alpha)$ is basically constant in the whole accessible temperature range. This observation of a direct correspondence between the conductivity and the relaxation frequency in a linear plot provides definitive proof of a perfect correlation between molecular reorientations and ionic conductivity in plastic SN. The validity of the Walden rule observed in the main panel of Figure 6.7 can be thought of as a consequence for the SN-GN co-crystal of the validity of the linear relation $\sigma_{dc} / (k_B T.f_\alpha) = const$ : as both $\sigma_{dc}/T$ and $f_\alpha$ depend exponentially on the temperature (with at most a weakly temperature-dependent prefactor), $\log(\sigma_{dc}/T)$ and $\log(f_\alpha)$ exhibit an almost perfect linear correlation. The analogy with the Stokes-Einstein relation is what has motivated our choice of the vertical axis in the inset to Figure 6.7.

The validity in a plastic crystal of relations that are equivalent to the Stokes-Einstein and Walden rules is surprising, given that it is not expected that the concept of viscosity against ion diffusion applies to a crystalline solid (although plastic crystals do display self-diffusion), nor that such viscosity should be correlated with on site motions in the lattice. Besides in ordinary solutions and supercooled liquid phases far enough from the glass transition, the validity of the Walden rule has been reported only in a disordered polymer; to the best of our knowledge, plastic-crystalline SN is the only ordered solid phase where such a connection has been ever reported, while other plastic crystals (and more generally orientationally disordered solids) show in general a decoupling of charge carrier diffusion and orientational dynamics.

As mentioned above, all studied $SN_{1-x}GN_x$ samples fulfill the Stokes-Einstein relation (at least at low temperature), which suggests a perfect correlation between molecular reorientations and ionic conductivity in the SN-GN co-crystals.

In the case of the $SN_{0.93}$ $GN_{0.07}$ sample, $\sigma_{dc}$ exhibits a kink at approximately the crystallization temperature of pure SN (233 K). The presence of a kink and the simultaneous observation of relaxation dynamics below this temperature are clear indications that the $SN_{0.93}$ $GN_{0.07}$ sample undergoes partial crystallization, *i.e.*, de-mixing into quasi-pure SN crystallites and plastic domains richer in GN, which display collective relaxation dynamics also below 233 K. For this sample, the Stokes-Einstein and Walden relations appear to be valid only at low temperature, where the GN concentration in the plastic domains is higher. Instead, both pure SN and the homogeneous $SN_{0.93}$ $GN_{0.07}$ sample above 233 K do not seem to follow a Walden behavior, although it should be noted that the temperature range available for the investigation of pure SN by conventional dielectric spectroscopy is quite limited.

Some authors have pointed out that the modulus representation M"($f$) is better suited than the ac conductivity to extract information on the microscopic (local) properties of ion transport.[44,45] Figure 6.8 and its inset represent the Walden plot and the Stokes-Einstein plot obtained for the same samples but using $f_\sigma$ instead of $\sigma_{dc}$. It is observed in the main panel that the Walden plot anomaly near the SN crystallization temperature is much less pronounced in the logarithmic plot of $f_\sigma$ *vs* $f_\alpha$, leading to an overlap of all Walden plots. This indicates that the microscopic (molecular) diffusion processes are not significantly affected by the partial crystallization. It may be seen in the inset that the ratio $f_\sigma$ / ($f_\alpha \cdot k_B T$) is independent of temperature in all cases, and moreover that it has approximately the same value for all GN stoichiometries. This confirms once more the validity of the Stokes-Einstein relation for these plastic crystals and thus that the microscopic diffusion of ionic species is perfectly correlated with the on-site molecular rotations.

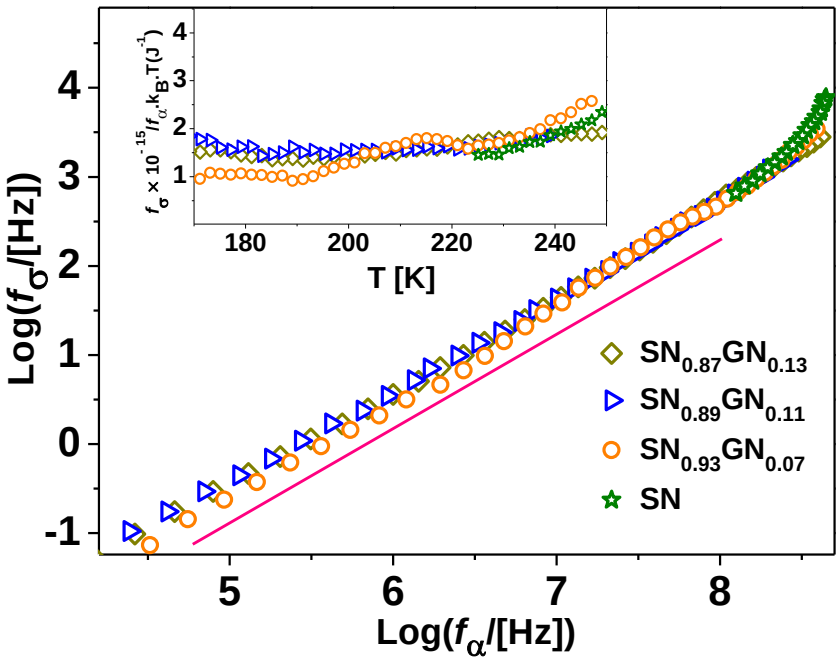


Figure 6.8: Walden plots of Log($f_\sigma$) *vs* Log($f_\alpha$) of $SN_{1-x}GN_x$ samples at different GN content ($x$ = 0, 0.07, 0.11, 0.13). The continuous line has slope equal to 1 (Walden rule). Inset: Plot of $f_\sigma$ / ($f_\alpha \cdot k_B T$) versus temperature for the same sample to verify the validity of the Stokes-Einstein relation.

The validity in a plastic crystal of the Stokes-Einstein rule involving molecular rotations is surprising, given that translational and rotational degrees of freedom are in general independent from one another. We argue that there are only two possible conduction mechanisms that may rationalize the results presented in Figures 6.7 and 6.8. The first one is the incoherent hopping between adjacent molecules of protons, small ions or other moieties able to form ionic complexes with the nitrile species. In such case, charge transport would be necessarily correlated with molecular reorientations: the sequential "hopping" (say, of a proton) in a given direction can only occur if between two consecutive hops the molecule on whose nitrile group the proton is sitting rotates, thereby swinging the proton from one side of the molecule to the other. In this scenario, charge hopping is effectively limited by the on-site molecular rotational dynamics.

Another, more likely explanation is if charge transport is due to the self-diffusion of a fraction of ionic nitriles, then a correlation between $\sigma_{dc}$ and $f_{\alpha}$ may result from the similarity of rotational and diffusional timescales reported in the SN-GN binary system at high GN content.[35] For example, pairs of oppositely charged molecular ions could be formed by loss of a molecular hydrogen via protonation of a nitrile group (although the equilibrium constant for such process is relatively low [20]), or more likely ionic species formed by trapping of a small-ion host at or near the highly polar nitrile (C≡N) group. Ionic nitrile species could also form by reaction with water molecules present as impurities. On the other hand, the simple scenario of small-ion drift through the intermolecular voids would not lead to the validity of the Stokes-Einstein relation, as it will be shown in the case of $Li^+$ ions in Section 6.6.

Although a perfect connection between the translational diffusion and the on-site orientational motion may at first be surprising, it is actually confirmed in studies of materials which can display at a given temperature either a plastic crystalline state or a supercooled liquid phase depending on the thermal history such as ethanol or glutaronitrile.[6,36] It has been shown in these systems that, quite unexpectedly, the rototranslational frequency in the supercooled liquid is at all temperatures very close to that of reorientational motions in the plastic crystal phase. In this sense, the results of this chapter are therefore a further, direct confirmation of the idea that the dynamics of glass-forming systems is fundamentally determined by rotational motions.[36,46,47] In detail, our findings imply that the correspondence of $\sigma_{dc}$ and $f_{\alpha}$ originates because both quantities are fundamentally linked to the diffusion of molecular species through lattice defects, which can be thought to be limited by an effective "diffusional" viscosity $\eta_{diff}$ that acts against the rototranslational diffusion of molecules between empty sites in the crystalline lattice.

The dc conductivity is the product of the charge density (proportional to the number density of charged species $n$) and the ion mobility $\mu$. Assuming singly ionized (monovalent) molecules and similar mobilities of both positive and negative molecular ions (or else a single dominant type of carrier), the dc conductivity can be written as $\sigma_{dc} = ne\mu$ where $e$ is the elementary charge. The molecular mobility can be estimated from the coefficient of self-diffusion $D$ by means of the Einstein

relation $D = \mu k_B T/e$. For pure SN, taking the value of $\sigma_{dc} \simeq 4 \cdot 10^{-5}$ S/m observed in Figure 6.6(*b)* at room temperature (298 K) and the diffusivity of $D = 1.3 \cdot 10^{-10}$ $m^2/s$ obtained by NMR pulsed field gradient diffusion experiments in Ref.48, the molecular ion density is found to be $n \sim 5 \cdot 10^{22}$ $m^{-3}$. Since the total number density of molecules in pure SN is [28] $7.867 \cdot 10^{27}$ $m^{-3}$, this entails that of the order of one molecule every $10^5$ in pure SN is charged (ionic) and mobile. If the observation of very similar relaxation frequency may be taken as indication that the diffusivity is the same in all samples, then the higher value of $\sigma_{dc}$ in SN-GN plastic crystals entails that the fraction of ionic and mobile molecules is higher in the SN-GN mixture by a factor equal to the ratio of the respective dc conductivities, i.e. at least by a factor of 2. Another possibility is that the self-diffusion rate is higher in the SN-GN mixture due to a less compact *bcc* arrangement. It should be recalled from Section 6.1 that an earlier study suggested that the *trans* succinonitrile isomers in pure SN act as "impurities" facilitating self-diffusion and ion conduction; the same might be true for GN moieties present in mixtures with low GN concentration.

### 6.5.2 Space-Charge Relaxation in Undoped Co-crystals

The data reported in Figures 6.7 and 6.8 show that all SN-GN mixtures at low GN content obey the Walden and Stokes-Einstein rules. The fact that these relations are not fulfilled in samples with high GN content [35] might be due to partial demixing, as discussed in this Section.

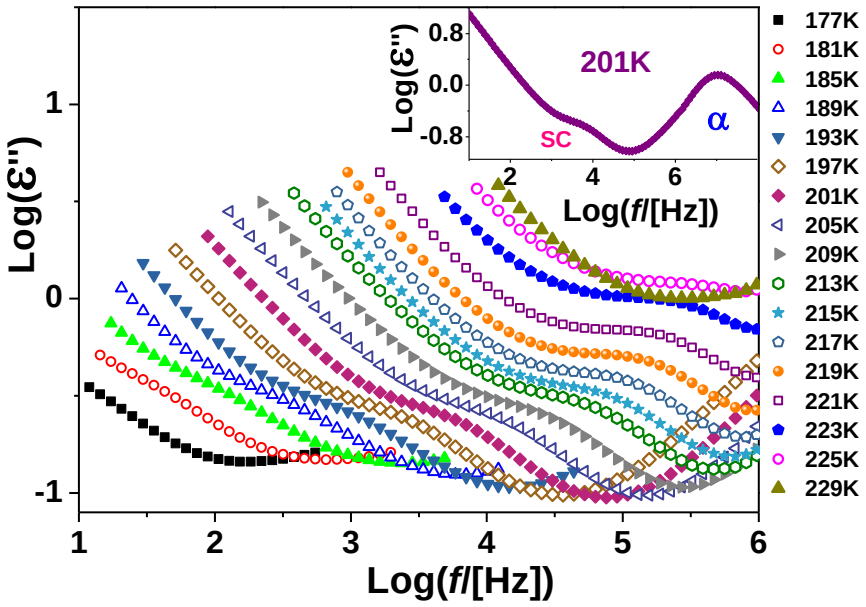


Figure 6.9: Dielectric loss spectra of a $SN_{0.93}GN_{0.07}$ sample between 163 and 235 K every 6 K. The inset shows a full spectrum where both the space-charge and primary relaxations are visible.

The inset to Figure 6.9 depicts the loss spectrum of the $SN_{0.93}$ $GN_{0.07}$ sample at 201 K. A second loss feature (denoted by SC in the inset) can be observed between the low-frequency conductivity background and the α relaxation. Figure 6.9 shows the temperature variation of this second feature, as measured upon cooling from just below 233 K, the transition temperature between plastic and fully-ordered phases in pure SN. The intensity of the feature is always lower than that of the α peak and varies non-monotonically with temperature: it is completely absent above 233 K (not shown), temperature at which it suddenly appears in the loss spectrum, and it then decreases with decreasing temperature until almost fading.

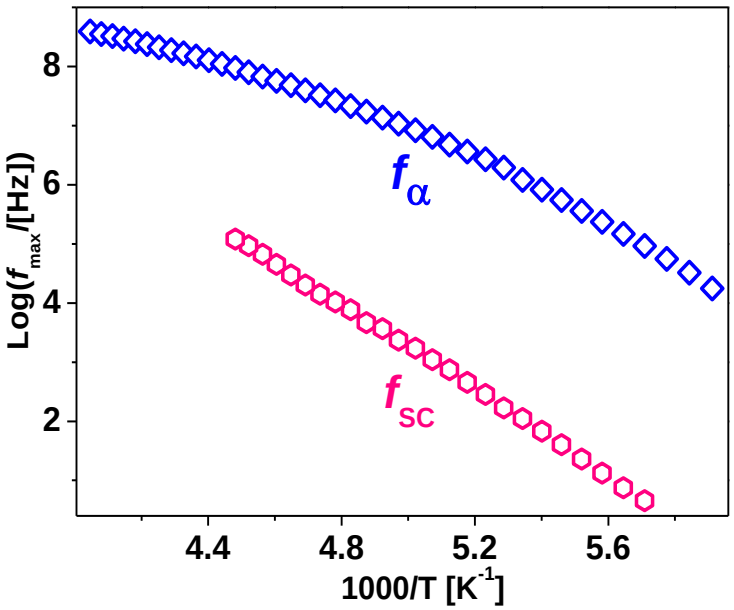


Figure 6.10: Arrhenius plot of the space-charge (SC) relaxation of the $SN_{0.93}GN_{0.07}$ sample. The α relaxation frequency is also shown for comparison.

The Arrhenius plot of the characteristic frequency of this loss feature, as extracted from a Debye fit (see chapter 2 section 2.4), is displayed in Figure 6.10. The origin of the loss feature is the spatial heterogeneity of the sample's conductivity and permittivity below 233 K: the partial phase transformation entails the appearance of fully-ordered crystallites with higher density, lower conductivity, and different static permittivity than the than the untransformed plastic matrix. When an ac field is applied, the sample's heterogeneity leads to accumulation of ions at the boundaries between the two solid phases resulting in a characteristic dipolar loss associated with space-charge effects [49] and/or with the heterogeneity of the permittivity, which is known to give rise to so-called space-charge relaxations. The phase boundaries are absent above 233 K, where the mixture is in a homogeneous plastic phase. As visible from Figure 6.5, the space-charge loss feature is absent in the $SN_{0.87}$ $GN_{0.13}$ sample at least above 170 K.

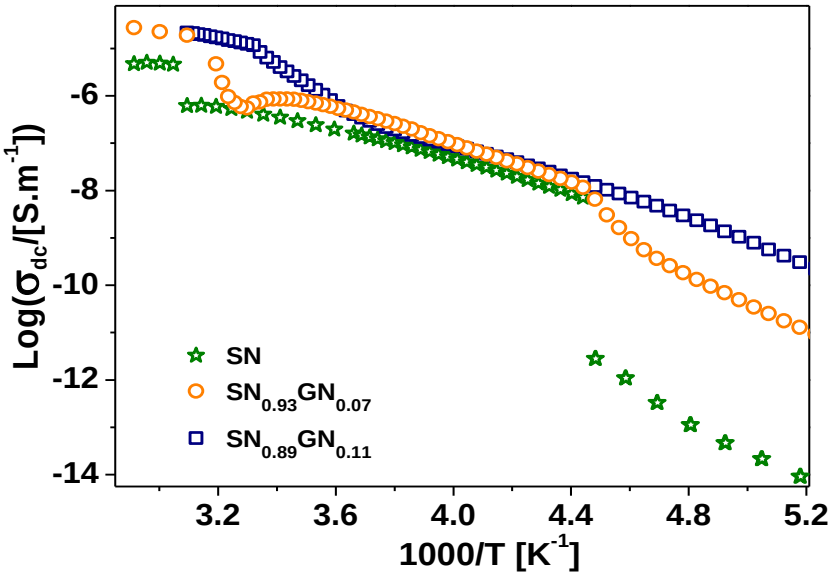


Figure 6.11: Arrhenius plot of the dc conductivity of pure SN, $SN_{0.93}GN_{0.07}$ and $SN_{0.89}GN_{0.11}$

Figure 6.11 shows the Arrhenius plot of the dc conductivity of $SN_{1-x}GN_x$ samples ($x$ = 0, 0.07, 0.11). At lower temperature the temperature-dependence of the dc conductivity is strongly affected by crystallization, which is marked by a sharp drop in pure SN and by a kink in the case of $SN_{0.93}GN_{0.07}$. Concerning the partial crystallization of the plastic phase, it is interesting to note that the spectra of the roughly equimolar SN-GN co-crystal [35] are characterized, apart from the α relaxation feature, also by a weaker loss feature at frequencies intermediate between the primary relaxation and the low-frequency conductivity background. The authors of Ref. 35 have indicated a possible conductivity-related origin of this feature. One possible explanation for the existence of this feature could be a partial phase separation leading to field-induced space-charge effects in the nearly equimolar stoichiometry (where the miscibility of binary systems is usually lowest). To test this idea, we compare our results on the SN-GN mixtures at lower GN stoichiometry with the results of Ref. 35 at higher GN content. From Figure 6.11 it is clear that the $\sigma_{dc}$ value for $SN_{0.93}GN_{0.07}$ near 233 K cannot be taken as indicative of the (homogeneous) mixture; rather, in such solid-state mixture ion transport is limited to the plastic domains, which represent only a fraction of the total volume of the

sample. This suggests that also the conductivity values reported in Ref. 35 may not be intrinsic to a homogeneous phase and that they may be actually limited by domain-boundary effects, which would rationalize why the Stokes-Einstein relation with $\sigma_{dc}$ is not verified in the equimolar SN-GN co-crystal. The heterogeneity of the $SN_{0.93}GN_{0.07}$ mixture could also be reflected in the anomalous behavior of the conductivity across the liquid-to-plastic transition, as visible in Figure 6.11: in the temperature region where plastic crystal and liquid phases coexist, $\sigma_{dc}$ displays non-monotonic behavior, which is absent in the $SN_{0.89}\,GN_{0.11}$ sample. It should be noted that in the temperature range of the liquid-to-plastic transition, the molecular dynamics is too fast to be measured with conventional dielectric spectroscopy, so that we have no information on the impact on the molecular dynamics due to phase segregation across the liquid-plastic transition. The above discussion indicates that the issue of phase separation is an important aspect of the phase behavior of SN-based mixtures, an aspect that has not been fully addressed in previous studies, and that, as we will show in the next section, is also relevant for SN mixtures with lithium salts.

## 6.6 Relaxation Dynamics and Ion Conduction in $Li^+$ Doped Mixtures

Since succinonitrile has been proposed as basis material for novel solid-state electrolytes supporting Li-ion conduction, it is interesting to study the conduction and molecular dynamics properties of SN-based systems upon doping with lithium salts.[3,4,19,50] The high polarity of SN ensures its ability to dissolve various types of salts. Previous studies showed that the dc conductivity of SN at ambient temperature reaches values up to $10^{-4}$ to $10^{-2}$ $\Omega^{-1}cm^{-1}$ when mixing it with selected salts like $LiBF_4$, $LiCF_3SO_3$, $LiN(CF_3SO_2)_2$ at molar fractions of few percent.[19] The highest ionic conductivities are obtained with $LiN(CF_3SO_2)_2$. As mentioned in Section 6.1, mixing SN with polymers enhances the ionic mobility, so that the conductivity of Li-salt doped SN polymer blends is higher by several decades than Li-doped SN. In

this section we discuss the relaxation dynamics and the conductivity enhancement of SN-GN binary co-crystals when doped with three different lithium salts.

### 6.6.1 The Walden Rule and Stokes-Einstein Relation are not Fulfilled in Salt-Doped Co-crystals

Figure 6.12 shows the Arrhenius plots of $f_{max}$ and of $\sigma_{dc}$ as obtained from the $SN_{0.89}$ $GN_{0.11}$ co-crystal together with the analogous data obtained on the same dinitrile mixture doped with $LiBF_4$. As already pointed out, the logarithmic plot of the maximum loss frequency and that of the dc conductivity display a curved lineshape, with more pronounced temperature dependence at low $T$ (closer to $T_g$).

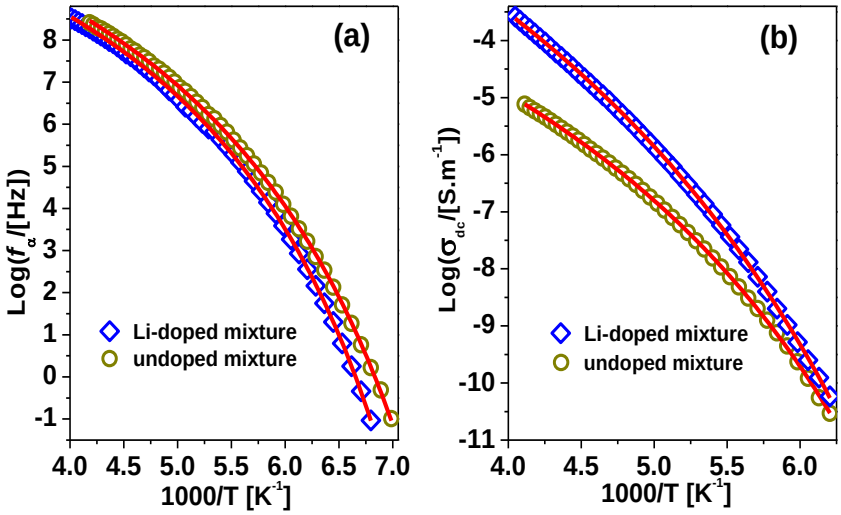


Figure 6.12: Semilogarithmic plot of $f_\alpha$ (*a*) and $\sigma_{dc}$ (*b*) *vs* 1000/*T*, for the $SN_{0.89}$ $GN_{0.11}$ and $LiBF_4$-doped $SN_{0.89}$ $GN_{0.11}$ (markers). Continuous lines are fits assuming a Vogel-Fulcher-Tammann temperature dependence (eq.s (6.1) and 6.(2)).

It may be observed from Figure 6.12 that the relaxation frequencies of the lithium-salt dopes sample are similar, though not identical, to those of the pristine mixture. The characteristic frequency is in fact slightly lower in the doped mixture, due to the stronger local interactions brought about by the presence of the $Li^+$ and $BF_4^-$ ions as reported in a recent THz study.[51] As may be expected, the effect of the ionic

interactions is more pronounced at lower temperature, where the characteristic orientational frequencies of the pure and doped mixtures differ by more than one decade. The dc conductivity values are quite different with and without salt: not only is $\sigma_{dc}$ higher when $Li^+$ ions are present, as expected, but also, it spans a larger number of decades in a given temperature interval between 240 and 160 K (on the contrary, in the same interval the relaxation frequency spans a smaller number of decades when $Li^+$ ions are present).

As stated in Section 6.5, non-Arrhenius behavior of the relaxation time (or frequency) is rather common feature in glass forming materials and plastic phases,[41,52] and it is consistent with earlier findings on the SN-GN binary system. [35] A widespread approach to model the non-linear inverse-temperature dependence of the α relaxation is based on a phenomenological modification of the Boltzmann exponential factor to yield the so called Vogel-Fulcher-Tammann (VFT) equation, which is given by:

$$f_\alpha = f_0 \exp\left[-\frac{s\,T_{\mathrm{VF}}}{(T-T_{\mathrm{VF}})}\right]. \qquad (6.1)$$

In this equation the prefactor $f_0$, the strength parameter $s$ and the so-called Vogel-Fulcher temperature $T_{\mathrm{VF}}$ are phenomenological parameters obtained by fitting the experimental data. A similar equation can also be used to model the non-simply activated temperature dependence of the ionic conductivity:[35] as visible in Figure 6.12, in fact, the experimental points for the pure and lithium-salt doped $SN_{0.89}\,GN_{0.11}$ mixture can be fitted accurately assuming a VFT dependence not only of $f_\alpha$ (panel *a*) but also of $\sigma_{dc}/T$ (panel *b*). This entails that the temperature dependence of the dc conductivity can be written as (with $c_0$ independent of temperature):

$$\sigma_{dc} = c_0 T \exp\left[-\frac{s'\,T'_{VF}}{(T-T'_{VF})}\right] \qquad (6.2)$$

The exact analytical form of the prefactors in the VFT equation is to some extent arbitrary, because the temperature dependence of both the conductivity and

frequency of maximum loss is largely dominated by the exponential term, so that the fit of the Arrhenius plots can equally well be obtained assuming any slowly varying function of $T$ in the prefactor. While it is customary to represent the temperature dependence of $\sigma_{dc}$ in studies of electrical conduction, in the case of organic or disordered semiconductors the Arrhenius plot of $\sigma_{dc}T$ is sometimes displayed; this amounts to assuming, in the analytical exponential expression for $\sigma_{dc}$, the prefactor to be inversely proportional to $T$, which is expected in some cases of electronic or polaronic hopping-mediated conduction.[53,54] In the present case the conductivity is ionic in nature, and the latter choice for the prefactor would be inappropriate. The choice of plotting the quantity $\sigma_{dc}/T$ instead of simply $\sigma_{dc}$ in Figure 6.12 will be justified in the following.

| **Quantity (sample)** | **prefactor** | ***S* (no units)** | **$T_{VF}$ (K)** |
|---|---|---|---|
| $f_{max}$ ($SN_{0.75}GN_{0.25}$) [Ref. 35] | $f_0 = 8.8 \cdot 10^{12}$ Hz | 12.8 | 106 |
| $f_{max}$ ($SN_{0.89}GN_{0.11}$) | $f_0 = 1.48 \pm 0.11 \cdot 10^{12}$ Hz | 9.7 ± 0.1 | 105.6 ± 0.3 |
| $\sigma_{dc}/T$ ($SN_{0.89}GN_{0.11}$) | $c_0 = 1144 \pm 50$ S cm$^{-1}$ K$^{-1}$ | 10.0 ± 0.1 | 107.3 ± 0.3 |
| $f_{max}$ ($LIBF_4$–doped $SN_{0.89}GN_{0.11}$) | $f_0 = 0.86 \pm 0.06 \cdot 10^{12}$ Hz | 10.8 ± 0.1 | 111.0 ± 0.3 |
| $\sigma_{dc}/T$ ($LiBF_4$–doped $SN0_{.89}GN_{0.11}$) | $c_0 = 3.0 \pm 0.4$ S cm$^{-1}$ K$^{-1}$ | 15.4 ± 0.3 | 98.9 ± 0.6 |

Table 6.1: Experimental parameters obtained by fitting the frequency of maximum loss and the dc conductivity of the indicated samples with the Vogel-Fulcher-Tammann equation.

The parameters obtained by fitting the data with Eq.s (6.1) and (6.2) are summarized in Table 6.1, together with the VFT parameters reported for the α relaxation of the $SN_{0.75}$ $GN_{0.25}$ mixture[35] for comparison purposes. The values of *s* and $T_{VF}$ for the α relaxation of the $SN_{0.89}$ $GN_{0.11}$ and $LiBF_4$-doped $SN_{0.89}$ $GN_{0.11}$ are in reasonable agreement with the published values for the $SN_{0.75}$ $GN_{0.25}$ mixture.[35]

It is evident from Figure 6.12 that ionic conductivity and orientational dynamics are correlated in the pure SN-GN mixture (in the absence of lithium ions). Furthermore, it can be seen in Table 6.1 that the Vogel-Fulcher temperature and the strength parameter are virtually identical, within experimental error, for both the conductivity and relaxation frequency of the undoped mixture. To further corroborate the correlation between the reorientational dynamics and the conductivity, in Figure 6.13 we have shown the Walden plots of undoped and lithium-doped $SN_{0.89}$ $GN_{0.11}$. It may be observed that in the undoped co-crystal the relationship between the two quantities is almost perfectly linear, with a slope virtually equal to 1 (confirming that the motion of charge carriers in plastic succinonitrile is perfectly correlated with the reorientational motion); instead, the linear correlation does not hold for the lithium-doped sample (especially at high temperature), which indicates that the connection between molecular reorientation and charge carrier diffusion does not hold for the small $Li^+$ ions.

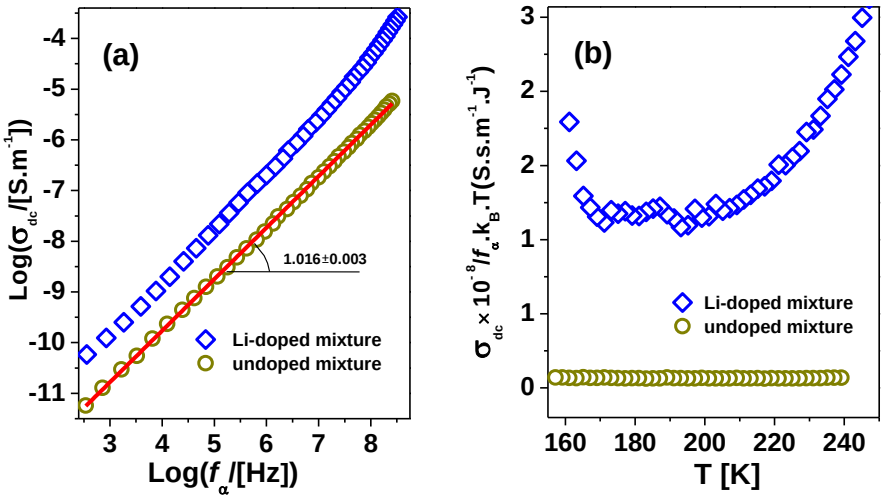


Figure 6.13: (*a*) Walden plot of the data acquired on the $SN_{0.89}$ $GN_{0.11}$ and $LiBF_4$-doped $SN_{0.89}$ $GN_{0.11}$ using the data of Figure 6.12. The continuous line is a linear fit to $SN_{0.89}$ $GN_{0.11}$ data. (*b*) Plot of $\sigma_{dc}/ (k_B T. f_\alpha)$ versus temperature for the undoped mixture, to verify the validity of the equivalent Stokes-Einstein relation (see the text).

As pointed out in previous section, the dc conductivities of pure SN and SN-GN mixtures are surprisingly high, despite the fact that the constituent molecules are neutral, so that they should not contribute to the ionic conduction. A likely explanation for the relatively high $\sigma_{dc}$ values is that they are due to a fraction of dinitrile molecules present as molecular ions, formed due to trapping of small (atomic) ion impurities at the nitrile (C≡N) end groups. Since it is known that in plastic-crystalline phases a minority of molecules undergo diffusive motions between lattice defects charge transport can result from ionized molecules diffusing through the plastic crystal matrix. The validity of the Walden and Stokes-Einstein relations for the SN-GN co-crystals would then imply a one-to-one correlation between the molecular orientational motion and the diffusion of a minority of ionized molecules. To further validate this idea, we analyze the results obtained on the lithium-salt doped mixture. In the case of lithium doped $SN_{0.89}$ $GN_{0.11}$ mixture, the dominant charge carriers are lithium ions, and the Arrhenius dependence of the conductivity is no longer perfectly correlated with the molecular relaxation, as visible in Figures 6.12 and 6.13. The fact that the Walden plot does not display a

linear behavior indicates that the motion of the $Li^+$ ions is decoupled from that of the organic matrix and suggests that diffusion of the small cations occurs on a faster timescale than that of the molecular reorientation. This rules out a paddling-wheel mechanism[13] for the small-ion conduction, and further confirms that electrical conduction in the undoped organic medium is due to molecular rather than atomic ions.

Here we discuss the temperature dependence of the dc conductivity prefactor. The data shown in Figure 6.13(*b)* implies that $\sigma_{dc}/f_\alpha \sim T$. If the VFT parameters describing the variation of $\sigma_{dc}$ and $f_\alpha$ with temperature are assumed to be equal, as supported by Table 6.1, then the temperature dependence of their ratio is actually a measure of the difference between the temperature dependences of the two prefactors, that is, $\sigma_{dc}/f_\alpha \simeq \sigma_0/f_0$. If the frequency prefactor is taken to be constant, as is customary, then $\sigma_0$ should scale like *T*, as shown in Figure 6.12(*b)*. The increase of the conductivity prefactor with temperature can be rationalized in light of recent studies of ion conduction in polar systems. It was found in highly polarizable liquid electrolytes that increasing the temperature leads, besides to a higher hopping rate (due to the higher thermal energy facilitating ions to overcome the corresponding potential energy barriers) which is responsible for the exponential dependence on temperature, also to an additional boost of the conductivity due to the lower static polarizability of the medium (implying a lower effective dielectric constant and thus a lower electrostatic hindrance against ion diffusion), which is responsible for the temperature-dependence of the prefactor.

We propose that a similar mechanism leads to the (linear) increase of the conductivity prefactor in SN. To justify this, in Figure 6.14 we plot the real part of the permittivity $\varepsilon'(f)$ of the mixture without lithium salt at few selected temperatures. The static permittivity $\varepsilon_s$ can be taken to be approximately the value of $\varepsilon'(f)$ just below the sudden decrease visible in the central portion of the spectra, which corresponds, by the Kramers-Kronig relations, to the onset frequency of the α-relaxation peak.

The value of the static permittivity in Figure 6.14 are significantly higher than the values in the liquid phases, namely $\varepsilon_s = 55$ at 333 K for pure SN and $\varepsilon_s = 34$ at 300 K

for pure GN. This is due to the fact that the temperature of the plastic phase is lower, so that thermal motions are less detrimental to the dipole reorientation with the field, but also due to the fact that in a plastic-crystal phase the rotational motion of the molecules are not hindered by the steric confinement imposed by the rototranslational diffusion of nearby molecules. It may be observed both from the spectra and from the plot of $\varepsilon_s$ *vs T*, shown in the inset to Figure 6.14 that the static permittivity decreases with increasing temperature, which is expected because the alignment of the molecular dipoles with the applied field is hampered by thermal motions at high temperature. The same behavior is also visible at other concentrations of the SN-GN binary system. The decrease of $\varepsilon_s$ in turn entails a less pronounced polarization cloud around charged species, hence further favoring charge transport.

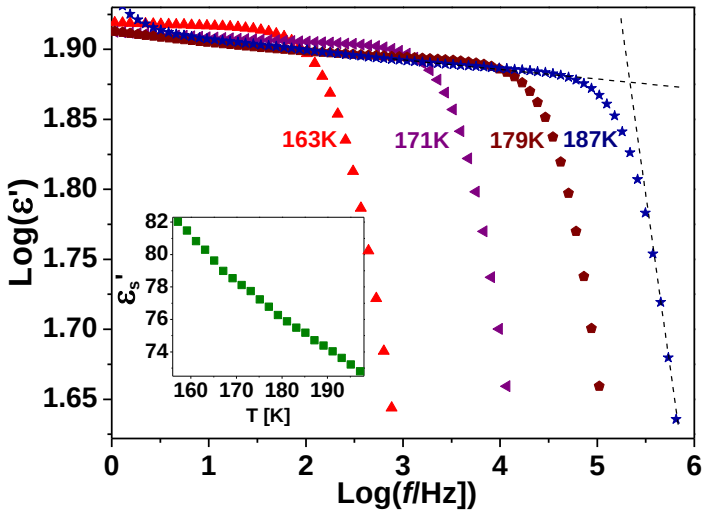


Figure 6.14: Permittivity spectra ε'(*f*) of the plastic phase of the undoped $SN_{0.89}$ $GN_{0.11}$ plastic co-crystal, at the indicated temperatures. Dashed lines show how the static permittivity value $\varepsilon_s$ was extracted from the spectra (for a particular isothermal spectrum). Inset: static permittivity $\varepsilon_s$ as a function of temperature for the same mixture.

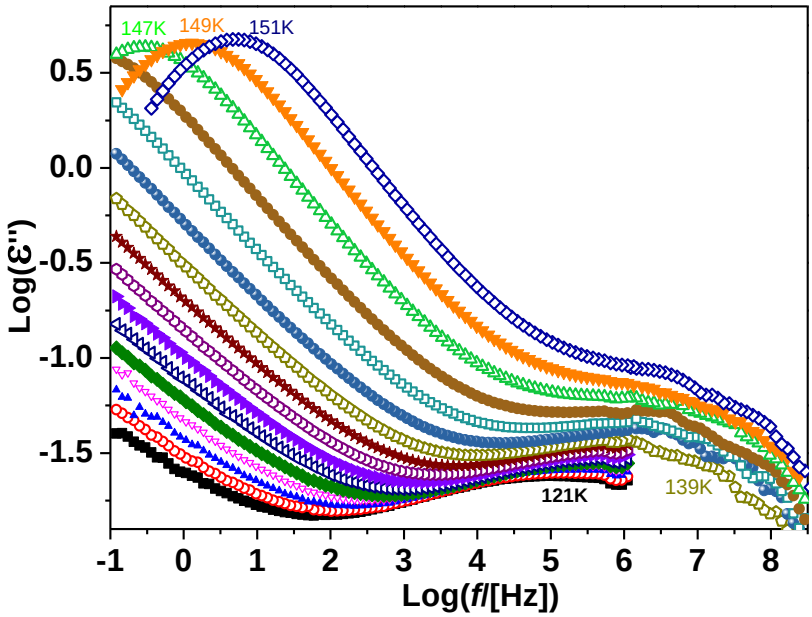


Figure 6.15: Dielectric loss spectra of the $SN_{0.89}GN_{0.11}$ plastic co-crystal, in the temperature range between 151 and 121 K, where a secondary (γ) relaxation is visible (at higher frequency than the α peak).

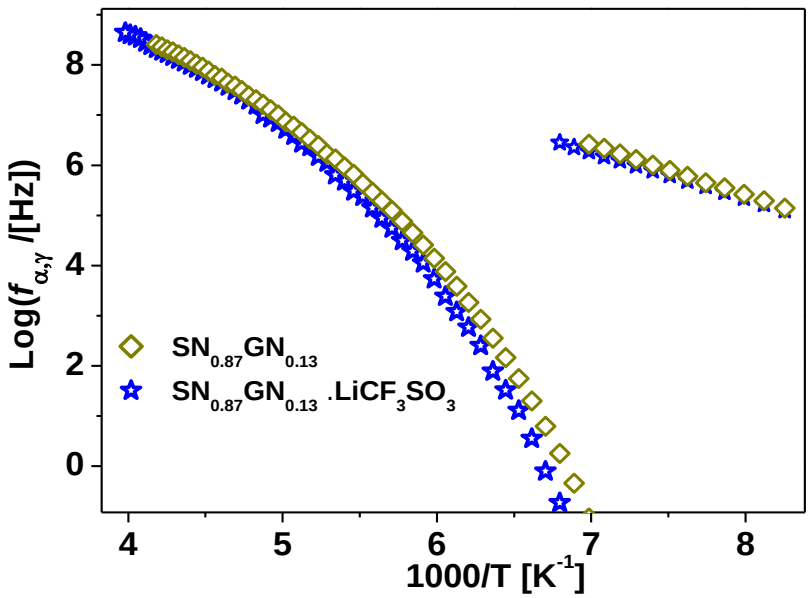


Figure 6.16: Arrhenius plot of $f_\alpha$ and $f_\gamma$ for the pure and $LiCF_3SO_3$-doped $SN_{0.87}$ $GN_{0.13}$ co-crystal.

Figure 6.15 displays low-temperature loss spectra acquired on the $SN_{0.89}GN_{0.11}$ plastic co-crystal. It is seen that the sample exhibits a secondary relaxation at higher frequency (lower temperature) than the primary α process. Such fast relaxation was reported also in the nearly equimolar co-crystal,[35,36] but its exact origin was not identified. We will refer to this relaxation as γ relaxation to maintain the nomenclature of Ref. 35. Figure 6.16 shows the Arrhenius plot of the α and γ relaxations of both a pristine and $LiCF_3SO_3$-doped SN-GN co-crystal. As visible in the plot, the characteristic frequency $f_\gamma$ of the fast relaxation (obtained by a fit of the dielectric loss data assuming a Cole-Cole profile) is fundamentally unchanged in the presence of $Li^+$ ions. Comparison with the data of Ref. 35 shows that it is also barely affected by a change in the stoichiometry. This entails that the γ relaxation is an intramolecular (conformational) dynamic process which is not affected by intermolecular interactions or by the presence of ions. The γ relaxation might correspond to transitions between different isomeric forms of the dinitrile species. As visible from the same Figure 6.16, compared to the undoped materials the characteristic relaxation frequency $f_\alpha$ was found in some cases to be lower in Li-doped co-crystals than in the pure ones. This might be due to the stronger local interactions brought about by the presence of the $Li^+$ ions and the counter-ions, as reported in recent studies.[51] The effect of the ionic interactions is more pronounced at lower temperature.

### 6.6.2 Ion conduction in $Li^+$ Doped Co-crystals

Figure 6.17 shows the Arrhenius plot of the dc conductivity for the $SN_{0.87}GN_{0.13}$ sample doped with three different lithium salts ($LiBF_4$, $LiCF_3SO_3$, and $LiN(CF_3SO_2)_2$) compared with that of pure SN. Previous studies reported that the dc conductivity of pure SN and of SN-polymer mixtures increases significantly upon doping with lithium salts[55], due to the higher ion density, which, as visible in Figure 6.17, is also true for the binary nitrile co-crystals studied here.

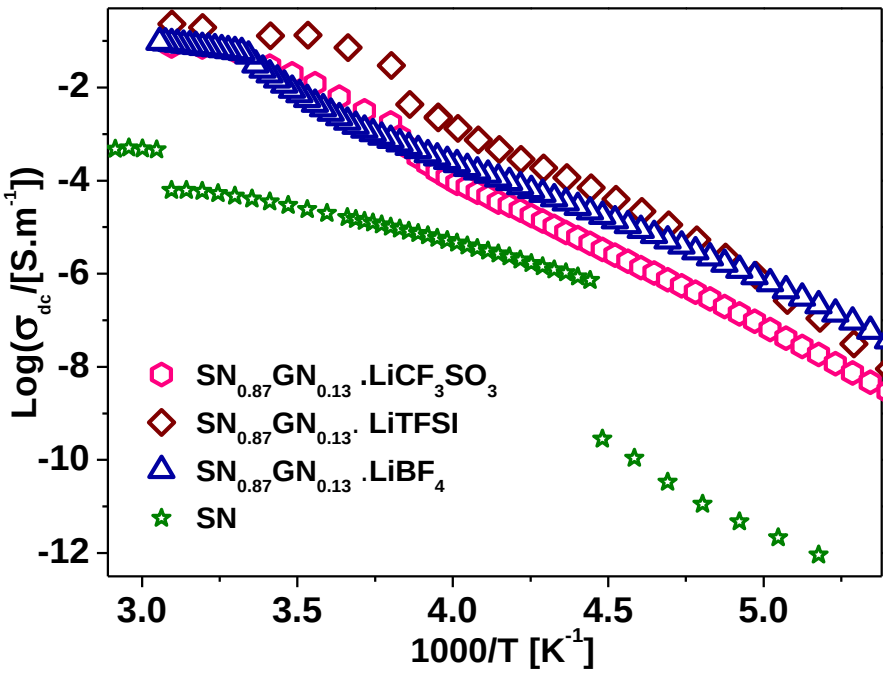


Figure 6.17: Arrhenius plot of the dc conductivity for the $SN_{0.87}GN_{0.13}$ sample doped with three different lithium salts, compared to that of pure SN.

All Li-doped co-crystals exhibit a kink at a temperature similar to or lower than that of the onset of the liquid-to-plastic transition in the SN-GN mixtures (see Figure 6.6). This kink is due to the fact that the Li-ion conductivity is lower in a (partially) plastic crystalline phase than in the liquid phase of the same sample. For all Li-salt doped samples we observed the breakdown of the Walden and Stokes-Einstein relation, as reported for the $LiBF_4$-doped mixture, which is indicative of a

decoupling between small-ion diffusion and nitrile reorientations when the conductivity is dominated by $Li^+$ ions. This again shows that the correlation between conductivity and molecular rotational dynamics is only present in the undoped materials, where conduction is dominated by self-diffusion of ionic molecules. If charge transport in the undoped mixtures were mediated by the simple drift of atomic or diatomic ions though the interstitial voids, one would expect the same lack of correlation between ion drift and rotational dynamics: in other words, the validity of the Stokes-Einstein relation only in the undoped co-crystals confirms our interpretation of the anomalously high ion conductivity of nitrile co-crystals as being due to molecular self-diffusion.

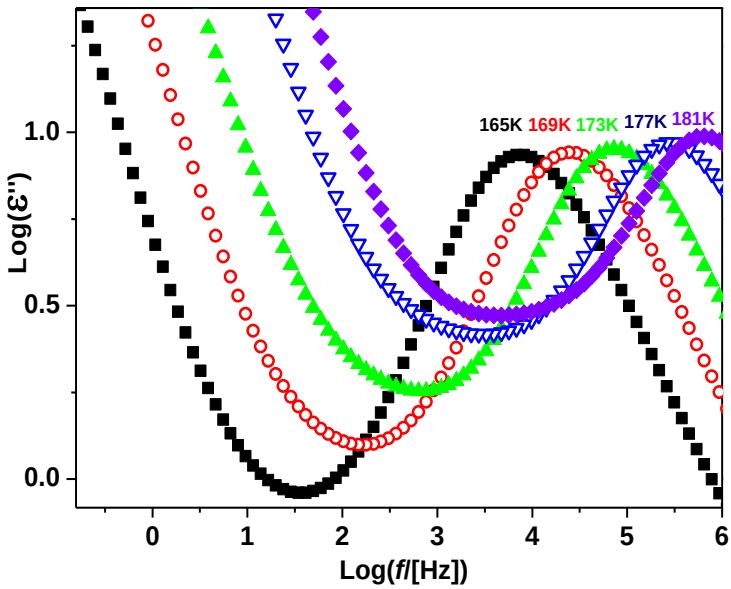


Figure 6.18: Series of dielectric loss spectra acquired on the $SN_{0.89}GN_{0.11}$ co-crystal doped with $LiBF_4$.

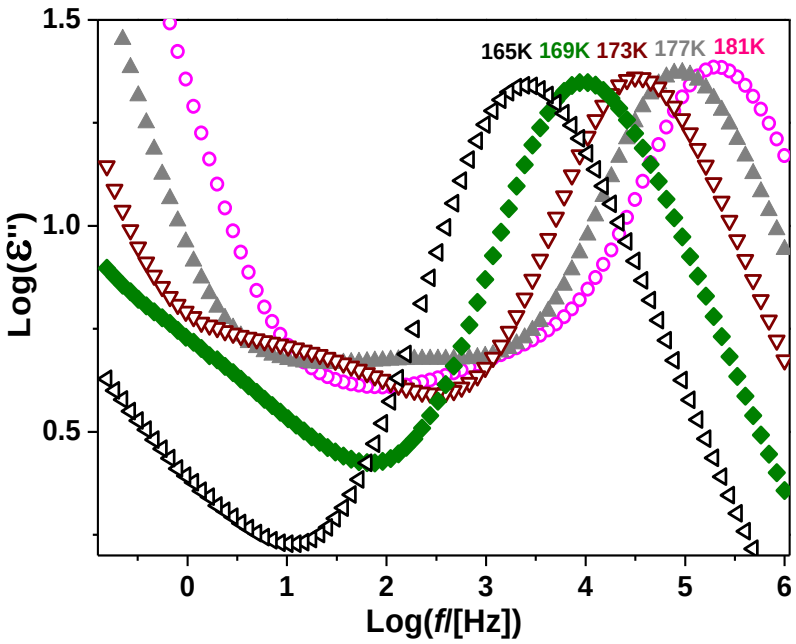


Figure 6.19: Series of dielectric loss spectra acquired on the $SN_{0.87}GN_{0.13}$ co-crystal doped with $LiCF_3SO_3$.

Figures 6.18 and 6.19 show series of spectra obtained on SN-GN co-crystals doped with two different salts ($LiBF_4$ and $LiCF_3SO_3$, respectively). In the $SN_{0.87}GN_{0.13}$ cocrystal doped with $LiCF_3SO_3$ (Figure 6.19), the spectra below 190 K are characterized by the presence, besides of the primary α feature, of a space-charge relaxation, indicating that the sample is in a mixed phase below the crystallization temperature of pure SN. It should be noted that the pristine (undoped) $SN_{0.87}GN_{0.13}$ mixture displays a partial crystallization only below 170 K, and that no space-charge relaxation is visible (Figure 6.5). As visible by comparison to Figure 6.18, the space-charge relaxation in the $LiCF_3SO_3$-doped $SN_{0.87}GN_{0.13}$ co-crystal is much more intense than the corresponding loss feature in $LiBF_4$- doped $SN_{0.89}GN_{0.11}$, where space-charge effects are negligible.

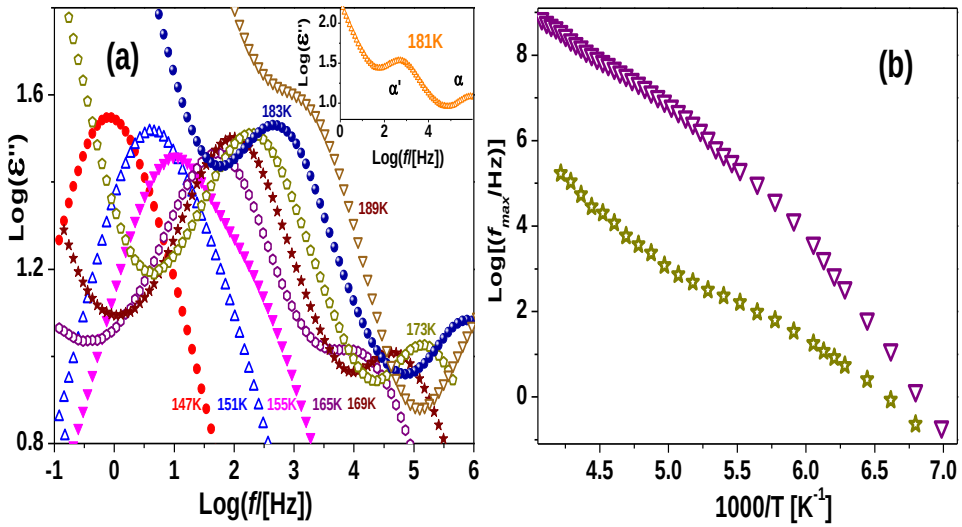


Figure 6.20: (*a*) Series of dielectric loss spectra acquired on the $SN_{0.87}GN_{0.13}$ mixture doped with LiTFSI. (*b*) Arrhenius plot of the relaxation frequency of both processes observed in (*a*).

Figure 6.20(*a*) depicts the temperature-dependent dielectric loss spectra of the $SN_{0.87}GN_{0.13}$ co-crystal doped with $LiN(CF_3SO_2)_2$, measured upon cooling below 190 K. Part of the interest in studying the effect of this particular salt is that, as mentioned at the beginning of this section, it generally leads to high ionic conductivity. It may be observed from Figure 6.20(*a*) that the sample exhibits two intense loss features (see the inset for more clarity). The high-frequency relaxation matches roughly the cooperative α relaxation of the undoped mixture and it is therefore assigned to the rotational dynamics of the dinitrile species. The most intense relaxation (labeled as α') is instead observed at lower frequency than the α relaxation of the dinitriles. Since the $N(CF_3SO_2)_2^-$ (TSFI) anion has non-zero dipole moment, we associate the α' process with the reorentational relaxation dynamics of the anion of the LiTSFI salt.

It is interesting to notice that while all dinitriles (SN, GN, AN) display a single dielectric loss, implying a coincidence of relaxation times, this is not the case for the TSFI moieties, likely due to the fact that their molecular structure and therefore their characteristic dynamics are quite different from those of the dinitriles. It may be

observed in the Arrhenius plot of Figure 6.20(*b*) that the relaxation frequencies of both processes (α and α') tend to merge together at low temperature, as also visible in the spectra of panel (*a*), where it is seen that the two spectral component merge together near their (common) glass transition temperature. The local morphology of the sample is not known, so that we refrain from further analysis of the origin of both features. Also, we cannot exclude that phase separation and space-charge effects could also contribute to the loss spectra.

The characterization presented in this section shows that if a specific SN-based system, doped with a specific lithium salt, is to be considered for electrolyte applications, the issue of phase separation (either intrinsic to the undoped system, or induced by Li-salt doping) should be investigated before conclusions about charge transport can be drawn.

## 6.7 Conclusions

We have probed, by means of calorimetry and dielectric relaxation spectroscopy, the plastic-crystalline succinonitrile mixtures with glutaronitrile and acetonitrile. The samples display in general a tendency to phase-segregate: the liquid-to-plastic transition takes place in two steps, as in most binary systems, and at least partial crystallization of succinonitrile-rich domains is usually observed, leading in some cases to the appearance of a space-charge relaxation. Stable and homogeneous plastic phases appear to form only when adding to succinonitrile sufficient but moderate amounts of glutaronitrile. The resulting solid cocrystals display self-diffusion of neutral and ionic molecules, which give rise to an exceptionally high ionic conductivity at room temperature. We reported in this Chapter the first and so-far only known example of molecular plastic crystal exhibiting a perfect agreement between the temperature dependences of the long-range ion drift and of the collective reorientational dynamics. These correlation breaks down in the samples doped with lithium ions, indicating that the rotation-drift correlation is only valid when charge transport is dominated by self-diffusion of bulky molecular ions, while the motion of smaller atomic ions is decoupled from the molecular dynamics. Given

that all mixtures are partially liquid at room temperature, they cannot be employed as solid-state $Li^+$-ion electrolytes. Doping with lithium salts boosts the ion conductivity and slows the collective molecular dynamics of the mixtures, while leaving unaffected the fast relaxation dynamics associated with intramolecular (configurational) changes.

# References


[1] Choi, K.-H.; Cho, S.-J.; Kim, S.-H.; Kwon, Y.H.; Kim, J.Y.; Lee, S.-Y. Flexible Batteries: Thin, Deformable, and Safety-Reinforced Plastic Crystal Polymer Electrolytes for High-Performance Flexible Lithium-Ion Batteries. *Adv. Funct. Mater.* **2014**, 24, 172.

[2] Hwang, D.; Kim, D.Y.; Jo, S.M.; Armel, V.; MacFarlane, D.R.; Kim, D.; Jang, S.-Y. Highly Efficient Plastic Crystal Ionic Conductors for Solid-State Dye-Sensitized Solar Cells. *Sci. Rep.* **2013**, 3, 3520.

[3] MacFarlane, D. R.; Huang, J.; Forsyth, M. Lithium-Doped Plastic Crystal Electrolytes Exhibiting Fast Ion Conduction for Secondary Batteries. *Nature* **1999**, 402, 792-794.

[4] Long, S.; MacFarlane, D.R.; Forsyth, M. Fast Ion Conduction in Molecular Plastic Crystals. *Solid State Ionics* **2003**, 161, 105-112.

[5] MacFarlane, D.R.; Forsyth, M. Plastic Crystal Electrolyte Materials: New Perspectives on Solid State Ionics. *Adv. Mater.* **2001**, **13**, 957-966.

[6] Brand, R.; Lunkenheimer, P.; Loidl, A. Relaxation dynamics in plastic crystals. *J. Chem. Phys.* **2002**, 116, 10386-10401.

[7] Romanini, M.; Negrier, Ph.; Tamarit, J.Ll.; Capaccioli, S.; Barrio, M.; Pardo, L.C.; Mondieig, D. Emergence of Glassy-like Dynamics in An Orientationally Ordered Phase. *Phys. Rev. B.* **2012**, 85, 134201.

[8] Romanini, M.; Martinez-Garcia, J.C.; Tamarit, J.Ll.; Rzoska, S.J.; Barrio, M.; Pardo, L.C.; Drozd-Rzoska, A. Scaling the Dynamics of Orientationally Disordered Mixed Crystals. *J. Chem. Phys.* **2009**, 131, 184504.

[9] Criado, A.; Jiménez-Ruiz, M.; Cabrillo, C.; Bermejo, F.J.; Fernández-Perea, R.; Fischer, H. E.; Trouwet, F.R. Rotational Dynamics in the Plastic-Crystal Phase of

Ethanol: Relevance for Understanding the Dynamics During the Structural Glass Transition. *Phys. Rev. B* **2000**, 61, 12082-12093.

[10] Sunarso, J.; Shekibi, Y.; Efthimiadis, J.; Jin, L.; Pringle, J.; Hollenkamp, A.; MacFarlane, D.; Forsyth, M.; Howlett, P. Optimising Organic Ionic Plastic Crystal Electrolyte for All Solid-State and Higher than Ambient Temperature Lithium Batteries. *J. Solid State Electrochem.* **2012**, 16, 1841-1848.

[11] MacFarlane, D.R.; Meakin, P.; Amini, N.; Forsyth, M. Structural Studies of Ambient Temperature Plastic Crystal Ion Conductors. *J. Phys. Condens. Matter* **2001**, 13, 8257-8267.

[12] Murugesan, S.; Quintero, O. A.; Chou, B. P.; Xiao, P.; Park, K.; Hall, J.W.; Jones, R. A.; Henkelman, G.; Goodenough, J. B.; Stevenson, K. J. Wide Electrochemical Window Ionic Salt for use in Electropositive Metal Electrodeposition and Solid State Li-Ion Batteries. *J. Mater. Chem. A* **2014**, 2, 2194-2201.

[13] Jansen, M. Volume Effect or Paddle-Wheel Mechanism—Fast Alkali-Metal Ionic Conduction in Solids with Rotationally Disordered Complex Anions. *Angew. Chem., Int. Ed.* **1991**, 30, 1547-1558.

[14] Jin, L.; Nairn, K.M.; Forsyth, C.M.; Seeber, A.J.; MacFarlane, D.R.; Howlett, P.C.; Forsyth, M.; Pringle, J.M. Structure and Transport Properties of a Plastic Crystal Ion Conductor: Diethyl(Methyl)(Isobutyl)Phosphonium Hexafluorophosphate. *J. Am. Chem. Soc.* **2012**, 134, 9688.

[15] Do, C.; Lunkenheimer, P.; Diddens, D.; Gotz, . M.; Weiss, M.; Loidl, A.; Sun, . X.G.; Allgaier J.; Ohl, M. $Li^+$ Transport in Poly(Ethylene Oxide) Based Electrolytes: Neutron Scattering, Dielectric Spectroscopy, And Molecular Dynamics Simulations. *Phys. Rev. Lett.* **2013**, 111, 018301.

[16] Aihara,Y.; Hayamizu, K.; Sugimoto, T.; Bando, T.; Iguchi, T.; Kuratomi, J.; Ono, T.; Kuwana, K. Ion diffusion mechanisms in the cross-linked poly(ether) doped with $LiN(CF_3SO_2)_2$ *J.Power Sources* **2001**, 97-98, 628-631.

[17] Patel, M.; Menezes, P.V.; Bhattacharyya, A.J. Ion Transport in a Polymer-Plastic Solid Soft Matter Electrolyte in the Light of Solvent Dynamics and Ion Association. *J. Phys. Chem. B* **2010**, 114, 5233-5240.

[18] Börjesson L. & Torell L. M. Reorientational Motion in Superionic Sulfates: A Raman Linewidth Study. *Phys. Rev. B* **2013**, 32, 2471-2477.

[19] Dai, Q.; MacFarlane, D.R.; Howlett, P.C.; Forsyth, M. Rapid I-/I3- Diffusion in a Molecular-Plastic-Crystal Electrolyte for Potential Application in Solid-State Photoelectrochemical Cells. *Angew. Chem., Int. Ed.* **2005**, 44, 313-316.

[20] Alarco, P.-J.; Abu-Lebdeh,Y.; Abouimrane, A.; Armand, M. The Plastic-Crystalline Phase of Succinonitrile as a Universal Matrix for Solid-State Ionic Conductors. *Nat. Mater.* **2004**, 3, 476-481.

[21] Fan, L.Z.; Hu, Y.S.; Bhattacharyya, A.J.; Maier, J. Succinonitrile as a Versatile Additive for Polymer Electrolytes. *Adv. Funct. Mater.* **2007**, 17, 2800-2807.

[22]MacFarlane, D. R.; Huang, J. & Forsyth, M. Lithium-doped plastic crystal electrolytes exhibiting fast ion conduction for secondary batteries. *Nature* **1999**,402, 792-794.

[23] Cardini, G.; Righini, R.; Califano, S. Computer Simulation of the Dynamics of the Plastic Phase of Succinonitrile. *J. Chem. Phys.* **1991**, 95, 679-685.

[24] Long, S.; MacFarlane, D. R.; Forsyth, M. Ionic Conduction in Doped Succinonitrile. *Solid State Ionics* **2004**,175, 733-738.

[25] Patel, M. & Bhattacharyya, A.J. Plastic-Polymer Composite Electrolytes: Novel Soft Matter Electrolytes for Rechargeable Lithium Batteries. *Electrochem. Commun.* **2008**, 10, 1912-1915.

[26] Hawthorne, H.M; Sherwood, J. N. Lattice defects in Plastic Organic Solids. Part 2.—Anomalous Self-Diffusion in Succinonitrile. *Trans. Faraday Soc.* **1970** 66, 1792-1798.

[27] Descamps, M. Space Correlations in Succinonitrile Observed by X-ray Scattering. *Solid State Commun.* **1974**, 14, 77-81.

[28] Tamarit, J.Ll.; Rietveld, I.B.; Barrio, M.; Céolin, R. The Relationship between Orientational Disorder and Pressure: The Case Study of Succinonitrile. *J. Molecular Structure* **2014**, 1078, 3-9.

[29] Derollez, P.; Lefebvre, J.; Descamps, M.; Press, W.; Fontaine, H. Structure of Succinonitrile in its Plastic Phase. *J. Phys. Condens. Matter* **1990**, 2, 6893-6903.

[30] Hawthorne, H. M. and Sherwood, J. N. Lattice defects in Plastic Organic Solids. Part 2. Anomalous Self-Diffusion in Succinonitrile. *Trans. Faraday Soc.* **1970**, 66, 1792−1798.

[31] Nowak, J.; Malecki, J.; Thiebaut, J.M.; Rivail, J.-L. Dielectric Study of the Rotational Equilibria of Succinonitrile. *J. Chem. Soc. Faraday Trans.* **1980,**76, 197-204.

[32] Wasylishen, R.E.; Pettitt, B.A. $^{13}C$ Spin-Lattice Relaxation in Rotationally Disordered Solids. *Mol. Phys.* **1978,** 36, 1459-1467.

[33] Wulff, C.A.; Westrum Jr., E.F. Heat Capacities and Thermodynamic Properties of Globular Molecules. VI. Succinonitrile. *J. Phys. Chem.* **1963,** 67, 2376-2381.

[34] Masui, A.; Yoshioka, S.; Kinoshita, S. Light Scattering Study of Liquid and Plastic Phases of Succinonitrile from 0.003 to 3000 $cm^{-1}$. *Chem. Phys. Lett.* **2001**, 341, 299-305.

[35] Bauer, Th.; Köhler, M.; Lunkenheimer, P.; Loidl, A.; Angell, C. A. Relaxation Dynamics and Ionic Conductivity in a Fragile Plastic Crystal. *J. Chem. Phys.* **2010**, 133, 144509.

[36] Götz, M.; Bauer, Th.; Lunkenheimer, P.; Loidl, A. Supercooled-Liquid and Plastic-Crystalline State in Succinonitrile-Glutaronitrile Mixtures. *J. Chem. Phys.* **2014**, 140, 094504.

[37] Kremer F.; Schönhals, A. *Broad Band Dielectric Spectroscopy*, Springer, Berlin **2003.**

[38] Pringle, J.M.; Howlett, P.C.; MacFarlane, D.R.; Forsyth, M. Organic Ionic Plastic Crystals: Recent Advances. *J. Mater. Chem.* **2010**, 20, 2056-2062.

[39] Pringle, J.M. Recent Progress in the Development and Use of Organic Ionic Plastic Crystal Electrolytes. *Phys. Chem. Chem. Phys.* **2013**, 15, 1339-1351.

[40] Angell, C.A. Structural Instability and Relaxation in Liquid and Glassy Phases near the Fragile Liquid Limit. *J. Non.Cryst. Solids* **1988**,102, 205-221.

[41] Angell, C.A. Relaxation in Liquids, Polymers and Plastic Crystals — Strong/Fragile Patterns and Problems. *J. Non.Cryst. Solids* **1991**, 131, 13-31.

[42] Barthel, J. Krienke, H. and Kunz, W. *Physical Chemisty of Electrolyte Solutions*; Steinkopff-Verlag: Darmstadt, Germany, **1998**.

[43] Walden, P. Z. Organic solvents and Ionization Media. III. Interior Friction and its Relation to Conductivity. *Phys.Chem.* **1906,** 55, 207.

[44] Ngai, K.L.; León, C. Relating Macroscopic Electrical Relaxation to Microscopic Movements of the Ions in Ionically Conducting Materials by Theory and Experiment. *Phys. Rev. B* **1999**, 60, 9396-9405.

[45] Wojnarowska, Z.; Paluch, K. J.; Shoifet, E.; Schick, C.; Tajber, L.; Knapik, J.; Wlodarczyk, P.; Grzybowska, K.; Hensel-Bielowka, S.; Verevkin, S. P.; Paluch, M.

Molecular Origin of Enhanced Proton Conductivity in Anhydrous Ionic Systems. *J. Am. Chem. Soc.* **2015**, 137, 1157–1164.

[46] Ramos, M. A.; Vieira, S.; Bermejo, F. J.; Dawidowski, J.; Fischer, H. E.; Schober, H.; Gonzalez, M. A.; Loong C. K.; Price, D. L. Quantitative Assessment of the Effects of Orientational and Positional Disorder on Glassy Dynamics. *Phys. Rev. Lett.* **1997**, 78, 82.

[47] Benkhof, S. ; Kudlik, A.; Blochowicz, T.; Rossler, E. Two Glass Transitions in Ethanol: A Comparative Dielectric Relaxation Study of the Supercooled Liquid and the Plastic Crystal. *J. Phys.:Condens. Matter*, **1998**, 10, 8155.

[48] Dai, Q.; MacFarlane, D.R.; Howlett, P.C.; Forsyth, M. Rapid I-/I3- Diffusion in a Molecular-Plastic-Crystal Electrolyte for Potential Application in Solid-State Photoelectrochemical Cells. *Angew. Chem., Int. Ed.* **2005**, 44, 313-316.

[49] van Staveren, M. P. J.; Brom, H. B.; de Jongh, L. J. Metal− Cluster Compounds and Universal Features of the Hopping Conductivity of Solids. *Phys. Rep.* **1991**, 208, 1−96.

[50] Das, S. and Bhattacharyya, A. J. Dielectric Relaxation Spectroscopy for valuation of the Influence of Solvent Dynamics on Ion Transport in Succinonitrile-Salt Plastic Crystalline Electrolytes. *J. Phys. Chem. B* **2011**,115, 2148–2154.

[51] Nickel, D.V.; Bian, H.; Zheng, J.; Mittleman, D.M. Terahertz Conductivity and Hindered Molecular Reorientation of Lithium Salt Doped Succinonitrile in its Plastic Crystal Phase. *J. Infrared Milli. Terahz Waves* **2014**, 35, 770-779.

[52] Brand, R.; Lunkenheimer, P.; Loidl, A. Relaxation Dynamics in Plastic Crystals. *J Chem. Phys.* **2002**, 116, 10386-10400.

[53] van Staveren, M. P. J.; Brom, H. B.; de Jongh, L. J. Metal− Cluster Compounds and Universal Features of the Hopping Conductivity of Solids. *Phys. Rep.* **1991**, 208, 1−96.

[54] J.T. Devreese, “Polarons,” in Digital Encyclopedia of Applied Physics, edited by G. L. Trigg (Wiley, online), (2008). Article also available at cond-mat/0004497v2.

[55] Geirhos, K.; Lunkenheimer, P.; Michl, M.; Reuter, D; Loidl, A. Conductivity Enhancement in Plastic-Crystalline Solid-State Electrolytes. *J. Chem. Phys.* **2015**, 143, 081101.

# Conclusions

In this thesis we focus on the molecular dynamics and conduction properties of three different organic solids, a class of materials that is employed in low-cost low-weight electrical and optoelectronic devices, and that may be interesting also for electrochemical applications. We study in particular two fullerene derivatives, namely $C_{60}Br_6$ and $C_{60}(ONa)_{24}$, both in polycrystalline powder form, and binary plastic co-crystals of nitrile molecules (succinonitrile with glutaronitrile or acetonitrile).

In $C_{60}Br_6$, electrical conduction is due to hopping processes of electronic charge carriers and it is well-described by Mott's variable-range hopping model below ca. 220 K. Above 215 K a new conduction mechanism sets in, likely also electronic in character, accompanied by a weak endothermic feature in the calorimetry thermogram, which might signal an orientational solid-solid transition. Two dielectric loss features are observed. The main loss is a conductivity-related loss associated with polaron hopping and the second loss feature is ascribed to the reorientational motions of labile dipolar $C_{60}Br_x$ moieties with $x \leq 6$ by comparison with an only partially brominated $C_{60}$ sample.

Solid $C_{60}(ONa)_{24}$, which is studied both in its pure form and as a crystalline hydrate, is found to display both electronic and protonic conduction. Charge conduction in the pure material is purely electronic in the whole temperature range studied (there is no evidence of cationic conduction due to Na ions) and well described by Mott's variable-range polaron hopping model. Exposure of the pure material to humid atmosphere results in an increase of the room-temperature conductivity by four orders of magnitude, due to the surface hydration of the crystalline grains (a situation encountered in many other weakly conducting systems). The surface water desorbs upon heating to moderate temperature (330 K)

which indicates that the surface conductivity enhancement is due to proton shuttling (Grotthus exchange) through the hydration water layers. The conductivity of the hydrate is dominated between 320 and 390 K by a contribution related to the structural water, and possibly also due to proton shuttling as in the case of the surface water. Due to such contribution, at 350 K the hydrate's conductivity is higher than that of the pure material by almost two orders of magnitude. A dielectric loss feature is visible in both hydrate and pure material. The loss feature in the pure material is found to have a conductivity origin (it is a space-charge loss associated with the accumulation of electrons at grain boundaries) but its frequency and intensity are affected by the presence of surface water: the adsorption of water from the atmosphere leads to an enhancement of the strength of the loss feature, which moreover exhibits non-monotonic temperature dependence upon water desorption, similar to that found in other water-containing systems. We argue that this effect is mainly due to the high dc conductivity value in the surface hydration layer. The hydrate also displays a space-charge loss, and possibly mixed electronic and protonic conduction. The structural water molecules in the hydrate do not display any dynamic molecular relaxation, in agreement with the expectation for a crystalline hydrate with a rigid hydrogen-bond network. Our study of hydrated and pure $C_{60}(ONa)_{24}$ illustrates two familiar but not fully understood phenomena, namely, the surface conductivity enhancement in porous materials upon adsorption of water vapor, and the variation of conductivity across the structural dehydration of crystalline hydrates. Our results demonstrate that the anomalous (non-monotonic) temperature evolution of relaxation times observed in porous water-containing systems is likely a result of the conductivity enhancement induced by the adsorbed water.

Finding new ionic conductors that enable significant advances in the development of energy-storage devices is a challenging goal of current material science. Plastic crystalline fast ion conductors have been a topic of intense research because of their potential use as a new type of solid state electrolytes for portable electrochemical devices (such as rechargeable batteries, dye sensitized solar cells, fuel cells, etc.) due to their high conductivity and favorable mechanical properties. Plastic crystals are

formed by molecules whose structural motifs are characterized by long-range positional order but orientational dynamic disorder. In the last chapter of this thesis we show that the conductivity of succinonitrile, the most prominent molecular plastic crystal electrolyte, can be increased when replacing part of the molecules in the crystalline lattice by acetonitrile or glutaronitrile. Addition of glutaronitrile effectively enlarges the experimental temperature range of the plastic crystalline phase of pure succinonitrile, allowing a study of the glass-like transition produced by the freezing of molecular reorientational motions. It is found that these solid mixtures display self-diffusion of neutral and ionic molecular species, which give rise to an exceptionally high ionic conductivity at room temperature. Quite unexpectedly, the succinonitrile-rich co-crystals with glutaronitrile display a perfect coupling between the molecular self-diffusion and the on-site reorientational dynamics. These co-crystals are found to obey the Walden rule obeyed by (ideal) liquid electrolytes, which entails that a viscosity against self-diffusion may be defined for these materials. Addition of lithium salts to succinonitrile-glutaronitrile mixture enhances the ionic conductivity but slows down the collective molecular dynamics of the mixtures, which lead to the breakdown of Walden rule, which indicates that the coupling is only valid when charge transport is dominated by self-diffusion of bulky molecular ions inherent to succinonitrile or glutaronitrile, while the motion of smaller atomic Lithium ions is decoupled from the molecular dynamics. We report the first and so-far only known example of molecular plastic crystal exhibiting a perfect agreement between the temperature dependence of the ionic motion and that of the collective reorientational dynamics. Our findings demonstrate a new path to a considerable conductivity enhancement in plastic crystals and may allow a full understanding of the correlation between ion diffusion and molecular dynamics in orientationally disordered phases. The samples show in general a tendency to phase-segregate: the liquid-to-plastic transition takes place in two steps, with a coexistence of liquid and plastic phase in a temperature interval, as found in many binary systems, and at least partial crystallization of succinonitrile-rich plastic domains in some cases. The latter leads to the presence of perfectly

ordered, high-density crystallites, which in some cases give rise to a space-charge relaxation associated with ion accumulation at the crystallite surfaces.

The conclusions reached in this thesis provide a solid basis for further research on molecular dynamics and conductivity properties of other fullerene derivatives and plastic crystalline ionic conductors.

# *List of Publications*

M. Zachariah, M. Romanini, P. Tripathi, J. LI.Tamarit and R. Macovez. Molecular Diffusion and Dc Conductivity Perfectly Correlated with Molecular Rotational Dynamics in A Plastic Crystalline Electrolyte. *Phys. Chem. Chem. Phys.* **2015**, 17, 16053-16057.

M. Zachariah, M. Romanini, P. Tripathi, M. Barrio J. LI.Tamarit and R. Macovez. Self-Diffusion, Phase Behavior, and $Li^+$ Ion Conduction in Succinonitrile-Based Plastic Cocrystals. *J. Phys. Chem. C* **2015**, 119, 27298-27306.

M. Zachariah, E. Mitsari, M. Romanini, P. Zygouri, D. Gournis, and J. Ll. Tamarit and R. Macovez. Water-Triggered Conduction Mediated by Proton Exchange in A Hygroscopic Fulleride and Its Hydrate. *J. Phys. Chem. C* **2015**,119, 685-694.

R. Macovez, M. Zachariah, M. Romanini, P. Zygouri, D. Gournis, and J. Ll. Tamarit, Hopping Conductivity and Polarization Effects in A Fullerene Derivative Salt. *J. Phys. Chem. C* **2014**, 118, 12170-12175.

M. Zachariah, M. Romanini, P. Zygouri, D. Gournis, M. Barrio, J. Ll. Tamarit R.Macovez. Variable-Range Electron Hopping, Conductivity Cross-Over and Space-Charge Relaxation in $C_{60}Br_6$. *Synthetic Metals* **2016**, 217, 123-128.

# Acknowledgement

This thesis becomes a reality with the support and help of many individuals. I would like to express my sincere thanks to all of them.

Foremost, I am grateful to the God, for His blessings for good health and wellbeing that were necessary to complete this thesis.

I would like to express my sincere gratitude to Prof. Josep Lluis Tamarit for giving an opportunity to do my research in GCM group and gave access to the laboratory and research facilities. Without this precious support it would not be possible to conduct this research.

I would like to express my deepest thanks and immeasurable appreciation to my supervisor Roberto Macovez for the continuous support in research, for his patience, motivation, and immense knowledge. His advices, valuable comments, suggestions and support helped me in all the time of research and in writing of this thesis. I could not have imagined having a better supervisor like you.

My thanks and appreciation goes to my friends in GCM group for the encouraging discussion and for the fun we have had in the last 4 years and also other members in GCM group who have willingly helped me in completing this thesis.

Last but not the least; I would like to thank my family for supporting me throughout these years.

! Thank you!  Gracias!